



UNIVERSITÀ DEGLI STUDI DI CAMERINO

DIPARTIMENTO DI FISICA

&

UNIVERSITEIT ANTWERPEN

DEPARTEMENT FYSICA

JOINT DOCTORAL COURSE IN

Theoretical and Experimental Physics

**Multi-band superfluidity and BEC-BCS
crossover in novel ultrathin materials**

Author:
Sara CONTI

Supervisors:
Prof. David NEILSON
Prof. Andrea PERALI
Prof. Francois PEETERS

Abstract

Multi-band superfluidity and BEC-BCS crossover in novel ultrathin materials

This thesis presents an inquiry into multi-component electron-hole superfluidity in coupled ultrathin layer systems. Multi-component superfluidity is a novel quantum phenomenon that arises in semiconductors when multiple bands provide multiple pairing channels. The thesis focuses on two systems that define two very different classes of multi-band systems. We find that they can generate multi-component superfluids with fundamentally different properties. One system consists of two parallel bilayer graphene sheets and the other system is a heterostructure of two Transition Metal Dichalcogenide monolayers MoSe₂ and WSe₂.

In the Double Bilayer Graphene system, superfluidity is multi-component because both conduction and valence band participate in the pairing. This is due to the small tunable band gap between the conduction and valence bands in bilayer graphene. This system is a novel multi-band system because, in contrast with conventional multi-band superconductors, here the multi-bands are not nested and there is a unique Fermi surface.

In the double TMD monolayer system, superfluidity is multi-component because of the splitting of the bands caused by strong spin-orbit coupling. This superfluid has the same concentric subbands as in the multi-band superconductors, implying the potential existence of all the associated novel quantum phenomena that can arise from interference between the multi-condensates.

The investigation of the pairing processes is carried out using a mean field multi-component approach. The Coulomb pairing interaction between electrons and holes is a long-range interaction and screening effects must be fully accounted for in our approach. We show that it is readily possible to tune these systems between the strongly interacting regime and the weakly interacting regime by tuning the carrier density.

Because of the different pairing symmetries, the two-component condensates in these two systems are strikingly different. In Double Bilayer Graphene, the two condensates are strongly coupled. However, the closeness of the valence band to the conduction band contributes in a strong way to the screening and this results in a weakening of the superfluidity. On the other hand, in double TMD monolayers, the spin-orbit coupling makes the two condensates decoupled, and the large band gap makes the screening from the valence band negligible.

We show that in both systems the multi-component nature of the superfluidity can be switched on and off. In Double Bilayer Graphene, by tuning the band gap, it is possible to continuously tune the proximity in energy of the conduction and valence bands and thus the importance of the valence band in the pairing and screening. In double TMD monolayers, by tuning the density and by choosing the doping in the monolayers, it is possible to activate or suppress the second component of the superfluidity.

This thesis provides new insights into the field of the multi-component superfluidity: we predict observable superfluidity in two systems confirmed with recent experimental observations and we demonstrate the possibility to tune the multi-component character in both the class of materials. As a further result, we determine optimal electronic conditions and optimal ranges of carrier densities for these systems for maximising the transition temperature of the superfluidity.

Samenvatting

Multicomponent superfluiditeit en BEC-BCS crossover in nieuwe ultradunne materialen.

Deze thesis presenteert een studie naar multicomponent elektron-holte superfluiditeit in gekoppelde ultradunne gelaagde systemen. Multicomponent superfluiditeit is een nieuw kwantumfenomeen dat zich voordoet in halfgeleiders wanneer meerdere banden meerdere koppelingskanalen bieden. De thesis richt zich op twee systemen die twee zeer verschillende klassen van multiband systemen definiëren. We vinden dat ze multicomponent superfluida genereren met fundamenteel verschillende eigenschappen. Het ene systeem bestaat uit twee parallelle bilagen van grafeen en het andere is een heterostructuur van twee transitiemetaal dichalcogenide monolagen MoSe_2 en WSe_2 .

In het dubbel bilaag grafeen systeem is superfluiditeit multicomponent omdat zowel de conductie- als de valentieband deelnemen aan de koppeling. Dit komt door de kleine afstembare bandkloof tussen de conductie- en valentiebanden in bilaag grafeen. Dit systeem is een nieuw multiband systeem omdat, in tegenstelling tot conventionele multiband supergeleiders, de multiband hier niet genest zijn en er een uniek Fermi-oppervlak is.

In het dubbele TMD monolaag systeem is superfluiditeit multicomponent vanwege de splitsing van de banden veroorzaakt door een sterke spin-baan koppeling. Dit superfluidum heeft dezelfde concentrische subbanden als de multiband supergeleiders, wat de potentiële aanwezigheid impliceert van alle bijbehorende nieuwe kwantumverschijnselen die kunnen ontstaan door inmenging tussen de multicondensaten.

Het onderzoek van de koppelingsprocessen wordt uitgevoerd met behulp van een multicomponent gemiddelde-veld aanpak. De Coulomb koppelingsinteractie tussen elektronen en holtes is een lange afstandsinteractie en screeningeffecten moeten in onze aanpak volledig in rekening worden gebracht. We laten zien dat deze systemen eenvoudig kunnen worden afgestemd tussen het sterk interagerende regime en het zwak interagerende regime door de ladingsdichtheid aan te passen.

Als gevolg van de verschillende koppelingsymmetrieën zijn de tweecomponent condensaten in deze twee systemen opvallend verschillend. In dubbel bilaag grafeen zijn de twee condensaten sterk gekoppeld. De nabijheid van de valentieband tot de conductieband draagt echter sterk bij aan de screening en dit leidt tot een verzwakking van de superfluiditeit. Aan de andere kant maakt de spin-baan koppeling in dubbele TMD monolagen de twee condensaten ontkoppeld en de grote bandkloof zorgt ervoor dat de afscherming van de valentieband te verwaarlozen is.

We tonen aan dat in beide systemen het multicomponent karakter van de superfluiditeit in- en uitgeschakeld kan worden. In dubbel bilaag grafeen is het door het afstemmen van de bandkloof mogelijk om het energieverval tussen de conductie- en valentiebanden continu af te stemmen en daarmee ook het belang van de valentieband bij het koppelen en screenen. Bij dubbele TMD monolagen is het mogelijk om, door de dichtheid af te stemmen en door de dotering in de monolagen te kiezen, de tweede component van de superfluiditeit te activeren of te onderdrukken.

Deze thesis biedt nieuwe inzichten op het gebied van multicomponent superfluiditeit: we voorspellen waarneembare superfluiditeit in twee systemen, wat bevestigd is in recente experimentele waarnemingen, en we demonstreren de mogelijkheid om het multicomponent karakter af te stemmen in beide materiaalklassen. Als een verder resultaat bepalen we voor deze systemen optimale elektronische omstandigheden en optimale

bereiken van ladingsdichtheden voor het maximaliseren van de overgangstemperatuur van de superfluiditeit.

Sommario

Superfluidità a bande multiple e BEC-BCS crossover in nuovi materiali ultrasottili

Questa tesi presenta un'indagine sulla superfluidità multi-componente di elettroni-lacune in strati accoppiati di materiali ultrasottili. La superfluidità multi-componente è un nuovo fenomeno quantistico che si manifesta nei semiconduttori dove sono presenti più bande elettroniche che forniscono canali di accoppiamento multipli. La tesi si concentra su due sistemi che definiscono due classi molto diverse di sistemi a multi-bande. In questi sistemi si possono generare superfluidi multi-componente con proprietà fondamentalmente diverse. Un sistema è costituito da una coppia di doppio foglio di grafene (DBG) e l'altro sistema è un'eterostruttura di due strati di metalli di transizione dicalcogenuri (TMD) MoSe_2 e WSe_2 .

Nel sistema DBG, la superfluidità è multi-componente perché sia la banda di conduzione che quella di valenza partecipano all'accoppiamento. Ciò è dovuto al piccolo gap energetico tra le bande di conduzione e di valenza nel doppio foglio di grafene. Questo sistema è un nuovo sistema multi-banda perché, contrariamente ai convenzionali superconduttori a multi-banda, qui le diverse bande non sono nidificate e c'è una sola superficie di Fermi.

Nel sistema a doppio TMD, la superfluidità è multi-componente a causa della divisione delle bande causata dal forte accoppiamento spin-orbita. Questo superfluido ha le stesse sottobande concentriche dei superconduttori a multi-banda, implicando la potenziale esistenza di tutti i nuovi fenomeni quantistici associati che possono derivare dall'interferenza tra i diversi condensati.

L'indagine dei processi di accoppiamento viene fatta utilizzando un approccio teorico multi-componente a campo medio. L'attrazione di Coulomb tra elettroni e lacune è un'interazione a lungo raggio e gli effetti di screening devono essere presi in considerazione nel nostro approccio. Mostriamo che è possibile far evolvere questi sistemi tra un regime fortemente interagente e un regime debolmente interagente modificando la densità dei portatori di carica.

A causa delle diverse simmetrie di accoppiamento, i condensati bi-componenti in questi due sistemi sono sorprendentemente diversi. Nel sistema DBG, i due condensati sono fortemente accoppiati. Tuttavia, la vicinanza della banda di valenza alla banda di conduzione contribuisce in modo forte allo screening e ciò si traduce in un indebolimento della superfluidità. D'altra parte, nei doppi strati di TMD, l'accoppiamento spin-orbita rende i due condensati disaccoppiati e l'ampio gap energetico tra le bande di conduzione e quelle di valenza rende trascurabile lo screening dalla banda di valenza.

Mostriamo che in entrambi i sistemi la natura multi-componente della superfluidità può essere attivata e disattivata. Nel sistema DBG, regolando il gap energetico tra le bande è possibile regolare continuamente la prossimità in energia delle bande e quindi l'importanza della banda di valenza nell'accoppiamento e nello screening. Nei doppi strati di TMD, regolando la densità e scegliendo il doping negli strati, è possibile attivare o sopprimere il secondo componente della superfluidità.

Questa tesi fornisce nuove intuizioni nel campo della superfluidità multi-componente: prevediamo una superfluidità osservabile in due sistemi confermata con recenti osservazioni sperimentali e dimostriamo la possibilità di cambiare il carattere multi-componente in entrambe le classi di materiali. Come ulteriore risultato, determiniamo condizioni elettroniche ottimali e intervalli ottimali di densità per questi sistemi per massimizzare la temperatura di transizione della superfluidità.

Acknowledgements

I want to start this thesis with the most important part: saying thank you and giving credit to all those who helped me and contributed to this work in many different ways.

First of all I would like to thank my promoters, because if two heads are better, then three are excellent. Thanks to Prof. David Neilson, for the precious guidance during these years, for the instructive, intense and enjoyable discussions and for the enormous patience with my English. Thanks to Prof. Andrea Perali, for letting me discover this exciting field in 2013, for the rich knowledge in the field transmitted to me during these years and for also giving me the opportunity to have experience in the field of didactics. Thanks to Prof. Francois Peeters, for the wonderful opportunity of the Joint Doctoral Program and for always giving me clear objectives that made me grow up as a young researcher.

I would like to thank the referees, for reviewing this work and providing me with their insightful comments.

I would like to thank my colleagues whose contributions enriched this thesis: Mohammad Zarenia, Michele Pini, Alfredo Vargas Paredes, Samira Saberi-Pouya, and Matthias Van Der Donck. I would also like to thank everyone in the CMT group of the University of Antwerp for the wonderful atmosphere and for the friendly support I received during these years.

Finally, I want to thank my family, because with their proud support they made all this possible. Thanks to my Italian friends that were there for me every time I needed advice or simply a hug. Last but not least, thanks to my best friend and partner Slavisa Milovanovic, that for three years has been holding my hand in all the happy and stressful situations.

Sara Conti
Antwerp and Camerino, May 2020

Contents

Abstract	iii
Acknowledgements	ix
Introduction and State of Art	1
1 Introduction and Motivation	3
1.1 Motivation of the Thesis	3
1.2 Organization of the Thesis	5
1.3 Collaborations and Publications	6
2 Electron-hole Superfluidity	7
2.1 Superconductivity and BCS-BEC Crossover	7
2.1.1 BCS-BEC Crossover	8
2.2 Indirect Exciton Superfluidity in 2D Materials	9
2.2.1 Experimental Techniques	11
2.3 GaAs Double Quantum-Wells	13
2.4 Double Monolayer Graphene	14
2.5 Double Bilayer Graphene	16
2.6 Double Monolayer Phosphorene	16
2.7 Double Monolayer Transition Metal Dichalcogenide	17
Research Activity and Publications	19
3 Multi-component Electron-Hole Superfluidity in Multi-band System	21
3.1 Multi-band Electron-Hole Superfluidity	21
3.2 Two-Band Mean Field Theory including Interband Pairing.	26
3.2.1 BEC-BCS crossover	31
3.3 Random Phase Approximation for the Screening	31
3.3.1 Screened Interaction in the Normal State	32
3.3.2 Screening Interaction in the Superfluid State	33
4 BCS-BEC Crossover in Double Bilayer Graphene	37
4.1 Double Bilayer Graphene	38
4.2 Mean Field Equations	39
4.3 Results	44
4.4 Conclusions	49
5 Multi-component Screening and Superfluidity in Biased DBG	51
5.1 The extended theoretical approach	52
5.1.1 Bilayer Graphene Dispersion	52
5.1.2 Screened Interaction in Double Bilayer Graphene	54
5.2 Results	56
5.2.1 Polarizabilities with Bilayer Graphene	56

5.2.2	Multi-band Screening	58
5.2.3	Superfluid Gaps	60
5.2.4	One-band Superfluidity from Multi-band Screening	63
5.3	Conclusion	64
6	Electron-Hole Superfluidity in Coupled TMD Monolayers	67
6.1	Double TMD Monolayer	68
6.2	Mean Field Equations	68
6.3	Results	74
6.3.1	Multi-component superfluidity in different TMD monolayers	77
6.4	Transition Temperature	77
6.5	Conclusion	78
7	3D Superlattice to exploit high-T_c electron-hole superfluidity	81
7.1	3D superlattice	82
7.2	Results	83
7.3	Conclusions	85
	Conclusions	87
8	Conclusions and Future perspectives	89
8.1	Conclusions	89
8.2	Future Outcomes	91
A	Two-Band Green Functions	93
A.1	Double Bilayer Graphene Green Functions	99
A.2	Double TMD monolayer Green Functions	99
B	Density Response Function in the Superfluid State	101
B.1	Double Bilayer Graphene Polarizabilities	101
B.2	Double TMD monolayer Polarizabilities	103
C	Two-Body Binding Energy	107
C.1	Double Bilayer Graphene Binding Energy	107
C.2	Double TMD monolayer Binding Energy	108
	Bibliography	109
	Curriculum Vitae	121

List of Abbreviations

2D	2-Dimensional
BCS	Bardeen-Cooper-Schiffer
BEC	Bose-Einstein Condensation
DQW	Double Quantum Well
DMG	Double Monolayer Graphene
DBG	Double Bilayer Graphene
DMP	Double Monolayer Phosphorine
TMD	Transition Metal Dichalcogenide
RPA	Random Phase Approximation
BKT	Berezinskii-Kosterlitz-Thouless

Introduction and State of Art

Chapter 1

Introduction and Motivation

Quantum matter is everywhere, from the interiors of neutron stars to the electrons in everyday metals. Among the many types of quantum physics phenomena, particularly spectacular are the phenomena of superconductivity and superfluidity where at low temperature, quantum mechanics manifests itself at the macroscopic scale. Ever since superconductivity was discovered in 1911 [1] and superfluidity was discovered in 1937 [2, 3], physicists have made enormous efforts to explain the behaviour observed in different systems.

Superfluidity is a state of matter with very strange properties. A superfluid is a fluid that flow with zero viscosity and thus without any loss of kinetic energy. At the heart of superfluidity lies the spontaneous quantum coherence. Coherence refers to the existence of spatial correlation of the quantum wave-function over the entire system, so components of the system are no longer individual but act together. The spontaneous coherence is a feature common to other quantum phenomena such as Bose-Einstein condensation (BEC) and superconductivity.

In Bose-Einstein condensation an ensemble of bosons is cooled below a critical temperature and condense to occupy a single quantum state. However not all Bose-Einstein condensates behave as superfluids, and not all superfluids are Bose-Einstein condensates.

Superconductivity is usually associated with regular metals, in which free charge carriers exist at the Fermi level and can feel an attraction. Superconductivity originates from the spontaneous coherence of pairs of these charged particles. As a result, when it is cooled below a characteristic critical temperature, electrons flow in the metal with zero electrical resistance and expulsion of magnetic flux fields can occur.

There is a countless number of experimental systems where a macroscopic quantum order is established, including helium liquids (^3He and ^4He), superconductors, Bose-Einstein condensates of ultracold alkali gases and, more recently, exciton condensates. Such systems are hard to describe theoretically because strong quantum correlations between particles from which they are composed produce phenomena that cannot be predicted by studying the behaviour of individual particles alone. Even the simplest models of strongly correlated systems are difficult to solve theoretically. Each of these systems has opened questions on our fundamental understanding of many-body physics and has led to novel research tools as well as applications.

1.1 Motivation of the Thesis

After the discovery of superconductivity and superfluidity, in a quest to build devices that carry electricity with low dissipation at high temperatures, researchers have explored the possibility of engineering electrical condensates out of strongly bound pairs of electrons and holes, called excitons. In 1961, a theory was proposed by Blatt, Böer and Brandt, according to which an electron and a hole optically excited within a solid, oppositely charged, bind together to form a bosonic exciton [4]. The binding energy between

the exciton electron and hole can be strong, greatly exceeding their thermal energy at room temperature.

Experimentally exciton condensation or superfluidity has proved challenging because excitons are not the ground state of the system and their recombination is so fast to make realization and measurement of such a phase extremely hard to achieve. There have been many attempts to address this problem, among them a promising one is the coupled layer system, where electrons and holes are physically separated by a tunnel barrier [5]. Exciton condensates have been realized in spatially separated semiconductor quantum wells. However, such devices either involved very high magnetic fields [6] or very low temperatures [7].

The quest for an optimal condition and the optimal system to realise electron-hole superfluidity was shaken up in 2004 by the discovery of graphene [8], that made real the confinement and control of carriers in atomically thin layers [9]. In the last 10 years, an increasing number of experiments demonstrated the possibility to grow or exfoliate single layers of material: the so-called two-dimensional (2D) materials. There has been an explosion of experimental and theoretical results showing that, because of their electronic properties, 2D materials can host a rich variety of strongly correlated phases, such as unconventional superconductivity, Mott-insulator and Wigner crystallization in presence of magnetic field. Because of this, a number of 2D coupled layer systems have been proposed to host electron-hole superfluidity also at temperatures as high as 100 K. In this thesis, we investigate two particular semiconductor configurations for double layer systems:

- Double bilayer graphene, two bilayer graphene sheets separated by a boron nitride insulating layer;
- Double Transition Metal Dichalcogenides monolayers, two Transition Metal Dichalcogenides monolayers separated by a boron nitride insulating layer.

The choice of these two particular systems is supported by theoretical works [10, 11] that show the possibility to have high-temperature superfluidity in these systems. An additional interest in these semiconductors is that the pairing symmetries are more complicated with respect to conventional metallic systems because they have electronic features driven by their multi-band characters. The presence of multiple pairing channels can lead to multi-component superfluidity and make the system resemble a multi-band superconductor, where the increased number of degrees of freedom allows for emergent quantum effects that are otherwise unattainable in single-component superconductors [12].

In this thesis, we explore the physics behind the multi-component superfluidity that is related to this unconventional pairing channels, with the aim to answer some important open questions: What possible ways are there to pair electrons and holes in a multi-band system? What differences does that make for the paired states and their properties? Do physical parameters exist that play a key role in explaining and controlling the observed types of pairing?

This thesis is the final result of a systematic and detailed investigation of superfluidity and BCS-BEC crossover phenomena in the two different systems. We will show that the two systems present significantly different multi-band pairing symmetries that lead to striking different quantitative and qualitative results. These results are in good agreement with important experimental observations on exciton condensation and superfluidity that have been reported in double layer systems extremely similar to the ones investigated here [13, 14].

1.2 Organization of the Thesis

The thesis is organized as follows.

In the **second chapter**, we recall some basics of BCS theory that successfully explains conventional superconductivity, and we cover the basics of superfluidity in semiconductor double layer systems generated by electron-hole pairing. We establish the central theoretical issues and experimental challenges associated with the study of electron-hole superfluidity, and we show advantages and limits of real systems we propose for the investigation of this phenomenon. This chapter is fundamental to understanding the background and the motivations of this work.

The **third chapter** deals with an analytical theoretical approach to describe double layer electron-hole superfluidity. We adapt mean field theory for superconductivity to the multi-component case and we derive superfluid equations valid for a multi-band electron-hole system. We discuss the Random Phase Approximation used to describe the screening, we describe the strong competition between superfluidity and the screening characteristic of double layer systems with Coulomb interactions. We also extend the screening approach to the case of a multi-band double layer system.

In the **fourth chapter**, the multi-band approach is applied to the double bilayer graphene system. We show that because of the small band gap between the conduction and valence band in bilayer graphene, the valence band also contributes to the pairing and the superfluidity has two components. The effects on the superfluidity of the proximity in energy of the bands in bilayer graphene are investigated by tuning the small band gap. We give numerical results obtained using the mean field equations at zero temperature and we discuss the results both in the BCS and BEC limits. We show that by tuning the band gap it is possible to modify the properties of the superfluidity in double bilayer graphene.

In the **fifth chapter**, the multi-band approach of Chapter 4 is extended to also include the contributions of the valence band to the screening in double bilayer graphene. In addition, we include the distortion of the low-energy band structure of bilayer graphene from parabolic to Mexican hat-like, which accompanies the opening of the band gap. We show that the competition between superfluidity and the screening is affected by these two effects in a significant way.

In the **sixth chapter**, the multi-band approach is applied to the double Transition Metal Dichalcogenide monolayer system. We include the effect of the splitting of the bands caused by the strong spin-orbit coupling. We show that because the spin splitting is larger in the valence band with respect to the conduction band, there is a large misalignment between the electron and hole bands in the two monolayers from the spin-orbit coupling. We give numerical results obtained using the mean field equations at zero temperature. The superfluidity can be multi-component, and the multi-condensates are strikingly different due to the band misalignment. We show that these properties display a remarkable sensitivity to the choice of doping of the two monolayers.

In the **seventh chapter**, we propose a new system based on a stack of Transition Metal Dichalcogenide alternating electron and hole monolayers to investigate electron-hole superfluidity in a three-dimensional (3D) superlattice. We show that, by considering a 3D superlattice, we overcome the restriction of the low critical temperatures associated with the Berezinskii-Kosterlitz-Thouless transition temperature associated with 2D systems.

The **eighth chapter** summarizes all our new results. We compare the expectations given in each chapter to the actual findings. This thesis ends with an overview of possible extensions in future works.

1.3 Collaborations and Publications

The research presented in this thesis is the result of the joint PhD project born from the collaboration between the University of Camerino (Italy) and the University of Antwerp (Belgium). The thesis is inspired by many discussions, research notes and joint publications. The research was supervised by Prof. David Neilson and Prof. Andrea Perali, from the University of Camerino, and by Prof. Francois Peeters, from the University of Antwerp. This work was partially supported by the Flemish Science Foundation (FWO-VI), and the Methusalem Funding of the Flemish Government. The research presented in this thesis was performed in collaboration also with other students of both Universities. The work has been published or submitted to scientific journals:

- Chapter 3: The theoretical approach was refined also thanks to discussions with Alfredo Vargas Paredes (University of Camerino and University of Antwerp).
- Chapter 4: A manuscript was published in Physical Review Letters [15] and a Feature Article was published in the Belgian Physics Society Magazine [16].
- Chapter 5: A manuscript was published in Physical Review B [17].
- Chapter 6: A manuscript has been submitted in Physical Review Letters [18] in collaboration with Matthias Van der Donck (University of Antwerp), and a Special issue Article was published to Condensed Matter Journal [19].

This thesis contains also results of three manuscripts published or submitted in collaboration with Mohammad Zarenia (University of Missouri (USA)) [20], Matthias Van der Donck (University of Antwerp) [21] and Samira Saberi-Pouya (University of Antwerp) [22].

The future outcomes presented in Chapter 7 are included in a Project submitted to the Research Foundation - Flanders (FWO) [23].

Chapter 2

Electron-hole Superfluidity

In a system of Bosons, a Bose-Einstein Condensate (BEC) can appear when below a certain critical temperature a macroscopic fraction of bosons occupies the lowest quantum state. The BEC concept has been used to elucidate the anomalies of superfluid helium [2, 3]. During the 1960s several authors proposed that compact excitons in crystals can show properties characteristic of bosonic systems and a tendency to Bose condense at low temperatures [4]. This is interesting because the small effective mass of the excitons can make the condensation temperature high. In 1985, Ref. [24] proposed Bose-Einstein condensation of compact electron pairs as the strongly interacting limit of a continuum that on the weakly interacting side terminates with BCS superconductivity.

In this chapter, we will introduce the electron-hole superfluidity. We will outline the key features of electron-hole superfluidity discussing similarities with BCS superconductivity. Comparing these two phenomena we will identify advantages and challenges that electron-hole superfluidity offers with respect to superconductivity.

2.1 Superconductivity and BCS-BEC Crossover

In 1957, Bardeen, Cooper and Schrieffer (BCS) successfully explained superconductivity microscopically in terms of electron-electron pairing [25]. Even though electrons mutually repel each other due to the Coulomb interactions, there can exist a net electron-electron attraction arising from the dynamic exchange of phonons associated with the crystal lattice. When an electron propagates through the crystal, other electrons are repelled and positive ions are attracted, so during the propagation, the electron-electron interaction is mediated also by the phonons in the crystal lattice. An electron in a state with momentum \mathbf{k} can excite a phonon of crystal momentum \mathbf{q} , leaving the electron in a state with crystal momentum $\mathbf{k}' = \mathbf{k} - \mathbf{q}$. Later a second electron can absorb the phonon and pick up the momentum \mathbf{q} . Such a displacement of the crystal lattice will produce a modulation of the electron charge density and of the effective potential for the electrons in the solid. There will be a weak attractive interaction for phonon frequencies ω that are below the Debye frequency ω_D . The restriction in frequency can be translated in terms of energy. The electron energies involved are all within the range $\pm\hbar\omega_D$ of the Fermi energy E_F . Therefore, electrons which mutually attract are near the Fermi surface [26].

The weak attractive interaction leads to the formation of a bound state made of two particles, a *Cooper pair*. The particles in the pairs has opposite momentum and opposite spin. The ground state of the weakly interacting Fermi liquid becomes unstable with respect to the formation of bound states and this lowers the energy. This instability leads to the appearance of an energy gap Δ in the single-particle excitation spectrum. This energy gap is large at low temperatures and vanishes at the transition temperature when superconductivity ceases to exist. The energy gap was first directly observed in 1960 [27], as a verification of the BCS theory.

2.1.1 BCS-BEC Crossover

The BCS theory gives an expression that shows how the gap grows with the strength of the attractive interaction and the single particle density of states at the Fermi level. An attractive fermionic system in a condensed state may exhibit different behaviours that depend on the strength of the attractive interaction. As the strength increases, the fermionic system varies continuously from a weakly interacting regime described by the BCS theory, to a strongly interacting regime that has BEC properties [28]. These two regimes are the two ends of a continuum of quantum mechanical behaviour, *BCS-BEC crossover* phenomenon.

In the BCS framework, Cooper pairs condense at low temperature into a coherent quantum state. As a result, the electron fluid can flow through the system without dissipation. The condensate of Cooper pairs is a superconductor. The Cooper pair average radius r_{pair} is large compared with the average electron spacing. A huge number of pairs is contained in a superconductor spheric volume of radius r_{pair} , so the Cooper pairs are greatly overlapping.

If the attraction strength in the pairs greatly increases so that the pairs radius r_{pair} , becomes smaller than the separation between particles, we reach a condition where the pairs are compact and there is no overlap. Two compact tightly bound fermions can be treated as a composite boson, therefore the pairs satisfy Bose-Einstein statistics. We expect that these composite bosons can undergo Bose-Einstein Condensation at low temperatures, condensing into a single quantum state. Being in a single quantum state leads the system to have superfluid properties. This regime is called the BEC limit.

In an attractive fermionic system, it is possible to observe a smooth evolution between the two limits, from overlapping Cooper pairs in a Fermi gas to a non-overlapping composite bosonic gas (Fig. 2.1) tuned by the attractive potential. In evolving continuously from one limit to the other the system passes through a regime called the *Crossover*, an intermediate regime between overlapping Cooper pairs and non-overlapping composite bosons.

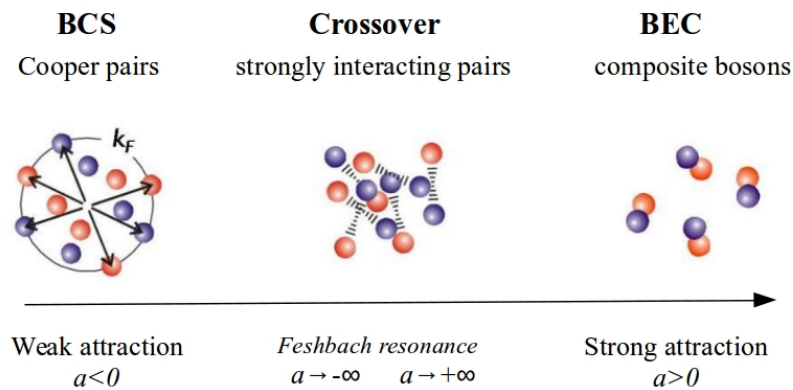


FIGURE 2.1: Three regimes of BEC-BCS crossover phenomenon in an attractive fermionic system. The BCS regime of overlapping Cooper pairs, the Crossover regime, and the BEC regime of localized composite bosons. a is the s -wave scattering length.

The BCS-BEC crossover phenomena have been extensively studied in experiments with cold atoms trapped by an external magnetic field [29]. The atoms especially used have been ^6Li and ^{40}K . These atoms have an odd number of electrons and even number of nucleons, so with an odd total number of fermions, they behave like fermions.

In a system of cold atoms, the interaction strength is described by a single parameter, the s-wave scattering length a . For a weak attractive interaction between atoms, the values of a are small and negative. If we increase the interaction, a becomes large and negative just before a bound state appears [30]. When the bound state appears we have a resonance. The molecular state responsible for the resonance has a magnetic moment that is different from the magnetic moment of the colliding atoms, this is the *Feshbach resonance*. a diverges to $-\infty$, at the Feshbach resonance the bound state appears, after which a diverges positively $+\infty$. As the attractive interaction is further increased the atoms become more deeply bound into molecules [31] (Fig. 2.1). This tuning of a can be used to drive the system continuously from the BCS regime, where $a < 0$, through the Crossover regime to the BEC regime, where $a > 0$ [32]. Experimentally the tuning of the scattering length requires the ability to manipulate the Feshbach resonances and this can be done by using a variety of magnetic trap configurations.

2.2 Indirect Exciton Superfluidity in 2D Materials

Trapped cold atoms represent an good testing ground to study BCS-BEC crossover phenomenon, but in recent years it has been studied also in semiconductor systems using excitons. Excitons, bound state of an electron and a hole optically excited within the crystal, have been used for the interpretation of certain optical properties in semiconductors. Excitons are bound states which can be regarded as hydrogen-like states of electron-hole pairs bound by the Coulomb interaction. The binding energy and the exciton radius are determined by the effective Rydberg energy, R_y and the effective Bohr radius, a_B ,

$$R_y = \frac{e^2}{4\pi\epsilon\epsilon_0} \frac{1}{2a_B}, \quad (2.1)$$

$$a_B = \frac{\hbar^2 4\pi\epsilon\epsilon_0}{m_r e^2}, \quad (2.2)$$

with ϵ the dielectric constant of the insulating barrier and m_r the reduced effective mass of the electron and hole.

Several authors proposed [4] and demonstrated [33] that excitons can be regarded as independent particles which obey Bose-Einstein statistics. At very low temperatures excitons show spontaneous phase coherence and they can undergo Bose-Einstein condensation [34, 35]. Here the attraction between the carriers is directly driven by the Coulomb force.

Because of the very fast electron-hole recombination rate, excitons have a finite lifetime. Experimentally, in order to create a cold exciton gas, the exciton lifetime should be large compared to the exciton cooling time [36, 37]. Furthermore, the realization of a cold and dense exciton gas requires for excitonic state to be the ground state [33]. These requirements can be fulfilled using a bound state of a electron and a hole that are kept spatially separated. We will use the term *indirect exciton*.

Semiconductor Double Quantum-Wells (DQW) were initially proposed to realize indirect excitons [38] with electrons confined in one well and holes in the other. The electrons and the holes are separated by a high insulating barrier to avoid tunnelling and recombination. The spatial separation allows one to reduce the overlap of the electron and hole wave functions. The lifetimes of the indirect excitons in the resulting structures can be orders of magnitude longer than those of conventional excitons [5, 39]. Later, the quest for an optimal system received a boost with the discovery of graphene [8]. This opened the way for development and fabrication of a large number of two-dimensional

(2D) materials as platforms for exciton devices. These devices are very stable under ambient conditions and their crystal quality is very high [40].

In a double layer system (Fig. 2.2), the electrons and holes can move along the layers and contribute to the conduction. At sufficiently low temperatures, electron-hole pairs may condense into a superfluid.

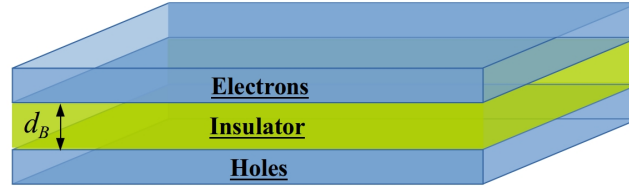


FIGURE 2.2: A double layer system with electrons in the upper layer and holes in the lower layer, d_B is the barrier thickness.

A key parameter in these double layer systems is the layer separation d_B :

- Electron-hole interaction is the Coulomb attraction so the distance between electron and hole should be small to make the interaction strong.
- Electron-hole recombination is driven by tunnelling processes between the layers. These will be negligible if the separation d_B is sufficiently large.

Typically the condition for superfluidity is satisfied when d_B is smaller than the effective Bohr radius a_B .

In 2D systems, the parameter that characterizes the strength of the correlations in the layer is $r_s = \langle V \rangle / \langle K \rangle$. When the average potential energy between the carriers V is larger than their average kinetic energy K , $r_s > 1$, correlation effects can be expected strong. An important advantage in these systems is that in atomically-thin 2D materials it is straightforward to tune r_s to large values:

- The kinetic energy can be modified by changing the electronic dispersion and the specific effective masses by means of external effects including gating, applying strain or an external magnetic field.
- The potential energy can be modified by tuning the density and thus the inter-particle distance r_0 , by means of gating or optical pumping, or by changing the dielectric environment of the 2D layer, that modifies the screening of the interaction.

This means that in a double layer system because we are able to tune r_s , we can in principle tune the BCS-BEC crossover [41]. When the average strength of the Coulomb interactions between carriers are much larger than their kinetic energies, the system is in the strongly interacting regime (BEC). A decrease in the average interaction brings the system across the Crossover regime to the weakly interacting regime (BCS).

We can write more explicitly r_s :

$$r_s = \frac{\langle V \rangle}{E_F} = \frac{e^2}{4\pi\epsilon\epsilon_0\langle r_0 \rangle} \frac{1}{E_F} = \frac{e^2\sqrt{\pi n}}{4\pi\epsilon\epsilon_0} \frac{1}{E_F(n)}. \quad (2.3)$$

where r_0 is the inter-particle distance and n is the density of the carriers. This means that, in contrast with ultracold atomic gases, in a double layer system we can experimentally tune the BCS-BEC crossover by tuning the carrier density n (Fig. 2.3).

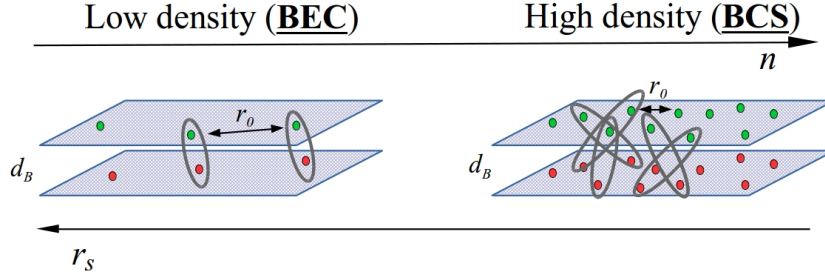


FIGURE 2.3: The BEC and BCS regimes of the BCS-BEC crossover phenomenon in a double layer system. r_0 is the average inter-particle separation. The different colors indicate electrons or holes.

At very low density, $r_s \gg 1$, the system is in the strongly interacting regime (BEC). This corresponds to large average inter-particle separation r_0 , $r_0 \gg d_B$. The size of the pair $r_{pair} < r_0$, so the pairs are compact.

At high density the inter-particle distance decreases and can be $r_0 < d_B$. The size of the pair is $r_{pair} < r_0$, so the pairs are overlapping. The system is in the weakly interacting regime (BCS).

Unlike in BCS superconductivity, in electron-hole superfluidity the interaction is a Coulomb interaction which is long-ranged, so the screening of the interaction needs to be taken into account. This represents a major new challenge. We will show in the next chapters that electron-hole superfluidity in double layer systems is a low-density phenomenon, because the screening of the pairing interaction at high densities ($r_0/a_B \leq 2.3$) is sufficiently strong and suppresses the superfluidity [10, 42].

2.2.1 Experimental Techniques

Different approaches have been suggested to detect electron-hole superfluidity, some signatures are based on transport measurements of Coulomb drag, some on tunnelling conductance between layers and others are based on optical observations of exciton luminescence.

Coulomb drag

Coulomb drag measures the friction between electrons and holes flowing in opposite layers arising from transfer of momentum between layers. The key technical requirement for this technique is to make independent electrical contact to the electron and hole parts of the condensate [43]. An electric current is driven in one layer, the *drive layer*, and this drags carriers in the other layer, the *drag layer*. The drag transresistivity ρ_D is defined as the ratio of the induced potential in the drag layer to the current density in the drive layer [44]. This measures how much the charges in one layer drag the charges in the other layer along with them. ρ_D is a sensitive signature of how electron and hole exchange momentum with each other.

In electron-hole layers when no condensate is present, the transresistivity is generally smaller than the isolated layer resistivity [45, 46]. At the temperature at which the condensate forms, the transresistivity is predicted to jump to a value comparable to the isolated layer resistivity. It then continues to increase with decreasing temperature, and it diverges in the limit of zero temperature [47].

As a function of temperature a deviation of ρ_D from the standard Fermi-liquid T^2 temperature dependence, which is based on the amount of phase space available for

thermal excitations, is expected as evidence of correlations [48] or the existence of exotic many-body phases.

Interlayer tunnelling

As discussed in Section 2.2, by adjusting the thickness of the barrier it is possible for the electrons and holes to interact strongly and yet have an extremely small probability of quantum mechanically tunnelling through the barrier. In an interlayer tunnelling conductance measurement, a voltage bias is applied between the two layers [6, 49].

Recently an enhancement of interlayer tunnelling conductance has been reported in a system of two graphene bilayers separated by a tungsten diselenide barrier [13]. This experimental observation is interpreted as evidence for the presence of coherent electron-hole pairs. The electrons in one layer are always positioned opposite holes in the other layer. To date there is no comprehensive theory of the mechanism, but the belief is that this effectively electrically shorts the two layers, allowing the electrons and holes to recombine without dissipation. In this way, enhanced tunnelling is an indirect signature of excitonic condensation.

Optical trap measurements

There are a number of techniques proposed to optically identify macroscopic spatial coherence using traps. Along with electrostatic traps [50], excitons have been studied in a variety of traps including strain-induced traps [51], traps created by laser-induced interdiffusion [52], magnetic traps [53], and laser-induced traps [54].

Optical identification techniques include:

- the appearance in photoluminescence measurements of bright localized spots with enhanced luminescence at fixed points on the sample [55];
- the abrupt appearance of a sharp inter-well exciton line in the photoluminescence spectra [56];
- an abrupt increase in the amplitude of interference fringes using shift-interferometry measurements, indicating a strong enhancement of the exciton coherence length [7];

However, optical measurement before 2007 were inconclusive because they discarded the key role of dark excitons in Bose-Einstein condensate [57]. Dark excitons are non-reactive optically because their electron and hole have the same spin. The role played by dark states in Bose-Einstein condensation is straightforward to understand theoretically since they have lower energy than the bright excitons for which the electron and hole have opposite spin. This is because dark excitons are not affected by repulsive interband Coulomb processes like photon emission. The Bose-Einstein condensate of excitons has an internal spin structure governed by exchanges between excitons. At large density, fermion exchanges between dark and bright excitons modifies the structure of the excitonic ground-state so that a fraction of bright excitons that can enter the condensate. On the other hand, in the very low-density regime, the condensate is made up only of dark excitons. Experimental studies are of necessity made above the density threshold for the emergence of a bright component in the exciton condensate. At high density the exciton condensate is no longer fully dark and radiates a weak photoluminescence. This emission can then be used as signature of the macroscopic spatial coherence of the condensate [58].

In the next section we give an overview of systems that have been proposed for observing electron-hole superfluidity in which these experimental techniques have been

applied. Interlayer tunnelling and optical measurements have successfully identified signatures of exciton condensation. However, drag measurements have not yet detected electron-hole superfluidity.

2.3 GaAs Double Quantum-Wells

One of the first systems proposed to study electron-hole superfluidity was a semiconductor heterostructure of Gallium Arsenide (GaAs) Double Quantum-Well (DQW) [38]. This consists of two GaAs quantum wells, where the electrons in one well and holes in the other well are confined with a static electric field [43, 59]. GaAs is a direct band gap material with a maximum valence band and a minimum conduction band separated by an energy band gap $E_g \sim 1.5$ eV. The dispersion of the single-particle bands at low energy is quadratic with effective masses $m^{(e)} = 0.067m_e$ for the conduction band and $m^{(h)} = 0.3m_e$ for the valence band. The quantum wells are separated by a thin insulating barrier of $\text{Al}_x\text{Ga}_{1-x}\text{As}$ which blocks recombination of the electrons and holes. The strength of the electron-hole pairing is controlled by the average effective separation between the electrons and the holes that in this system is determined by the thickness of the insulating barrier, d_B , and by the widths of the quantum wells, d_W (Fig. 2.4).

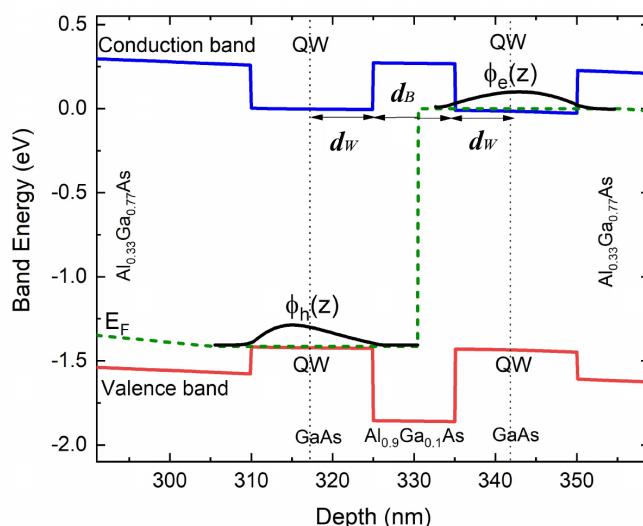


FIGURE 2.4: Conduction and valence bands for a GaAs DQW with quantum well widths $d_W = 15$ nm and $\text{Al}_{0.9}\text{Ga}_{0.1}\text{As}$ barrier thickness $d_B = 10$ nm [22]. The dashed green line is the Fermi level E_F . The vertical back dotted lines mark the centres of the wells. $\phi_e(z)$ and $\phi_h(z)$ are the resulting electron and hole single-particle wavefunctions confined in the wells. Note that the separation of the peaks in the $\phi_e(z)$ and $\phi_h(z)$ is larger than the distance between the centres of the two wells.

It is challenging to identify the optimal configurations for the wells and the insulating barriers [22]. In transport measurements [60, 61], the wells cannot be too narrow or else interface roughness scattering makes mobilities impractically low. The interface roughness scattering arises from Al atoms in the insulating barrier diffusing into the well regions ($d_W \sim 15$ nm $d_B \sim 10$ nm).

In two independent experiments on samples with quantum well of width 15 nm and an $\text{Al}_{0.9}\text{Ga}_{0.1}\text{As}$ barrier of thickness 10 nm, a sharp turn up in the electron-hole drag resistivity was observed for temperatures $T_c \sim 1$ K [60, 61]. Such an increase can be a signature of a superfluid transition [47]. However, the deviations from the T^2 dependence

of the drag resistivity expected for a Fermi liquid were not monotonic and the resistivity sometimes changed sign.

Because the average effective separation is so large in this sample configuration, $d \gtrsim a_B \sim 12$ nm, the interaction is weak and the screening too strong, the superfluidity is predicted to occur only for densities $\lesssim 10^{10}$ cm $^{-2}$ [22]. Thus, superfluidity would not be expected at the relatively high-density range that was experimentally accessible ($n > 4 \times 10^{10}$ cm $^{-2}$). The predicted transition temperatures for this system are relatively low, $T < 1$ K.

The problem of large separations can be overcome in optical measurements, where electron-hole pairs are optically excited in a quantum well and then spatially separated across the barrier by means of a perpendicular electric field [56, 58, 62]. This allows the existing optical experiments to use samples with quantum wells and barriers which are narrower than in samples for transport measurements ($d_W \sim 8 - 12$ nm, $d_B \sim 1 - 4$ nm). Thinner barriers make the coupling of the electron-hole pairs stronger for optical measurements than for the system for the drag measurement. Evidences of coherent condensation were observed at temperatures of a few Kelvin for carrier densities equal to few 10^{10} cm $^{-2}$ which are experimentally accessible.

To date, there are no definitive observations of superfluidity in GaAs DQWs. Nevertheless, GaAs DQWs remains a fascinating system to study because of the large difference in electron and hole effective masses in GaAs. This has significant consequences for the superfluidity which is weaker with respect to the equal mass case, but on the other hand, the GaAs DQW is likely to have a rich phase diagram of exotic superfluid phases [63]. The large mass difference makes double quantum wells in GaAs a solid state system uniquely suitable for generating and enhancing exotic superfluid phases that span the BCS-BEC crossover. The phases include the Fulde-Ferrell-Larkin-Ovchinnikov phase (FFLO) [64] and the Sarma phase [65] with two Fermi surfaces (breached pair phase). In ultracold atomic gases, Dy-K Fermi mixtures [66] have been used to explore the physics of mass-imbalanced strongly interacting Fermi-Fermi mixtures [67]. Such phases can also be expected but only at currently inaccessible temperatures, $T_c \sim 50$ nK [68].

2.4 Double Monolayer Graphene

Following the discovery of graphene [8], a single atomic layer of carbon atoms, and the discovery that a few layers of hexagonal Boron Nitride (hBN) act as an extremely effective insulating layer [69, 70], Double Monolayer Graphene (DMG) was proposed as a promising candidate for high-temperature electron-hole superfluidity [9, 71]. The DMG system consists of two graphene monolayers, one with electrons (n -doped) and the other with holes (p -doped), insulated from each other by as little as three atomic layers of hBN (Fig. 2.5).

In the heterostructure the layers are vertically coupled by van der Waals interactions [72], and it is stable and clean [73]. In comparison with the GaAs DQW, this system has certain potential advantages:

- it allows precise confinement of the carriers within a single atomically thin layer, thus overcoming the problem of the large well widths in DQW,
- the insulating barrier consists of an hBN trilayer that corresponds to a thin barrier with $d_B \sim 1$ nm.

As a result, the minimum distance between electrons and holes is reduced by one order of magnitude with respect to the GaAs DQW and the average electron-hole Coulomb interaction is very strong.

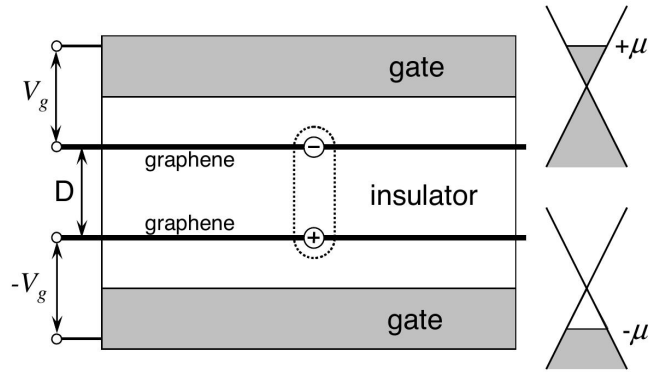


FIGURE 2.5: Schematic set-up of a DMG system (From Ref. [9]). On the right: chemical potential positions in two graphene layers, adjusted by gate voltages V_g and $-V_g$.

Pristine monolayer graphene has remarkable and unique features due to the electronic structure. The carbon atoms are arranged in a honeycomb lattice due to their sp^2 hybridization. The honeycomb structure consists of the triangular Bravais lattice with a basis of two inequivalent neighbouring atoms, labelled A and B. The six corners of the first Brillouin Zone (hexagon) consist of three pairs of inequivalent points K and K' . The interesting physics occurs at low-energy, around these points, and therefore these points play an essential role in the electronic properties of graphene [74].

The energy spectrum is linear for small values of wave-vector k around the K (or K') points, given by the Dirac-Weyl equation,

$$\varepsilon = \pm \hbar v_F |k|, \quad (2.4)$$

with fixed Fermi velocity, $v_F \sim 10^6$ m/s. The conduction and valence bands are identical and touch at the K and K' points, called Dirac points. In the absence of an external potential, the Fermi energy is located exactly at the Dirac points which makes graphene a zero-gap semiconductor. At the Dirac points, there is a double degenerate zero-energy solution associated with the K and K' valley, the so-called valley degeneracy.

Graphene has a large carrier mobility of about 2×10^4 $\text{cm}^2/(\text{Vs})$ at room temperature and is even higher at low temperature [75]. This makes graphene an excellent candidate for nanoelectronic applications.

Unfortunately, the linear dispersion of the energy bands of monolayer graphene is an enormous obstacle for accessing the strongly interacting regime where superfluidity is expected to occur [76]. Equation (2.3) for monolayer graphene gives:

$$r_s = \frac{e^2}{\kappa \langle r_0 \rangle} \frac{1}{\hbar v_F k_F} = \frac{e^2 \sqrt{\pi n}}{\kappa} \frac{1}{\hbar v_F \sqrt{\pi n}} = \frac{e^2}{\kappa \hbar v_F}. \quad (2.5)$$

The parameter r_s in graphene is thus a fixed constant due to the linear dispersion and is $r_s < 1$. This means that the strongly interacting regime is not experimentally accessible even at very low densities. For this reason, the interaction between electron and holes remains weak and screening is found to always kill the superfluidity [76]. This result was confirmed in an electron-hole drag experiment on DMG [77].

2.5 Double Bilayer Graphene

Double Bilayer Graphene (DBG), using bilayer graphene in place of monolayer graphene, was proposed to access the strongly interacting regime and realize an electron-hole condensate in graphene [10, 78]. Unlike monolayer graphene, the single-particle energy dispersion of the bands at low energies in bilayer graphene is approximately parabolic, as in conventional semiconductors, with effective masses $m^{(e)} = m^{(h)} \sim 0.04m_e$. The early theoretical studies [10] did not fully take into account the multi-band nature of the graphene. Multi-component effects should be important because of the small band gaps in bilayer graphene [79]. We will investigate the DBG system including multi-component effects in Chapters 4 and 5.

Two research groups have independently fabricated and characterized such double graphene bilayer devices [80, 81]. Both groups measured the Coulomb drag resistivity ρ_D as a function of the carrier density in the bilayers. The electron and hole densities were controlled with voltages applied between the bilayers and metallic gates above and below the bilayers [82]. There were surprising results that differ dramatically from observations in DMG [77]. Reference [81] focused on DBG system with low carrier densities and at low temperatures, $T_c = 1.5$ K. Unexpectedly they found that when the carrier density in both bilayers is equal, the drag resistance is huge, close to the resistance of bilayer graphene itself. Usually, the drag resistivity is a small fraction of the layer resistivity. A second surprising observation is that the drag was sometimes observed negative. Negative drag is usually associated with charge carriers of the same sign in both layers, so contributions from excitons to this drag is unlikely. The origin of this behaviour has been shown to be linked to multi-band effects in bilayer graphene that have a dramatic effect on the drag even for a Fermi liquid [83].

The presence of an exciton condensate in DBG was recently confirmed by using tunnelling current measurements [13]. Enhanced interlayer tunnelling as a signature of condensation was reported in a DBG system with transition temperatures of $T_c \sim 1.5$ K. The range of carrier densities was $n < 8 \times 10^{11} \text{ cm}^{-2}$.

2.6 Double Monolayer Phosphorene

Development of other 2D exfoliated materials like phosphorene followed graphene. Phosphorene, a monolayer of black phosphorus [84], is a semiconductor with direct energy band gap, $E_g > 1.5$ eV [85], and exhibits high carrier mobility of about $4 \times 10^3 \text{ cm}^2/(\text{Vs})$ at low temperature [86]. Similarly to graphene, phosphorene has a honeycomb lattice structure. However, in contrast with graphene, phosphorene is non-planar. It is possible to distinguish two directions in the phosphorene lattice, armchair or zigzag. The characteristic *puckering* results in a high in-plane anisotropy of the phosphorene energy band structure. The anisotropic effective masses along the armchair(x) and zigzag(y) directions are $m_x^{(e)} = m_x^{(h)} \sim 0.15m_e$ and $m_y^{(e)} \sim 0.7m_e$ and $m_y^{(h)} \sim m_e$ [87]. Because of these anisotropic effective masses, excitons in phosphorene are characterized by a strong spatial anisotropy and are predicted to exist at elevated temperatures with large binding energies [88].

Several theoretical and experimental studies investigated different anisotropic properties of phosphorene [89], including superconductivity [90], collective excitation modes [91] in a doped monolayer and Coulomb drag in coupled phosphorene sheets [92].

A highly anisotropic superfluid state has been predicted in Double Monolayer Phosphorene (DMP) arising from the anisotropic low energy bands in phosphorene [93, 94]. The system consists of two parallel monolayer phosphorene separated by a thin hBN

insulating barrier, $2 < d < 10$ nm. The anisotropy of the energy band structure in phosphorene causes the critical velocity of the superfluidity to depend on the direction of motion of dipolar excitons [93].

A key advantage of phosphorene with respect to graphene is the large values of the effective masses. The Rydberg energy, R_y , (Eq. (2.1)) is proportional to the effective masses, so in a system with large effective masses the binding energy will be stronger. In the zigzag direction, due to the large effective masses, the superfluid gap is about twice as large as along the armchair direction [94]. The maximum transition temperatures are estimated to be as high as 90 K in a range of carrier densities as high as $4 \times 10^{12} \text{ cm}^{-2}$.

Bright interlayer excitons in a double layer phosphorene encapsulated and separated by germanium sulphide (GeS) or hBN have been observed with exciton binding energies $E_B \sim 0.9$ eV [95]. However, to date there is no evidence of Bose-Einstein condensation or superfluidity in DMP.

2.7 Double Monolayer Transition Metal Dichalcogenide

Over the past five years, the class of materials that have attracted the attention because large effective masses and exciton binding energies is 2D semiconductors of the group-VI Transition Metal Dichalcogenides (TMDs)

These TMD monolayers, with the formula MX_2 (M is a transition metal (Molybdenum, Tungsten, Titanium) and X is a chalcogen (Sulphur or Selenium)), have a hexagonal structure, with each monolayer comprising three stacked layers (X-M-X). The effective masses of the low-energy states are one order of magnitude larger than in bilayer graphene. The band gaps are $E_g > 1.5$ eV and the excitons with the lowest energy, corresponding to the direct band gap, have binding energies as high as $E_B \sim 1$ eV [96–98].

High-quality TMD heterobilayers, with two different TMD monolayers are directly and vertically coupled by the van der Waals interaction [72], provide an interesting platform because they host strong interlayer excitons [99, 100]. The heterobilayer exciton properties are also due to the *type-II* alignment of the electron and hole bands [101]. Fascinating control over the excitonic optical properties has been shown to be experimentally possible [102, 103], including control of the exciton lifetime by an out-of-plane electric field that modifies the overlap of the electron and hole wave-functions [104].

Because large effective masses and exciton binding energies in 2D semiconductors favour electron-hole condensation with high transition temperatures, high-temperature superfluidity in double monolayer TMDs has been predicted [11] and studied [105]. The system consists of two TMD monolayers, one *n*-doped and one *p*-doped, separated by an insulating barrier of hBN.

Recently Bose-Einstein condensation of indirect excitons has been reported in $\text{MoSe}_2/\text{hBN}/\text{WSe}_2$ using tunnelling current and electroluminescence measurements [14]. The enhanced electroluminescence is observed at temperatures up to $T_c \sim 100$ K, consistent with the prediction of a high transition temperature.

We investigate this system in detail in Chapter 6. The earlier theoretical studies did not take into account the multi-band nature of the TMD monolayers, and they neglected the effects in the superfluidity due to the presence of strong spin-orbit coupling [106].

Research Activity and Publications

Chapter 3

Multi-component Electron-Hole Superfluidity in Multi-band System

In this chapter we introduce the theoretical approach used to describe electron-hole superfluidity in coupled layer systems. We use an extended multi-band approach to derive the fundamental equations for multi-component electron-hole superfluidity and we introduce the quantities used to characterize the BCS-BEC crossover phenomena. We extend the Random Phase Approximation to include the effect of the Coulomb screening in case of a multi-band system. The theoretical approach that we present here is used to obtain the results published in Refs. [15–19, 22]

Multi-component superconductivity is a novel quantum phenomenon in multi-band superconducting materials, in which different superconducting gaps open in different Fermi surfaces. Very soon after the formulation of the BCS theory, the prediction of multi-band superconductivity and the first extension of BCS theory to two-band two-gap superconductors were offered by Suhl, Matthias and Walker [107]. The discovery of the two-band superconductor MgB_2 in 2001 [108] has been a prominent issue because it marked the formal appearance of the new class of multi-band superconductors. The most recently discovered iron-based superconductors also belong to this class of materials [109]. In all these systems different electronic orbitals or different carriers participate in the formation of the superconducting condensate [110]. The increased number of degrees of freedom of the multi-component superconducting wave-function allows for emergent quantum effects that are otherwise unattainable in single-component superconductors.

In this chapter, we want to explicitly calculate the mean field equations for a system characterized by multiple electronic bands. The pairing of the particles in these systems has origin in the different bands and raises the possibility to have multi-component superfluidity, with multiple condensates.

3.1 Multi-band Electron-Hole Superfluidity

We want to describe the phenomena of electron-hole superfluidity using a microscopic approach. We use an approach similar to the one introduced by Bardeen, Cooper and Schrieffer in 1957 [25] and extended to finite temperature by Gorkov [111]. The system consists of an electron-doped layer separated from a hole-doped layer and is described by the total Grand-Canonical Hamiltonian for electron gas in second-quantization:

$$\hat{H} = \sum_{\lambda} \int \Psi_{\lambda}^{\dagger}(\mathbf{x}) \hat{T}_{\lambda}(\mathbf{x}) \Psi_{\lambda}(\mathbf{x}) d\mathbf{x} + \frac{1}{2} \sum_{\lambda\lambda'} \int \hat{V}_{\lambda\lambda'}(\mathbf{x}, \mathbf{y}) \Psi_{\lambda}^{\dagger}(\mathbf{x}) \Psi_{\lambda'}^{\dagger}(\mathbf{y}) \Psi_{\lambda'}(\mathbf{y}) \Psi_{\lambda}(\mathbf{x}) d\mathbf{x} d\mathbf{y}, \quad (3.1)$$

where Ψ and Ψ^{\dagger} are the annihilation and creation field operators at \mathbf{x} for electrons layer with index $\lambda = e$ and \mathbf{y} for holes layer $\lambda = h$. For the p -doped layer we use the standard

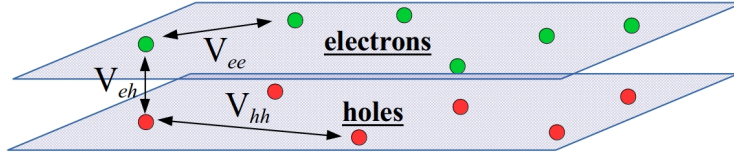


FIGURE 3.1: Schematic representation of a bilayer system with top electron layer and bottom hole layer. Interlayer interaction, \hat{V}_{eh} , and intralayer interactions, \hat{V}_{ee} and \hat{V}_{hh} are indicated.

hole-particle transformation. We mapped the valence band to a conduction band, so that the bands are filled with positively charged holes up to the Fermi level. The spin indices are implicit because the Coulomb interaction does not select the spin.

In Eq. (3.1), \hat{T}_λ is the kinetic energy operator. $\hat{V}_{\lambda\lambda'}$ is the Coulomb potential operator that depends on the relative distance between carriers. It describes the repulsion between carriers in the same layer ($\lambda = \lambda'$ intralayer interaction) or the attraction between carriers in opposite layers ($\lambda \neq \lambda'$ interlayer interaction),

$$\begin{aligned} \hat{H} = & \sum_{\lambda} \int \Psi_{\lambda}^{+}(\mathbf{x}) \hat{T}_{\lambda}(\mathbf{x}) \Psi_{\lambda}(\mathbf{x}) d\mathbf{x} + \frac{1}{2} \sum_{\lambda} \int \hat{V}_{\text{intra}}(\mathbf{x}, \mathbf{y}) \Psi_{\lambda}^{+}(\mathbf{x}) \Psi_{\lambda}^{+}(\mathbf{y}) \Psi_{\lambda}(\mathbf{y}) \Psi_{\lambda}(\mathbf{x}) d\mathbf{x} d\mathbf{y} \\ & + \frac{1}{2} \sum_{\lambda \neq \lambda'} \int \hat{V}_{\text{inter}}(\mathbf{x}, \mathbf{y}) \Psi_{\lambda}^{+}(\mathbf{x}) \Psi_{\lambda'}^{+}(\mathbf{y}) \Psi_{\lambda'}(\mathbf{y}) \Psi_{\lambda}(\mathbf{x}) d\mathbf{x} d\mathbf{y}. \end{aligned}$$

In this work, we focus on low densities to work in the strongly interacting regime. At low density the average inter-particle distance in each layer, r_0 , is larger with respect to the distance between the layers, so the interlayer potential, \hat{V}_{eh} , is stronger with respect to the intralayer interactions \hat{V}_{ee} and \hat{V}_{hh} that can be neglected. The effect of \hat{V}_{ee} and \hat{V}_{hh} can be very important in presence of electron-hole density imbalance and can be readily included in a mean field treatment [38].

The reduced Hamiltonian is:

$$\hat{H} = \sum_{\lambda} \int \Psi_{\lambda}^{+}(\mathbf{x}) \hat{T}_{\lambda}(\mathbf{x}) \Psi_{\lambda}(\mathbf{x}) d\mathbf{x} + \frac{1}{2} \sum_{\lambda \neq \lambda'} \int \hat{V}_{eh}(|\mathbf{x} - \mathbf{y}|) \Psi_{\lambda}^{+}(\mathbf{x}) \Psi_{\lambda'}^{+}(\mathbf{y}) \Psi_{\lambda'}(\mathbf{y}) \Psi_{\lambda}(\mathbf{x}) d\mathbf{x} d\mathbf{y}, \quad (3.2)$$

where

$$\hat{V}_{eh}(|\mathbf{x} - \mathbf{y}|) \Psi_e^{+}(\mathbf{x}) \Psi_h^{+}(\mathbf{y}) \Psi_h(\mathbf{y}) \Psi_e(\mathbf{x}) = \hat{V}_{eh}(|\mathbf{x} - \mathbf{y}|) \Psi_h^{+}(\mathbf{x}) \Psi_e^{+}(\mathbf{y}) \Psi_e(\mathbf{y}) \Psi_h(\mathbf{x}), \quad (3.3)$$

thus

$$\hat{H} = \sum_{\lambda} \int \Psi_{\lambda}^{+}(\mathbf{x}) \hat{T}_{\lambda}(\mathbf{x}) \Psi_{\lambda}(\mathbf{x}) d\mathbf{x} + \int \hat{V}_{eh}(|\mathbf{x} - \mathbf{y}|) \Psi_{\lambda}^{+}(\mathbf{x}) \Psi_{\lambda'}^{+}(\mathbf{y}) \Psi_{\lambda'}(\mathbf{y}) \Psi_{\lambda}(\mathbf{x}) d\mathbf{x} d\mathbf{y}. \quad (3.4)$$

The carriers are confined to move in a 2D layer. We write the kinetic term separable with respect to the in-plane $\bar{\mathbf{x}}$ and out-of-plane x_{\perp} spatial components:

$$\hat{T}_{\lambda}(\mathbf{x}) = \hat{T}_{\lambda}(\bar{\mathbf{x}}) + \hat{T}_{\lambda}(x_{\perp}) - \mu_{\lambda}, \quad (3.5)$$

where μ_{λ} is the chemical potential for the carriers. The interlayer interaction depends on the interlayer distance d and on the in-plane difference between electron and hole

position, $|\bar{\mathbf{x}} - \bar{\mathbf{y}}|$: $\hat{V}_{eh}(|\mathbf{x} - \mathbf{y}|) = \hat{V}_{eh}(\sqrt{d^2 + (\bar{\mathbf{x}} - \bar{\mathbf{y}})^2})$.

Also the field operator is separable in the variables with respect to the in-plane and out-of-plane components,

$$\Psi_\lambda(\bar{\mathbf{x}}, x_\perp) = \sum_n \psi_{\lambda,n}(\bar{\mathbf{x}}) \phi_{\lambda,n}(x_\perp), \quad (3.6)$$

and here we introduce the multiple bands with n sub-band index. The $\psi_{\lambda,n}(\bar{\mathbf{x}})$ is:

$$\psi_{\lambda,n}(\bar{\mathbf{x}}) = \frac{1}{\sqrt{S}} \sum_{\mathbf{k},n} e^{i\mathbf{k}\bar{\mathbf{x}}} a_{\lambda,n,\mathbf{k}}, \quad (3.7)$$

where $a_{\lambda,n,\mathbf{k}}^\dagger$ and $a_{\lambda,n,\mathbf{k}}$ are fermionic creation and annihilation operators for a carrier λ in quantum state n , \mathbf{k} and S is the layer surface area.

We rewrite the Hamiltonian in Eq. (3.4) in terms of sub-bands operators. For the kinetic part of the Hamiltonian, $\hat{T}_\lambda(\bar{\mathbf{x}})\psi_{\lambda,n}(\bar{\mathbf{x}}) = \varepsilon_{\lambda,n}\psi_{\lambda,n}(\bar{\mathbf{x}})$ and $\hat{T}(x_\perp)\phi_{\lambda,n}(x_\perp) = 0$, because the carriers are confined in the layers.

$$\begin{aligned} \hat{K} &= \sum_\lambda \sum_{n,m} \int \psi_{\lambda,n}^\dagger(\bar{\mathbf{x}}) \phi_{\lambda,n}^*(x_\perp) \hat{T}_\lambda(\bar{\mathbf{x}}) \psi_{\lambda,m}(\bar{\mathbf{x}}) \phi_{\lambda,m}(x_\perp) d\bar{\mathbf{x}} dx_\perp \\ &= \sum_\lambda \sum_{n,m} \int \psi_{\lambda,n}^\dagger(\bar{\mathbf{x}}) \phi_{\lambda,n}^*(x_\perp) (\hat{T}_\lambda(\bar{\mathbf{x}}) + \hat{T}_\lambda(x_\perp) - \mu_\lambda) \psi_{\lambda,m}(\bar{\mathbf{x}}) \phi_{\lambda,m}(x_\perp) d\bar{\mathbf{x}} dx_\perp \\ &= \sum_\lambda \sum_{n,m} \int \psi_{\lambda,n}^\dagger(\bar{\mathbf{x}}) \phi_{\lambda,n}^*(x_\perp) (\phi_{\lambda,m}(x_\perp) \hat{T}_\lambda(\bar{\mathbf{x}}) \psi_{\lambda,m}(\bar{\mathbf{x}}) - \mu_\lambda \psi_{\lambda,m}(\bar{\mathbf{x}}) \phi_{\lambda,m}(x_\perp)) d\bar{\mathbf{x}} dx_\perp \\ &= \sum_\lambda \sum_{n,m} \int \psi_{\lambda,n}^\dagger(\bar{\mathbf{x}}) \phi_{\lambda,n}^*(x_\perp) \phi_{\lambda,m}(x_\perp) (\hat{T}_\lambda(\bar{\mathbf{x}}) \psi_{\lambda,m}(\bar{\mathbf{x}}) - \mu_\lambda \psi_{\lambda,m}(\bar{\mathbf{x}})) d\bar{\mathbf{x}} dx_\perp \\ &= \sum_\lambda \sum_{n,m} \int \psi_{\lambda,n}^\dagger(\bar{\mathbf{x}}) (\varepsilon_{\lambda,n} - \mu_\lambda) \psi_{\lambda,m}(\bar{\mathbf{x}}) d\bar{\mathbf{x}} \int \phi_{\lambda,n}^*(x_\perp) \phi_{\lambda,m}(x_\perp) dx_\perp \\ &= \sum_\lambda \sum_n \int \psi_{\lambda,n}^\dagger(\bar{\mathbf{x}}) \hat{\zeta}_{\lambda,n} \psi_{\lambda,n}(\bar{\mathbf{x}}) d\bar{\mathbf{x}} \end{aligned}$$

with $\int \phi_{\lambda,n}^*(x_\perp) \phi_{\lambda,m}(x_\perp) dx_\perp = \delta_{n,m}$.

The interaction part of the Hamiltonian becomes:

$$\begin{aligned} \hat{V} &= \sum_{\substack{i,j \\ m,n}} \int \hat{V}_{eh}(\bar{\mathbf{x}} - \bar{\mathbf{y}}) \psi_{\lambda,i}^\dagger(\bar{\mathbf{x}}) \phi_{\lambda,i}^*(x_\perp) \psi_{\lambda',j}^\dagger(\bar{\mathbf{y}}) \phi_{\lambda',j}^*(y_\perp) \psi_{\lambda',m}(\bar{\mathbf{y}}) \phi_{\lambda',m}(y_\perp) \psi_{\lambda,n}(\bar{\mathbf{x}}) \phi_{\lambda,n}(x_\perp) d\bar{\mathbf{x}} d\bar{\mathbf{y}} dx_\perp dy_\perp \\ &= \sum_{\substack{i,j \\ m,n}} \int \hat{V}_{eh}(\bar{\mathbf{x}} - \bar{\mathbf{y}}) \psi_{\lambda,i}^\dagger(\bar{\mathbf{x}}) \psi_{\lambda',j}^\dagger(\bar{\mathbf{y}}) \psi_{\lambda',m}(\bar{\mathbf{y}}) \psi_{\lambda,n}(\bar{\mathbf{x}}) d\bar{\mathbf{x}} d\bar{\mathbf{y}} \int \phi_{\lambda,i}^*(x_\perp) \phi_{\lambda',j}^*(y_\perp) \phi_{\lambda',m}(y_\perp) \phi_{\lambda,n}(x_\perp) dx_\perp dy_\perp \\ &= \sum_{\substack{i,j \\ n,m}} \int \mathcal{F}_{ij,nm} \hat{V}_{eh}(\bar{\mathbf{x}} - \bar{\mathbf{y}}) \psi_{\lambda,i}^\dagger(\bar{\mathbf{x}}) \psi_{\lambda',j}^\dagger(\bar{\mathbf{y}}) \psi_{\lambda',m}(\bar{\mathbf{y}}) \psi_{\lambda,n}(\bar{\mathbf{x}}) d\bar{\mathbf{x}} d\bar{\mathbf{y}} \end{aligned}$$

where

$$\mathcal{F}_{ij,nm} = \int \phi_{\lambda,i}^*(x_\perp) \phi_{\lambda',j}^*(y_\perp) \phi_{\lambda',m}(y_\perp) \phi_{\lambda,n}(x_\perp) dx_\perp dy_\perp. \quad (3.8)$$

This factor accounts for the overlap of the wave functions and we will see later in this chapter that it has important effects on the electron-hole pairing.

We can write the total Hamiltonian using a new notation able to differentiate the carriers to reduce the number of indexes: $\psi_{e,n}(\bar{\mathbf{x}}) = c_n(\bar{\mathbf{x}})$, $\psi_{h,n}(\bar{\mathbf{y}}) = d_n(\bar{\mathbf{y}})$.

$$\begin{aligned} \hat{H} = & \sum_n \int c_n^+(\bar{\mathbf{x}}) \hat{\xi}_{e,n} c_n(\bar{\mathbf{x}}) d\bar{\mathbf{x}} + \int d_n^+(\bar{\mathbf{y}}) \hat{\xi}_{h,n} d_n(\bar{\mathbf{y}}) d\bar{\mathbf{y}} \\ & + \sum_{\substack{i,j \\ n,m}} \int \mathcal{F}_{in,jm} \hat{V}_{eh}(\bar{\mathbf{x}}-\bar{\mathbf{y}}) \left[c_i^+(\bar{\mathbf{x}}) d_j^+(\bar{\mathbf{y}}) d_m(\bar{\mathbf{y}}) c_n(\bar{\mathbf{x}}) \right] d\bar{\mathbf{x}} d\bar{\mathbf{y}}. \end{aligned} \quad (3.9)$$

The above Hamiltonian is still an interacting electron problem and is too hard to solve exactly. Hence we introduce the mean field approximation and we replace the operators with their average value:

$$c_n^+(\bar{\mathbf{x}}) d_m^+(\bar{\mathbf{y}}) d_m(\bar{\mathbf{y}}) c_n(\bar{\mathbf{x}}) \approx \langle c_n^+(\bar{\mathbf{x}}) d_m^+(\bar{\mathbf{y}}) \rangle d_m(\bar{\mathbf{y}}) c_n(\bar{\mathbf{x}}) + c_n^+(\bar{\mathbf{x}}) d_m^+(\bar{\mathbf{y}}) \langle d_m(\bar{\mathbf{y}}) c_n(\bar{\mathbf{x}}) \rangle, \quad (3.10)$$

and we define the order parameter,

$$\Delta_{nm}(\bar{\mathbf{x}}, \bar{\mathbf{y}}) = \sum_{i,j} \hat{V}_{eh}(\bar{\mathbf{x}}-\bar{\mathbf{y}}) \mathcal{F}_{ij, nm} \langle c_i(\bar{\mathbf{x}}) d_j(\bar{\mathbf{y}}) \rangle, \quad (3.11)$$

that describes the pairing potential between electrons and holes from subbands n and m .

We can write the mean field BCS-Bogoliubov Hamiltonian from Eq. (3.9) :

$$\hat{H} = \sum_n \int [c_n^+(\bar{\mathbf{x}}) \hat{\xi}_{e,n} c_n(\bar{\mathbf{x}}) + d_n^+(\bar{\mathbf{x}}) \hat{\xi}_{h,n} d_n(\bar{\mathbf{x}})] d\bar{\mathbf{x}} + \sum_{n,m} \int [c_n^+(\bar{\mathbf{x}}) d_m^+(\bar{\mathbf{y}}) \Delta_{nm}(\bar{\mathbf{x}}, \bar{\mathbf{y}}) + h.c.] d\bar{\mathbf{x}} d\bar{\mathbf{y}}. \quad (3.12)$$

We pass to the Heisenberg picture where the $\psi_{\lambda,n}$ and $\psi_{\lambda,n}^+$ are,

$$\psi_{\lambda,n}(\bar{\mathbf{x}}, \tau) = e^{\hat{H}\tau/\hbar} \psi_{\lambda,n}(\bar{\mathbf{x}}) e^{-\hat{H}\tau/\hbar}, \quad \psi_{\lambda,n}^+(\bar{\mathbf{x}}, \tau) = e^{\hat{H}\tau/\hbar} \psi_{\lambda,n}^+(\bar{\mathbf{x}}) e^{-\hat{H}\tau/\hbar}, \quad (3.13)$$

and we write the equations for the field operators,

$$-\hbar \partial_\tau \psi_{\lambda,n}(\bar{\mathbf{x}}, \tau) = [\psi_{\lambda,n}(\bar{\mathbf{x}}, \tau), \hat{H}]. \quad (3.14)$$

Using the anti-commutation relations:

$$\begin{aligned} \{\psi_{\lambda,n}(\bar{\mathbf{x}}), \psi_{\lambda,m}(\bar{\mathbf{y}})\} &= \{\psi_{\lambda,n}^+(\bar{\mathbf{x}}), \psi_{\lambda,m}^+(\bar{\mathbf{y}})\} = 0, \\ \{\psi_{\lambda,n}(\bar{\mathbf{x}}), \psi_{\lambda,m}^+(\bar{\mathbf{y}})\} &= \delta_{n,m} \delta(\bar{\mathbf{x}}-\bar{\mathbf{y}}), \\ \{c_n(\bar{\mathbf{x}}), d_m(\bar{\mathbf{y}})\} &= \{c_n^+(\bar{\mathbf{x}}), d_m^+(\bar{\mathbf{y}})\} = \{c_n(\bar{\mathbf{x}}), d_m^+(\bar{\mathbf{y}})\} = 0, \end{aligned}$$

we calculate the kinetic term of Eq. (3.14),

$$\begin{aligned}
 [\psi_{\lambda,n}(\bar{\mathbf{x}}, \tau), \hat{K}] &= \left[\psi_{\lambda,n}(\bar{\mathbf{x}}, \tau), \sum_{\lambda',m} \int \psi_{\lambda',m}^+(\bar{\mathbf{y}}) \hat{\xi}_{\lambda',m} \psi_{\lambda',m}(\bar{\mathbf{y}}) d\bar{\mathbf{y}} \right] \\
 &= \sum_{\lambda',m} \int d\bar{\mathbf{y}} \left[\psi_{\lambda,n}(\bar{\mathbf{x}}, \tau) \psi_{\lambda',m}^+(\bar{\mathbf{y}}) \hat{\xi}_{\lambda',m} \psi_{\lambda',m}(\bar{\mathbf{y}}) - \psi_{\lambda',m}^+(\bar{\mathbf{y}}) \hat{\xi}_{\lambda',m} \psi_{\lambda',m}(\bar{\mathbf{y}}) \psi_{\lambda,n}(\bar{\mathbf{x}}, \tau) \right] \\
 &= \sum_{\lambda',m} \int d\bar{\mathbf{y}} \left[\left(\delta_{n,m} \delta_{\lambda,\lambda'} \delta(\bar{\mathbf{x}} - \bar{\mathbf{y}}) - \psi_{\lambda',m}^+(\bar{\mathbf{y}}) \psi_{\lambda,n}(\bar{\mathbf{x}}, \tau) \right) \hat{\xi}_{\lambda',m} \psi_{\lambda',m}(\bar{\mathbf{y}}) - \psi_{\lambda',m}^+(\bar{\mathbf{y}}) \hat{\xi}_{\lambda',m} \psi_{\lambda',m}(\bar{\mathbf{y}}) \psi_{\lambda,n}(\bar{\mathbf{x}}, \tau) \right] \\
 &= \hat{\xi}_{\lambda,n} \psi_{\lambda,n}(\bar{\mathbf{x}}, \tau) - \sum_{\lambda',m} \int d\bar{\mathbf{y}} \left[\psi_{\lambda',m}^+(\bar{\mathbf{y}}) \psi_{\lambda,n}(\bar{\mathbf{x}}, \tau) \hat{\xi}_{\lambda',m} \psi_{\lambda',m}(\bar{\mathbf{y}}) + \psi_{\lambda',m}^+(\bar{\mathbf{y}}) \hat{\xi}_{\lambda',m} \psi_{\lambda',m}(\bar{\mathbf{y}}) \psi_{\lambda,n}(\bar{\mathbf{x}}, \tau) \right] \\
 &= \hat{\xi}_{\lambda,n} \psi_{\lambda,n}(\bar{\mathbf{x}}, \tau) - \sum_{\lambda',m} \int d\bar{\mathbf{y}} \left[\psi_{\lambda',m}^+(\bar{\mathbf{y}}) \psi_{\lambda,n}(\bar{\mathbf{x}}, \tau) \hat{\xi}_{\lambda',m} \psi_{\lambda',m}(\bar{\mathbf{y}}) - \psi_{\lambda',m}^+(\bar{\mathbf{y}}) \hat{\xi}_{\lambda',m} \psi_{\lambda,n}(\bar{\mathbf{x}}, \tau) \psi_{\lambda',m}(\bar{\mathbf{y}}) \right] \\
 &= \hat{\xi}_{\lambda,n} \psi_{\lambda,n}(\bar{\mathbf{x}}, \tau)
 \end{aligned}$$

and then the interaction term of Eq. (3.14),

$$\begin{aligned}
 [c_n(\bar{\mathbf{x}}, \tau), \hat{V}] &= \left[c_n(\bar{\mathbf{x}}, \tau), \sum_{ij} \int d\bar{\mathbf{y}} d\bar{\mathbf{y}}' [c_i^+(\bar{\mathbf{y}}) d_j^+(\bar{\mathbf{y}}') \Delta_{ij}(\bar{\mathbf{y}}, \bar{\mathbf{y}}') + \Delta_{ij}^+(\bar{\mathbf{y}}, \bar{\mathbf{y}}') d_j(\bar{\mathbf{y}}) c_i(\bar{\mathbf{y}}')] \right] \\
 &= [c_n(\bar{\mathbf{x}}), \sum_{ij} \int d\bar{\mathbf{y}} d\bar{\mathbf{y}}' c_i^+(\bar{\mathbf{y}}) d_j^+(\bar{\mathbf{y}}') \Delta_{ij}(\bar{\mathbf{y}}, \bar{\mathbf{y}}')] + \\
 &\quad [c_n(\bar{\mathbf{x}}), \sum_{ij} \int d\bar{\mathbf{y}} d\bar{\mathbf{y}}' \Delta_{ij}^+(\bar{\mathbf{y}}, \bar{\mathbf{y}}') d_j(\bar{\mathbf{y}}) c_i(\bar{\mathbf{y}}')]
 \end{aligned}$$

The first term of the interaction term will give us:

$$\begin{aligned}
 &\left[c_n(\bar{\mathbf{x}}), \sum_{ij} \int d\bar{\mathbf{y}} d\bar{\mathbf{y}}' c_i^+(\bar{\mathbf{y}}) d_j^+(\bar{\mathbf{y}}') \Delta_{ij}(\bar{\mathbf{y}}, \bar{\mathbf{y}}') \right] \\
 &= \sum_{ij} \int d\bar{\mathbf{y}} d\bar{\mathbf{y}}' \left[c_n(\bar{\mathbf{x}}) c_i^+(\bar{\mathbf{y}}) d_j^+(\bar{\mathbf{y}}') \Delta_{ij}(\bar{\mathbf{y}}, \bar{\mathbf{y}}') - d_j^+(\bar{\mathbf{y}}) c_i^+(\bar{\mathbf{x}}) \Delta_{ij}(\bar{\mathbf{y}}, \bar{\mathbf{y}}') c_n(\bar{\mathbf{x}}) \right] \\
 &= \sum_{ij} \int d\bar{\mathbf{y}} d\bar{\mathbf{y}}' \left[(\delta_{n,i} \delta(\bar{\mathbf{x}} - \bar{\mathbf{y}}) - c_i^+(\bar{\mathbf{y}}) c_n(\bar{\mathbf{x}})) d_j^+(\bar{\mathbf{y}}') \Delta_{ij}(\bar{\mathbf{y}}, \bar{\mathbf{y}}') - d_j^+(\bar{\mathbf{y}}') c_i^+(\bar{\mathbf{y}}) \Delta_{ij}(\bar{\mathbf{y}}, \bar{\mathbf{y}}') c_n(\bar{\mathbf{x}}) \right] \\
 &= \sum_{ij} \int d\bar{\mathbf{y}} d\bar{\mathbf{y}}' \left[d_j^+(\bar{\mathbf{y}}', \tau) \Delta_{nj}(\bar{\mathbf{x}}, \bar{\mathbf{y}}') - c_i^+(\bar{\mathbf{y}}) c_n(\bar{\mathbf{x}}) d_j^+(\bar{\mathbf{y}}') \Delta_{ij}(\bar{\mathbf{y}}, \bar{\mathbf{y}}') - d_j^+(\bar{\mathbf{y}}') c_i^+(\bar{\mathbf{y}}) \Delta_{ij}(\bar{\mathbf{y}}, \bar{\mathbf{y}}') c_n(\bar{\mathbf{x}}) \right] \\
 &= \sum_{ij} \int d\bar{\mathbf{y}} d\bar{\mathbf{y}}' \left[d_j^+(\bar{\mathbf{y}}', \tau) \Delta_{nj}(\bar{\mathbf{x}}, \bar{\mathbf{y}}') + c_i^+(\bar{\mathbf{y}}) d_j^+(\bar{\mathbf{y}}') c_n(\bar{\mathbf{x}}) \Delta_{ij}(\bar{\mathbf{y}}, \bar{\mathbf{y}}') + c_i^+(\bar{\mathbf{y}}) d_j^+(\bar{\mathbf{y}}') \Delta_{ij}(\bar{\mathbf{y}}, \bar{\mathbf{y}}') c_n(\bar{\mathbf{x}}) \right] \\
 &= \sum_j \int d\bar{\mathbf{y}}' d_j^+(\bar{\mathbf{y}}', \tau) \Delta_{nj}(\bar{\mathbf{x}}, \bar{\mathbf{y}}'),
 \end{aligned}$$

while the second term:

$$\begin{aligned}
 & \left[c_n(\bar{\mathbf{x}}), \sum_{ij} \int d\bar{\mathbf{y}} d\bar{\mathbf{y}}' \Delta_{ij}^+(\bar{\mathbf{y}}, \bar{\mathbf{y}}') d_j(\bar{\mathbf{y}}') c_i(\bar{\mathbf{y}}) \right] \\
 &= \sum_{ij} \int d\bar{\mathbf{y}} d\bar{\mathbf{y}}' \left[c_n(\bar{\mathbf{x}}) \Delta_{ij}^+(\bar{\mathbf{y}}, \bar{\mathbf{y}}') d_j(\bar{\mathbf{y}}') c_i(\bar{\mathbf{y}}) + \Delta_{ij}^+(\bar{\mathbf{y}}, \bar{\mathbf{y}}') d_j(\bar{\mathbf{y}}') c_i(\bar{\mathbf{y}}) c_n(\bar{\mathbf{x}}) \right] \\
 &= \sum_{ij} \int d\bar{\mathbf{y}} d\bar{\mathbf{y}}' \left[c_n(\bar{\mathbf{x}}) \Delta_{ij}^+(\bar{\mathbf{y}}, \bar{\mathbf{y}}') d_j(\bar{\mathbf{y}}') c_i(\bar{\mathbf{y}}) + \Delta_{ij}^+(\bar{\mathbf{y}}, \bar{\mathbf{y}}') c_n(\bar{\mathbf{x}}) d_j(\bar{\mathbf{y}}') c_i(\bar{\mathbf{y}}) \right] = 0.
 \end{aligned}$$

so we obtain:

$$[\psi_{\lambda,n}(\bar{\mathbf{x}}, \tau), \hat{V}] = \sum_j \Delta_{nj}(\bar{\mathbf{x}}, \bar{\mathbf{y}}) \psi_{\lambda',j}^+(\bar{\mathbf{y}}, \tau)$$

Finally, the equation of motion Eq. (3.14) for $\psi_{\lambda,n}$ becomes,

$$-\hbar \partial_\tau \psi_{\lambda,n}(\bar{\mathbf{x}}, \tau) = \hat{\xi}_{\lambda,n} \psi_{\lambda,n}(\bar{\mathbf{x}}, \tau) + \sum_j \Delta_{nj}(\bar{\mathbf{x}}, \bar{\mathbf{y}}) \psi_{\lambda',j}^+(\bar{\mathbf{y}}), \quad (3.15)$$

and with the same procedure we have the equation of motion for $\psi_{\lambda,n}^+$,

$$-\hbar \partial_\tau \psi_{\lambda,n}^+(\bar{\mathbf{x}}, \tau) = -\hat{\xi}_{\lambda,n}^+ \psi_{\lambda,n}^+(\bar{\mathbf{x}}, \tau) + \sum_j \Delta_{nj}^+(\bar{\mathbf{x}}, \bar{\mathbf{y}}) \psi_{\lambda',j}(\bar{\mathbf{y}}). \quad (3.16)$$

3.2 Two-Band Mean Field Theory including Interband Pairing.

In Chapters 4, 5 and 6 we will study two different systems where the pairing has two-band character, so we reduce the approach to a two-band approach. We will see that these two systems define two very different classes of two-band systems:

- In the Double Bilayer Graphene system, the two bands contributing to the pairing are the conduction and valence bands. In contrast with conventional multi-band superconductors, the bands here are not nested and there is a unique Fermi surface.
- In the double TMD monolayer system there are two bands contributing to the pairing because of the splitting of the bands caused by strong spin-orbit coupling. The bands are concentric subbands as in the multi-band superconductors.

A preliminary result was derived for two-band superconductors in 1963 [112], here we will derive the most general set of equations to describe these two-band systems including all the possible pairing channels.

In a two-band system, we write Eqs. (3.15)-(3.16) in a matrix form as:

$$-\hbar \partial_\tau \begin{pmatrix} c_1(\bar{\mathbf{x}}) \\ d_1^+(\bar{\mathbf{y}}) \\ c_2(\bar{\mathbf{x}}) \\ d_2^+(\bar{\mathbf{x}}) \end{pmatrix} = \begin{pmatrix} \xi_{e,1} & \Delta_{11} & 0 & \Delta_{12} \\ \Delta_{11}^+ & -\xi_{h,2}^+ & \Delta_{12}^+ & 0 \\ 0 & \Delta_{21} & \xi_{e,2} & \Delta_{22} \\ \Delta_{21}^+ & 0 & \Delta_{22}^+ & -\xi_{h,2}^+ \end{pmatrix} \begin{pmatrix} c_1(\bar{\mathbf{x}}) \\ d_1^+(\bar{\mathbf{y}}) \\ c_2(\bar{\mathbf{x}}) \\ d_2^+(\bar{\mathbf{x}}) \end{pmatrix} \quad (3.17)$$

We have in principle four pairing channels, each one associated to a Δ_{nm} . We refer to Δ_{11}, Δ_{22} as intraband pairing channels, that involve an electron and a hole from the same band, and Δ_{12}, Δ_{21} interband pairing channel, where the carriers come from different bands [113].

Now we define the set of Green functions [111], the normal Green functions (within a layer),

$$G_{nm}^{(e)}(\bar{\mathbf{x}}\tau, \bar{\mathbf{x}}'\tau') = -\frac{1}{\hbar} \langle T_\tau c_n(\bar{\mathbf{x}}, \tau) c_m^\dagger(\bar{\mathbf{x}}', \tau') \rangle, \quad (3.18)$$

$$G_{nm}^{(h)*}(\bar{\mathbf{x}}\tau, \bar{\mathbf{x}}'\tau') = -\frac{1}{\hbar} \langle T_\tau d_n^\dagger(\bar{\mathbf{x}}, \tau) d_m(\bar{\mathbf{x}}', \tau') \rangle, \quad (3.19)$$

and the anomalous Green functions (for different layers),

$$F_{nm}(\bar{\mathbf{x}}\tau, \bar{\mathbf{x}}'\tau') = -\frac{1}{\hbar} \langle T_\tau c_n(\bar{\mathbf{x}}, \tau) d_m(\bar{\mathbf{x}}', \tau') \rangle, \quad (3.20)$$

$$F_{nm}^*(\bar{\mathbf{x}}\tau, \bar{\mathbf{x}}'\tau') = -\frac{1}{\hbar} \langle T_\tau d_n^\dagger(\bar{\mathbf{x}}, \tau) c_m^\dagger(\bar{\mathbf{x}}', \tau') \rangle, \quad (3.21)$$

where T_τ is the time-ordering operator.

We write the Green functions evolution on the basis of Eqs. (3.15)-(3.16) as,

$$\begin{aligned} -\hbar\partial_\tau G_{nm}(\bar{\mathbf{x}}\tau, \bar{\mathbf{x}}'\tau') &= \delta(\tau-\tau')\delta(\bar{\mathbf{x}}-\bar{\mathbf{x}}')\delta_{nm} + \hat{\xi}_{e,n} G_{nm}(\bar{\mathbf{x}}\tau, \bar{\mathbf{x}}'\tau') + \\ &\quad \sum_j^2 \Delta_{nj}(\bar{\mathbf{x}}, \bar{\mathbf{y}}) F_{jm}^*(\bar{\mathbf{x}}\tau, \bar{\mathbf{x}}'\tau'), \end{aligned} \quad (3.22)$$

$$-\hbar\partial_\tau F_{nm}(\bar{\mathbf{x}}\tau, \bar{\mathbf{x}}'\tau') = \hat{\xi}_{e,n} F_{nm}(\bar{\mathbf{x}}\tau, \bar{\mathbf{x}}'\tau') + \sum_j^2 \Delta_{nj}(\bar{\mathbf{x}}, \bar{\mathbf{y}}) G_{jm}^*(\bar{\mathbf{x}}\tau, \bar{\mathbf{x}}'\tau'), \quad (3.23)$$

$$\begin{aligned} -\hbar\partial_\tau G_{nm}^*(\bar{\mathbf{x}}\tau, \bar{\mathbf{x}}'\tau') &= \delta(\tau-\tau')\delta(\bar{\mathbf{x}}-\bar{\mathbf{x}}')\delta_{nm} - \hat{\xi}_{h,n}^+ G_{nm}^*(\bar{\mathbf{x}}\tau, \bar{\mathbf{x}}'\tau') - \\ &\quad \sum_j^2 \Delta_{nj}^*(\bar{\mathbf{x}}, \bar{\mathbf{y}}) F_{jm}(\bar{\mathbf{x}}\tau, \bar{\mathbf{x}}'\tau'), \end{aligned} \quad (3.24)$$

$$-\hbar\partial_\tau F_{nm}^*(\bar{\mathbf{x}}\tau, \bar{\mathbf{x}}'\tau') = -\hat{\xi}_{h,n}^+ F_{nm}^*(\bar{\mathbf{x}}\tau, \bar{\mathbf{x}}'\tau') + \sum_j^2 \Delta_{nj}^*(\bar{\mathbf{x}}, \bar{\mathbf{y}}) G_{jm}^{(e)}(\bar{\mathbf{x}}\tau, \bar{\mathbf{x}}'\tau'). \quad (3.25)$$

We now introduce the Fourier transforms:

$$G_{nm}(\bar{\mathbf{x}}\tau, \bar{\mathbf{x}}'\tau') = -\frac{k_B T}{\hbar} \sum_\omega e^{-i\omega(\tau-\tau')} G_{nm}(\omega, \bar{\mathbf{x}}, \bar{\mathbf{x}}'),$$

$$G_{nm}^*(\bar{\mathbf{x}}\tau, \bar{\mathbf{x}}'\tau') = -\frac{k_B T}{\hbar} \sum_\omega e^{-i\omega(\tau-\tau')} G_{nm}^*(\omega, \bar{\mathbf{x}}, \bar{\mathbf{x}}'),$$

$$F_{nm}(\bar{\mathbf{x}}\tau, \bar{\mathbf{x}}'\tau') = -\frac{k_B T}{\hbar} \sum_\omega e^{-i\omega(\tau-\tau')} F_{nm}(\omega, \bar{\mathbf{x}}, \bar{\mathbf{x}}'),$$

$$F_{nm}^*(\bar{\mathbf{x}}\tau, \bar{\mathbf{x}}'\tau') = -\frac{k_B T}{\hbar} \sum_\omega e^{-i\omega(\tau-\tau')} F_{nm}^*(\omega, \bar{\mathbf{x}}, \bar{\mathbf{x}}'),$$

with

$$G_{nm}(\omega, \bar{\mathbf{x}}, \bar{\mathbf{x}}') = \langle \bar{\mathbf{x}} | G_{nm}(\omega) | \bar{\mathbf{x}}' \rangle, \quad F_{nm}(\omega, \bar{\mathbf{x}}, \bar{\mathbf{x}}') = \langle \bar{\mathbf{x}} | F_{nm}(\omega) | \bar{\mathbf{x}}' \rangle,$$

where T is the temperature and $\omega = k_B T(2n + 1)\pi$ are the fermionic Matsubara frequencies.

Using

$$\langle \bar{\mathbf{x}} | \hat{\xi}_{\lambda,n} | \bar{\mathbf{x}}' \rangle = \delta(\mathbf{x} - \bar{\mathbf{x}}') \hat{\xi}_{\lambda,n}(\bar{\mathbf{x}}), \quad \langle \bar{\mathbf{x}} | \Delta_{nj} | \bar{\mathbf{x}}' \rangle = \delta(\mathbf{x} - \bar{\mathbf{x}}') \Delta_{nj}(\bar{\mathbf{x}}),$$

we can rewrite Eqs. (3.22)-(3.25):

$$i\hbar\omega G_{nm}(\omega) = \delta_{nm} + \hat{\xi}_{e,n} G_{nm}(\omega) + \sum_j^2 \Delta_{nj} F_{jm}^*(\omega), \quad (3.26)$$

$$i\hbar\omega F_{nm}(\omega) = \hat{\xi}_{e,n} F_{nm}(\omega) + \sum_j^2 \Delta_{nj} G_{jm}^*(\omega), \quad (3.27)$$

$$i\hbar\omega G_{nm}^*(\omega) = \delta_{nm} - \hat{\xi}_{h,n} G_{nm}^*(\omega) - \sum_j^2 \Delta_{nj}^* F_{jm}(\omega), \quad (3.28)$$

$$i\hbar\omega F_{nm}^*(\omega) = -\hat{\xi}_{h,n} F_{nm}^*(\omega) + \sum_j^2 \Delta_{nj}^* G_{jm}(\omega). \quad (3.29)$$

We introduce the Nambu matrices:

$$\tilde{\xi}_\lambda = \begin{pmatrix} \tilde{\xi}_1^{(\lambda)} & 0 \\ 0 & \tilde{\xi}_2^{(\lambda)} \end{pmatrix}, \quad \mathbf{G}_\omega = \begin{pmatrix} G_{11} & G_{12} \\ G_{21} & G_{22} \end{pmatrix}, \quad \underline{\Delta} = \begin{pmatrix} \Delta_{11} & \Delta_{12} \\ \Delta_{21} & \Delta_{22} \end{pmatrix}, \quad \mathbf{F}_\omega = \begin{pmatrix} F_{11} & F_{12} \\ F_{21} & F_{22} \end{pmatrix}, \quad (3.30)$$

and we rewrite the equations in a more compact way:

$$(i\hbar\omega - \tilde{\xi}_e) \mathbf{G}_\omega = \mathbf{I} + \underline{\Delta} \mathbf{F}_\omega^*, \quad (3.31)$$

$$(i\hbar\omega - \tilde{\xi}_e) \mathbf{F}_\omega = \underline{\Delta} \mathbf{G}_\omega^*, \quad (3.32)$$

$$(i\hbar\omega + \tilde{\xi}_h) \mathbf{G}_\omega^* = \mathbf{I} - \underline{\Delta}^* \mathbf{F}_\omega, \quad (3.33)$$

$$(i\hbar\omega + \tilde{\xi}_h) \mathbf{F}_\omega^* = \underline{\Delta}^* \mathbf{G}_\omega. \quad (3.34)$$

We pass in the reciprocal space for the uniform case,

$$\langle \mathbf{k} | \mathbf{G}_\omega | \mathbf{k}' \rangle = (2\pi)^2 \delta(\mathbf{k} - \mathbf{k}') \mathbf{G}_\omega(\mathbf{k}),$$

$$\langle \mathbf{k} | \tilde{\xi}_\lambda | \mathbf{k}' \rangle = (2\pi)^2 \delta(\mathbf{k} - \mathbf{k}') \tilde{\xi}_\lambda(k),$$

$$\langle \mathbf{k} | \underline{\Delta} | \mathbf{k}' \rangle = \underline{\Delta}(\mathbf{k} - \mathbf{k}'),$$

and from Eq. (3.31) we get:

$$\begin{aligned} \langle \mathbf{k} | (i\hbar\omega - \tilde{\xi}_e) \mathbf{G}_\omega | \mathbf{k}' \rangle &= \langle \mathbf{k} | \mathbf{I} | \mathbf{k}' \rangle + \langle \mathbf{k} | \underline{\Delta} \mathbf{F}_\omega^* | \mathbf{k}' \rangle \\ \int \frac{d^2 \mathbf{k}''}{(2\pi)^2} \langle \mathbf{k} | (i\hbar\omega - \tilde{\xi}_e) | \mathbf{k}'' \rangle \langle \mathbf{k}'' | \mathbf{G}_\omega | \mathbf{k}' \rangle &= (2\pi)^2 \delta(\mathbf{k} - \mathbf{k}') \mathbf{I} \\ &\quad + \int \frac{d^2 \mathbf{k}''}{(2\pi)^2} \langle \mathbf{k} | \underline{\Delta} | \mathbf{k}'' \rangle \langle \mathbf{k}'' | \mathbf{F}_\omega^* | \mathbf{k}' \rangle \\ \int d^2 \mathbf{k}'' \delta(\mathbf{k} - \mathbf{k}'') (i\hbar\omega - \tilde{\xi}_e) (2\pi)^2 \delta(\mathbf{k}'' - \mathbf{k}') \mathbf{G}_\omega(\mathbf{k}'') &= (2\pi)^2 \delta(\mathbf{k} - \mathbf{k}') \mathbf{I} \\ &\quad + \int d^2 \mathbf{k}'' \underline{\Delta}(\mathbf{k} - \mathbf{k}'') \delta(\mathbf{k}'' - \mathbf{k}') \mathbf{F}_\omega^*(\mathbf{k}'') \end{aligned}$$

$$(2\pi)^2\delta(\mathbf{k} - \mathbf{k}')(i\hbar\omega - \xi_e)\mathbf{G}_\omega(\mathbf{k}) = (2\pi)^2\delta(\mathbf{k} - \mathbf{k}')\mathbf{I} + \underline{\Delta}(\mathbf{k} - \mathbf{k}')\mathbf{F}_\omega^*(\mathbf{k}')$$

making the further assumption $\underline{\Delta}(\mathbf{k} - \mathbf{k}') = (2\pi)^2\delta(\mathbf{k} - \mathbf{k}')\underline{\Delta}(\mathbf{k})$, and applying the same procedure to all the other Eqs. (3.31)-(3.34) we obtain:

$$\begin{aligned} (i\hbar\omega - \xi_e)\mathbf{G}_\omega(\mathbf{k}) &= \mathbf{I} + \underline{\Delta}\mathbf{F}_\omega^*(\mathbf{k}), \\ (i\hbar\omega - \xi_e)\mathbf{F}_\omega(\mathbf{k}) &= \underline{\Delta}\mathbf{G}_\omega^*(\mathbf{k}), \\ (i\hbar\omega + \xi_h)\mathbf{G}_\omega^*(\mathbf{k}) &= \mathbf{I} - \underline{\Delta}^*\mathbf{F}_\omega(\mathbf{k}), \\ (i\hbar\omega + \xi_h)\mathbf{F}_\omega^*(\mathbf{k}) &= \underline{\Delta}^*\mathbf{G}_\omega(\mathbf{k}), \end{aligned}$$

We arrange the equations in a matrix:

$$\begin{pmatrix} i\hbar\omega - \xi_1^{(e)} & 0 & \Delta_{11} & \Delta_{12} \\ 0 & i\hbar\omega - \xi_2^{(e)} & \Delta_{21} & \Delta_{22} \\ -\Delta_{11}^* & -\Delta_{12}^* & i\hbar\omega + \xi_1^{(h)} & 0 \\ -\Delta_{21}^* & -\Delta_{22}^* & 0 & i\hbar\omega + \xi_2^{(h)} \end{pmatrix} \begin{pmatrix} G_{11} & G_{12} & F_{11} & F_{12} \\ G_{21} & G_{22} & F_{21} & F_{22} \\ F_{11}^* & F_{12}^* & G_{11}^* & G_{12}^* \\ F_{21}^* & F_{22}^* & G_{21}^* & G_{22}^* \end{pmatrix} = \begin{pmatrix} 1 & 0 & 0 & 0 \\ 0 & 1 & 0 & 0 \\ 0 & 0 & 1 & 0 \\ 0 & 0 & 0 & 1 \end{pmatrix} \quad (3.35)$$

and we solve the system of the equations (See details of the resolution in Appendix A).

We finally determine the normal Green functions in all the channels:

$$\begin{aligned} G_{11}[i\omega, \mathbf{k}] &= \frac{(i\hbar\omega - \xi_2^{(e)})(i\hbar\omega + \xi_1^{(h)})(i\hbar\omega + \xi_2^{(h)}) - (i\hbar\omega + \xi_1^{(h)})\Delta_{22}^2 - (i\hbar\omega + \xi_2^{(h)})\Delta_{12}\Delta_{21}}{(i\hbar\omega - \chi_1)(i\hbar\omega - \chi_2)(i\hbar\omega + \chi_3)(i\hbar\omega + \chi_4)}, \\ G_{21}[i\omega, \mathbf{k}] &= \frac{(i\hbar\omega + \xi_2^{(h)})\Delta_{11}\Delta_{21} + (i\hbar\omega + \xi_1^{(h)})\Delta_{21}\Delta_{22}}{(i\hbar\omega - \chi_1)(i\hbar\omega - \chi_2)(i\hbar\omega + \chi_3)(i\hbar\omega + \chi_4)}, \\ G_{12}[i\omega, \mathbf{k}] &= \frac{(i\hbar\omega + \xi_2^{(h)})\Delta_{11}\Delta_{12} + (i\hbar\omega + \xi_1^{(h)})\Delta_{22}\Delta_{12}}{(i\hbar\omega - \chi_1)(i\hbar\omega - \chi_2)(i\hbar\omega + \chi_3)(i\hbar\omega + \chi_4)}, \\ G_{22}[i\omega, \mathbf{k}] &= \frac{(i\hbar\omega - \xi_1^{(e)})(i\hbar\omega + \xi_1^{(h)})(i\hbar\omega + \xi_2^{(h)}) - (i\hbar\omega + \xi_2^{(h)})\Delta_{11}^2 - (i\hbar\omega + \xi_1^{(h)})\Delta_{12}\Delta_{21}}{(i\hbar\omega - \chi_1)(i\hbar\omega - \chi_2)(i\hbar\omega + \chi_3)(i\hbar\omega + \chi_4)}, \end{aligned} \quad (3.36)$$

and the anomalous Green functions:

$$\begin{aligned}
 F_{11}[i\omega, \mathbf{k}] &= \frac{(i\hbar\omega - \tilde{\zeta}_2^{(e)})(i\hbar\omega + \tilde{\zeta}_2^{(h)})\Delta_{11} - (\Delta_{11}\Delta_{22} - \Delta_{12}\Delta_{21})\Delta_{22}}{(i\hbar\omega - \chi_1)(i\hbar\omega - \chi_2)(i\hbar\omega + \chi_3)(i\hbar\omega + \chi_4)}, \\
 F_{21}[i\omega, \mathbf{k}] &= \frac{(i\hbar\omega - \tilde{\zeta}_1^{(e)})(i\hbar\omega + \tilde{\zeta}_2^{(h)})\Delta_{21} + (\Delta_{11}\Delta_{22} - \Delta_{12}\Delta_{21})\Delta_{21}}{(i\hbar\omega - \chi_1)(i\hbar\omega - \chi_2)(i\hbar\omega + \chi_3)(i\hbar\omega + \chi_4)}, \\
 F_{12}[i\omega, \mathbf{k}] &= \frac{(i\hbar\omega - \tilde{\zeta}_2^{(e)})(i\hbar\omega + \tilde{\zeta}_1^{(h)})\Delta_{12} + (\Delta_{11}\Delta_{22} - \Delta_{12}\Delta_{21})\Delta_{12}}{(i\hbar\omega - \chi_1)(i\hbar\omega - \chi_2)(i\hbar\omega + \chi_3)(i\hbar\omega + \chi_4)}, \\
 F_{22}[i\omega, \mathbf{k}] &= \frac{(i\hbar\omega - \tilde{\zeta}_1^{(e)})(i\hbar\omega + \tilde{\zeta}_1^{(h)})\Delta_{22} - (\Delta_{11}\Delta_{22} - \Delta_{12}\Delta_{21})\Delta_{11}}{(i\hbar\omega - \chi_1)(i\hbar\omega - \chi_2)(i\hbar\omega + \chi_3)(i\hbar\omega + \chi_4)},
 \end{aligned} \tag{3.37}$$

with

$$\chi_1 = \delta\tilde{\zeta}_1 + \sqrt{\frac{a+b}{2}}, \quad \chi_2 = \delta\tilde{\zeta}_2 + \sqrt{\frac{a-b}{2}}, \quad \chi_3 = -\delta\tilde{\zeta}_1 + \sqrt{\frac{a+b}{2}}, \quad \chi_4 = -\delta\tilde{\zeta}_2 + \sqrt{\frac{a-b}{2}},$$

$$a = E_1^2 + E_2^2 + 2\Delta_{12}\Delta_{21},$$

$$b = \delta\tilde{\zeta}_1^2 - \delta\tilde{\zeta}_2^2 + \sqrt{(T_1^2 - T_2^2)^2 + 4\Delta_{12}\Delta_{21}((\tilde{\zeta}_1^{(e)} - \tilde{\zeta}_2^{(e)})(\tilde{\zeta}_1^{(h)} - \tilde{\zeta}_2^{(h)}) + (\Delta_{11} + \Delta_{22})^2)}, \tag{3.38}$$

where we introduced the notation:

$$\delta\tilde{\zeta}_n = \frac{\tilde{\zeta}_n^{(e)} - \tilde{\zeta}_n^{(h)}}{2}, \quad \tilde{\zeta}_n = \frac{\tilde{\zeta}_n^{(e)} + \tilde{\zeta}_n^{(h)}}{2}, \quad E_n^2 = \Delta_{nn}^2 + \tilde{\zeta}_n^2, \quad T_n^2 = \Delta_{nn}^2 + \tilde{\zeta}_n^{(e)}\tilde{\zeta}_n^{(h)}. \tag{3.39}$$

Using the anomalous Green functions and the definition of the order parameter (Eq. (3.11)), we can derive the self-consistent mean field equations for Δ_{nm} :

$$\Delta_{nm}(\mathbf{k}) = -\frac{k_B T}{L^2} \sum_{i,j=1}^2 \sum_{\mathbf{k}'} \mathcal{F}_{nm,ij}(\mathbf{k}, \mathbf{k}') V_{eh}(|\mathbf{k} - \mathbf{k}'|) \sum_{\omega} e^{-i\omega 0^+} F_{ij}[i\omega, \mathbf{k}'], \tag{3.40}$$

where

$$\mathcal{F}_{nm,ij}(\mathbf{k}, \mathbf{k}') = \langle i\mathbf{k}' | n\mathbf{k} \rangle \langle m\mathbf{k} | j\mathbf{k}' \rangle, \tag{3.41}$$

is the form factor representing the overlap of the single-particle wave functions [114].

Equation (3.40) describes the superfluid gap Δ that opens in the excitation quasi-particle energy when electron-hole pairs are formed. In a multi-component system, each Δ_{nm} is associated with a $\{nm\}$ -partial condensate. On the right hand side of Eq. (3.40), the superfluid gaps $\Delta_{ij}(\mathbf{k})$ appear implicitly in the F_{ij} , meaning that the condensate is a coherent mixture of intraband ($i = j$) and interband ($i \neq j$) condensates. The condensates are coupled when form factor $\mathcal{F}_{nm,ij}(\mathbf{k}, \mathbf{k}') \neq 0$. The form factor describes the probability of Josephson-like virtual transfer of a pair from bands nm to bands ij .

Using the normal Green functions we can derive the density equation:

$$n = g_s g_v \frac{k_B T}{L^2} \sum_{n=1}^2 \sum_{\mathbf{k}, \omega} e^{-i\omega 0^+} G_{nm}[i\omega, \mathbf{k}], \quad (3.42)$$

The factor g_s accounts for the spin degeneracy and g_v for the valley degeneracy of a system.

After performing the summation over the Matsubara frequencies ω , in the limit of zero temperature, we can solve Eq. (3.40) coupled with Eq. (3.42) in order to obtain the zero temperature superfluid gaps Δ_{nm} and the chemical potential μ .

3.2.1 BEC-BCS crossover

The evolution of the BEC-BCS crossover with the density can be investigated studying the superfluid gap and the chemical potential. The properties of these two quantities provide some of the criteria used to distinguish the different regimes of the BEC-BCS crossover [115].

In the strongly interacting BEC regime, the superfluid gap Δ , as a function of k has a high and broad peak. The maximum Δ_{max} is greater or of the order of the Fermi energy E_F . The peak is centred at $k = 0$, and it extends to large values of k . In the BEC regime the chemical potential is negative $\mu \ll E_F$ and in the limit of very low density $\mu = -E_B/2$, where E_B is the two-body binding energy.

In the weakly interacting BCS regime, the superfluid gap Δ , as a function of k has small and narrow peak centred at k_F (Fermi wave-vector). The maximum of the gap is $\Delta_{max} \ll E_F$. In the BCS regime the chemical potential coincides with the Fermi level E_F .

The different regimes of the BEC-BCS crossover can also be identified by introducing the superfluid condensate fraction c [116, 117]. This is defined as the fraction of carriers in pairs, n_{pair} , relative to the total number of carriers. The number of the pairs is given by [117],

$$n_{pair} = \int |\langle c_n(\bar{\mathbf{x}}) d_m(\bar{\mathbf{x}}) \rangle|^2 d\bar{\mathbf{x}} d\bar{\mathbf{y}}. \quad (3.43)$$

In a one-band system, it is straightforward to show that the condensate fraction is:

$$c = \frac{\sum_{\mathbf{k}, \omega} e^{-i\omega 0^+} |F[i\omega, \mathbf{k}]|^2}{\sum_{\mathbf{k}, \omega} e^{-i\omega 0^+} G[i\omega, \mathbf{k}]}. \quad (3.44)$$

The classification is for $c > 0.8$ the condensate is in the BEC regime, for $c < 0.2$ in the BCS regime. Otherwise the condensate is in the Crossover regime [118].

The definition in Eq. (3.44) can be extended for multi-band systems in case of multi-condensates [119], where for each condensate we can define a condensate fraction. We will calculate the condensate fractions for the specific systems in Chapters 4 and 6.

As introduced in Section 2.2, the obstacle for an observation of the BCS regime is given by the screening that becomes more and more effective with the increase of the density. In the next section we will deal with the approximation we use to include the screening effects in the interaction $V_{eh}(|\mathbf{k} - \mathbf{k}'|)$ in Eq. (3.42).

3.3 Random Phase Approximation for the Screening

Unlike in superconductors, the long-range nature of the bare Coulomb interaction means that screening of interactions must be taken into account. With carriers in two different layers, the Coulomb interaction in one layer induces a charge response not only in

the same layer but also in the opposite layer. We use the linear-response Random Phase Approximation (RPA) to describe the screening. A comparison of the good agreement of zero-temperature superfluid properties for a double layer electron-hole system calculated using the present mean field RPA approach [42], with the corresponding results calculated using diffusion quantum Monte Carlo [118], indicates that the present RPA approach should be a quantitatively good approximation.

In the RPA, electrons respond as mutually non interacting particles to a sum of the external potentials plus the mean field Hartree potentials from the charge densities induced by the electrons. The effective potential is:

$$\mathbb{W}(\mathbf{q}, \Omega) = \left(1 + \mathbb{V}(q) \underline{\chi}^{(RPA)}(\mathbf{q}, \Omega)\right) \mathbb{V}(q), \quad (3.45)$$

where $q = |\mathbf{k} - \mathbf{k}'|$.

$\hat{V}(q)$ is the matrix of the bare interactions:

$$\mathbb{V}(q) = \begin{pmatrix} V_{ee} & V_{eh} \\ V_{eh} & V_{hh} \end{pmatrix}, \quad V_{ee}(q) = V_{hh}(q) = \frac{2\pi e^2}{\epsilon_\lambda \epsilon_0} \frac{1}{q}, \quad V_{eh}(q) = -\frac{2\pi e^2}{\epsilon \epsilon_0} \frac{e^{-dq}}{q}. \quad (3.46)$$

V_{ee} and V_{hh} are the bare repulsive potentials between same carriers within a single layer, V_{eh} is the bare interlayer attraction and d is the interlayer distance. ϵ_λ is the relative dielectric permittivity of the layers and ϵ is the relative dielectric permittivity of the surrounding medium. For simplicity, we consider the two layers embedded and separated using the same material. (This corresponds to the actual experimental situation where Boron Nitride is used both as substrate and as a spacer [14, 81, 120]). This choice allows us to treat $V_{ee} = V_{hh}$. For simplicity we use $V_{ee} = V_S$ and $V_{eh} = V_D$

In Eq. (3.45), $\underline{\chi}^{(RPA)}$ is the matrix of density-density response functions in the RPA:

$$\underline{\chi}^{(RPA)}(\mathbf{q}, \Omega) = [1 - \mathbb{V}(q) \underline{\Pi}(\mathbf{q}, \Omega)]^{-1} \underline{\Pi}(\mathbf{q}, \Omega). \quad (3.47)$$

Here $\underline{\Pi}$ is the matrix of the dynamic polarizabilities.

3.3.1 Screened Interaction in the Normal State

In the Normal State (there is no pairing between opposite carriers) the carriers in each layer do not respond to the opposite layer charge distribution. The polarizabilities of the system are Π_e , for the n -doped layer, and Π_h for the p -doped layer, so we can write the $\underline{\Pi}$ as:

$$\underline{\Pi}(\mathbf{q}, \Omega) = \begin{pmatrix} \Pi_e & 0 \\ 0 & \Pi_h \end{pmatrix}. \quad (3.48)$$

The off-diagonal terms that account for the interlayer polarizabilities are identically zero in this case. In the case of equal densities, due to the particle-hole symmetry, polarizabilities are equal in both layers: $\Pi_e = \Pi_h = \Pi_N$.

For a multi-band system we can write:

$$\Pi_N(\mathbf{q}, \Omega) = g_s g_v \sum_{i,j} \Pi_N^{ij}(\mathbf{q}, \Omega). \quad (3.49)$$

where g_s and g_v are the spin and valley degeneracies. The lowest-order polarizability of the non-interacting 2D electron gas is the Stern-Lindhard function [121]. In the static

limit ($\Omega \rightarrow 0$) for bands i and j it is written:

$$\Pi_N^{ij}(\mathbf{q}, T) = \frac{1}{L^2} \sum_{\mathbf{k}} \mathcal{F}_{ij}(\mathbf{k}, \mathbf{k} + \mathbf{q}) \frac{n_F[\varepsilon_i(\mathbf{k}), T] - n_F[\varepsilon_j(\mathbf{k} + \mathbf{q}), T]}{\varepsilon_i(\mathbf{k}) - \varepsilon_j(\mathbf{k} + \mathbf{q})}, \quad (3.50)$$

where $n_F[\varepsilon_i(\mathbf{k}), T]$ is the Fermi distribution of the particle function for the i band at temperature T . Note that we adopt a sign convention for which the real part of Π_N is negative.

Using Π_N we can now write the eigenvalues of the RPA matrix (Eq. (3.47)) in the static limit as

$$\begin{aligned} \chi_1^{(RPA)} &= \frac{\Pi_N(\mathbf{q})}{1 - (V_S(q) + V_D(q))\Pi_N(\mathbf{q})}, \\ \chi_2^{(RPA)} &= \frac{\Pi_N(\mathbf{q})}{1 - (V_S(q) - V_D(q))\Pi_N(\mathbf{q})}, \end{aligned} \quad (3.51)$$

and from Eq. (3.45) we get [122]:

$$W_S(\mathbf{q}) = \frac{V_S(q) - \Pi_N(\mathbf{q}) (V_S^2(q) - V_D^2(q))}{1 - 2\Pi_N(\mathbf{q})V_S(q) + \Pi_N^2(\mathbf{q}) (V_S^2(q) - V_D^2(q))}, \quad (3.52)$$

$$W_D(\mathbf{q}) = \frac{V_D(q)}{1 - 2\Pi_N(\mathbf{q})V_S(q) + \Pi_N^2(\mathbf{q}) (V_S^2(q) - V_D^2(q))}. \quad (3.53)$$

W_S is the statically screened intralayer repulsion between same carriers and W_D is the the statically screened interlayer attraction between electrons and holes in different layers.

For a one-band 2D electron gas, Π_N is negative. For $q < 2k_F$, it is equal to the Density Of States (DOS) $\Pi_N(q) = -DOS$, and for $q > 2k_F$ it falls to zero [121]. Because of negative sign, Π_N reduces the strength of the electron-hole attraction W_D (Eq. (3.53)) for $q < 2k_F$. This leads to the familiar effect of the screening in real space: the screened potential is cut off to zero when $r \simeq r_c$, defining a screening length r_c . The effect of the screening due to the normal polarizability increases with the increase of k_F , thus with the density.

3.3.2 Screening Interaction in the Superfluid State

When the system is in the Superfluid State, the formation of electron-hole pairs gives rise to a direct response of charge density in one layer on the electric field in the other layer. This is described by anomalous polarizability Π_A and the polarizability matrix is:

$$\underline{\Pi}(\mathbf{q}, \Omega) = \begin{pmatrix} \Pi_N & \Pi_A \\ \Pi_A & \Pi_N \end{pmatrix}. \quad (3.54)$$

The normal intralayer polarizabilities of each layer (Eq. (3.50)) also change with respect to intrinsic polarizabilities due to the appearance of the superfluid gap in the energy spectrum. The normal and anomalous polarizabilities are calculated as loops consisting of two normal or anomalous Green functions, respectively [76]:

$$\Pi_N^{nm,ij}(\mathbf{q}, \Omega) = \frac{T}{L^2} \sum_{\mathbf{k}, \omega} \mathcal{F}_{nm,ij}(\mathbf{k}, \mathbf{k} + \mathbf{q}) G_{nm}[i\omega + i\Omega, \mathbf{k} + \mathbf{q}] G_{ij}[i\omega, \mathbf{k}], \quad (3.55)$$

$$\Pi_A^{nm,ij}(\mathbf{q}, \Omega) = \frac{T}{L^2} \sum_{\mathbf{k}, \omega} \mathcal{F}_{nm,ij}(\mathbf{k}, \mathbf{k} + \mathbf{q}) F_{nm}[i\omega + i\Omega, \mathbf{k} + \mathbf{q}] F_{ij}[i\omega, \mathbf{k}], \quad (3.56)$$

$\omega = k_B T(2n + 1)\pi$ are the fermionic Matsubara frequencies and $\Omega = k_B T 2n\pi$ are the bosonic Matsubara frequencies. The total polarizabilities are:

$$\Pi_N(\mathbf{q}) = g_s g_v \sum_{n,m,i,j} \Pi_N^{nm,ij}(\mathbf{q}, \Omega), \quad (3.57)$$

$$\Pi_A(\mathbf{q}) = g_s g_v \sum_{n,m,i,j} \Pi_A^{nm,ij}(\mathbf{q}, \Omega), \quad (3.58)$$

At zero temperature and in the static limit $\Omega \rightarrow 0$, Eq. (3.55) will result in a negative Π_N , similar to the normal state, while Eq. (3.56) will result in a positive Π_A . In Eq. (3.56) we also see that Π_A is proportional to the superfluid gaps Δ_{ij} , since $F_{ij}[i\omega, \mathbf{k}] \propto \Delta_{ij}$. This means that, while the normal polarizability depends on the carrier population, the anomalous polarizability depends on the population of electron-hole pairs.

We can rewrite the eigenvalues of the RPA matrix (Eq. (3.47)) in the superfluid state as

$$\begin{aligned} \chi_+^{(RPA)} &= \frac{\Pi_N(\mathbf{q}) + \Pi_A(\mathbf{q})}{1 - [V_S(q) + V_D(q)][\Pi_N(\mathbf{q}) + \Pi_A(\mathbf{q})]}, \\ \chi_-^{(RPA)} &= \frac{\Pi_N(\mathbf{q}) - \Pi_A(\mathbf{q})}{1 - [V_S(q) - V_D(q)][\Pi_N(\mathbf{q}) - \Pi_A(\mathbf{q})]}, \end{aligned} \quad (3.59)$$

and we find the statically screened interaction in the superfluid state:

$$W_S(\mathbf{q}) = \frac{V_S(q) - \Pi_N(\mathbf{q})[V_S^2(q) - V_D^2(q)]}{1 - 2[V_S(q)\Pi_N(\mathbf{q}) - V_D(q)\Pi_A(\mathbf{q})] + [\Pi_N^2(\mathbf{q}) - \Pi_A^2(\mathbf{q})][V_S^2(q) - V_D^2(q)]}, \quad (3.60)$$

$$W_D(\mathbf{q}) = \frac{V_D(q) + \Pi_A(\mathbf{q})[V_S^2(q) - V_D^2(q)]}{1 - 2[V_S(q)\Pi_N(\mathbf{q}) - V_D(q)\Pi_A(\mathbf{q})] + [\Pi_N^2(\mathbf{q}) - \Pi_A^2(\mathbf{q})][V_S^2(q) - V_D^2(q)]}. \quad (3.61)$$

The electron-hole interaction V_{eh} in the gap equation (Eq. (3.40)) is replaced with the statically screened interlayer interaction W_D [76, 123, 124] and this then is:

$$V_{eh}(\mathbf{q}) = \frac{V_S e^{-qd} + \Pi_A(\mathbf{q}) V_S^2 (1 - e^{-2qd})}{1 - 2V_S [\Pi_N(\mathbf{q}) + e^{-qd} \Pi_A(\mathbf{q})] + [\Pi_N^2(\mathbf{q}) - \Pi_A^2(\mathbf{q})] V_S^2 (1 - e^{-2qd})}. \quad (3.62)$$

There are three competing length scales characterizing a double layer system: the barrier thickness d , the average inter-particle separation in a layer r_0 , and the radius of the electron-hole bound pairs r_{pair} . The most favourable conditions for the pairing are achieved at small interlayer separation, $d \ll r_0$. In this regime, $k_F d \ll 1$ and the electron-hole interaction is well approximated by:

$$V_{eh}(\mathbf{q}) = \frac{V_S(q) e^{-qd}}{1 - 2V_S(q)(\Pi_N(\mathbf{q}) + \Pi_A(\mathbf{q}))}. \quad (3.63)$$

Equation (3.63) shows that because of their opposite signs there is significant cancellation between Π_N and Π_A . For a fixed density, so fixed Π_N , the cancellation between Π_A and Π_N is more effective as the superfluid gap Δ increases [76]. From a physical point of view, this effect due to the superfluid gap in the energy spectrum reducing the number of states available for the normal state screening. The presence of a condensate reduces the population of free carriers available for screening and so the superfluidity weakens the screening [42].

By comparing the superfluid properties calculated using diffusion quantum Monte Carlo [125] with the results for the same system calculated within mean field without screening, Ref. [42] demonstrated that neglecting screening becomes an excellent approximation at low density, in the BEC regime (see Fig. 3.2). In this regime the strong interactions tightly bind the pairs (r_s is large). This makes the pairs compact on the scale of the inter-particle separations, $r_{pair} \ll r_0$. In this regime the superfluid gap Δ in the single-particle excitation spectrum is much larger than the Fermi energies E_F . This completely suppresses the long wavelength excitations needed for screening. The majority of the particles are in the condensate, the condensate fraction $c > 0.8$, and there are few free particles available for screening. In Eq. (3.63), the cancellation between normal and anomalous polarizability is almost complete, $\Pi_N = -\Pi_A$, so the net result is the unscreened electron-hole interaction.

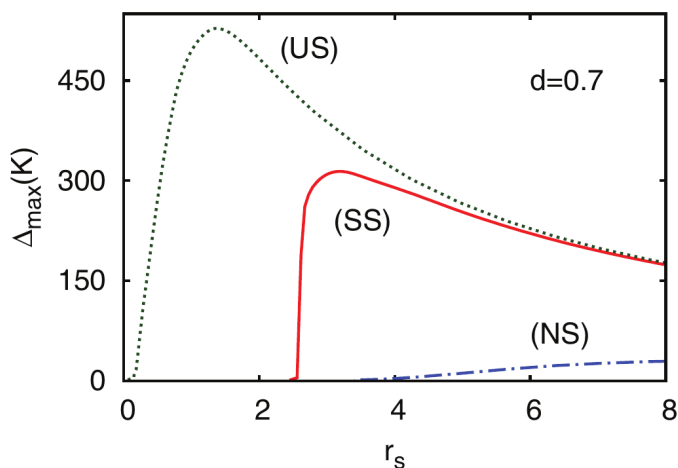


FIGURE 3.2: Superfluid gap Δ_{max} at $T = 0$ as a function of $r_s = r_0/a_B$, calculated with Coulomb electron-hole interaction which is unscreended (US) (dotted green line); screened in the superfluid state (SS) (solid red line); screened in the normal state (NS) (dash-dotted blue line) (From Ref.[42]).

The competition between superfluidity and screening changes when we increase the density (r_s decreases). At high density the inter-particle separation is small and the pairs are in the weak-coupling BCS regime, so they are overlapping $r_{pair} > r_0$. In the BCS regime, the superfluid gap Δ is small compared with E_F and so cannot suppress the long wavelength excitations needed for screening. The condensate fraction is small so the number of free particles available for screening is large. This is reflected in Eq. (3.63), because at high density Π_A is very small and cannot cancel with Π_N , so the electron-hole interaction is strongly screened. We will see in Chapters 5 and 6 that after a certain *threshold density*, for $r_s < 2.3$, the screening is so strong that it kills the superfluidity.

Chapter 4

BCS-BEC Crossover in Double Bilayer Graphene

In this chapter, we apply our multi-component approach to a Double Bilayer Graphene system to investigate electron-hole pairing properties. We include valence band contributions to the pairing mechanism and we investigate the multi-component superfluidity resulting in this system. We find the BEC-BCS crossover phenomena properties depend sensitively not only on the carrier densities but also on the tunable energy band gap [15, 16].

The recent fabrication of two very close conducting bilayer graphene sheets, one containing electrons and the other holes encapsulated in thin hexagonal boron nitride (hBN) [81, 120] (Fig. 4.1), raises exciting possibilities of observing high-temperature superfluidity.

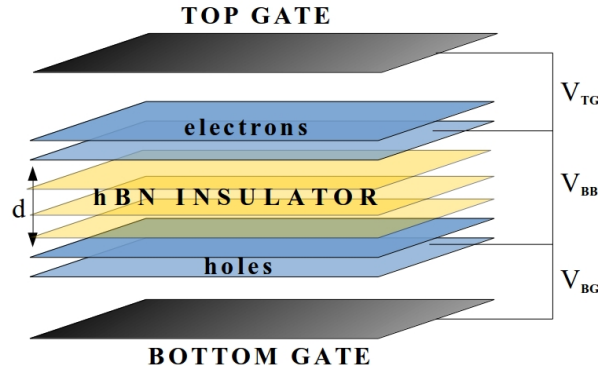


FIGURE 4.1: Double Bilayer Graphene system. V_{TG} and V_{BG} are the potentials applied by the Top and Bottom Gates, and V_{BB} is the bias applied between them. The potentials are used to change independently the carrier densities of the layer and to induce a perpendicular electric field that opens a band gap.

The Double Bilayer Graphene system (DBG) was proposed in 2013 [10] to overcome problems due to the linear dispersion of the energy bands in monolayer graphene (See Section 2.4). The reason for the substitution of monolayers with bilayers is that the hybridization between graphene layers modifies the energy dispersion from linear to approximately parabolic at low energy. In parabolic bands the Fermi energy is linearly proportional to the density n , $E_F = \frac{\hbar^2 4\pi n}{2mg_s g_v}$, so it can be tuned continuously relative to the strength of the electron-hole Coulomb attraction [78] by varying the electron and hole densities. From Eq. (2.3), r_s for a parabolic band system is:

$$r_s = \frac{e^2}{4\pi\epsilon\epsilon_0 \langle r_0 \rangle} \frac{1}{E_F} = \frac{e^2}{4\pi\epsilon\epsilon_0} \frac{2mg_s g_v}{\hbar^2 \sqrt{4\pi n}} = g_s g_v \frac{r_0}{a_B}. \quad (4.1)$$

By decreasing the densities, the system is moved from the region of weak interactions to the region where the Coulomb interactions dominate over kinetic energies. Experimentally this is possible because in DBG system the graphene bilayers can be made electrically independent. This means that the top and bottom bilayer carrier densities can be independently controlled with potentials in external metal gates deposited on the graphene bilayer [82] (Fig. 4.1).

The perpendicular electric field produced by top and bottom gates induces a band gap E_g in the energy spectrum between the conduction and valence bands, by creating a charge imbalance between the two graphene layers [126]. This band gap can also be continuously tuned from zero to 250 meV at room temperature [79]. The existence of such a tunable band gap is remarkable and opens up additional appealing possibilities for this system:

- The small band gap energy (much smaller than the band gaps in conventional semiconductors) is the same order as the energies for the pairing processes, ~ 100 meV, predicted in this system from Ref. [10]. This means that we cannot neglect the valence band. We expect additional electron-hole pairing from this second band, making of DBG a multi-component superfluidity system.
- In contrast with multi-component high-temperature superconductors such as iron-based materials where the carrier densities are difficult to tune and the energy separation between the bands is fixed [110, 127], in DBG system we can tune both the carrier densities and the band gap.

Interestingly multi-component superfluidity in this system is unconventional and novel. In iron-based, magnesium diborides, and similar materials with strong multi-band and multi-gap character [128, 129], the multi-bands are nested [107] so there are multiple Fermi surfaces for the different bands. In contrast, in DBG the conduction and valence bands are inverted relative to one another, so the remote band provides additional phase space for the pairs but there is only one Fermi surface.

In this chapter, we investigate multi-component superfluidity in DBG at zero temperature, and we focus on the effects on the pairing and on the BCS-BEC crossover phenomena of the closeness of the conduction and valence bands.

4.1 Double Bilayer Graphene

The system consists of two AB stacked bilayers (a hexagon centre in one layer is above a carbon atom below it) where the layers are arranged so that half of top layer atoms lie directly over the centre of a hexagon in the bottom layer, and half of the atoms lie over an atom of the bottom layer. The two aligned atoms belong to the A sub-lattice in one layer and B sub-lattice in the other. The two bilayers are separated by a trilayer of hexagonal Boron Nitride (hBN) of thickness $d \sim 1$ nm. This thin insulating barrier has been shown to be sufficiently strong to suppress tunnelling and the resulting recombination of electrons and holes from opposite bilayers [69, 70, 130].

The electronic bands of bilayer graphene can be described using a tight-binding approach that describes the properties of tightly bound electrons in solids [131]. The tight-binding parameters for graphene are the intercell distance $a = 0.246$ nm and the intralayer hopping parameter $t_0 \sim 3.16$ eV [132]. The hybridization between layers is driven by the interlayer coupling between A and B sub-lattices with interlayer hopping parameter $t_1 \sim 0.4$ eV. The tight-binding Hamiltonian with symmetric band gap is then

[133]:

$$H_k = \begin{pmatrix} E_g/2 & \hbar v_F k e^{-i\phi_k} & 0 & -t_1 \\ \hbar v_F k e^{i\phi_k} & E_g/2 & 0 & 0 \\ 0 & 0 & -E_g/2 & \hbar v_F k e^{-i\phi_k} \\ t_1 & 0 & \hbar v_F k e^{i\phi_k} & -E_g/2 \end{pmatrix}, \quad (4.2)$$

where k is the wave vector in a layer centred in the K valley. There is a double degenerate energy solution for the two inequivalent K and K' valley. $v_F = \sqrt{3}at_0/2\hbar$ is the Fermi velocity $\sim 10^6$ m/s in monolayer graphene.

The eigenvalues of this Hamiltonian give the four bands energy dispersion [134]:

$$\varepsilon_{\gamma\pm}(k) = \gamma \frac{1}{2} \sqrt{(t_1 \pm \Gamma)^2 + E_g^2 \left(1 - \frac{4(\hbar v_F k)^2}{t_1^2}\right)} \quad \Gamma = \sqrt{t_1^2 + 4(\hbar v_F k)^2 + \frac{4(\hbar v_F k)^2 E_g^2}{t_1^2}}. \quad (4.3)$$

where the index γ indicates the conduction bands $\gamma = +$ or the valence bands $\gamma = -$. The valley degeneracy effect appears only in the valley degeneracy factor, $g_v = 2$.

For a gapless system, $E_g = 0$, Eq. (4.3) reduces to:

$$\varepsilon_{\gamma\pm}(k) = \gamma \frac{t_1}{2} \pm \sqrt{\frac{t_1^2}{4} + (\hbar v_F k)^2}. \quad (4.4)$$

The two lowest energy bands, ε_{+-} and ε_{--} , touch each other at the K point and for energies $|\varepsilon_{\gamma-}| < t_1$ are approximately parabolic. While the two high energy bands, ε_{++} and ε_{-+} , which result from the strong coupling between layers, have energies $|\varepsilon_{\gamma+}| \geq t_1$. For E_g non-zero a band gap is opened at $k = 0$, the two low energy bands are increasingly deformed from parabolas and the separation in energy between the two high energy band increases.

In this chapter we are interested in the effect of the proximity in energy between conduction and valence band in our calculation for superfluidity, so we focus on energy processes of the order of the E_g . Because $E_g < t_1$, we can neglect the two high-energy bands and we take the single-particle energy dispersions equal to the low energy bands. The resulting 2×2 reduced Hamiltonian is [135]:

$$H_k = \frac{\hbar^2}{2m^*} \begin{pmatrix} 0 & (k_x - ik_y)^2 \\ (k_x - ik_y)^2 & 0 \end{pmatrix} + \begin{pmatrix} E_g/2 & 0 \\ 0 & E_g/2 \end{pmatrix}, \quad (4.5)$$

Thus the low energy conduction and valence bands for each bilayer graphene sheet ε_γ are identical and can be approximated as parabolic:

$$\varepsilon_+(k) = \frac{\hbar^2 k^2}{2m^*} + \frac{E_g}{2}, \quad \varepsilon_-(k) = -\frac{\hbar^2 k^2}{2m^*} - \frac{E_g}{2}, \quad (4.6)$$

The effective masses for the electrons and the holes are equal, $m^* = m_e^* = m_h^* = 0.04 m_e$, where m_e is the bare electron mass [136].

4.2 Mean Field Equations

We apply the theoretical approach introduced in Chapter 3 to derive the zero temperature mean field equations in DBG system.

Because of the standard transformation for hole in valence band in particle (see discussion below Eq. (3.1)) we can write $\varepsilon_\gamma^{(e)}(k) = \varepsilon_\gamma^{(h)}(k) = \varepsilon_\gamma(k)$. The band index $\gamma = +$

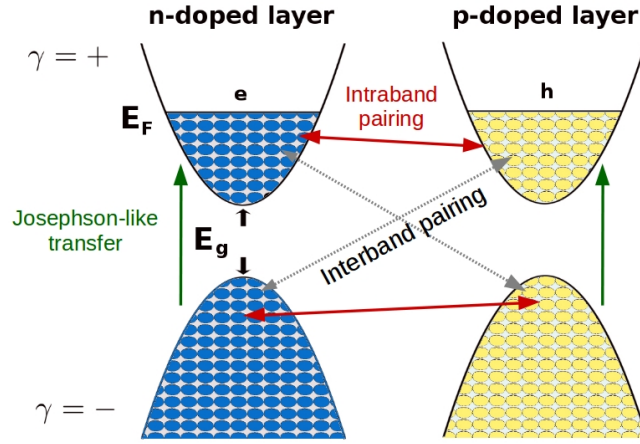


FIGURE 4.2: Bilayer graphene electron and hole bands after standard particle-antiparticle transformation and with parabolic approximation. The arrows indicate all the possible channels of pairing.

accounts for the contribution of the conduction bands (where the Fermi level is located) and $\gamma = -$ accounts for the valence bands. There are two bands in each bilayer, the pairing can occur between an electron and hole coming from the conduction or the valence band, so there are in principle 4 pairing channels (Fig. 4.2).

We will restrict the calculation to equal electron and hole density so the Fermi energies for electrons and holes are equal and the chemical potential is $\mu_{(e)} = \mu_{(h)} = \mu$. Because the electron and hole bands are identical, from Eq. (3.39), we can write:

$$\xi_{\gamma}^{(e)}(k) = \xi_{\gamma}^{(h)}(k) = \xi_{\gamma}(k) = \varepsilon_{\gamma}(k) - \mu, \quad (4.7)$$

$$T_{\gamma}^2(k) = E_{\gamma}^2(k) = \xi_{\gamma}^2(k) + \Delta_{\gamma\gamma}^2(k). \quad (4.8)$$

Because the electron and hole band gap are equal, the two interband pairing terms will be symmetric, so $\Delta_{+-} = \Delta_{-+}$. With these simplifications, the terms in Eq. (3.38) become:

$$\chi_1 = \chi_3 = \sqrt{\frac{a+b}{2}}, \quad \chi_2 = \chi_4 = \sqrt{\frac{a-b}{2}},$$

$$a = E_+^2 + E_-^2 + 2\Delta_{+-}^2, \quad b = \sqrt{(E_+^2 - E_-^2)^2 + 4\Delta_{+-}^2((\xi_+ - \xi_-)^2 + (\Delta_{++} + \Delta_{--})^2)}. \quad (4.9)$$

The normal Green functions for DBG are (see Eq. (3.36)):

$$G_{++}[i\omega, \mathbf{k}] = \frac{-(i\hbar\omega + \xi_+)(\hbar^2\omega^2 + E_-^2) - (i\hbar\omega + \xi_-)\Delta_{+-}^2}{(i\hbar\omega - \chi_1)(i\hbar\omega - \chi_2)(i\hbar\omega + \chi_1)(i\hbar\omega + \chi_2)},$$

$$G_{+-}[i\omega, \mathbf{k}] = \frac{\Delta_{+-}[(i\hbar\omega + \xi_-)\Delta_{++} + (i\hbar\omega + \xi_+)\Delta_{--}]}{(i\hbar\omega - \chi_1)(i\hbar\omega - \chi_2)(i\hbar\omega + \chi_1)(i\hbar\omega + \chi_2)}, \quad (4.10)$$

$$G_{--}[i\omega, \mathbf{k}] = \frac{-(i\hbar\omega + \xi_-)(\hbar^2\omega^2 + E_+^2) - (i\hbar\omega + \xi_+)\Delta_{+-}^2}{(i\hbar\omega - \chi_1)(i\hbar\omega - \chi_2)(i\hbar\omega + \chi_1)(i\hbar\omega + \chi_2)},$$

and the anomalous Green functions are (see Eq. (3.37)):

$$\begin{aligned}
 F_{++}[i\omega, \mathbf{k}] &= \frac{-(\hbar^2\omega^2 + E_-^2)\Delta_{++} + \Delta_{+-}^2\Delta_{--}}{(i\hbar\omega - \chi_1)(i\hbar\omega - \chi_2)(i\hbar\omega + \chi_1)(i\hbar\omega + \chi_2)}, \\
 F_{+-}[i\omega, \mathbf{k}] &= \frac{\Delta_{+-}[(i\hbar\omega - \xi_-)(i\hbar\omega + \xi_+) - \Delta_{+-}^2 + \Delta_{++}\Delta_{--}]}{(i\hbar\omega - \chi_1)(i\hbar\omega - \chi_2)(i\hbar\omega + \chi_1)(i\hbar\omega + \chi_2)}, \\
 F_{--}[i\omega, \mathbf{k}] &= \frac{-(\hbar^2\omega^2 + E_+^2)\Delta_{--} + \Delta_{+-}^2\Delta_{++}}{(i\hbar\omega - \chi_1)(i\hbar\omega - \chi_2)(i\hbar\omega + \chi_1)(i\hbar\omega + \chi_2)}.
 \end{aligned} \tag{4.11}$$

We note that Eqs. (4.10) and (4.11) have a similar structure of the Green functions for multi-band superconductors in Ref. [137] even though, in contrast with the superconducting concentric bands of Ref. [137], the DBG has *counter-centric* bands.

We here neglect the interband pairing and we will justify this choice in the discussion of the results. There are two condensates, a condensate with electrons and holes from conduction band and superfluid gap Δ_{++} , and a condensate with electrons and holes from valence band and superfluid gap Δ_{--} [114]. With $\Delta_{+-} = 0$, $\chi_1 = E_+$ and $\chi_2 = E_-$ and Eqs. (4.10)-(4.11) give $G_{+-} = 0$ and $F_{+-} = 0$.

With only intraband pairing, the Green functions become:

$$\begin{aligned}
 G_{++}[i\omega, \mathbf{k}] &= \frac{(i\hbar\omega + \xi_+)}{(i\hbar\omega - E_+)(i\hbar\omega + E_+)}, & G_{--}[i\omega, \mathbf{k}] &= \frac{(i\hbar\omega + \xi_-)}{(i\hbar\omega - E_-)(i\hbar\omega + E_-)}, \\
 F_{++}[i\omega, \mathbf{k}] &= \frac{\Delta_{++}}{(i\hbar\omega - E_+)(i\hbar\omega + E_+)}, & F_{--}[i\omega, \mathbf{k}] &= \frac{\Delta_{--}}{(i\hbar\omega - E_-)(i\hbar\omega + E_-)}.
 \end{aligned} \tag{4.12}$$

We introduce the Bogoliubov amplitudes v_γ and u_γ for the conduction and valence bands:

$$v_\gamma^2(k) = \frac{1}{2} \left(1 - \frac{\xi_\gamma(k)}{E_\gamma(k)} \right), \quad u_\gamma^2(k) = \frac{1}{2} \left(1 + \frac{\xi_\gamma(k)}{E_\gamma(k)} \right), \tag{4.13}$$

and we then rewrite Eqs. (4.12):

$$\begin{aligned}
 G_{++}[i\omega, k] &= \frac{u_+^2}{(i\hbar\omega - E_+)} + \frac{v_+^2}{(i\hbar\omega + E_+)}, \\
 G_{--}[i\omega, k] &= \frac{u_-^2}{(i\hbar\omega - E_-)} + \frac{v_-^2}{(i\hbar\omega + E_-)}, \\
 F_{++}[i\omega, k] &= \frac{u_+v_+}{(i\hbar\omega - E_+)} - \frac{u_+v_+}{(i\hbar\omega + E_+)}, \\
 F_{--}[i\omega, k] &= \frac{u_-v_-}{(i\hbar\omega - E_-)} - \frac{u_-v_-}{(i\hbar\omega + E_-)}.
 \end{aligned} \tag{4.14}$$

The sum over the Matsubara frequencies, ω , (see Appendix Sec. A.1 for details) gives:

$$\sum_\omega e^{-i\omega 0^+} G_{\gamma\gamma}[i\omega, k] = v_\gamma^2(k)(1 - n_F[E_\gamma, T]) + u_\gamma^2(k)n_F[E_\gamma, T], \tag{4.15}$$

and

$$\sum_\omega e^{-i\omega 0^+} F_{\gamma\gamma}[i\omega, k] = \frac{\Delta_{\gamma\gamma}}{2E_\gamma}(1 - 2n_F[E_\gamma, T]), \tag{4.16}$$

In the limit of zero temperature, the Fermi distributions $n_F[E_\gamma, 0] = 0$, so we have:

$$G_{\gamma\gamma}[k] = v_\gamma^2(k), \quad F_{\gamma\gamma}[k] = \frac{\Delta_{\gamma\gamma}(k)}{2E_\gamma(k)}. \quad (4.17)$$

Superfluid Gap Equations in DBG

We introduce the more compact notation with $\Delta_{\gamma\gamma} \equiv \Delta_\gamma$. The zero temperature the coupled superfluid gap equations are derived from Eq. (3.40):

$$\begin{cases} \Delta_+(k) = - \int \frac{d^2\mathbf{k}'}{(2\pi)^2} V_{eh}(|\mathbf{k} - \mathbf{k}'|) \left[\mathcal{F}_{++}(\mathbf{k}, \mathbf{k}') \frac{\Delta_+(k')}{2E_+(k')} + \mathcal{F}_{+-}(\mathbf{k}, \mathbf{k}') \frac{\Delta_-(k')}{2E_-(k')} \right], \\ \Delta_-(k) = - \int \frac{d^2\mathbf{k}'}{(2\pi)^2} V_{eh}(|\mathbf{k} - \mathbf{k}'|) \left[\mathcal{F}_{--}(\mathbf{k}, \mathbf{k}') \frac{\Delta_-(k')}{2E_-(k')} + \mathcal{F}_{-+}(\mathbf{k}, \mathbf{k}') \frac{\Delta_+(k')}{2E_+(k')} \right]. \end{cases} \quad (4.18)$$

The form factors (Eq. (3.41)) are non-zero only for $n = m = \gamma$ ($i = j = \gamma'$):

$$\mathcal{F}_{\gamma,\gamma'}(\mathbf{k}, \mathbf{k}') = \langle \gamma' \mathbf{k}' | \gamma \mathbf{k} \rangle \langle \gamma \mathbf{k} | \gamma' \mathbf{k}' \rangle = |\langle \gamma \mathbf{k} | \gamma' \mathbf{k}' \rangle|^2. \quad (4.19)$$

These form factors are determined from the eigenvectors of the reduced matrix in Eq. (4.5) [135]. The 2-component eigenvectors $\Psi_+(k)$ and $\Psi_-(k)$ are:

$$\Psi_+ = \begin{pmatrix} \cos(\alpha_k/2) \\ -\sin(\alpha_k/2)e^{i2\phi_k} \end{pmatrix} e^{i\mathbf{k}r}, \quad \Psi_- = \begin{pmatrix} \sin(\alpha_k/2) \\ \cos(\alpha_k/2)e^{i2\phi_k} \end{pmatrix} e^{i\mathbf{k}r}, \quad (4.20)$$

where $\alpha_k = \tan^{-1} \left\{ \hbar^2 k^2 / (m^* E_g) \right\}$. Calculating the overlap of $\Psi_\gamma(k)$ with $\Psi_{\gamma'}(k')$ we obtain:

$$\mathcal{F}_{\gamma\gamma'}(\mathbf{k}\mathbf{k}') = \frac{1}{2} [1 + \gamma\gamma' (\cos(\alpha_k) \cos(\alpha_{k'}) + \sin(\alpha_k) \sin(\alpha_{k'}) \cos(2\phi))], \quad (4.21)$$

where $\phi = \cos^{-1}(\widehat{\mathbf{k}\mathbf{k}'})$. Because of the identical conduction and valence band we have $\mathcal{F}_{+-}(\mathbf{k}\mathbf{k}') = \mathcal{F}_{-+}(\mathbf{k}\mathbf{k}')$. Note that $\mathcal{F}_{++}(\mathbf{k}\mathbf{k}')$ for the conduction bands is different from the form factor for a one-band system [10] because of the effect of the modification of the single-particle distribution function caused by band gap E_g .

In the superfluid gap equations, Eqs. (4.18), the coupling of Δ_+ with Δ_- arises only from Josephson-like transfers of pairs. In a Josephson-like transfer a pair from a band is virtually excited into the other band. Pairs in the valence band can excite into the conduction band where they reinforce the strength of the Δ_+ . At the same time, the excitations of pairs increases the population of valence-band vacancies (Fig. 4.3). Since we are using the term ‘‘holes’’ for the carriers in the p -doped bilayer, to avoid confusion we will refer to an absence of a carrier in the otherwise filled valence band as a *anti-particle*. The pairs in the valence band are formed from the pairing of anti-particles. The number of anti-particles available to form pairs in the two bilayers determines the strength of the valence band superfluid gap Δ_- .

The coupling and the strength of the Josephson-like transfer are regulated by E_g through its appearance in the form factors in Eqs. (4.18). This means that, for the first time, when we tune E_g we are able to tune the magnitude of the Josephson-like pair transfer.

In this chapter, we take the interaction term in Eqs. (4.18) as unscreened,

$$V_{eh}(|\mathbf{k} - \mathbf{k}'|) = - \frac{2\pi e^2}{\epsilon\epsilon_0} \frac{e^{-d|\mathbf{k}-\mathbf{k}'|}}{|\mathbf{k} - \mathbf{k}'|}, \quad (4.22)$$

where d is the thickness of the insulating barrier separating the two bilayer sheets. The dielectric constant for a hBN insulating barrier of thickness $d \geq 1$ nm is $\epsilon \sim 2$ [138]. The effective Rydberg energy of the system is $R_y = 68$ meV (Eq. (2.1)) and the effective Bohr radius $a_B = 5.4$ nm (Eq. (2.2)).

As discussed in Section 3.3.2, neglecting the screening is an excellent approximation in the BEC regime because the strong interaction tightly binds the pairs and makes them compact on the scale of the average inter-particle separations r_0 [42]. For example, at density of 1×10^{11} cm $^{-2}$ ($r_s \sim 13$), $r_0 = 18$ nm is much larger than the minimum electron-hole separation, $d = 1$ nm, and the effective Bohr radius in DBG ($r_0/a_B \sim 3.4$). The unscreened approximation remains surprisingly accurate even in the Crossover regime at intermediate densities [10], predicting superfluid gaps correctly to within $\sim 20\%$ [42]. However, at larger densities where BCS regime is expected, $n \geq 5 \times 10^{11}$ cm $^{-2}$ ($r_s \leq 6$), the ratio $r_0/a_B \sim 1.5$, and the unscreened approximation completely breaks down since at these densities there is very strong screening which kills the superfluidity [10, 76]. For this reason we restrict our results here to densities $n \leq 5 \times 10^{11}$ cm $^{-2}$ ($r_s \geq 6$).

Density Equation in DBG

The total density equation is derived from Eq. (3.42):

$$n = n_+ + n_- = g_s g_v \sum_{\gamma} \int \frac{d^2 \mathbf{k}}{(2\pi)^2} v_{\gamma}^2(k). \quad (4.23)$$

In graphene the spin and valley degeneracy are $g_s = 2$ and $g_v = 2$.

Equation (4.23) presents two problems:

1. The equation includes all occupied states in the valence band. This results in an impractically large n_- .
2. The closeness in energy of the valence band and Josephson-like transfers, means that we must distinguish between the total density of carriers in the conduction band n_+ and the doping density n_{0+} . This is because for a small band gap, particles near the top of the valence band can be readily excited by the interactions into the low lying states of the conduction band. This has the effect of increasing the number of the particles in the conduction band, so $n_+ > n_{0+}$, and of depleting the number of particles at the top of the valence band (Fig. 4.3). This corresponds to introducing a density of anti-particles into the valence band.

We write the doping density as [139, 140]:

$$n_{0+} = g_s g_v \sum_k [v_+^2(k) - u_-^2(k)]. \quad (4.24)$$

n_{0+} is equal to the total number of carriers in the conduction band $n_+ = g_s g_v \sum_k v_+^2(k)$ less the number of carriers in the conduction band that have been excited by the interactions from the valence band. The number of excited carriers equals the number of empty states (anti-particle states) left behind in the valence band. This can be written as $g_s g_v \sum_k u_-^2(k)$.

The chemical potential μ is obtained by solving the n_{0+} density equation, Eq. (4.24), coupled with the gap equations, Eqs. (4.18). The increase in the number of carriers in the conduction band will push up the Fermi energy. We define an effective Fermi momentum $k_F^* = \sqrt{\pi n_{0+}}$, and an effective Fermi energy in the conduction band $E_F^* = (\hbar k_F^*)^2 / 2m^*$.

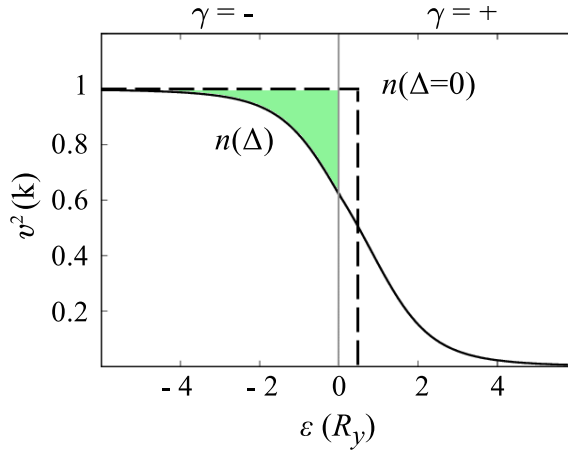


FIGURE 4.3: The density distribution $v_{\gamma}^2(k)$ for electrons, as a function of $\varepsilon_{\gamma}(k)$ for a system at low density with $E_g = 0$. The dashed line indicates the density distribution for the normal system ($\Delta = 0$) at the same density. The green area represents the number of *anti-particle* in the valence band. The energy scale is in units of the effective Rydberg energy.

BCS-BEC Crossover in DBG

As we introduced in Section 3.2.1 we use three criteria to identify the BCS-BEC crossover regimes. The ratio of the superfluid gap Δ_{γ} to E_F^* is a criterion to determine if the system is in the strongly interacting regime, $\Delta_{\gamma}/E_F^* \gg 1$, or in the weakly interacting regime, $\Delta_{\gamma}/E_F^* < 1$. A second criterion uses the chemical potential. μ is equal to the E_F^* in the BCS regime, detaches from E_F^* when the Crossover regime is entered and becomes negative when the BEC regime is entered. The different regimes of the BCS-BEC crossover can also be identified by the value of the superfluid condensate fraction c .

In our system there are two condensate fractions, for the conduction band c_+ and for the valence band c_- . For the conduction band, the usual one-band expression for the condensate fraction (Eq. (3.44)) is readily generalized to be the number of pairs divided by the total number of carriers in the conduction band,

$$c_+ = \frac{\sum_k u_+^2(k) v_+^2(k)}{\sum_k v_+^2(k)}. \quad (4.25)$$

The pairs in the valence band are formed from the pairing of anti-particles of the two sheets, so the corresponding definition of c_- is the ratio of the number of pairs in the valence band to the number of anti-particles in the valence band,

$$c_- = \frac{\sum_k u_-^2(k) v_-^2(k)}{\sum_k u_-^2(k)}. \quad (4.26)$$

The usual classification is used with $c_{\gamma} > 0.8$ for the BEC regime, $c_{\gamma} < 0.2$ for the BCS regime and $0.2 < c_{\gamma} < 0.8$ for the Crossover regime.

4.3 Results

Figure 4.4 compares the contributions to pair formation from the conduction and valence bands as a function of n_{0+} . In terms of importance in the pair formation, the conduction and valence bands have different roles depending on the magnitude of the band gap and

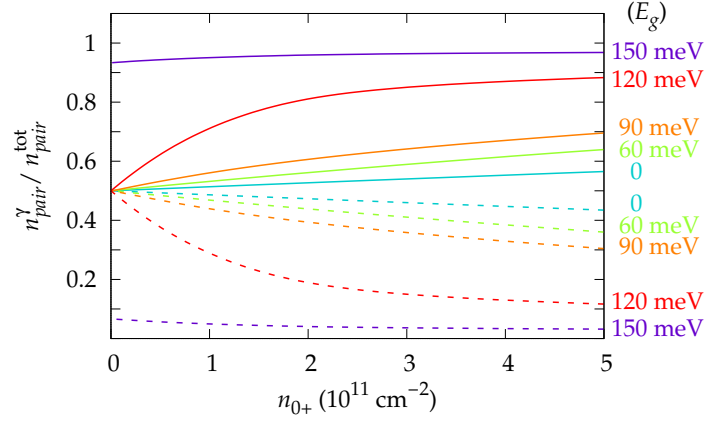


FIGURE 4.4: The relative number of condensate pairs in the conduction band (solid lines) and valence band (dashed lines) as functions of n_{0+} . Values of the energy band gap E_g are labelled.

on the density. The ratios $n_{pair}^{\pm} / (n_{pair}^{+} + n_{pair}^{-})$ are shown for different energy band gaps, where $n_{pair}^{\gamma} = \sum_k u_{\gamma}^2(k) v_{\gamma}^2(k)$.

We see in Fig. 4.4 that for large values of E_g , pair formation is confined to the conduction band and is independent of n_{0+} . This is due to the weak contribution of the Josephson-like transfer. For smaller E_g , we distinguish two behaviours with respect to density n_{0+} . For large n_{0+} , the average kinetic energy of the carriers in the conduction bands $\langle K \rangle$ is large relative to the average strength of the Coulomb interactions, $\langle V \rangle$. Since $\sum_k v_{+}^2(k) \gg \sum_k u_{-}^2(k)$, there are only a negligible number of carriers excited out of the valence band, so a negligible number of anti-particle pairs are present. On the other hand, small n_{0+} does not necessarily imply that the average kinetic energy of the carriers in the conduction bands is small relative to the average strength of the Coulomb interactions, since for sufficiently small energy band gaps E_g , both $\sum_k v_{+}^2(k)$ and $\sum_k u_{-}^2(k)$ can be large and nearly equal. In the limit $E_g = 0$, they become equal, $\sum_k v_{+}^2(k) = \sum_k u_{-}^2(k)$ and both bands contribute equally to the pair formation, whether the interactions are strong or weak.

Figure 4.5 shows the condensate fractions and the chemical potential as functions of n_{0+} for different E_g . We recall for $n_{0+} > 5 \times 10^{11} \text{ cm}^{-2}$ that screening is expected to suppress superfluidity in what would otherwise be the BCS regime [10], so we focus on density range $n_{0+} < 5 \times 10^{11} \text{ cm}^{-2}$. For a large bandgap, $E_g = 150 \text{ meV}$, (Fig. 4.5(a)), the behaviour of c_{\pm} and μ is as expected close to results for a one-band system [115]. For large $n_{0+} \sim 5 \times 10^{11} \text{ cm}^{-2}$, $c_{+} \sim 0.8$, so the conduction band condensate is already in the Crossover regime. As n_{0+} decreases, c_{+} becomes > 0.8 and the conduction band condensate enters the BEC regime. The chemical potential goes negative at the BEC boundary, and it is everywhere less than E_F^* . As n_{0+} goes to zero, the conduction band condensate enters the deep BEC limit and $\mu \rightarrow -E_B/2$, half the binding energy of an independent electron-hole pair (Fig. 4.6). The value of the binding energy E_B is calculated as a two-body bound state (see details in Appendix C). In notable contrast with the behaviour of c_{+} , we see that $c_{-} \sim 1$ always, so the valence band condensate remains in the BEC regime over the full range of n_{0+} shown. This is because there are very few anti-particles in the valence band when E_g is large.

For a smaller gap, $E_g = 90 \text{ meV}$ (Fig. 4.5(b)), the conduction band condensate is slower to enter the BEC regime with decreasing n_{0+} . This is because excitations from the valence band now significantly increase the total population of carriers in the conduction

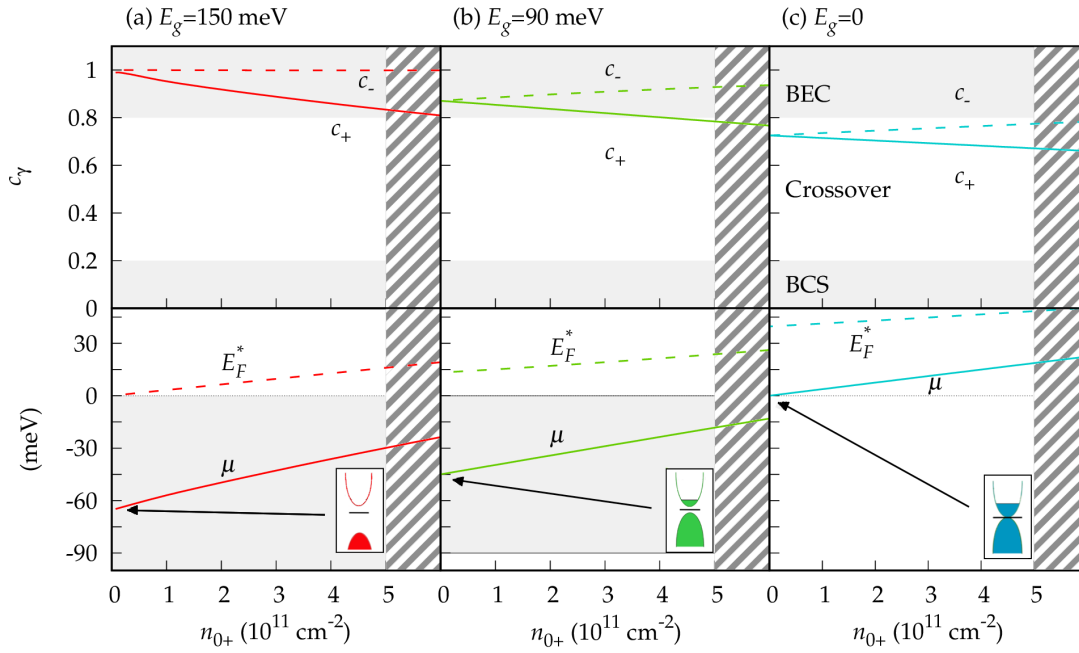


FIGURE 4.5: The condensate fraction and the chemical potential as functions of n_{0+} for different values of E_g , as labelled. In the upper panels, the solid and dashed lines indicate the condensate fraction in the conduction band and valence band, respectively. In the lower panels, the solid lines show the chemical potential μ and the dashed lines the effective Fermi energy E_F^* . The light shaded area represents the energy band gap. Screening is expected to suppress the superfluidity for $n_{0+} > 5.0 \times 10^{11} \text{ cm}^{-2}$.

band. The chemical potential μ therefore goes negative only at very low n_{0+} . It is interesting that in the zero n_{0+} limit, μ approaches the mid-point of the band gap, $\mu \rightarrow -E_g/2$ instead of $-E_B/2$, behaviour analogous to the intrinsic limit in a conventional semiconductor.

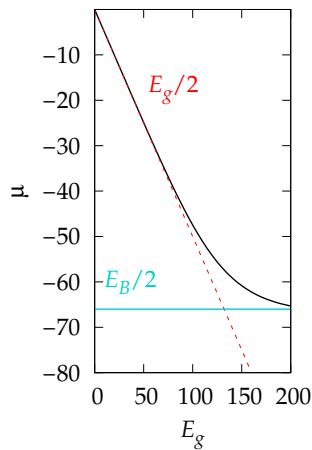


FIGURE 4.6: Low-density limit of chemical potential as a function of E_g . E_B is the binding energy.

Figure 4.6 shows the behaviour of the chemical potential in the zero-density limit as a function of E_g . The one-band limit $\mu \rightarrow -E_B/2$ is only recovered when $E_g > E_B$, while

for $E_g < E_B$ the conventional semiconductor value is recovered.

Figure 4.5(c) is for the gapless system, $E_g = 0$. In this case, there are many carriers in the conduction band excited from the valence band. This makes the effective Fermi energy E_F^* as a function of n_{0+} significantly larger than in Figs. 4.5(a) and 4.5(b), and at the same time a large number of anti-particles are created in the valence band. For this reason, both the conduction and valence band condensates remain always in the Crossover regime for all n_{0+} with the chemical potential μ always positive. A curious point is that for $E_g = 0$, a negative value of μ would signify only an inversion of the carrier populations in the bands, so that even for negative values of μ , the system would remain in the Crossover regime.

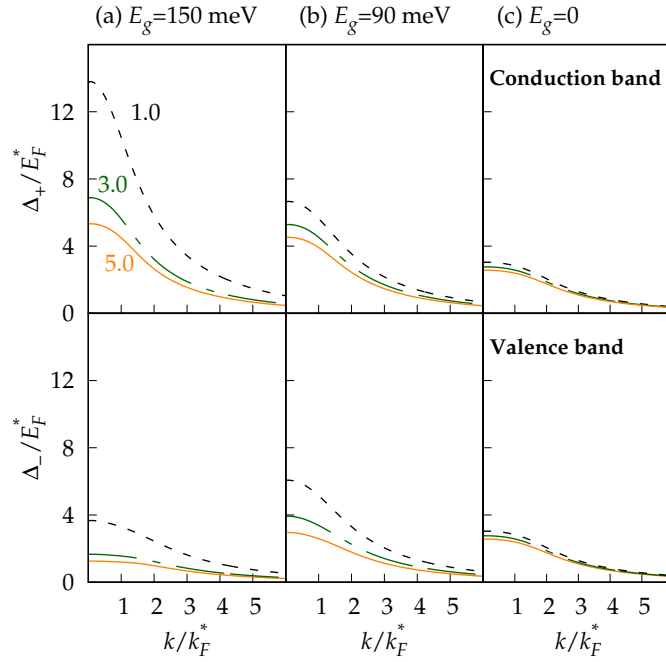


FIGURE 4.7: The superfluid gap energy $\Delta_{\pm}(k)$ in the conduction and valence bands, for different values of energy band gap E_g and different densities n_{0+} as labelled.

Figure 4.7 shows the momentum dependent superfluid energy gaps $\Delta_{\pm}(k)$. The results are for low density $n_{0+} = 0.5 \times 10^{11} \text{ cm}^{-2}$, $r_s = 19$ (dotted lines), intermediate density $n_{0+} = 1.5 \times 10^{11} \text{ cm}^{-2}$, $r_s = 10$ (dashed lines), and high density $n_{0+} = 5 \times 10^{11} \text{ cm}^{-2}$, $r_s = 6$ (solid lines). For large E_g , Fig. 4.7(a), $\Delta_+(k) \gg \Delta_-(k)$. This result is due to the large E_g in the form factor (Eq. (4.21)) that suppresses $\mathcal{F}_{\gamma\gamma'}(\mathbf{k}, \mathbf{k}')$ for $\gamma \neq \gamma'$ and nearly decouples the gap equations (Eqs. (4.18)). This means that the number of paired anti-particles in the valence band, $\sum_k (u_k^-)^2$, remains small for all n_{0+} . Consistent with the conclusion in Fig. 4.5(a), the very broad peaks in $\Delta_-(k)$ for all n_{0+} , indicate that the valence band condensate for large E_g always remains in the BEC regime. Because the $\sum_k (u_k^-)^2$ is small, the conduction band contains very few carriers excited from the valence band, so the evolution of the conduction band condensate with n_{0+} , is very similar to the one-band system:

- for small n_{0+} , $\Delta_+(k) \gg E_F^*$, its peak is at $k = 0$ and it is very broad, characteristics of the BEC regime;
- for large n_{0+} , the peak in $\Delta_+(k)$ becomes of order E_F^* , it narrows and detaches from $k = 0$, though never reaching $k = k_F^*$, characteristics of the Crossover regime.

For smaller E_g , Figs. 4.7(b) and 4.7(c), the $\Delta_{\pm}(k)$ are comparable and are not very sensitive to n_{0+} . This is because the $\mathcal{F}_{\gamma\gamma'}(\mathbf{k}\mathbf{k}')$ for $\gamma \neq \gamma'$ are no longer small, and so strongly couple the two gap equations. The insensitivity of the superfluid gaps to n_{0+} is a consequence of the large number of carriers in the conduction band excited from the valence band for all n_{0+} . This means that the total number of carriers in the conduction band remains large for all n_{0+} . Thus the conduction band condensate remains trapped in the Crossover regime and is unable to reach the BEC regime even when n_{0+} becomes very small.

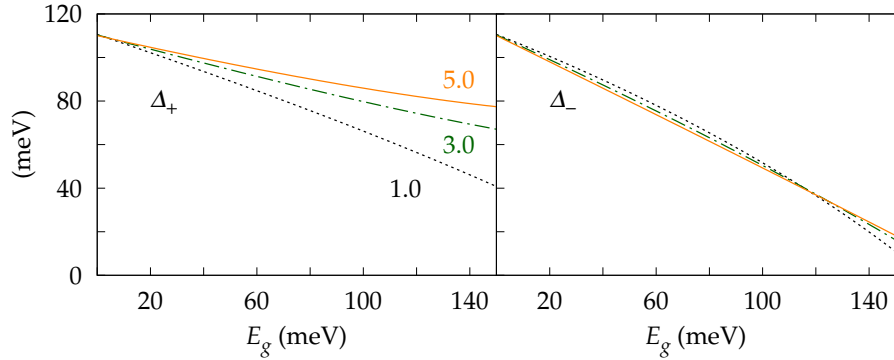


FIGURE 4.8: Maximum superfluid gap energy Δ_{\pm} in the conduction and valence bands as functions of the energy band gap E_g . Dotted lines: $n_{0+} = 0.5 \times 10^{11} \text{ cm}^{-2}$; dashed lines: $n_{0+} = 1.5 \times 10^{11} \text{ cm}^{-2}$; solid lines: $n_{0+} = 5 \times 10^{11} \text{ cm}^{-2}$.

Figure 4.8 further characterizes the multi-component nature of the superfluidity. As expected, for zero band gap the Josephson-like transfer is strong and the consequent reinforcement of the anti-particle population will strongly couple the superfluid condensates. The maximum superfluid gap energy for the conduction band Δ_+ is equal to Δ_- , the maximum superfluid gap for the valence band. We see that for small band gaps, there is a significant boost of both Δ_+ and Δ_- until $E_g < \Delta^+$. For large band gap, $E_g > \Delta^+$, pairs have insufficient energy to excite into the other band and the superfluidity is not able to take advantage of the valence band. The valence band condensate is completely decoupled from the conduction band condensate. This results in $\Delta_+ \gg \Delta_-$ and there is only one significant superfluid gap and one significant condensate.

We can also present a phase diagram of the BEC-BCS crossover regimes as a function of the energy band gap and of the density. Figure 4.9 shows that by using the tunable band gap E_g , we can move the boundaries of the BCS-BEC crossover while keeping the density fixed.

We recall we have neglected interband pairing. Our results justifies this approximation both for large and small gaps E_g . For large E_g it is clear because of the large energy differences in the corresponding denominators. For small E_g , the large number of carriers in the conduction band excited from the valence band means a large effective Fermi energy, so the interband pairing terms again contain large energy difference denominators, reflecting the large energy separation of the carriers in the valence band from the effective Fermi energy. In addition, the matrix elements for the interband pairing terms in both cases are expected to be small (see Ref. [141]), and this would further reduce the interband pairing contribution.

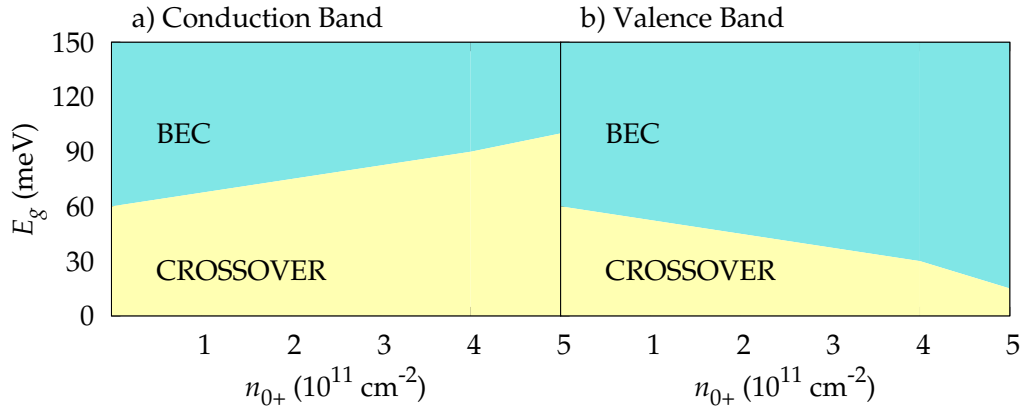


FIGURE 4.9: The BEC and Crossover regimes in (a) conduction band and (b) valence band, as a function of the energy band gap and the density n_{0+} .

4.4 Conclusions

In summary, we have shown that the tunable band gap E_g in DBG is important to determine the properties of the multi-component electron-hole superfluidity in this system because it controls the coupling between the conduction and valence band condensates. When E_g is small and the density low ($\sum_k v_+^2(k) \sim \sum_k u_-^2(k)$), the multi-component character becomes evident. Continuously tuning E_g up to higher values will induce a switching-over of the number of superfluid components from two to one.

We can distinguish two regions defined by the energy competition between the band gap E_g and the effective Fermi energy E_F^* :

- For $E_g \ll E_F^*$, the superfluidity is always in the Crossover regime even when n_{0+} is very small. The conduction band condensate does not enter the BEC regime because excitations from the valence band maintain a large number of carriers in the conduction band.
- When $E_g \geq E_F^*$, the conduction band condensate enters the BEC regime for small n_{0+} because a large E_g suppresses excitations from the valence band.

These multi-component properties are reflected in the asymptotic behaviour of the chemical potential in the small n_{0+} limit (Fig. 4.6).

We conclude that a compromise is necessary to have optimal conditions for superfluidity. The band gap E_g must not be too small, otherwise excitations from the valence band will maintain too high the density of carriers in the conduction band. This keeps the conduction band in the high-density regime that is not favourable for superfluidity because of the screening. On the other hand, a too large E_g weakens the superfluidity since it excludes the reinforcing contributions from the valence band. We find that an optimal choice for E_g is in the range 80-120 meV.

Chapter 5

Multi-component Screening and Superfluidity in Biased Electron-Hole Double Bilayer Graphene

In this chapter, we extend the investigation on Double Bilayer Graphene by using a complete theoretical approach that includes both conduction and valence band contributions to the screened Coulomb interaction and the real low-energy band structure of bilayer graphene. By tuning of the band gap we investigate the effect of the different screening contributions and of the effect of distortion of the bands into a Mexican hat-like shape that accompanies the band gap opening. We find there is strong competition between superfluidity and the screening and that this competition affects in different way the intraband and interband screening. We find significant effects due to the flattening of the bands. We find our results are in agreement with the experimental observations [17].

In the previous chapter, we demonstrated the competition in this system at zero temperature of three competing energy scales: the Fermi energy E_F , the band gap E_g , and the magnitudes of the valence and conduction band superfluid gaps. There is a fourth competing energy not yet included: the strength of the electron-hole attraction for a given separation of the bilayers.

In contrast with most works on superconductors, for electron-hole superfluidity the long-range nature Coulomb attraction between the electrons and holes means that screening must be fully accounted for [42, 76, 124]. As discussed in Section 3.3.2, Ref. [42] demonstrated that neglecting screening is an excellent approximation at low density, which is BEC regime, where the pairs are compact on the scale of the inter-particle separations, $r_{pair} \ll r_0$. However, the screening effect becomes more important at high density, when the system enters the BCS regime, where the pairs are overlapping, $r_{pair} > r_0$.

References [10, 118] took into account screening in DBG and they showed that superfluidity exists only over a finite density range. However, they considered only the conduction band of bilayer graphene approximated with a parabola. In Chapter 4 we neglected screening, but we took into account both the valence and conduction bands. We demonstrated that the proximity in energy of the valence band affects the pairing processes. Thus a complete theoretical approach is required to include both conduction and valence bands also in the screening.

In Chapter 4 we used the parabolic approximation for both bands. In doing so, we neglect the bilayer graphene property that the opening of the band gap is accompanied by a distortion of the bands from parabola. By increasing the band gap the band becomes flatter, leading to van Hove-like singularities and to large Density Of States (DOS) [78], and develops a *Mexican hat*-like shape, leading to a low doping Fermi surface which is a ring. This unusual topology of the Fermi surface greatly enhances electron-electron interactions and strongly affects the polarizability of bilayer graphene [142]. Because the

effects of flattening and of the Fermi ring are important at low densities, where superfluidity is predicted, the theoretical approach need to include the distortion of graphene bilayer bands.

In this chapter, in our unified calculation, we systematically examine the competing effects driving and impeding the emergence of a superfluid state in DBG:

- The small band gaps compared with the Fermi energy that makes multi-band pairing significant;
- the combination of intraband and interband screening effects;
- and the graphene bilayer Mexican hat bands when there is a band gap.

In a recent experiment enhanced tunnelling conductance at equal carrier densities was reported in a DBG system with a 1.4 nm WSe₂ insulating barrier [13]. As introduced in Section 2.2.1 this is a signature that strongly points to the existence of an electron-hole superfluid condensate, as predicted theoretically. The signature was observed only at lower densities and is in quantitative agreement with the theoretical predictions [10] of an upper limit of the carrier density for the superfluidity.

5.1 The extended theoretical approach

The DBG system was introduced in Section 4.1 of the previous chapter. The distortion of the band from parabolic does not affect the pairing symmetries (Fig. 4.2). We focus on equal electron and hole densities, and we neglect the interband pairing. This means that we can retain the mean field equations obtained in Section 4.2.

The superfluidity is described by the coupled conduction and valence band gap equations (Eqs. (4.18)), Δ_+ and Δ_- . The chemical potential is calculated from the density equation, Eq. (4.23). The approach is extended by substituting:

- the parabolic $\varepsilon_\gamma(k, E_g)$ in Eqs. (4.18) and (4.23) with the Mexican hat-like shape;
- and the unscreened $V_{eh}(|\mathbf{k} - \mathbf{k}'|)$ in Eqs. (4.18) with the screened interaction.

5.1.1 Bilayer Graphene Dispersion

We recall that the energy band dispersions for a single bilayer graphene in AB stacking are given by Eq. (4.3), calculate from a tight-binding Hamiltonian with a symmetric opening of the gap (Eq. (4.2)).

In the previous chapter, we have shown in Fig. 4.8 that, with unscreened approximation, the energy scale of the pairing processes, $\Delta \sim 100$ meV, is smaller than $t_1 \sim 400$ meV. Thus, we retain in the calculation only the two low-energy bands as we did previously.

$$\varepsilon_\gamma(k) = \gamma \frac{1}{2} \sqrt{(t_1 - \Gamma)^2 + E_g^2 \left(1 - \frac{4(\hbar v_F k)^2}{t_1^2}\right)} \quad \Gamma = \sqrt{t_1^2 + 4(\hbar v_F k)^2 + \frac{4(\hbar v_F k)^2 E_g^2}{t_1^2}}. \quad (5.1)$$

Without a band gap, the conduction and valence bands in bilayer graphene are parabolic at low energies. However, the opening of a band gap E_g is accompanied by a flattening of the low-energy bands and the appearance of a small maximum centred on the K point, the Mexican hat shape [143]. The small maximum grows in height with increasing E_g (Fig. 5.1). In addition, the DOS around the K point is strongly enhanced by the development of van Hove-like singularities [78], resulting in a significant decrease in the Fermi

5.1. The extended theoretical approach

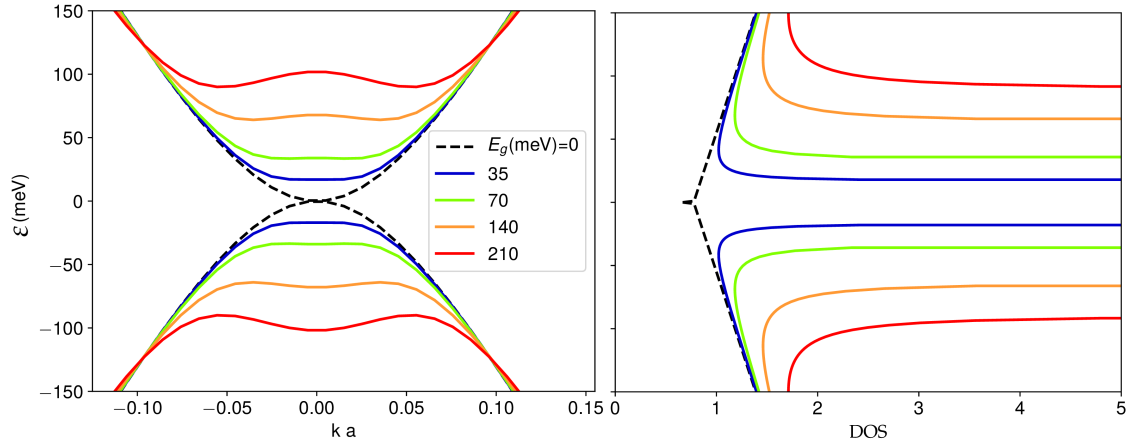


FIGURE 5.1: a) Low-energy band structure of a single bilayer graphene $\varepsilon_{\gamma=\pm}(k)$, with zero band gap (dashed black curve) and with finite band gap E_g (solid coloured curves), as labelled. b) Corresponding Density Of States (DOS), for different E_g .

energy E_F (Fig. 5.7). The large build-up of the DOS at the bottom of the bilayer conduction band significantly reduces E_F at a given density compared with E_F for the parabolic band, but the flattening of the bands increases k_F . In addition, at low densities E_F lies below the central maximum of the conduction band defining a Fermi ring.

Form factor

The form factor in Eqs. (4.18) is modified together with the bilayer graphene energy dispersion. To obtain the complete form factor we calculate the 4-component eigenvalues $\Psi_\gamma(k, \phi_k)$ of the Hamiltonian Eq. (4.2). The form factors $\mathcal{F}_{\gamma\gamma'}(\mathbf{k}\mathbf{k}')$ are calculate numerically as $|\Psi_\gamma(k, \phi_k)\Psi_{\gamma'}(k', \phi_{k'})|^2$ (Eq. (4.19))

Figure 5.2 shows the comparison between $\mathcal{F}_{\gamma\gamma'}(\mathbf{k}\mathbf{k}')$ with bilayer real dispersion and with parabolic approximation (Eq. (4.21)).

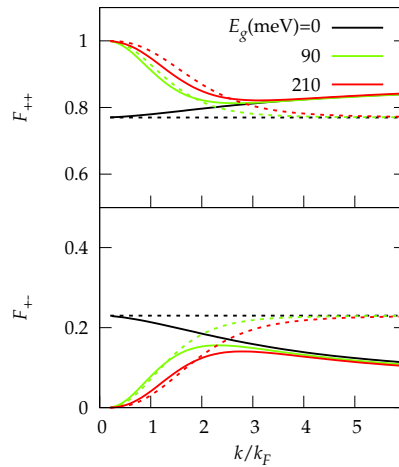


FIGURE 5.2: The form factor for equal bands $F^{++} = F^{--}$ and opposite bands F^{+-} , in the case $|k| \sim |k'|$ and $\phi_{k'} - \phi_k \neq 0$ but small. The solid lines are form factors with real dispersion and the dashed lines are the form factor in low energy parabolic approximation. The k_F is calculated for the maximal density reported in this work, $n = 7 \times 10^{11} \text{ cm}^{-2}$. The values of the band gap E_g are labelled.

We show the form factors at small $q = |k - k'|$, where the interaction is stronger, thus the effect of the form factor should be more relevant. The curves are in good agreement for $k < 2k_F$. We will see this correspond to the q -region where the screening is more important (See discussion after Eq. (3.53) and discussion in Section 5.2.1). Changing the value of $\phi_{k'} - \phi_k$, the magnitude of the terms $F^{++} = F^{--}$ and F^{+-} is modified, but the agreement for $k < 2k_F$ is not affected. For these reasons, in the gap equations (Eqs. (4.18)) we retain the analytic expression for the form factor (Eq. (4.21)) as a good approximation.

5.1.2 Screened Interaction in Double Bilayer Graphene

To include the screening of the interaction in the superfluid gap equations (Eqs. (4.18)), we use the Random Phase Approximation introduced in Section 3.3 for static screening.

Screening in Normal State

The screened interlayer Coulomb potential in the normal state is described by Eq. (3.53) [123],

$$V_{eh}(q) = \frac{V_D(q)}{1 - 2\Pi_N(q)V_S(q) + \Pi_N^2(q)(V_S^2(q) - V_D^2(q))}, \quad (5.2)$$

where $q = |\mathbf{k} - \mathbf{k}'|$. $V_S(q)$ is the bare repulsive Coulomb interaction between carriers in the same bilayer and $V_D(q) = -V_S(q)e^{-dq}$ the bare attractive Coulomb interaction between electrons and holes in the opposite bilayers. $\Pi_N(q)$ is the static polarizability in a single graphene bilayer, and is given by,

$$\Pi_N(q) = g_s g_v \sum_{\gamma, \gamma'} \sum_{\mathbf{k}} \mathcal{F}_{\gamma, \gamma'}(\mathbf{k}, \mathbf{k}') \frac{n_F[\varepsilon_\gamma(k)] - n_F[\varepsilon_{\gamma'}(k')]}{\varepsilon_\gamma(k) - \varepsilon_{\gamma'}(k')}, \quad (5.3)$$

where it is useful to distinguish $\Pi^{\text{intra}}(q)$, the intraband contributions in the sum with $\gamma = \gamma'$ for which the stimulus and response are in the same band, and $\Pi^{\text{inter}}(q)$, the interband contributions with $\gamma = -\gamma'$, for which the stimulus and response occur in opposite bands [144].

References [122, 135, 145–147] investigated the separate properties of Π^{intra} and Π^{inter} for bilayer graphene in the normal Fermi liquid state. They showed that the two terms have qualitatively different dependencies on the momentum transfer q .

For $\Pi^{\text{intra}}(q)$, only the conduction band contributes, $\Pi^{\text{intra}}(q) \simeq \Pi_{++}(q)$. The valence band contribution $\Pi_{--}(q)$ is always zero because the valence band is completely full. The conduction band contribution $\Pi_{++}(q)$ scales with the DOS in the conduction band and increases with conduction band density n . $\Pi_{++}(q) = 0$ for $n = 0$. There is a peak in $\Pi_{++}(q)$ at $q = 2k_F$, and then for $q > 2k_F$ it falls to zero (See solid green line in Fig. 5.3(c)) This behaviour leads to the familiar effect of the screening in real space: the screened potential is cut off to zero when $r \geq r_c$, defining a screening length r_c .

For $\Pi^{\text{inter}}(q)$ the enormous reservoir of carriers in the valence band ensures that $\Pi^{\text{inter}}(q)$ is not zero even when the conduction band density $n = 0$. At $q = 0$, we always have $\Pi^{\text{inter}}(0) = 0$, because interband vertical scatterings and back scatterings are forbidden, $\mathcal{F}_{+-}(\mathbf{k}, \mathbf{k}) = 0$ in Eq. (5.3). $\Pi^{\text{inter}}(q)$ grows monotonically from zero with q , and becomes larger than $\Pi^{\text{intra}}(q)$ for $q > 2k_F$ (See dashed green line in Fig. 5.3(c)). In real space, the large- q behaviour of $\Pi^{\text{inter}}(q)$ reduces the strength of screened interaction at small $r < r_c$. Since $\Pi^{\text{inter}}(q)$ involves excitations across the band gap E_g , $\Pi^{\text{inter}}(q)$ should be sensitive to E_g , being strongest for small E_g .

Since they worked at high densities, Refs. [122, 135, 145, 146] neglected the small maximum in $\varepsilon_\gamma(k)$ centred at the K point and the flattening of the bands, the effect of which become non-negligible at low densities [147].

Screening in Superfluid State

As introduced in Section 3.3.2, in the the superfluid state, the pairing between electrons and holes modifies the density-response of the system and thus the screening. The RPA screened interaction in the superfluid state is given by [76, 124],

$$V_{eh}(q) = \frac{V_D(q) + \Pi_A(q)(V_S^2(q) - V_D^2(q))}{1 - 2(V_S(q)\Pi_N(q) - V_D(q)\Pi_A(q)) + (\Pi_N^2(q) - \Pi_A^2(q))(V_S^2(q) - V_D^2(q))}. \quad (5.4)$$

The normal polarizability $\Pi_N(q)$ is modified from the polarizability in the Fermi liquid state (Eq. (5.3)) by the superfluidity. To calculate the normal and anomalous polarizabilities, $\Pi_N(q)$ and $\Pi_A(q)$, we use Eqs. (3.55) and (3.56) in the case of DBG with only intraband pairing with $n = m = \gamma (i = j = \gamma')$.

$$\Pi_N^{\gamma\gamma'}(q, \Omega) = \frac{T}{L^2} \sum_{\mathbf{k}, \omega} \mathcal{F}_{\gamma, \gamma'}(\mathbf{k}, \mathbf{k}') G_{\gamma\gamma}[i\omega + i\Omega, k'] G_{\gamma'\gamma'}[i\omega, k], \quad (5.5)$$

$$\Pi_A^{\gamma\gamma'}(q, \Omega) = \frac{T}{L^2} \sum_{\mathbf{k}, \omega} \mathcal{F}_{\gamma, \gamma'}(\mathbf{k}, \mathbf{k}') F_{\gamma\gamma}[i\omega + i\Omega, k'] F_{\gamma'\gamma'}[i\omega, k]. \quad (5.6)$$

We use the Green functions derived in the Section 4.2, in Eq. (4.14). We perform the summation over the Matsubara frequencies ω , in the static limit $\Omega \rightarrow 0$ and at zero temperature (see details in Appendix Sec. B.1). We obtain:

$$\begin{aligned} \Pi_N(q) &= g_s g_v \sum_{\gamma, \gamma'} \Pi_N^{\gamma\gamma'}(q), \\ \Pi_N^{\gamma\gamma'}(q) &= - \int \frac{d^2\mathbf{k}'}{(2\pi)^2} \mathcal{F}_{\gamma, \gamma'}(\mathbf{k}, \mathbf{k}') \frac{u_\gamma^2(k)v_{\gamma'}^2(k') + v_\gamma^2(k)u_{\gamma'}^2(k')}{E_\gamma(k) + E_{\gamma'}(k')}, \end{aligned} \quad (5.7)$$

$$\begin{aligned} \Pi_A(q) &= g_s g_v \sum_{\gamma, \gamma'} \Pi_A^{\gamma\gamma'}(q), \\ \Pi_A^{\gamma\gamma'}(q) &= \int \frac{d^2\mathbf{k}'}{(2\pi)^2} \mathcal{F}_{\gamma, \gamma'}(\mathbf{k}, \mathbf{k}') \frac{2u_\gamma(k)v_\gamma(k)v_{\gamma'}(k')u_{\gamma'}(k')}{E_\gamma(k) + E_{\gamma'}(k')}, \end{aligned} \quad (5.8)$$

From Eq. (5.8), we see that $\Pi_A(q)$ is directly proportional to the superfluid gaps since $u_\gamma(k)v_\gamma(k) = \Delta_\gamma(k)/2E_\gamma(k)$. $\Pi_A(q)$ strictly depends on the population of electron-hole pairs in the bands. We again define intraband and interband contributions,

$$\Pi_{n,a}^{\text{intra}}(q) = \sum_{\gamma} \Pi_{n,a}^{\gamma\gamma}(q), \quad \Pi_{n,a}^{\text{inter}}(q) = \sum_{\gamma} \Pi_{n,a}^{\gamma, -\gamma}(q). \quad (5.9)$$

We recall from the discussion in Section 3.3.2 that in the superfluid state, the presence of the superfluid gap in the energy spectrum blocks the low-lying small- q excitations needed for screening, and superfluid pairing reduces the population of free carriers available for screening. Thus in the superfluid state, screening of the long-range interactions is weakened compared with screening in the Fermi liquid state. Analytically, the

reduction in screening is caused by the partial cancellation of the normal and anomalous polarizabilities (Eqs. (5.7)-(5.8)) (See solid green line in Fig. 5.3(d)).

References [10, 42, 76] considered only the conduction band, and found within mean field that superfluidity can significantly weaken screening in DBG. Recently, quantum Monte Carlo calculations on this system have produced results in good quantitative agreement with the mean field results [118]. In Refs. [10, 42, 118], no solutions to Eqs. (4.18), (4.23), (5.7) and (5.8) of physical relevance existed in the weak-coupled BCS superfluid regime for $\Delta \ll E_F$. Only in the strong-coupled Crossover and BEC regimes, with superfluid gaps $\Delta > E_F$, did solutions exist. This result means that when $\Delta > E_F$, such a wide range of low-lying excited states in the energy spectrum are blocked, that the screening of the electron-hole attractive interaction is sufficiently weakened to allow the superfluidity to exist. Further, the large superfluid condensate fraction in the strong-coupled Crossover and BEC regimes, means that the population of free carriers available for screening is significantly reduced. Since the weak-coupled regime would occur at high density, this leads to the prediction of a maximum value of the density for superfluidity to exist, that is a threshold density for superfluidity.

5.2 Results

Here we present the results of the self-consistent calculation of the screened interaction $V_{eh}(q)$ between electron-hole bilayers for the superfluid state with intraband and interband contributions. We solve Eqs. (4.18) with Eq. (5.4) for fixed band gap E_g and density n . At each iteration, the superfluid gaps and the normal and anomalous polarizabilities (Eqs. (5.7)-(5.8)) are calculated until convergence, using the superfluid gaps from the preceding iteration.

5.2.1 Polarizabilities with Bilayer Graphene

Figure 5.3 shows that the polarizabilities $\Pi(q)$ for the normal and superfluid states are sensitive to the evolution in the shape of the bands accompanying the development of a band gap. This result shows the polarizabilities for fixed density and a fixed E_g . r_0 is the inter-particle spacing within each bilayer.

Figures 5.3(a)-(c) compares $\Pi(q)$ for the normal state (Eq. (5.3)) calculated using the bilayer bands for a small band gap at low density, with $\Pi(q)$ calculated for parabolic bands for the same band gap and density. Figures 5.3(b)-(d) makes a similar comparison for $\Pi(q) = \Pi_N + \Pi_A$ in the superfluid state (Eqs. (5.7)-(5.8)).

In the normal state (Fig. 5.3(a)), the polarizability with the bilayer bands is stronger than the polarizability with the parabolic bands over the full range of momentum transfers q that affect screening, $qr_0 \lesssim 4$. The additional peak in $\Pi(q)$ near $qr_0 = 2$ for the bilayer bands comes from the small maximum in the conduction band around the K point. The peak only appears at densities low enough for E_F to lie below this maximum. The maximum generates conduction-band vacancies which add to the intraband screening contribution in this region. $\Pi(q)$ then continues larger for the bilayer bands out to $qr_0 \sim 4$, because the flattening of the bands increases k_F for a given density.

Figure 5.3(c) separates the intraband and interband contributions to $\Pi(q)$ in the normal state. For the bilayer bands, the momentum-transfer range $0 \lesssim qr_0 \lesssim 5$ is dominated by the intraband contributions, while for $qr_0 > 5$ the interband contributions are larger. In contrast, for the parabolic bands the intraband contributions dominate only for $0 \lesssim qr_0 \lesssim 3$, with the interband contributions larger for $qr_0 > 3$. The switch-over from predominantly intraband to predominantly interband screening occurs at a larger qr_0 for

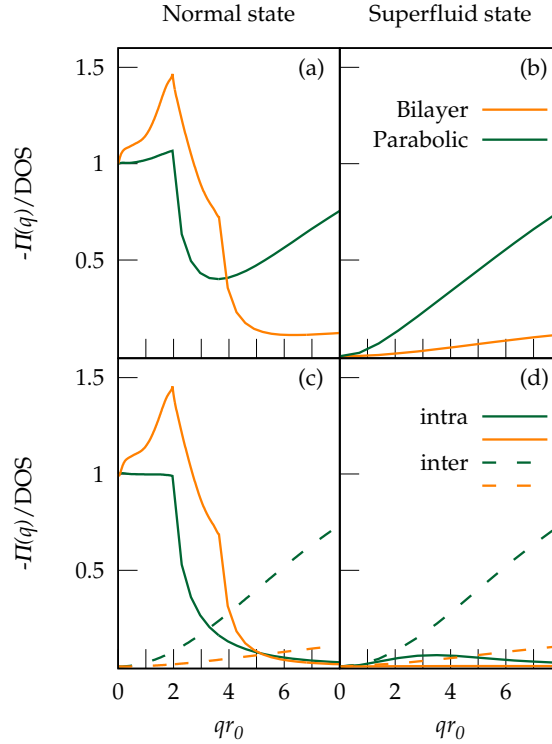


FIGURE 5.3: (a) Comparison of polarizability in the normal state using bilayer bands (orange line) and for parabolic bands (green line) for the same density $n = 0.25 \times 10^{11} \text{ cm}^{-2}$ and same band gap $E_g = 35 \text{ meV}$. (b) Comparison of the corresponding polarizabilities in the superfluid state. (c) Intraband contributions (solid lines) and interband contributions (dashed lines) to the polarizability in the normal state for bilayer bands (orange lines) and for parabolic bands (green lines). (d) Corresponding intraband and interband contributions to the polarizability in the superfluid state.

the bilayer bands because of the flattening of the bilayer bands. The flattening increases k_F for a given density compared with the parabolic bands. The interband polarizability for the bilayer bands is smaller because of their much larger DOS.

In the superfluid state (Fig. 5.3(b)), the polarizability for the bilayer bands is very small for $qr_0 < 4$, while for the parabolic bands it is small only for $qr_0 \lesssim 2$. The source of this difference is that in the presence of superfluidity, the cancellation between the $\Pi_A(q)$ and $\Pi_N(q)$ contributions to the screening, only occurs for the intraband screening. The interband anomalous polarizability is negligible for the following reason. The interband screening arises from excitations from the huge reservoir of carriers in the valence band into the conduction band, and vice versa. The number of pairs in the condensates in both bands contributing to the anomalous polarizability is thus always much smaller than the enormous population of free carriers available for the normal polarizability. Since the intraband contribution for the bilayer bands is significant up to $qr_0 \sim 5$ (Fig. 5.3(c)), the $\Pi_A(q)$ is much more effective in cancelling the screening for the bilayer bands than it is for the parabolic bands, where the screening is suppressed only up to $qr_0 \sim 3$. This property also blocks the extra low-lying screening excitations coming from the small maximum at the bottom of the bilayer conduction band that caused the peak near $qr_0 = 2$ in the normal state $\Pi(q)$ in Fig. 5.3(a). Once the superfluidity has blocked the intraband screening, what remains is the interband screening. We have already seen that interband screening is much weaker for the bilayer bands than for the parabolic bands because of

the large DOS at the bottom of the bilayer conduction bands.

To summarize, the primary new effects of the bilayer bands are that (i) the intraband contributions dominate out to significantly larger values of qr_0 than for parabolic bands, and we recall that only intraband contributions are suppressed by superfluidity; and (ii) the residual interband contributions to the screening are much smaller for bilayer bands than for parabolic bands, because of the large enhancement of the DOS in the low-lying states of the bilayer conduction bands. The net result of these two effects is a screening effect weaker when the band gap is opened because of the flattening of the band.

5.2.2 Multi-band Screening

Figure 5.4 shows the electron-hole interactions $V_{eh}(q)$ in the normal (Eq. (5.2)) and in the superfluid state (Eq. (5.4)) plotted as a function of momentum-transfer q . Also the unscreened interaction $V_D(q)$ is shown.

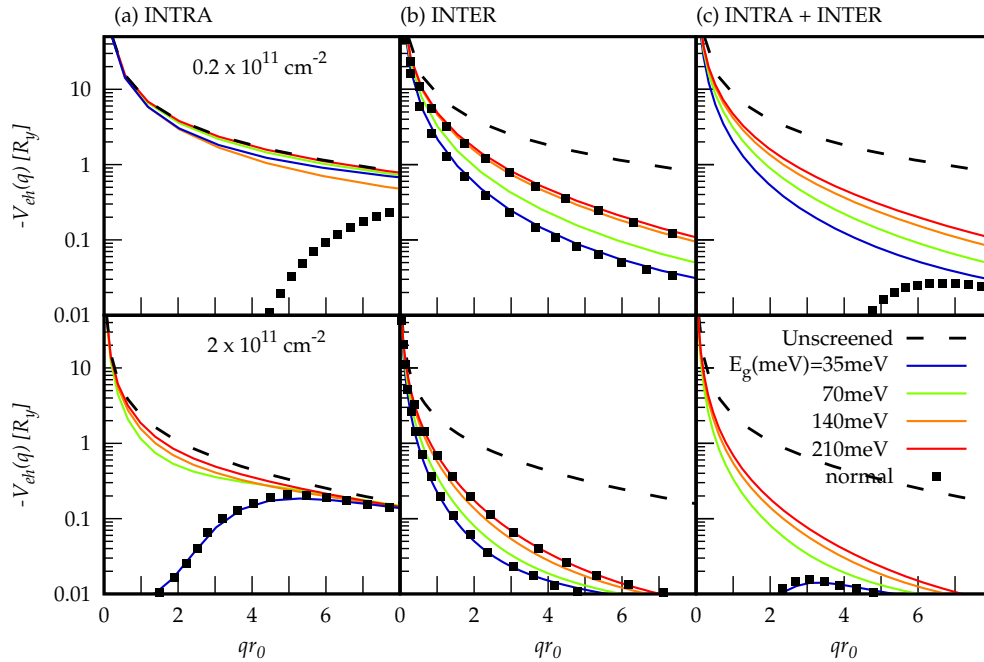


FIGURE 5.4: Unscreened (dashed lines) and screened electron-hole interaction in momentum-transfer space for the superfluid state (coloured curves for different band gaps E_g , as labelled) and for the normal state (squares). For clarity, for the normal state, results are only shown for $E_g = 35$ and 210 meV. The upper and lower rows show densities $n = 0.2 \times 10^{11}$ and $n = 2 \times 10^{11}$ cm^{-2} , respectively. Column (a) is with only intraband contributions to the screening. Column (b) is with only interband contributions to the screening. Column (c) is with both intraband and interband contributions to the screening. $R_y = 68$ meV is the effective Rydberg.

Figure 5.5 compares the self-consistent $V_{eh}(r)$ for the superfluid state in real space with the corresponding screened interaction for the normal state. These are the Fourier transforms of the curves $V_{eh}(q)$ shown in Fig. 5.4. r is the component of the electron-hole separation parallel to the bilayers, and r_0 is the average inter-particle distance within a bilayer calculated from the density.

Figure 5.4(a) isolates the effect of the intraband screening processes, that is, what the screened interaction $V_{eh}(q)$ would be if only the $\Pi^{\text{intra}}(q)$ contribution to $\Pi(q)$ taken from the full self-consistent calculation, were retained. At low density, in the normal state, the

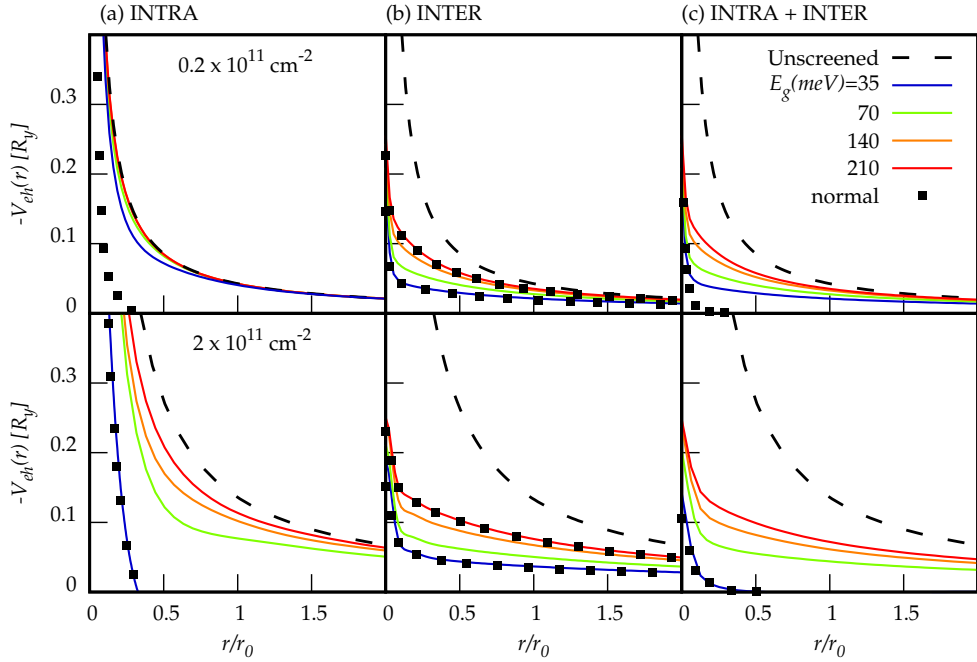


FIGURE 5.5: The electron-hole interaction as displayed in Fig. 5.4, but in real space. The color codes and the symbols are the same as in Fig. 5.4.

large intraband polarizability up to $qr_0 \simeq 4$ (Fig. 5.3) kills the interaction for $qr_0 \geq 4$. $V_{eh}(r)$ is completely screened out to zero by $r/r_0 \geq 0.3$ (Fig. 5.5(a)). However in the superfluid state, the intraband screened potential is, instead, completely unscreened. This is because the anomalous polarizability $\Pi_A^{\text{intra}}(q)$ fully cancels the normal polarizability $\Pi_N^{\text{intra}}(q)$. As the density is increased, the anomalous intraband polarizability becomes ineffective, the cancellation of $\Pi_N^{\text{intra}}(q)$ by $\Pi_A^{\text{intra}}(q)$ is no longer complete, so the intraband screened potential in the superfluid state is weaker than the unscreened potential. A new effect in the superfluid state is introduced at this density for the smallest band gap shown, $E_g = 35$ meV: the range of the intraband screened potential in the superfluid state becomes similar to the screened interaction for the normal state. This makes the interaction short-ranged (Fig. 5.5(a)), completely cut off by $r/r_0 \geq 0.4$. This effect is shown first for small band gaps and later, increasing the density, for large gaps. When the interaction becomes short-ranged, it is too weak to sustain superfluidity (Fig. 5.6).

Figure 5.4(b) isolates the effect of the interband screening processes, that is, what the screened interaction $V_{eh}(q)$ would be if only the $\Pi^{\text{inter}}(q)$ contribution to $\Pi(q)$ taken from the full self-consistent calculation, were retained. In contrast to the intraband screening, we see that for interband screening there is no cancellation at all of $\Pi_N^{\text{inter}}(q)$ by $\Pi_A^{\text{inter}}(q)$ (Fig. 5.3). Therefore $\Pi^{\text{inter}}(q)$ is unchanged from the normal to the superfluid state, and so in the absence of intraband screening, the screened interaction $V_{eh}(r)$ would be the same in the normal and superfluid states. The large interband contributions to the normal polarizability significantly weaken the short-range part of $V_{eh}(r)$. This effect is E_g -dependent, since the population of free carriers in both bands increases with decreasing E_g . The interband screening at large q leads to the weakening of the real-space interaction at small r (Fig. 5.5(b)).

Finally, Fig. 5.4(c) shows the complete screened interaction when both intraband and interband contributions to $\Pi(q)$ taken from the full self-consistent calculation, are included. In the normal state, the total screened interaction is always very weak. In the

superfluid state, at low density there is only the interband screening, so there is no screening of the total interaction at small q . Thus for $E_g = 35$ meV, $V_{eh}(r)$ is completely screened out by $r/r_0 \simeq 0.4$. The interband contributions weaken $V_{eh}(r)$ and in this way affect the threshold density for superfluidity. A smaller E_g results in more interband screening, weakening the electron-hole pairing interactions, and leading to a lower threshold density. Because of interband screening, when superfluidity does exist, the superfluid gaps are significantly smaller than for the corresponding system with unscreened interactions. For screening as strong as in the normal state, the superfluidity is always killed.

5.2.3 Superfluid Gaps

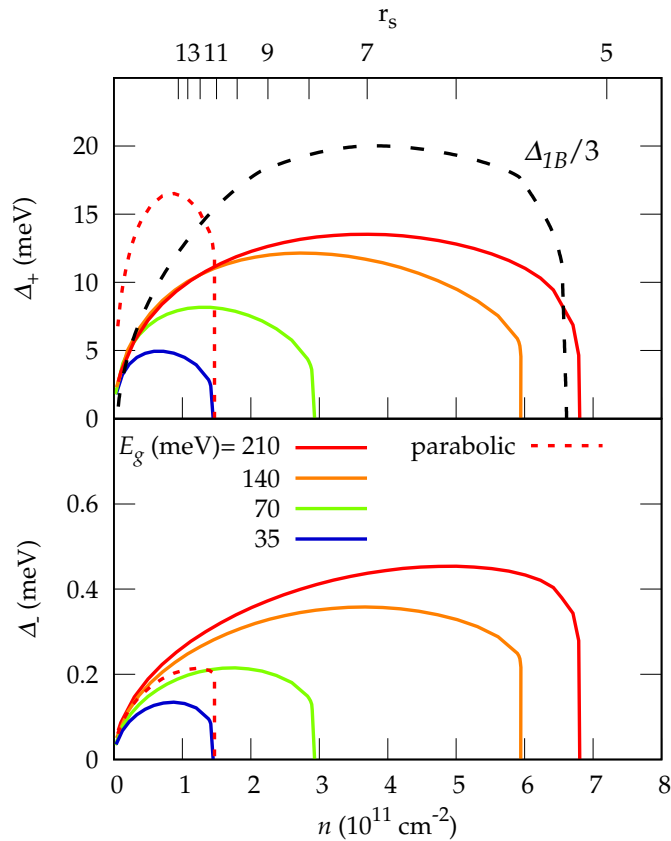


FIGURE 5.6: Solid lines: maximum of the conduction and valence band superfluid gaps $\Delta_{\pm} = \max_k \Delta_{\pm}(k)$ as a function of density for different band gaps E_g , as labelled. The upper x-axis shows the parameter r_s . Dotted red line: Parabolic bands with band gap $E_g = 210$ meV. Dashed black line: maximum of the superfluid gap $\Delta = \max_k \Delta(k)$ for the corresponding system when only the conduction band is considered. For reference, the superfluid gap for one band is shown as $\Delta_{1B}/3$.

Figure 5.6 shows the dependence on density of the maximum of our calculated superfluid gaps $\Delta_{\pm} = \max_k \Delta_{\pm}(k)$ for the conduction and valence bands (Eqs. (4.18)). The maxima initially increases with density, since the number of carriers available for pairing is increasing. For very small densities, the Δ_+ and Δ_- are independent of E_g . This is because, as we have discussed, the intraband screening is totally suppressed by the superfluidity and the interband screening is negligible when E_F becomes less than E_g . As the density increases, the curves eventually pass through a broad maximum and then turn over. This is because intraband screening becomes increasingly effective as the density is increased, so the superfluid gaps decrease. E_F is increasing with the density, so

eventually Δ_+ becomes less than E_F . At this point, the condensate fraction drops below $\lesssim 0.2$, so there is now a large population of normal-state free carriers available for screening, and the presence of these free carriers enhances the screening. Finally, as the density continues to increase, there is a superfluid threshold density at which Δ_+ and Δ_- drop to zero. Above the threshold density, screening of the electron-hole interactions is so strong that it kills superfluidity. For very small band gaps $E_g < E_F$, the interband contributions to the screening are strong, and the threshold density is very low. In the other limit, for large band gaps, the threshold density is large.

In Fig. 5.6, for comparison we also show the superfluid gaps for a corresponding system with $E_g = 210$ meV but for parabolic conduction and valence bands with effective masses $m_e^* = m_h^* = 0.04m_e$. We note that with the real graphene bilayer bands, the superfluidity extends over a much wider density range than for the parabolic bands. As discussed in Section 5.2.1 because the bilayer bands become flatter with increasing E_g , the screening becomes weaker as E_g increases. For the same E_g , the density range for the superfluidity is four times larger with the bilayer graphene bands than with parabolic bands.

Finally, Fig. 5.6 shows the maximum of Δ for the system with only a parabolic conduction band discussed in Ref. [10], again for $m_e^* = m_h^* = 0.04m_e$.

We note in the multi-band system, that for larger band gaps $E_g \gtrsim 140$ meV, the predicted density range over which the superfluidity occurs is similar to the density range for the one-band system.

It is important to note that, while we present Fig. 5.6 for fixed band gaps E_g and tunable density, in real experiments E_g has a weak dependence on the carrier density n because it is sensitive to the transverse electric fields E from the metallic gates used to tune the density. The transverse electric fields across the bottom (E_B) and top (E_T) bilayer graphene can be described as [81],

$$\begin{aligned} E_B &= (en_B/2\epsilon_0) + en_T/\epsilon_0 + E_{B0}, \\ E_T &= en_T/2\epsilon_0 + E_{T0}, \end{aligned} \quad (5.10)$$

where E_{B0} (E_{T0}) is the electric field from unintentional doping at the density neutrality point in the bottom (top) bilayer graphene. E_{B0} and E_{T0} can be determined experimentally. For weak E , E_g can be approximated by $E_g \sim \alpha E$, with $\alpha \sim 0.1$ e C nm [133].

An unexpected result in Fig. 5.6 is that, even for large band gaps, $E_g \sim 200$ meV, the conduction band superfluid gap Δ_+ remains nearly an order of magnitude weaker than the superfluid gap in the one-band system. This is due to the interband contributions to the screening which we have seen are not weakened by the superfluidity.

Another unexpected result in Fig. 5.6 is that, even for small band gaps E_g , the valence band superfluid gap $\Delta_- \ll \Delta_+$ for the conduction band. As we have discussed, this result indicates a decoupling of the two superfluid gap equations, Eqs. (4.18), with Josephson-like transfer of pairs always remaining negligible. The reason is that the multi-band screening always results in superfluid gaps that are much smaller than the band gaps, that is, $\Delta_+ \ll E_g$ (Fig. 5.7). It is difficult to generate large $\Delta_+ > E_g$ because the resulting Josephson-like transfer of electron-hole pairs from the valence to the conduction bands would leave in the valence bands a significant population of vacancies. These free valence-band vacancies would add to the screening and hence reduce Δ_+ . When the band gap is reduced, the interband screening becomes stronger, which weakens the superfluid gaps. In this way, the superfluid gap remains smaller than the band gap, $\Delta_+ < E_g$.

To illustrate why Josephson-like transfer of electron-hole pairs are small when $\Delta_{\pm} \ll E_g$, Fig. 5.8 shows the Bogoliubov amplitudes (Eq. (4.13)) for this case. The density of

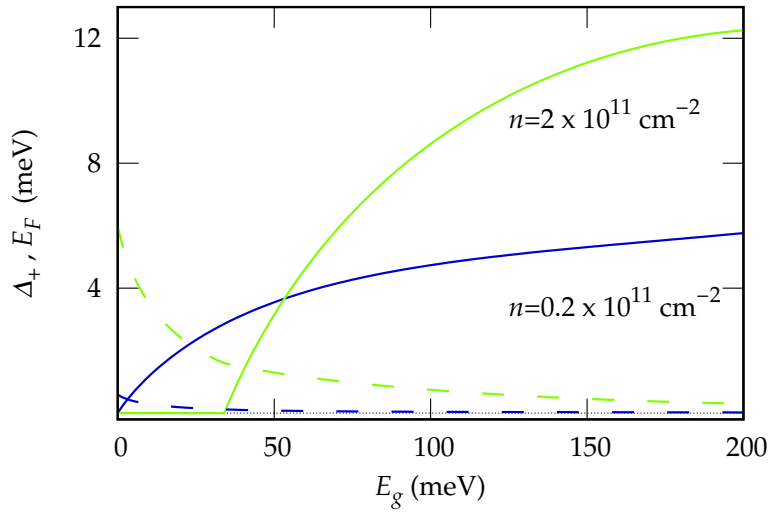


FIGURE 5.7: The dependence of the maximum of the superfluid gap in the conduction band Δ_+ as a function of the band gap E_g for two fixed densities (solid lines). In all cases, $\Delta_+ \ll E_g$. Δ_- remains always negligible on this scale of energy and so is not shown. The dashed lines are the Fermi energies for the same two densities as a function of E_g .

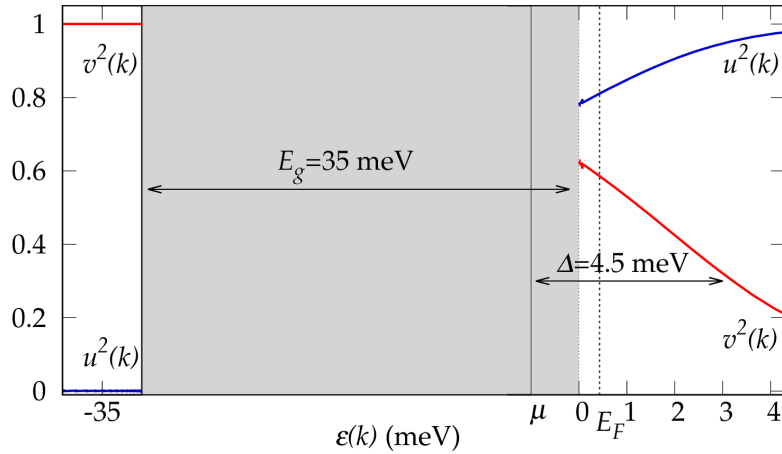


FIGURE 5.8: Bogoliubov amplitudes $u(k)$ and $v(k)$ as function of energy, for density $n = 1 \times 10^{11} \text{ cm}^{-2}$ and band gap $E_g = 35 \text{ meV}$.

valence-band vacancies available to form pairs in the valence-band condensate is determined by the overlap of the Bogoliubov amplitudes, $v_-k(k)u_-(k)$. Figure 5.8 shows that this overlap will be vanishingly small whenever $\Delta_{\pm} \ll E_g$, and hence the valence band superfluid gap $\Delta_-(k)$, which is proportional to $v_-k(k)u_-(k)$, will be extremely small. If $\Delta_-(k)$ is small, the interband coupling term for $\Delta_+(k)$ will also be very small. Interband pairing terms, in which superfluid pairs form with carriers from different bands, will also be extremely small because of the vanishingly small population of valence-band vacancies available to contribute to such pairs.

We can neglect intralayer interactions between carriers within the same bilayer compared with interlayer interactions between electrons and holes in opposite bilayers in our

density range of interest. The average separation of the electrons and holes is of the order of the barrier thickness $d = 1$ nm, while for $n \lesssim 7 \times 10^{11} \text{ cm}^{-2}$ ($r_s \gtrsim 5$) the average separation of carriers within each layer is much larger, $r_0 \gtrsim 6.7$ nm ($r_0/a_B \gtrsim 1.3$).

We have chosen for this example a DBG system with a $d = 1$ nm hBN barrier ($d/a_b = 0.18$). An increase of the barrier thickness not only reduces of the average strength of the bare interlayer interaction V_D , but the effect of screening is also increased. This is because of the presence in the denominator of Eq. (5.4) of the V_D factor attached to the anomalous polarizability Π_A . Therefore, we expect a decrease in the threshold density analogous to Ref. [10] for all the values of E_g .

5.2.4 One-band Superfluidity from Multi-band Screening

In the absence of screening, the system naturally divides into two regimes depending on the energy scales [15]: (i) for $E_g \gtrsim E_F$, the system resembles a one-band system because the contributions from the valence band are negligible; (ii) for $E_g \lesssim E_F$, the contribution from the valence band is significant.

However, when the electron-hole pairing attraction is screened, the compensatory nature of multi-band screening pushes the system to resemble a one-band system, even when the band gap E_g is small. We have seen that interband screening keeps $\Delta_+ < E_g$. The near complete absence of valence-band vacancies generated by the superfluid, together with negligible Josephson-like pair transfers, keeps Δ_- very small. The large DOS at the bottom of the bilayer conduction band keeps E_F smaller than E_g , even for relatively large densities and very small band gaps.

Further independent confirmation of the nearly one-band nature of the superfluidity comes from the behaviour of the chemical potential in the limit of small conduction band density, $\lim_{n \rightarrow 0} \mu$ (Fig. 5.9).

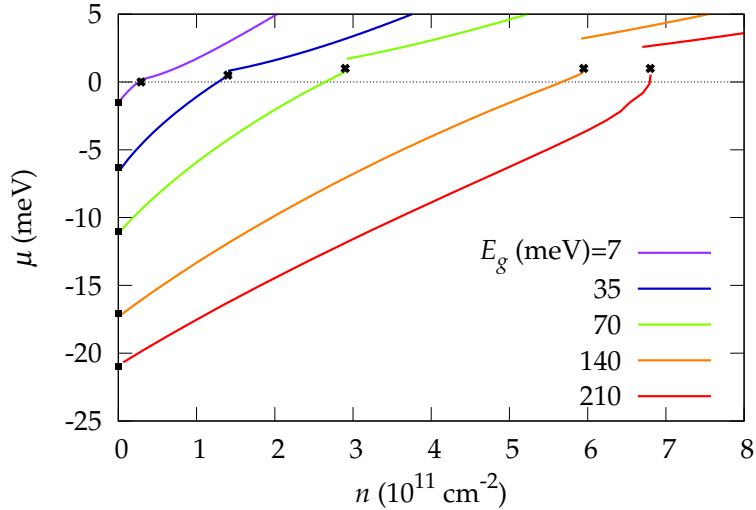


FIGURE 5.9: The chemical potential μ as a function of density n . The squares mark the low-density limiting values $\lim_{n \rightarrow 0} \mu$ (see Table 5.1). The crosses mark the threshold densities at which superfluidity disappears. Above the threshold density, the system is in the normal state, and thus $\mu = E_F$.

For one-band, the chemical potential goes to one-half the binding energy of a single electron-hole pair. The binding energy of an isolated electron-hole pair in a single graphene bilayer, E_B , has been calculated as a function of band gap E_g (See details in Appendix C) and are in agreement with the values in Ref. [148]. If the conduction and

E_g	210	140	70	35	7
$\lim_{n \rightarrow 0} \mu$	-21	-17	-11	-6	-2
$E_B/2$	-23	-17	-9	-5	-1

TABLE 5.1: Comparison of the binding energy E_B of one isolated electron-hole pair in a single graphene bilayer of band gap E_g , [148] with the low-density limiting behaviour of the chemical potential μ in double bilayer graphene with the same E_g , from Fig. 5.9. Units are meV.

valence band condensates were strongly coupled, they would become symmetric in the low density limit, in analogy with an intrinsic semiconductor. In this case, the limiting value of the chemical potential would lie at the mid-point of the band gap, $E_g/2$, rather than at half the binding energy [15]. In fact, Table 5.1 shows that $\lim_{n \rightarrow 0} \mu$ in the superfluid state always lies close to the value of $E_B/2$ taken from Ref. [148], which is behaviour consistent with a one-band system.

5.3 Conclusion

In summary, we have shown that the small band gaps characteristic of bilayer graphene is responsible for an enhancement of the overall screening. This is due to the additional interband contributions to the screening provided by carriers from the filled valence bands.

Despite the small band gaps, Josephson-like pair transfers between the condensates in the valence and conduction bands are negligible. This unexpected result is because multi-band screening always keeps the superfluid gaps small compared with the band gap: any Josephson-like transfer of electron-hole pairs from the valence to the conduction bands leaves behind an increased population of free valence-band vacancies, and these add to the screening. The increased screening reduces the superfluid gap. The net effect of this compensation is to keep the superfluid gap smaller than the band gap.

The suppression of Josephson-like pair transfers means that the superfluid condensates in the valence and conduction bands are decoupled, with the superfluid condensate in the valence band very weak, so that the superfluidity is dominated by the decoupled conduction band condensate. The conduction band superfluid gap is significantly weakened by the additional interband screening arising from excitations from the valence band.

We have shown that the distortion of the parabolic bands in Mexican-hat shape significantly affects the pairing processes. The very large DOS at the bottom of the bilayer conduction band from van Hove-like singularities, together with the flattening of the band results, for a given density, in a much smaller Fermi energy E_F than for the parabolic band. The small Fermi energies permit the superfluidity to be very effective in suppressing screening, with the superfluid gap blocking a wide range of low-lying excitations on the scale of E_F .

The net result of the multi-component screening and of the evolution of the low-energy bilayer graphene bands with variable band gap, is a complex interplay of energy and length scales beyond the already rich mean field results discussed in the previous Chapter. The comprehensive results presented here, demonstrate the robustness of double bilayer graphene as an optimum platform for realizing and exploiting electron-hole superfluidity under practical experimental conditions.

The recent report of observation of enhanced interlayer tunnelling in electron-hole DBG [13] strongly points to the existence of an electron-hole condensate, as predicted theoretically. The experimental system consists of a DBG with a 1.4 nm tungsten diselenide (WSe_2) insulating barrier. The WSe_2 barrier has a dielectric constant $\epsilon \sim 7$, significantly larger than the hBN dielectric constant of the barrier we have been studying. However, the barrier thickness $d/a_B = 0.07$ ($a_B = 19$ nm for WSe_2) for the experimental system is significantly smaller than our value $d/a_B = 0.18$ ($a_B = 5.4$ nm for hBN). These two differences push the threshold density in opposite directions, meaning that we can expect the threshold densities for the theoretical and experimental systems to be comparable. In the experimental system, enhanced interlayer tunnelling at equal densities was reported for $n < 8 \times 10^{11} \text{ cm}^{-2}$. For the theoretical system, we recall that the maximum threshold density was $n \sim 7 \times 10^{11} \text{ cm}^{-2}$.

We will show in the next chapter, how our approach is valid for other van der Waals heterostructures [72] that share common features with double bilayer graphene, such as double monolayers of transition metal dichalcogenides, separated by an atomically thin insulating barrier [73]. Interest in these van der Waals heterostructures continues to grow and their quality is increasing.

Chapter 6

Electron-Hole Superfluidity in Coupled Transition Metal Dichalcogenides Monolayers

In this chapter, our multi-component approach is applied to study electron-hole superfluidity in a double Transition Metal Dichalcogenide monolayer system. We consider the multi-band nature of the TMDs due to the splitting of the bands caused by the strong spin-orbit coupling. We include the self-consistently screened Coulomb interaction. We show that the large misalignment of the bands in the two monolayers results in interesting new effects. The superfluidity can be multi-component and dominated by two band condensates with strikingly different properties. These properties display a remarkable sensitivity to the doping of the monolayers. We find that the multi-component nature of the superfluidity contributes to the high transition temperatures observed in a TMD system [18, 19].

The hunt for electron-hole superfluidity received impetus from the discovery of atomically thin graphene and from the observation of a strong signature of superfluidity in DBG [13]. Development of other 2D materials like the Transition Metal Dichalcogenides (TMDs) followed graphene. Over the past 5 years, TMD bilayers have attracted a lot of attention because interlayer excitons have a large binding energy, long life-time and they are stable at room temperature [149].

As introduced in Section 2.7, because of these excitonic properties these TMD bilayers have been proposed to observe high-temperature exciton superfluidity [11]. Furthermore, in the quest of electron-hole superfluidity TMD monolayers are appealing for other two reasons:

- Because of the large band gap $E_g \gtrsim 1$ eV [150, 151], the problems due to the detrimental effect of the valence band screening are overcome.
- Because of the strong spin-orbit coupling [106, 152], the TMD heterostructures are interesting platforms for investigating novel multi-component effects for electron-hole superfluidity.

In this chapter, we discuss a double layer system consisting of coupled TMD monolayers. We investigate the effects of multi-component superfluidity in double TMD monolayers using a mean field multi-band approach that includes the band splitting caused by the strong spin-orbit coupling of the conduction and valence band. We find that the splitting of the conduction and valence bands by spin-orbit coupling into multi-bands, consisting of two concentric parabolic spin-polarised subbands, makes superfluidity in double TMD monolayers resemble high-temperature multi-band superconductivity. There are close relations with multi-band superfluidity in ultracold Fermi gases [153] and with electric-field induced superconductivity at oxide surfaces [154, 155].

6.1 Double TMD Monolayer

We focus on the group-VI TMD monolayers MoS₂, MoSe₂, WS₂, and WSe₂. These are semiconductors with large and direct band gaps, $E_g \gtrsim 1$ eV [150, 151].

The electronic bands of a TMD monolayer can be described using the tight-binding approach. The tight-binding Hamiltonian is [152]:

$$H = \begin{pmatrix} (E_g + \lambda_c)/2 & atke^{i\phi_k} & 0 & 0 \\ atke^{-i\phi_k} & (-E_g + \lambda_v)/2 & 0 & 0 \\ 0 & 0 & (E_g - \lambda_c)/2 & atke^{-i\phi_k} \\ 0 & 0 & atke^{i\phi_k} & -(E_g + \lambda_v)/2 \end{pmatrix}. \quad (6.1)$$

The electronic dispersion in a single valley is [156]:

$$\varepsilon_{\sigma,\pm}(k) = \sigma \frac{\lambda_c + \lambda_v}{2} \pm \sqrt{a^2 t^2 k^2 + \frac{(E_g - \sigma(\lambda_v - \lambda_c))^2}{4}}, \quad (6.2)$$

with the plus (minus) sign labelling the conduction (valence) band and $\sigma = \pm$ as spin index. Table 6.1 gives the tight-binding parameters for these TMDs monolayers.

	a (nm)	t (eV)	E _g (eV)	λ _c (eV)	λ _v (eV)	m _e [*] (m _e)	m _h [*] (m _e)
MoS₂	0.32	1.10	1.66	-0.003	0.15	0.40	0.48
MoSe₂	0.33	0.94	1.47	-0.021	0.18	0.43	0.50
WS₂	0.32	1.37	1.79	0.027	0.33	0.30	0.44
WSe₂	0.33	1.19	1.60	0.038	0.36	0.30	0.39

TABLE 6.1: TMD monolayer Lattice constant (a), hopping parameter (t), band gap (E_g), and spin-orbit coupling splitting of conduction bands (λ_c) and valence bands (λ_v) [106, 152, 157]. The effective masses are calculated in the low-energy parabolic approximation.

The effective masses in the low-lying nearly parabolic bands are large, resulting in very strong coupling of the electron-hole pairs [11].

We present results for the specific system MoSe₂-hBN-WSe₂, with one TMD monolayer *n*-doped and the other *p*-doped, and then draw general conclusions for the class of semiconductor TMDs. The monolayers can be independently doped [99] and are separated by an insulating trilayer of hexagonal Boron Nitride (hBN) with thickness $d = 1$ nm. The few monolayers of insulating hexagonal Boron Nitride (hBN) inhibit electron-hole recombination [14, 158], avoid hybridization, and leave the bands of the MoSe₂ and WSe₂ little changed [100, 159]. Figure 6.1 shows their low-lying band structures of the MoSe₂ and WSe₂ monolayers.

6.2 Mean Field Equations

We apply the theoretical approach introduced in Chapter 3 to derive the zero temperature mean field equations in double TMD monolayer system. For the *p*-doped monolayer, we are using the standard particle-hole transformation (see discussion below Eq. (3.1)). Thanks to the large band gaps, we only need to consider conduction band processes. A Coulomb pairing interaction, in contrast with conventional BCS pairing, does not depend on the electron and hole spins. Therefore for each monolayer, we label the bottom and top conduction subbands by $\beta = b$ and $\beta = t$.

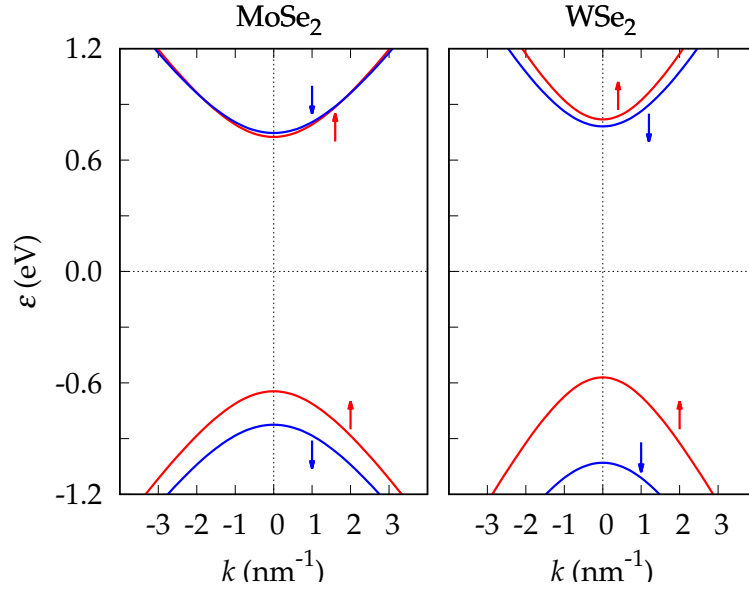


FIGURE 6.1: The low-lying band structures of monolayer MoSe₂ and WSe₂ centred in the *K* valley. Red and blue lines are for the opposite spins. The spin configuration is opposite in the two valleys [152].

In principle there are four possible electron-hole pairings, corresponding to four superfluid condensates [137] $\{\beta\beta'\}$. The first index β refers to the electron subbands and the second β' to the hole subbands. Figure 6.2 shows a schematic representation of the active bands with the possible pairing channels.

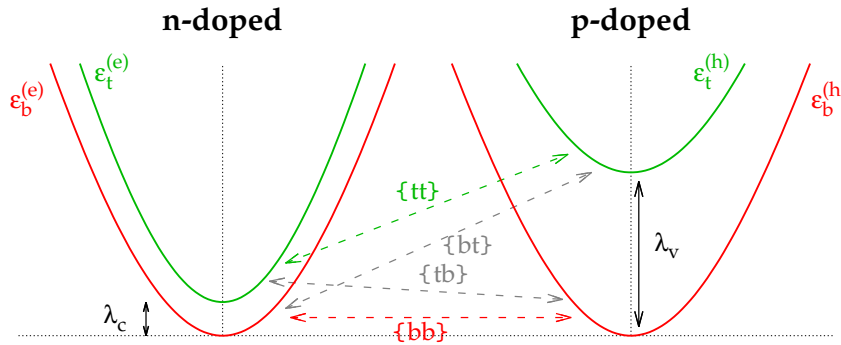


FIGURE 6.2: Subbands of double TMD monolayers. For the *p*-doped monolayer, the valence band has been mapped into a conduction band using the standard particle-hole transformation. The bottom electron $\varepsilon_b^e(k)$ and hole $\varepsilon_b^h(k)$ subbands have been aligned. Zero energy is set at $\varepsilon_b^e(k=0)$. The arrows show the possible pairing channels $\{\beta\beta'\}$.

Due to the large valley separation in momentum space, intervalley scattering is negligible, so the effect of the two valleys appears only in a valley degeneracy factor, $g_v = 2$.

Table 6.1 shows that monolayer TMDs are characterized by the spin-orbit splitting and the spin splitting of the valence bands λ_v is an order of magnitude larger than the spin splitting of the conduction bands λ_c . This results in a misalignment between the electron and hole bands. The misalignment strongly affects the electron-hole pairing processes, and due to the very different misalignment of the bands (Fig. 6.3), the *n*-doped-MoSe₂ with *p*-doped-WSe₂ (denoted as system A) has markedly different properties from the *p*-doped-MoSe₂ with *n*-doped-WSe₂ (system B).

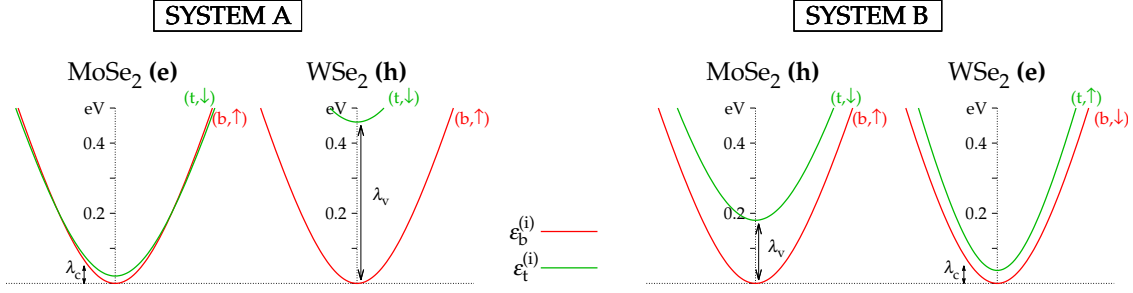


FIGURE 6.3: Subbands of system A (the n -doped-MoSe₂ with p -doped-WSe₂) and system B (p -doped-MoSe₂ with n -doped-WSe₂) centred in the K valley.

Because the electron and hole effective masses are very similar, for simplicity in the calculation of the superfluid gaps we use parabolic band approximation for electrons and holes of equal curvature $m_e^* = m_h^* = m^*$. The trigonal warping is negligible for $n < 10^{13}$ cm⁻² [160].

We consider the two bottom bands aligned, so there is a misalignment between the two top bands:

$$\varepsilon_b^{(e)}(k) = \varepsilon_b^{(h)}(k) = \frac{\hbar^2 k^2}{2m^*}, \quad \varepsilon_t^{(e)}(k) = \frac{\hbar^2 k^2}{2m^*} + |\lambda_c^e|, \quad \varepsilon_t^{(h)}(k) = \frac{\hbar^2 k^2}{2m^*} + |\lambda_v^h|, \quad (6.3)$$

where λ_c^e is the spin splitting of the conduction bands in the n -doped layer and λ_v^h the splitting of the valence bands in the p -doped layer. The misalignment between the top bands is $\delta\lambda = |\lambda_v^h| - |\lambda_c^e|$.

The kinetic energy terms are $\tilde{\zeta}_\beta^{(i)}(k) = \varepsilon_\beta^{(i)}(k) - \mu^{(i)}$ where $\varepsilon_\beta^{(i)}(k)$ is the energy dispersion for the $i = e, h$ monolayer. We will restrict the calculation to equal electron and hole density and the chemical potential is $\mu = (\mu^{(e)} + \mu^{(h)})/2$. From Eq. (3.39), we can write:

$$\tilde{\zeta}_\beta(k) = (\tilde{\zeta}_\beta^{(e)} + \tilde{\zeta}_\beta^{(h)})/2, \quad \delta\tilde{\zeta}_b = 0, \quad \delta\tilde{\zeta}_t = -\delta\lambda/2, \quad (6.4)$$

$$E_\beta^2(k) = \tilde{\zeta}_\beta^2(k) + \Delta_{\beta\beta}^2(k), \quad T_b^2(k) = E_b^2(k), \quad T_t^2(k) = \tilde{\zeta}_t^{(e)}(k)\tilde{\zeta}_t^{(h)}(k) + \Delta_{tt}^2(k). \quad (6.5)$$

With these simplifications, the terms in Eq. (3.38) become:

$$\chi_1 = \chi_3 = \sqrt{\frac{a+b}{2}}, \quad \chi_2 = -\frac{\delta\lambda}{2} + \sqrt{\frac{a-b}{2}}, \quad \chi_4 = \frac{\delta\lambda}{2} + \sqrt{\frac{a-b}{2}},$$

$$a = E_b^2 + E_t^2 + 2\Delta_{12}\Delta_{21}, \quad b = -\delta\tilde{\zeta}_t^2 + \sqrt{(E_b^2 - T_t^2)^2 + 4\Delta_{12}\Delta_{21}(|\lambda_c^e\lambda_v^h| + (\Delta_{bb} + \Delta_{tt})^2)}. \quad (6.6)$$

The normal Green functions for double TMD monolayers are (Eq. (3.36)):

$$\begin{aligned}
 G_{bb}[i\omega, \mathbf{k}] &= \frac{(i\hbar\omega + \xi_b)[(i\hbar\omega - \xi_t^{(e)})(i\hbar\omega + \xi_t^{(h)}) - \Delta_{tt}^2] - (i\hbar\omega + \xi_t^{(h)})\Delta_{bt}\Delta_{tb}}{(i\hbar\omega - \chi_1)(i\hbar\omega - \chi_2)(i\hbar\omega + \chi_1)(i\hbar\omega + \chi_4)}, \\
 G_{tb}[i\omega, \mathbf{k}] &= \frac{\Delta_{tb}[(i\hbar\omega + \xi_t^{(h)})\Delta_{bb} + (i\hbar\omega + \xi_b)\Delta_{tt}]}{(i\hbar\omega - \chi_1)(i\hbar\omega - \chi_2)(i\hbar\omega + \chi_1)(i\hbar\omega + \chi_4)}, \\
 G_{bt}[i\omega, \mathbf{k}] &= \frac{\Delta_{bt}[(i\hbar\omega + \xi_t^{(h)})\Delta_{bb} + (i\hbar\omega + \xi_b)\Delta_{tt}]}{(i\hbar\omega - \chi_1)(i\hbar\omega - \chi_2)(i\hbar\omega + \chi_1)(i\hbar\omega + \chi_4)}, \\
 G_{tt}[i\omega, \mathbf{k}] &= \frac{(i\hbar\omega + \xi_t^{(h)})(i\hbar\omega - \xi_b)(i\hbar\omega + \xi_b) - \Delta_{bb}^2 - (i\hbar\omega + \xi_b)\Delta_{bt}\Delta_{tb}}{(i\hbar\omega - \chi_1)(i\hbar\omega - \chi_2)(i\hbar\omega + \chi_1)(i\hbar\omega + \chi_4)},
 \end{aligned} \tag{6.7}$$

and the anomalous Green functions are (Eq. (3.37)):

$$\begin{aligned}
 F_{bb}[i\omega, \mathbf{k}] &= \frac{(i\hbar\omega - \xi_t^{(e)})(i\hbar\omega + \xi_t^{(h)})\Delta_{bb} - (\Delta_{bb}\Delta_{tt} - \Delta_{bt}\Delta_{tb})\Delta_{tt}}{(i\hbar\omega - \chi_1)(i\hbar\omega - \chi_2)(i\hbar\omega + \chi_1)(i\hbar\omega + \chi_4)}, \\
 F_{tb}[i\omega, \mathbf{k}] &= \frac{\Delta_{tb}[(i\hbar\omega - \xi_b)(i\hbar\omega + \xi_t^{(h)}) + (\Delta_{bb}\Delta_{tt} - \Delta_{bt}\Delta_{tb})]}{(i\hbar\omega - \chi_1)(i\hbar\omega - \chi_2)(i\hbar\omega + \chi_1)(i\hbar\omega + \chi_4)}, \\
 F_{bt}[i\omega, \mathbf{k}] &= \frac{\Delta_{bt}[(i\hbar\omega - \xi_t^{(e)})(i\hbar\omega + \xi_b) + (\Delta_{bb}\Delta_{tt} - \Delta_{bt}\Delta_{tb})]}{(i\hbar\omega - \chi_1)(i\hbar\omega - \chi_2)(i\hbar\omega + \chi_1)(i\hbar\omega + \chi_4)}, \\
 F_{tt}[i\omega, \mathbf{k}] &= \frac{(i\hbar\omega - \xi_b)(i\hbar\omega + \xi_b)\Delta_{tt} - (\Delta_{bb}\Delta_{tt} - \Delta_{bt}\Delta_{tb})\Delta_{bb}}{(i\hbar\omega - \chi_1)(i\hbar\omega - \chi_2)(i\hbar\omega + \chi_1)(i\hbar\omega + \chi_4)}.
 \end{aligned} \tag{6.8}$$

Unlike in DBG and in two-band superconductors where the bands are symmetric, here $F_{tb} \neq F_{bt}$, because of the bands misalignment. We find that the interband pairing more advantageous in the $\{tb\}$ channel with respect to the $\{bt\}$. This is due to the large energy separation, λ_v^h , between the $\xi_b^{(e)}$ and the $\xi_t^{(h)}$ [113]. We find that the $\{bt\}$ and $\{tb\}$ interband pairing make negligible contributions to the condensates, so for simplicity, we confine our attention to the mean field equations for the superfluid gaps $\Delta_{bb}(k)$ and $\Delta_{tt}(k)$.

We consider only the $\{bb\}$ and $\{tt\}$ pairing with different superfluid gaps Δ_{bb} and Δ_{tt} . We put $\Delta_{bt} = 0$ and $\Delta_{tb} = 0$, so $G_{bt} = 0$, $G_{tb} = 0$, $F_{bt} = 0$, $F_{tb} = 0$. This results in

$\chi_1 = E_b$, $\chi_2 = -\delta\lambda/2 + E_t$ and $\chi_4 = \delta\lambda/2 + E_t$ and the Green functions become:

$$\begin{aligned} G_{bb}[i\omega, \mathbf{k}] &= \frac{(i\hbar\omega + \xi_b)}{(i\hbar\omega - E_b)(i\hbar\omega + E_b)}, \\ G_{tt}[i\omega, \mathbf{k}] &= \frac{(i\hbar\omega + \xi_t^{(h)})}{(i\hbar\omega + \delta\lambda/2 - E_t)(i\hbar\omega + \delta\lambda/2 + E_t)}, \\ F_{bb}[i\omega, \mathbf{k}] &= \frac{\Delta_{bb}}{(i\hbar\omega - E_b)(i\hbar\omega + E_b)}, \\ F_{tt}[i\omega, \mathbf{k}] &= \frac{\Delta_{tt}}{(i\hbar\omega + \delta\lambda/2 - E_t)(i\hbar\omega + \delta\lambda/2 + E_t)}. \end{aligned} \quad (6.9)$$

We can rewrite Eq. (6.9) in terms of the Bogoliubov amplitudes v_β^2 and u_β^2

$$v_\beta^2(k) = \frac{1}{2} \left(1 - \frac{\xi_\beta(k)}{E_\beta(k)} \right), \quad u_\beta^2(k) = \frac{1}{2} \left(1 + \frac{\xi_\beta(k)}{E_\beta(k)} \right), \quad (6.10)$$

so

$$\begin{aligned} G_{bb}[i\omega, k] &= \frac{u_b^2}{(i\hbar\omega - E_b)} + \frac{v_b^2}{(i\hbar\omega + E_b)}, \\ G_{tt}[i\omega, k] &= \frac{u_t^2}{(i\hbar\omega + \delta\lambda/2 - E_t)} + \frac{v_t^2}{(i\hbar\omega + \delta\lambda/2 + E_t)}, \\ F_{bb}[i\omega, k] &= \frac{u_b v_b}{(i\hbar\omega - E_b)} - \frac{u_b v_b}{(i\hbar\omega + E_b)}, \\ F_{tt}[i\omega, k] &= \frac{u_t v_t}{(i\hbar\omega + \delta\lambda/2 - E_t)} - \frac{u_t v_t}{(i\hbar\omega + \delta\lambda/2 + E_t)}. \end{aligned} \quad (6.11)$$

We sum over the Matsubara frequencies ω (see Appendix Sec. A.2 for details), and we obtain:

$$\sum_\omega e^{-i\omega 0^+} G_{bb}[i\omega, k] = v_b^2(k)(1 - n_F[E_b, T]) + u_b^2(k)n_F[E_b, T], \quad (6.12)$$

$$\sum_\omega e^{-i\omega 0^+} G_{tt}[i\omega, k] = v_t^2(k)(1 - n_F[\chi_4, T]) + u_t^2(k)n_F[\chi_2, T], \quad (6.13)$$

$$\sum_\omega e^{-i\omega 0^+} F_{bb}[i\omega, k] = -\frac{\Delta_{bb}(k)}{2E_b}(1 - 2n_F[E_b, T]), \quad (6.14)$$

$$\sum_\omega e^{-i\omega 0^+} F_{tt}[i\omega, k] = -\frac{\Delta_{tt}(k)}{2E_t}(1 - n_F[\chi_4, T] - n_F[\chi_2, T]). \quad (6.15)$$

We want to calculate the limit of zero temperature for the Fermi distributions n_F . Because $|\lambda_v^h| \gg |\lambda_c^e|$ then $\delta\lambda > 0$, so the energy term $\chi_4 > 0$ always but $\chi_2 > 0$ only when $E_t(k) > \delta\lambda/2$. Thus for $T \rightarrow 0$ we have $n_F[E_b, 0] = 0$, $n_F[\chi_4, 0] = 0$, and

$$n_F[\chi_2, 0] = \begin{cases} 1 & \chi_2 < 0 \\ 0 & \chi_2 > 0 \end{cases} = 1 - \theta[\chi_2] = 1 - \theta \left[E_t(k) - \frac{\delta\lambda}{2} \right], \quad (6.16)$$

where $\theta[\chi_2]$ is a Heaviside step function.

From Eqs. (6.13)-(6.15) we have,

$$G_{bb}[k] = v_b^2(k), \quad G_{tt}[k] = v_t^2(k) + u_t^2(k)(1 - \theta[E_t - \delta\lambda/2]), \quad (6.17)$$

$$F_{bb}[k] = -\frac{\Delta_{bb}(k)}{2E_b(k)}, \quad F_{tt}[k] = -\frac{\Delta_{tt}(k)}{2E_t(k)}\theta[E_t(k) - \delta\lambda/2]. \quad (6.18)$$

Since we are neglecting the interband pairing contributions, we retain the form factors only for $n = m(i = j)$, $\mathcal{F}_{nm,ii}(\mathbf{k}, \mathbf{k}') \equiv \mathcal{F}_{n,i}(\mathbf{k}, \mathbf{k}')$. Furthermore, the screened Coulomb interaction $V_{eh}(|\mathbf{k} - \mathbf{k}'|)$ conserves the spin of the electron-hole pair and there are no spin-flip scattering processes. Since there are no spin-flip scattering processes, Josephson-like pair transfers between different bands are forbidden. This means that $\mathcal{F}_{n,i}(\mathbf{k}, \mathbf{k}') = 0$ for $n \neq i$. The resulting zero temperature superfluid gap equations (Eq. (3.40)) are thus decoupled:

$$\Delta_{bb}(k) = -\int \frac{d^2\mathbf{k}'}{(2\pi)^2} \mathcal{F}_{b,b}(\mathbf{k}, \mathbf{k}') V_{eh}(|\mathbf{k} - \mathbf{k}'|) \frac{\Delta_{bb}(k')}{2E_b(k')}, \quad (6.19)$$

$$\Delta_{tt}(k) = -\int \frac{d^2\mathbf{k}'}{(2\pi)^2} \mathcal{F}_{t,t}(\mathbf{k}, \mathbf{k}') V_{eh}(|\mathbf{k} - \mathbf{k}'|) \frac{\Delta_{tt}(k')}{2E_t(k')} \theta[E_t(k') - \delta\lambda/2]. \quad (6.20)$$

Equation (6.19) has the same form as for a decoupled one-band system, because the two bottom bands are aligned [112]. In contrast, Eq. (6.20) shows explicitly the effect of misalignment of the top bands (Fig. 6.3) through the term $\theta[\sqrt{\xi_t(k)^2 + \Delta_{tt}^2(k)} - \delta\lambda/2]$. This can only drop below unity at higher densities, where the pair coupling strength is weak compared with the misalignment.

The form factors are obtained numerically by calculating the overlap of the wave functions, eigenvectors of the tight-binding Hamiltonian (Eq. 6.1)

$V_{kk'}^{eh}$ in Eqs. (6.19)-(6.20) is the screened electron-hole interaction. To include the screening of the interaction we use the Random Phase Approximation for static screening in the superfluid state (Eq. (5.4)) described in Section 3.3.2. To calculate the normal and anomalous polarizabilities, $\Pi_N(q)$ and $\Pi_A(q)$, we use Eqs. (3.55) and (3.56) in the specific case of double TMD monolayers with only intraband scattering allowed due to spin-orbit coupling ($n = m = i = j = \beta$).

$$\Pi_N^{\beta\beta}(q, \Omega) = \frac{T}{L^2} \sum_{\mathbf{k}, \omega} \mathcal{F}_{\beta,\beta}(\mathbf{k}, \mathbf{k}') G_{\beta\beta}[i\omega + i\Omega, k'] G_{\beta\beta}[i\omega, k], \quad (6.21)$$

$$\Pi_A^{\beta\beta}(q, \Omega) = \frac{T}{L^2} \sum_{\mathbf{k}, \omega} \mathcal{F}_{\beta,\beta}(\mathbf{k}, \mathbf{k}') F_{\beta\beta}[i\omega + i\Omega, k'] F_{\beta\beta}[i\omega, k]. \quad (6.22)$$

with $q = |\mathbf{k} - \mathbf{k}'|$

We use the Green functions in Eq. (6.11). We perform the sum over the Matsubara frequencies ω , in the static limit $\Omega \rightarrow 0$ and at zero temperature (see details in Appendix Sec. B.2).

$$\Pi_N^{bb}(q) = -\frac{1}{L^2} \sum_{\mathbf{k}} \mathcal{F}_{b,b}(\mathbf{k}, \mathbf{k}') \frac{v_b^2(k)u_b^2(k') + u_b^2(k)v_b^2(k')}{E_b(k) + E_b(k')}, \quad (6.23)$$

$$\Pi_A^{bb}(q) = \frac{1}{L^2} \sum_{\mathbf{k}} \mathcal{F}_{b,b}(\mathbf{k}, \mathbf{k}') \frac{2u_b(k)v_b(k)u_b(k')v_b(k')}{E_b(k) + E_b(k')}. \quad (6.24)$$

While for the top bands we obtain:

$$\begin{aligned} \Pi_N^{tt}(q) = & -\frac{1}{L^2} \sum_{\mathbf{k}} \mathcal{F}_{t,t}(\mathbf{k}, \mathbf{k}') \left[u_t^2(k) u_t^2(k') \frac{\theta[E_t(k) - \frac{\delta\lambda}{2}] - \theta[E_t(k') - \frac{\delta\lambda}{2}]}{E_t(k) - E_t(k')} \right. \\ & \left. + v_t^2(k) u_t^2(k') \frac{\theta[E_t(k') - \frac{\delta\lambda}{2}]}{E_t(k) + E_t(k')} + u_t^2(k) v_t^2(k') \frac{\theta[E_t(k) - \frac{\delta\lambda}{2}]}{E_t(k) + E_t(k')} \right], \end{aligned} \quad (6.25)$$

$$\begin{aligned} \Pi_A^{tt}(q) = & \frac{1}{L^2} \sum_{\mathbf{k}} \mathcal{F}_{t,t}(\mathbf{k}, \mathbf{k}') u_t(k) v_t(k) u_t(k') v_t(k') \\ & \frac{\theta[E_t(k) - \frac{\delta\lambda}{2}] + \theta[E_t(k') - \frac{\delta\lambda}{2}]}{E_t(k) + E_t(k')} - \frac{\theta[E_t(k) - \frac{\delta\lambda}{2}] - \theta[E_t(k') - \frac{\delta\lambda}{2}]}{E_t(k) - E_t(k')}, \end{aligned} \quad (6.26)$$

For a given chemical potential μ , equal electron and hole densities $n^e = n^h = n$ in one monolayer is determined as a sum of the subband carrier densities n_b and n_t by (Eq. (3.42)):

$$n = g_s g_v \sum_{\beta=b,t} n_{\beta}, \quad (6.27)$$

$$n_b = \int \frac{d^2\mathbf{k}}{(2\pi)^2} v_b^2(k), \quad (6.28)$$

$$n_t = \int \frac{d^2\mathbf{k}}{(2\pi)^2} v_t^2(k) + u_t^2(k) (1 - \theta[E_t(k) - \delta\lambda/2]). \quad (6.29)$$

Because of the spin polarization in the valleys, the spin degeneracy is $g_s = 1$.

As we have discussed in Section 3.2.1 we can identify the regimes of the superfluid BEC-BCS crossover, by investigating the evolution of the superfluid gaps (Eqs. (6.19)-(6.20)) and the evolution of the chemical potential evaluated in Eq. (6.27). We also introduce, for this system, the two superfluid condensate fractions c_{bb} and c_{tt} corresponding to the $\{bb\}$ and $\{tt\}$ condensates. These are the number of pairs in a $\{\beta\beta\}$ divided by the total number of carriers in the β bands (Eq. (3.44)),

$$c_{\beta\beta} = \frac{\sum_k u_{\beta}^2(k) v_{\beta}^2(k)}{\sum_k v_{\beta}^2(k)}. \quad (6.30)$$

6.3 Results

We took equal effective masses $m_e^* = m_h^* = 0.44 m_e$, a barrier thickness $d = 1$ nm, and dielectric constant $\epsilon = 2$, for monolayers encapsulated in a few layers of hBN [138]. The effective Rydberg energy of the system is $R_y = 800$ meV and the effective Bohr radius $a_B = 0.43$ nm.

Figure 6.4 shows the dependence on WSe₂ electron density of the maximum of the superfluid gaps $\Delta_{\beta\beta} = \max_k \Delta_{\beta\beta}(k)$ (Eqs. (6.19)-(6.20)) in systems A and B. Figure 6.5 shows the corresponding evolution of the chemical potential μ and Fig. 6.6 shows the evolution of the condensate fractions (Eq. (6.30)).

We see in Fig. 6.4 that, at low densities, electrons and holes occupy only the bottom bands so there is only a $\{bb\}$ condensate. The form of Δ_{bb} is similar for systems A and B. In the low-density limit, the paired electrons and holes occupy the two-body bound state with its binding energy $E_B^b \sim 375$ meV. The chemical potential for this state is given by

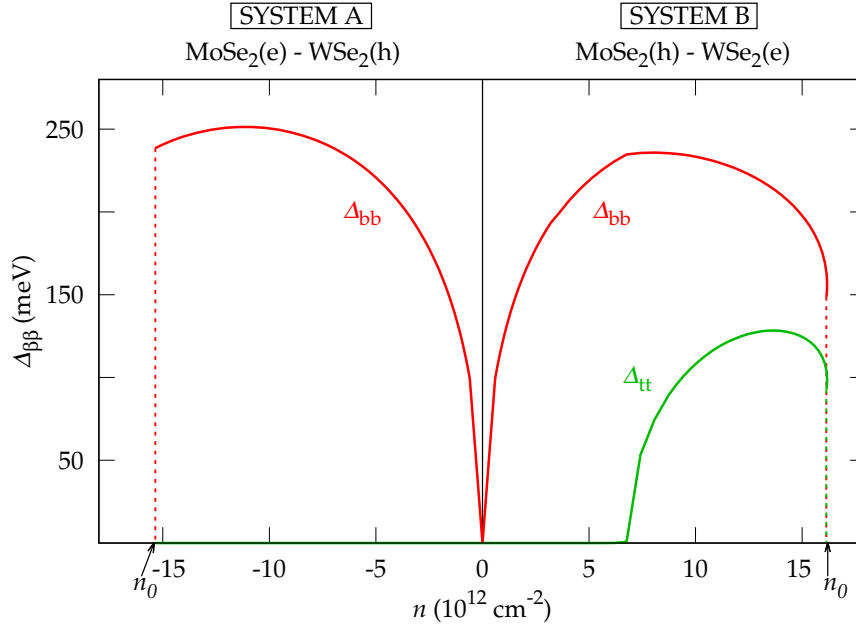


FIGURE 6.4: The maximum of the superfluid gaps Δ_{bb} and Δ_{tt} as a function of n of WSe₂. Positive density corresponds to system A, negative density to system B.

the well-known one-band limit, $\mu \sim -E_B^b/2$ [161, 162], (Fig. 6.5). Note that at very low density $\mu^{(e)} = \mu^{(h)}$ for the carrier of the bottom bands.

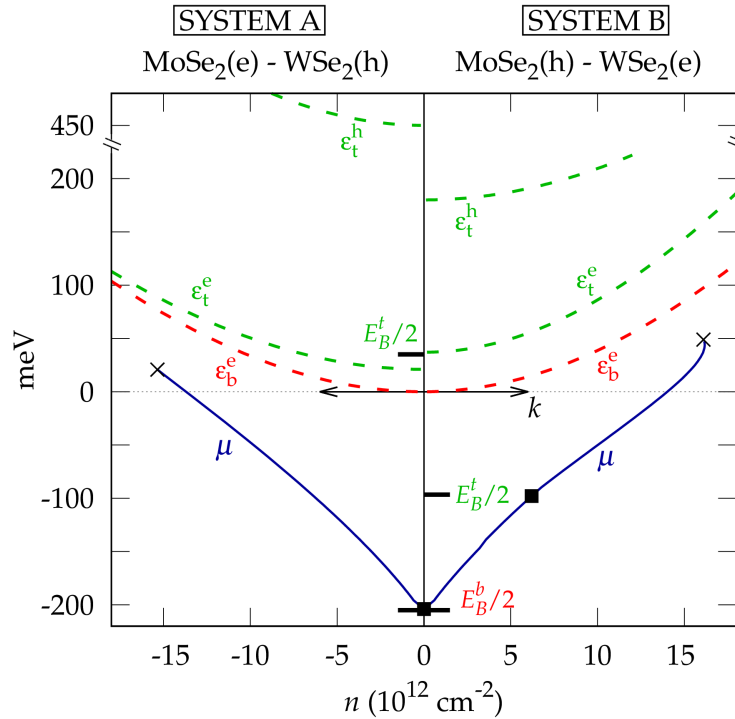


FIGURE 6.5: Chemical potential as function of density n of WSe₂. For reference, the energy bands are shown as a function of k with the same energy scale. The bound state energies $E_B^b/2$, $E_B^t/2$ are also indicated with respect to the bands.

In this case, the $\{bb\}$ condensate is in the strong-coupled BEC regime, with condensate fraction $C_{bb} > 0.8$ (Fig. 6.6).

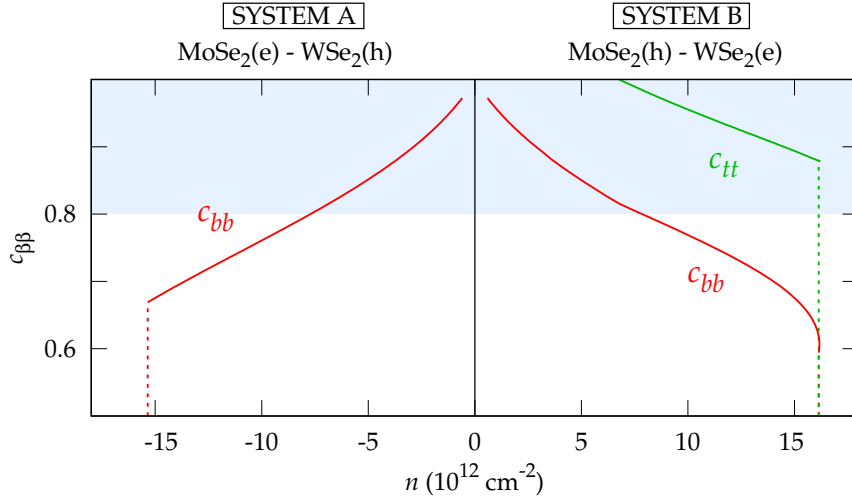


FIGURE 6.6: Corresponding condensate fraction C_{bb} and C_{tt} as function of density n of WSe_2 . The blue shaded area is the BEC regime.

As the density is increased Δ_{bb} also increases, since the number of electrons and holes available for pairing increases. The pairs start to overlap, and this results in an increasing chemical potential μ and a decreasing C_{bb} .

In contrast, for the top bands, Δ_{tt} is only non-zero in system B. At low density, $\Delta_{tt} = 0$ also in system B, since the pairing population is zero. In the low-density limit of the top bands, the paired electrons and holes will occupy a two-body bound state with a binding energy that lies $E_B^b - \delta\lambda$ below the top band $\epsilon_t^{(e)}$. Relative to the zero of energy, the two-body bound state for the top bands is located at,

$$-\frac{1}{2}E_B^t = -\frac{1}{2}(E_B^b - \delta\lambda) + \lambda_c^e. \quad (6.31)$$

For the $\{tt\}$ condensate to be populated and Δ_{tt} to be non-zero μ must exceed $-\frac{1}{2}E_B^t$. (Fig. 6.5)

With increasing density, C_{bb} drops below 0.8 and the $\{bb\}$ condensate enters the Crossover regime, while the $\{tt\}$ condensate is always in the BEC regime with $C_{tt} > 0.8$. This results in an interesting new mixture of condensates that are in different regimes of pairing. Δ_{bb} then passes through a maximum because of screening that becomes increasingly important and weakens the interaction. Δ_{tt} follows a similar sequence of behaviour, however the step function in Eq. (6.20), reduces the pairing strength because of the misalignment of the top bands. This is the reason that Δ_{tt} is everywhere weaker than Δ_{bb} .

When μ becomes positive, the weakening due to screening is accelerated due to the build-up of the free carriers in the bottom bands. Eventually screening, combined with the misalignment of the top bands, kills the superfluidity. Δ drops sharply to zero in both $\{bb\}$ and $\{tt\}$ channels at the same threshold density n_0 ($r_0/a_B = 3.3$). For $n > n_0$, the screening of the pairing interaction is so strong that it kills superfluidity [10].

We see in Fig. 6.4 that the behaviour of Δ_{tt} in systems A and B is completely different. In system A the chemical potential remains below the isolated bound state E_B^t associated with the top bands over the full range of densities up to n_0 . With μ lying below $\frac{1}{2}E_B^t$ (Fig. 6.5), the population of pairs in the $\{tt\}$ channel remains zero. Interestingly, the only difference between system A and B is the choice of doping which results in the markedly different misalignment of the top bands, leading to one-component or two-components superfluidity.

6.3.1 Multi-component superfluidity in different TMD monolayers

The results on MoSe₂-hBN-WSe₂ indicates that the presence of a second component in the superfluidity for double TMD monolayers depends on the position of the two-body bound state for $\{tt\}$ bands, and Eq. (6.31) show that this position is determined by the misalignment of the top bands.

Fig. 6.5 indicates that the two-body bound state for $\{tt\}$ condensate can only exist if it lies below the minimum of the top bands. Otherwise there is a decay channel to continuum states. This means that in Eq. (6.31), $(E_B^b - \delta\lambda)$ must be positive for a two-body bound state in the top bands to exist. This is a condition for the second condensate to exist: $\delta\lambda < E_B^b$.

By using this condition we can draw more general conclusions about the multi-component nature of the superfluidity in different double TMD monolayers. Table 6.2 shows $(E_B^b - \delta\lambda)$ for different combinations of TMD monolayers. Multi-component superfluidity is possible only when $(E_B^b - \delta\lambda) > 0$. The E_B^b are calculated for double TMD monolayers with separation $d = 1$ nm (See details in Appendix C).

	p-MoS ₂	p-MoSe ₂	p-WS ₂	p-WSe ₂
n-MoS₂	249	228	-37	-69
n-MoSe₂	276	253	-9	-49
n-WS₂	252	232	-28	-65
n-WSe₂	260	233	-24	-57

TABLE 6.2: $(E_B^b - \delta\lambda)$ in meV for different combinations of TMD monolayers. $\delta\lambda$ is determined from Table 6.1. The values marked in bold identify those systems where multi-component superfluidity is possible ($(E_B^b - \delta\lambda) > 0$).

6.4 Transition Temperature

The strikingly high transition temperatures for electron-hole superfluidity in double TMD monolayer structures comes from two properties in which they greatly differ from other double layer systems:

- large threshold densities for superfluidity;
- multi-component superfluidity that can be switched on and off.

In 2D, the superfluid transition temperatures are given by T_{BKT} , the Berezinskii-Kosterlitz-Thouless (BKT) temperature [163]. The monolayers have near parabolic bands, so we can approximate [164, 165],

$$T_{BKT} = \frac{\pi}{2} \rho_s(T_{BKT}) \simeq n \frac{\pi \hbar^2}{2g_s g_v m^*}. \quad (6.32)$$

$\rho_s(T)$ is the superfluid stiffness. T_{BKT} is proportional to the density, so to achieve high transition temperature the density must be maximized. In Fig. 6.4, we note that the threshold densities n_0 for the superfluidity are much larger than $n_0 \sim 8 \times 10^{11} \text{ cm}^{-2}$ observed in DBG [13, 17], $n_0 \sim 4 \times 10^{12} \text{ cm}^{-2}$ for phosphorene [94], and $n_0 \sim 5 \times 10^{10} \text{ cm}^{-2}$ for GaAs [22]. n_0 is large for the double TMD monolayers for two main reasons: (i) the large effective masses of the electrons and holes means a large effective Rydberg energy, thus large superfluid gaps Δ that strongly suppress the screening; (ii) the large TMD monolayer band gaps E_g eliminate valence band screening, making the electron-hole

pairing interaction very strong [17]. These large threshold densities in the double TMD monolayers lead to high BKT transition temperatures. Equation (6.32) gives maximum transition temperatures for systems A and B at their threshold densities $n = 15 \times 10^{12} \text{ cm}^{-2}$ of $T_{BKT}^A = 110 \text{ K}$ and $T_{BKT}^B = 120 \text{ K}$.

While at first sight, the coupling in DBG between the conduction and valence band condensates should reinforce the superfluid gaps as shown in Chapter 4, because of the small band gaps in bilayer graphene there are a large number of free carriers that are easily excited from the valence band, and these greatly enhance the screening. The enhanced screening weakens the superfluid gaps. We showed in Chapter 5 that this effect dominates over the reinforcement of the superfluid gaps. In TMDs, the large band gap means that screening from the remote bands is negligible. Because of spin selection, the condensates are not directly coupled in the superfluid gap equations (Eqs. (6.19)-(6.20)), but there is anyway a great advantage in having a second condensate. The pairing in the $\{tt\}$ condensate removes free carriers from the top bands that would otherwise strengthen the screening. Thus two-component superfluidity persists up to higher densities compared to the one-component system.

As a final extra remark, unlike DBG, there are no chiral symmetry degrees of freedom in TMDs. Reference [114] has suggested that these additional degrees of freedom in DBG would lead to topological excitations of quarter vortices. If so, in DBG but not in TMDs, there would be a prefactor of $1/16$ in Eq. (6.32). This would dramatically reduce T_{BKT} .

To identify the double TMD monolayers with the highest transition temperatures, we look for the highest binding energies in combination with multi-component superfluidity.

Table 6.3 gives the corresponding two-body binding energy for the $\{bb\}$ bands, E_B^b , for different combinations of TMD monolayers. Of the double monolayers which are predicted in Table 6.2 to exhibit multi-component superfluidity (marked in bold), we see from Table 6.3, it is MoSe₂-MoSe₂ which has the highest two-body binding energy. MoSe₂-MoSe₂ has the largest transition temperature: $T_{BKT} \sim 160 \text{ K}$.

	p-MoS ₂	p-MoSe ₂	p-WS ₂	p-WSe ₂
n-MoS₂	396	405	390	388
n-MoSe₂	405	412	400	390
n-WS₂	375	385	375	368
n-WSe₂	372	375	368	365

TABLE 6.3: Two-body binding energy for the $\{bb\}$ bands: E_B^b in meV for different combinations of TMD monolayers calculated using the parameters in Table 6.1.

6.5 Conclusion

In summary, we have investigated multi-component effects for electron-hole multi-band superfluidity in n - p and p - n doped MoSe₂-hBN-WSe₂ heterostructures (Systems A and B, respectively). Both systems are multi-band and can stabilize superfluidity at temperatures above 100 K. Surprisingly, we find that only in system B can superfluidity have two components. For both systems, we would have expected to be able to tune from one- to two-component superfluidity by increasing the density, as recently observed in multi-band superconductors [155], and this is indeed the case for system B. However for system A, the very large misalignment of the electron and hole top bands, means that there are no carriers available for pairing in the topmost band before screening has become so strong that it completely suppresses superfluidity. Therefore only one-component superfluidity is possible in system A. This is a remarkable result: activation of the second-component

of the superfluidity in this heterostructure depends crucially on the choice of which TMD monolayer is n -doped and which p -doped.

Another intriguing result is that one can see from Fig. 6.3 that it is possible to tune from a system of purely dark excitons (System A) to a system of only bright excitons (System B) simply by interchanging the doping.

The strikingly different behaviour of Δ_{tt} in the two systems can be probed using Angle-Resolved Photoemission Spectroscopy (ARPES) [166]. ARPES measures the spectral function which, in a one-component superfluid state like system A, will have a single peak centred at a negative frequency corresponding to Δ_{bb} . However in system B, when it switches from one-component to two-components superfluidity, two peaks associated with the superfluid gaps Δ_{bb} and Δ_{tt} will appear in the spectral function at negative frequencies [167]. Other experimental techniques that can be used to detect the presence or absence of the second superfluid gap Δ_{tt} are Andreev reflection spectroscopy [168, 169] and scanning tunnelling microscopy (STM) [170].

The large superfluid gaps at zero temperature and in the Crossover regime should lead to pseudogaps in the single-particle excitation spectra [171] above T_{BKT} that persist up to high temperatures. These could also be detected by the ARPES and STM. System B, at densities where both the superfluid components are close to their maximum gaps, would favour large pseudogaps, while configurations with one large gap and one small or zero gap would lead to screening of superfluid fluctuations and suppression of the pseudogap [172].

Experimental evidence for exciton condensation, based on interlayer tunnelling and electroluminescence, was reported in n -MoSe₂/ p -WSe₂ [14], which is our system A. The high transition temperatures, 100 K at density 10^{12} cm⁻², suggest an exciton condensate with short-range coherence [173], associated with the pseudogap state [174].

This approach can be generalised to determine electron-hole superfluidity properties in different combinations of double TMD monolayers. Among the different double TMD monolayer systems we can select the configurations where the superfluidity can be tuned from one- to two-components. These correspond to TMD monolayer configurations where the misalignment between the higher energy bands is smaller than the exciton binding energy. We show that MoSe₂-MoSe₂ has the largest transition temperature, as high as $T_{BKT} \sim 160$ K.

Chapter 7

3D Superlattice to exploit high-temperature electron-hole superfluidity

In this chapter, we propose a new system based on a stack of Transition Metal Dichalcogenide alternating electron and hole monolayers to exploit electron-hole superfluidity in a three-dimensional superlattice. We show that with a 3D superlattice, we overcome the restriction of low critical temperatures associated with the Berezinskii-Kosterlitz-Thouless transition temperature characteristic of 2D systems [21].

The presence of superfluidity is associated with the spontaneous breaking of the continuous symmetry, allowing for the formation of long-range order with a fixed phase. The phase correlation is a constant for temperature below a critical temperature T_c , falls off exponentially with the distance for $T > T_c$, and falls off according to a power law for $T = T_c$, the latter indicating quasi-long-range order. T_c is defined as the temperature at which the superfluid gap vanishes. One might reasonably expect that the critical temperature could be further increased towards the limit set by the large pair binding energies and the large superfluid gaps which can be as large as 1000K. However, Mermin, Wagner [175] and Hohenberg [176] provided rigorous proofs that a spontaneous breaking of continuous symmetry is not possible in 2D (or lower dimensions) at non-zero temperature. This general theorem, which precludes the existence of long-range order in 2D systems, seems to preclude also the existence of 2D superfluidity.

In 2D systems, it is in fact still possible to have a phase transition and quasi-long-range order below a critical temperature. This phase transition is associated with the dissociation of bound vortex-antivortex pairs into unbound vortices and antivortices. A vortex is the flow of the condensate phase around a region of normal fluid known as the vortex core. This phase transition was first described by Berezinskii [177] and Kosterlitz and Thouless [163] and is referred to as the BKT transition. A single vortex or antivortex destroys the phase ordering in the system, but for a vortex-antivortex pair, there is still a near uniform phase order at distances far from the pair. This means that bound vortex-antivortex pairs do not destroy the superfluidity but formation of single vortices or antivortices does. Vortex-antivortex pairs have lower energies and entropy than free vortices. In order to minimize free energy, the system undergoes a transition at a critical temperature T_{BKT} . Below T_{BKT} , there are only bound vortex-antivortex pairs. Above T_{BKT} , there are free vortices. Thus the maximum transition temperature in 2D is not limited by the electron-hole binding energy or superfluid gap, but by the BKT topological transition introduced in Section 6.4 (Eq. (6.32)). The transition temperature T_{BKT} is proportional to the carrier density and does not directly depend on the coupling strength. As we have discussed in the previous chapter, the density for superfluidity cannot be

increased indefinitely because strong screening of the Coulomb interactions at high densities kills superfluidity.

In this chapter, we overcome these restrictions associated with Mermin-Wagner and exploit strong electron-hole coupling, by considering superfluidity in a three-dimensional (3D) superlattice, consisting of a stack of alternating electron and hole monolayers.

7.1 3D superlattice

While we focus on a superlattice of alternating n -doped WS_2 and p -doped WSe_2 monolayers, the same approach would work for other systems of stacked 2D layers (Fig. 7.1). We consider an AA stacked superlattice of WS_2 and WSe_2 monolayers, with the tungsten atoms horizontally aligned, and the chalcogen atoms horizontally aligned. The distance between the atoms of different layers is $d \sim 0.6$ nm.

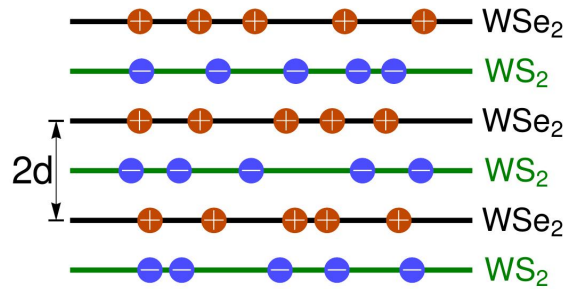


FIGURE 7.1: Schematic representation of the infinite superlattice of alternating n - and p -doped monolayers of two different TMDs, indicated by green and black lines.

The WS_2/WSe_2 band alignment is type-II: conduction band and valence band edges are located in different layers [101]. This keeps the electrons and the holes spatially separated in their monolayers without the need for an insulating barrier, and ensures long lifetime for the interlayer excitons [104]. There are by now many examples of superlattice-based superconductors [178], including the high-temperature cuprates [179, 180].

To investigate this system we use a self-consistent mean-field approach. We restrain the calculation to low densities so only the lowest energy bands are occupied and the pairing is single-component.

Here the nature of the interactions is 3D. The average inter-particle distances for the densities we are considering are much larger than the small distance between layers. Due to the hybridization between the bands of the different type monolayers, there is a small intralayer contribution to the electron-hole potential. This is because, while the electrons and holes in the hybridized bands are mostly in opposite layers, there is a small probability they will be in the same layer.

It is interesting to note that since pairing by the screened Coulomb attraction is primarily generated by two-particle scattering processes with small momentum exchange, pair formation is 3D in character.

We determine the 3D superfluid gap $\Delta(\mathbf{k})$ at zero temperature, where in $\mathbf{k} = \vec{k}_{\parallel} + \vec{k}_z$ we can distinguish the in-plane \parallel -direction and in the perpendicular z -direction.

$$\Delta(\mathbf{k}) = -\frac{1}{AN2d} \sum_{\mathbf{k}} V^{RPA}(\mathbf{k}, \mathbf{k}') \frac{\Delta(\mathbf{k}')}{2E(k')}, \quad (7.1)$$

where $E(k) = \sqrt{\tilde{\zeta}^2(k) + \Delta^2(k)}$, with $\tilde{\zeta}(k) = \frac{1}{2}(\varepsilon_e(k) + \varepsilon_h(k)) - \mu$. N is the number of the layers of surface area A .

In Eq. 7.1, the terms in the summation over \mathbf{k}'_{\parallel} are non-negligible only at low energies, but the summation over k'_z has significant contributions across the full Brillouin zone, *i.e.* between $\pm\pi/2d$. The details and the expression of the electron-hole interaction $V^{RPA}(\vec{k}, \vec{k}')$ are given in the paper [21].

The dielectric constant $\epsilon = \sqrt{\epsilon_z \epsilon_{\parallel}}$ accounts for static screening. For WS₂ it is $\epsilon = 9.9$, and for WSe₂ $\epsilon = 11.2$ [181]. In the limit of no hybridization between the different TMD types, the system would effectively consist of two decoupled bulk TMDs with an inter-layer distance twice that of their normal bulk forms. The dielectric constant is approximately halved when the inter-layer distance is doubled [96]. For the WS₂/WSe₂ superlattice, we therefore take as the value of the dielectric constant for the heterostructure superlattice $\epsilon = 5.5$, half of the average of the two bulk TMDs.

The density equation is:

$$n = \frac{g_v g_s}{AN2d} \sum_{\mathbf{k}} v^2(k). \quad (7.2)$$

Where $g_v = 2$ and $g_s = 1$ for the same reasons discussed in Section 6.2, and $v^2(k)$ is the Bogoliubov amplitude.

7.2 Results

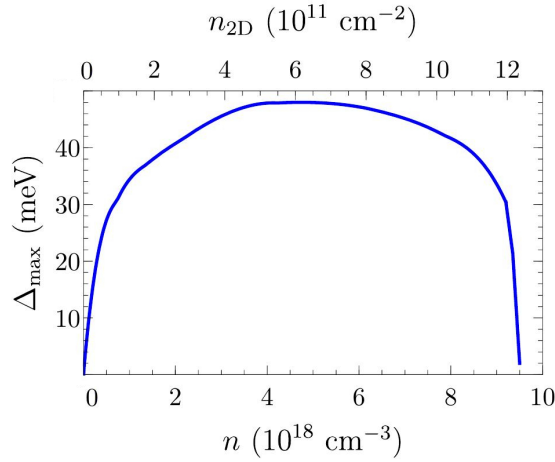


FIGURE 7.2: Maximum superfluid gap Δ as function of equal electron and hole densities n .

Figure 7.2 shows the maximum of the momentum-dependent superfluid gap $\Delta(\mathbf{k})$, as a function of the 3D electron and hole densities n . For reference the top axis shows an effective 2D carrier density, defined as $n_{2D} = 2dn$. At large densities, Coulomb screening suppresses the superfluidity. Below an onset density n_0 , large gap superfluidity self-consistently weakens the screening sufficiently for superfluidity to appear. As the density is further decreased, Δ increases to a maximum value of 48 meV (560 K), and then decreases. Note that even for very small values of n , Δ remains in excess of 10 meV (120 K). These large values of Δ reflect the strong electron-hole Coulomb pairing interaction.

At high densities at weak-coupling, the superfluid transition temperature T_c can be determined from the mean-field equations, generalized to finite temperatures,

$$\Delta(\mathbf{k}, T) = - \sum_{\mathbf{k}'} V^{RPA}(\mathbf{k}, \mathbf{k}', T) \frac{\Delta(\mathbf{k}', T)}{2E(k')} \tanh \left[\frac{E(k')}{2k_B T} \right]. \quad (7.3)$$

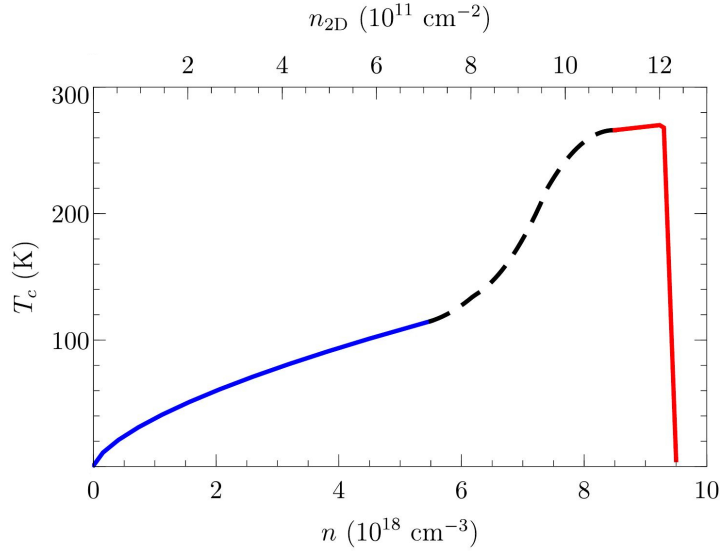


FIGURE 7.3: BEC (solid, blue) and BCS (solid, red) critical temperature calculated as a function of the 3D and effective 2D density. The dashed black curve is a possible interpolation of the critical temperature between the BEC and BCS expressions.

As the density is lowered, we enter the Crossover regime. With the increased pairing strength, the chemical potential μ must drop below the Fermi energy E_F to keep the density fixed. This drop incorporates a large part of the effect of the fluctuations that build up as the Crossover regime is penetrated. Although within the Crossover regime, the T_c determined from the Eq. (7.3) using the self-consistent μ , starts to overestimate the actual transition temperature, this overestimate is expected to be no more than 20% across the full Crossover regime [182, 183].

In the self-consistent screening, we retain the superfluid gap at zero T , since the pseudogap arising from the pair fluctuations should remain of the order of $\Delta(T=0)$ in the intermediate coupling regime [171], and so to a large extent the low-lying excited states will continue to be excluded from the screening excitations, thus suppressing the detrimental Coulomb screening. In this way, we take into account a major part of the fluctuation effects that renormalize T_c to lower values, by incorporating a large part of the fluctuations through the reduction of the chemical potential and through the development of the pseudogap.

In the deep BEC regime at low densities ($C > 0.9$), this method for determining T_c becomes unreliable, primarily because the pseudogap is replaced by a real gap of the order of the pair binding energy. In the deep BEC, we can approximate the electron-hole pairs as point-like bosons, so we can use the T_c for BEC of non-interacting bosons. The T_c for BEC of non-interacting bosons is determined by inverting the equation [184],

$$n = \frac{g_v g_s}{AN2d} \sum_{\mathbf{k}} \frac{1}{e^{\tilde{\epsilon}(\mathbf{k})/k_B T_c} - 1}. \quad (7.4)$$

The T_c thus obtained is known to underestimate the actual T_c for BEC as determined by Quantum Monte Carlo [185]. Finally, in the density range from the upper boundary of the BEC regime to the start of the deep BEC, we use a smooth interpolation of T_c between the high- and low-density results.

Figure 7.3 shows the resulting superfluid transition temperature in the superlattice. In the deep-BEC regime, T_c (blue curve) can approach 100 K. This is many orders of magnitude larger than the BEC transition temperatures found in ultra-cold atom systems

[29, 186, 187]. These BEC transition temperatures are so much larger because the effective electron and hole masses are tiny compared to atomic masses, and because our densities are several orders of magnitudes larger than in ultra-cold atom systems. Note that this result is in agreement with the result in the corresponding 2D system, reported in Chapter 6. This is because in the deep-BEC the electron-hole pairs are compact. The electron-hole interaction is maximal for electrons and holes in two close layers and the superfluidity reverts to a 2D character.

Increasing the density causes T_c to rapidly rise, pushing it to a maximum in the Crossover regime (red curve) very close to room temperature, $T_c = 270\text{K}$, conveniently accessible in a domestic refrigerator.

7.3 Conclusions

The superfluid transition in a 3D superlattice is not topological, and for strong electron-hole pair coupling, the transition temperature can approach room temperature. A further advantage of a 3D system over 2D systems is that it is much less susceptible to disorder because percolation and screening favour 3D conduction. Our results open the way to generating 3D electron-hole superfluidity at room temperature in this and related superlattices.

While for calculating convenience we use the realistic band structure of an infinite superlattice, our conclusions remain valid for corresponding finite superlattices consisting of more than a few monolayers. To detect the superfluidity, a neutral supercurrent parallel to the superlattice layers that is uniform in the perpendicular direction, could be set up in a counterflow configuration by electrically contacting together the n-doped layers, and similarly with the p-doped layers. Alternatively, a capacitance spectroscopy measurement [188] could detect the drop in the density of states for the superfluid state relative to the normal state. The onset of superfluidity will be characterized by a jump in the inverse of the total capacitance across the sample [22], and then, as the density is decreased, the total capacitance will monotonically increase.

Conclusions

Chapter 8

Conclusions and Future perspectives

8.1 Conclusions

We have investigated multi-component electron-hole superfluidity in coupled layer systems, focusing on two very different systems. One system consists of two parallel bilayer graphene sheets (DBG), the other system is a bilayer heterostructure of Transition Metal Dichalcogenides (TMD). Table 8.1 collects properties for superfluidity in these two systems. For reference we also include other double layer systems that have been proposed for electron-hole superfluidity. We summarize results obtained in Table 8.2.

	mass-ratio	$m_e^*(m_e)$	$m_h^*(m_e)$	$E_g(\text{eV})$	valence band screening	multi-component superfluidity
DQW	$m_h^* \sim 10 m_e^*$	0.067	0.3	1.5	no	no
DMG	$m_h^* = m_e^*$	0	0	0	yes	no superfluidity
DBG	$m_h^* = m_e^*$	0.04	0.04	≤ 0.25	yes	no
DMP	$m_h^* = m_e^*$	0.15	0.15	1.5	no	no
TMD	$m_h^* \sim 1.3 m_e^*$	0.3 - 0.5	0.4 - 0.6	1.5 - 2.0	no	yes

TABLE 8.1: Double layer system properties relevant for electron-hole superfluidity. DMP values are for the zigzag direction. m_e^* and m_h^* : electron and hole effective masses; E_g : energy band gap.

	$d^T(\text{nm})$	$d^E(\text{nm})$	n_0^T	n_0^E	$T_{BKT}(\text{K})$	$T_c^E(\text{K})$
DQW	12 - 25 [22]	25 [60, 61]	< 0.7 [22]	—	< 0.5 [22]	—
DMG	1.0 [189]	1.0 [77]	—	—	—	—
DBG	0.5 - 2.0 [10, 17]	1.4 [13]	7 [17]	8 [13]	14 - 27 [10]	1.5 [13]
DMP	2.0 - 10 [94]	—	10 - 40 [94]	—	10 - 90 [94]	—
TMD	1.0 [18]	1.0 [14]	150 [18]	10 [14]	> 100 [18]	100 [14]

TABLE 8.2: Experimental (E) and theoretical (T) parameters of the different systems. d : layer separation; n_0 : superfluid threshold density (10^{11}cm^{-2}); T_{BKT}, T_c^E : predicted and observed transition temperature for superfluidity.

In Chapter 4 we extended the one-band approach used in Ref. [10] in order to further investigate Double Bilayer Graphene. Unlike monolayer graphene, the energy dispersion of the conduction and valence bands at low energies in bilayer graphene is approximately parabolic, and it is possible to tune the small band gaps. We demonstrated that because the band gaps are so small, the valence band provides an additional channel of pairing and hence an additional condensate. Thus the superfluidity is multi-component. The conduction and valence band condensates are coupled through a Josephson-like transfer of the pairs between the condensates. We show for the first time that by tuning the band

gaps we can tune the Josephson-like transfer and thus tune the coupling between the condensates. By tuning this coupling one can change the strength of the pairing and in this way move between the different regimes of the BEC-BCS crossover.

In Chapter 5, we extended the investigation of Double Bilayer Graphene to include the intraband and interband screening and the distortion of the bilayer graphene band from parabolic to Mexican hat-like which accompanies the opening of the band gap. We confirmed that the presence of intraband screening results in an upper limit of the carrier density for the superfluidity [42]. Above this threshold density, screening kills the superfluidity. The presence of the additional interband screening from the valence band strongly reduces the threshold density. We demonstrated that the effect of the strong interband screening is weaker for large band gaps. This is due to the large separation between the bands that weakens the interband processes and to the Mexican-hat flattening of the bands that favours the intraband correlations over the interband correlations.

In Chapter 6 we proposed the TMD heterostructure $\text{MoSe}_2\text{-hBN-WSe}_2$ to observe high-temperature electron-hole superfluidity. The TMD monolayers MoS_2 , MoSe_2 , WS_2 , and WSe_2 are semiconductors with direct band gaps comparable to that in GaAs. The large band gap eliminates the detrimental effects of the interband screening mentioned above for graphene. The electron and hole effective masses in TMDs are larger than for bilayer graphene, and this also increases the coupling strength of the electron-hole pairs [11]. We show that in the double TMD system, because of the strong spin-orbit coupling, each conduction and valence band is split into two subbands. This raises the interesting possibility of multi-component superfluidity arising because of the existence of two subbands. The spin-orbit coupling splitting of the conduction bands λ_c is an order of magnitude smaller than the splitting of the valence bands λ_v . We find that the misalignment of the bands that results from this, determines if the superfluidity is one- or two-component, and the misalignment strongly affects the properties of the second component. We show that the choice of the doping of the TMD monolayers determines the misalignment and thus the multi-component nature of the superfluidity. The choice of doping also permits the excitons to be tuned from purely dark excitons to purely bright excitons. If the superfluidity is multi-component we are able to tune from one- to two-components by increasing the density, as was recently observed in multi-band superconductors [155]. We predicted maximum transition temperatures of $T_{BKT} \sim 100$ K in $\text{MoSe}_2\text{-hBN-WSe}_2$. Very recently enhanced tunnelling conductance signatures of BEC was reported in this same system with transition temperature $T_c \sim 100$ K [14], consistent with these predictions.

In Chapter 6 we discussed the transition temperatures of electron-hole superfluidity in 2D systems, recalling how larger threshold densities lead to higher Berezinskii-Kosterlitz-Thouless transition temperatures. To achieve high transition temperatures in double layer systems a requirement is to be able to access the strongly interacting BEC regime. In this regime, superfluidity suppresses the screening, thus allowing stronger electron-hole pairing. The stronger the pairing interaction, the larger is the density range across which the superfluidity persists. We have shown that the double TMD monolayers are optimal candidates for achieving high-temperature superfluidity, because:

- The effective masses in TMD monolayers are large, resulting in a binding energies and electron-hole pairing interactions stronger than in other coupled layer systems.
- The effective masses in TMD monolayers are almost equal, in contrast to GaAs DQWs, where the mass imbalance weakens the pairing.
- Valence band screening, which has a detrimental effect on the electron-hole pairing strength in DBG, is negligible in double TMD monolayer system because of the large band gap.

- The presence of the second condensate in double TMD monolayers reinforces the superfluidity.

In Chapter 7 we have shown that a stack of alternating electron and hole TMD monolayers can be used to exploit electron-hole superfluidity in a three-dimensional (3D) superlattice. We show that with a 3D superlattice, we overcome the restriction of low critical temperatures associated with the BKT transition temperature characteristic of 2D systems, so that strong electron-hole coupling results in high transition temperatures.

8.2 Future Outcomes

A very interesting result of this thesis illustrates the importance in the pairing processes of a quasi-flat electronic band. In Chapter 5 we found that the flattening of the bands, associated with the Mexican-hat dispersion in the DBG system, causes a significant enhancement of the electron-hole superfluidity. Because of the increase in the Density of States from the flattening of the band, the interaction between electron and holes becomes stronger. Stronger electron-hole pairing corresponds to larger threshold densities for superfluidity. We recall that larger threshold densities lead to higher BKT transition temperatures.

In the last two years it has become experimentally possible to engineer and tune the flat bands in van der Waals bilayers by twisting one layer relative to the other [190]. Twisting induces a moiré pattern, the resulting lattice potential modulates the interlayer hybridization and modifies the electronic structure [191]. At specific *magic* twist angles the bands become completely flat.

By controlling the flatness of the bands it should be possible not only to generate exciton superfluidity but also a large number of the other strongly-correlated exotic phases that have been predicted in the literature, including enhanced Wigner crystal [192], exciton-insulator [193], exciton supersolid [194], Charge Density Wave [195], FFLO and Sarma superfluid phases [63].

1st Research Line - Interlayer Excitons

A number of observations in TMD heterobilayers have shown that the moiré lattice leads to very strongly bound exciton states [196], and that these interlayer moiré excitons have very different optical properties depending on the twisting angle [197, 198]. The flattening of the bands modifies the electron and hole wave-functions, affecting the exciton binding energy and lifetime. To date there is little theoretical study on this. One research line focuses on how the properties of the interlayer excitons can be tuned by flattening the bands.

2nd Research Line - Flat Band Exciton Superfluidity

A second research line would investigate electron-hole superfluidity with tunable flat bands to determine the dependence of the pairing on the bands up to high temperatures. The flattening of the bands makes the excitons strongly bound, causing the system to maintain the strong pairing up to large densities. This would increase the BKT transition temperature.

The flattening of the bands will also modify the competition between the screening and the superfluidity in a subtle way [17]. The possibility of using the twisting angle to control the flattening of the bands means we can experimentally tune the interaction strength and so move the boundaries of the BEC-BCS crossover phenomenon. This effect has not been investigated.

3rd Research Line - Exotic Phases

With van der Waals stacking, we can couple electron and hole bilayers that are designed to have different electronic configurations (different twisting angles). A third research line would study excitonic properties in systems with different flatness for the electron and hole bands. This also opens up the possibility of exotic superfluid phases like the FFLO and Sarma phases which occur when the electron and hole bands have different flattening [63].

4th Research Line - New Phase Diagrams

A fourth research line would examine competing strongly correlated phases in electron-hole coupled layers, with the flattening of the bands as a control parameter. Flattening the bands removes kinetic energy as a phase diagram parameter, leaving the intralayer and interlayer interactions as the parameters. The flattening of the bands also affects all the Coulomb interactions because it modifies the screening [17].

Phase diagrams with density, interlayer distance and temperature as parameters have been proposed for strongly correlated exotic phases including enhanced Wigner crystal [192], exciton-insulator [193], exciton supersolid [194] and Charge Density Wave [195]. The flattening of the bands could be used as a new parameter to move in a controlled way the boundaries of the phases in these phase diagrams.

Appendix A

Two-Band Green Functions

This Appendix contains the explicit calculation of the Green functions of a two-band system. We solve here the Green function matrix (3.35) defined in Chapter 3.

$$\begin{pmatrix} i\hbar\omega - \zeta_1^{(e)} & 0 & \Delta_{11} & \Delta_{12} \\ 0 & i\hbar\omega - \zeta_2^{(e)} & \Delta_{21} & \Delta_{22} \\ -\Delta_{11}^* & -\Delta_{12}^* & i\hbar\omega + \zeta_1^{(h)} & 0 \\ -\Delta_{21}^* & -\Delta_{22}^* & 0 & i\hbar\omega + \zeta_2^{(h)} \end{pmatrix} \begin{pmatrix} G_{11} & G_{12} & F_{11} & F_{12} \\ G_{21} & G_{22} & F_{21} & F_{22} \\ F_{11}^* & F_{12}^* & G_{11}^* & G_{12}^* \\ F_{21}^* & F_{22}^* & G_{21}^* & G_{22}^* \end{pmatrix} = \begin{pmatrix} 1 & 0 & 0 & 0 \\ 0 & 1 & 0 & 0 \\ 0 & 0 & 1 & 0 \\ 0 & 0 & 0 & 1 \end{pmatrix} \quad (\text{A.1})$$

where $\omega = k_B T(2n + 1)\pi$ are the fermionic Matsubara frequencies.

To make the calculation more clean, we use the following notation:

$$z_1 = i\hbar\omega - \zeta_1^{(e)}, \quad z_2 = i\hbar\omega - \zeta_2^{(e)}, \quad z_3 = i\hbar\omega + \zeta_1^{(h)}, \quad z_4 = i\hbar\omega + \zeta_2^{(h)}. \quad (\text{A.2})$$

We write explicitly the system from the first column of the Green function matrix (Eq. (A.1)):

$$\begin{cases} z_1 G_{11} - \Delta_{11} F_{11}^* - \Delta_{12} F_{21}^* = 1 \\ z_2 G_{21} - \Delta_{21} F_{11}^* - \Delta_{22} F_{21}^* = 0 \\ -\Delta_{11}^* G_{11} - \Delta_{12}^* G_{21} + z_3 F_{11}^* = 0 \\ -\Delta_{21}^* G_{11} - \Delta_{22}^* G_{21} + z_4 F_{21}^* = 0 \end{cases} \quad (\text{A.3})$$

that becomes

$$\begin{cases} z_1 G_{11} = 1 + \Delta_{11} F_{11}^* + \Delta_{12} F_{21}^* \\ z_2 G_{21} = \Delta_{21} F_{11}^* + \Delta_{22} F_{21}^* \\ z_1 z_2 [-\Delta_{11}^* G_{11} - \Delta_{12}^* G_{21} + z_3 F_{11}^*] = 0 \\ z_1 z_2 [-\Delta_{21}^* G_{11} - \Delta_{22}^* G_{21} + z_4 F_{21}^*] = 0 \end{cases} \quad (\text{A.4})$$

We substitute the first two equation in the last two equations:

$$\begin{cases} -z_2 \Delta_{11}^* (1 + \Delta_{11} F_{11}^* + \Delta_{12} F_{21}^*) - z_1 \Delta_{12}^* (\Delta_{21} F_{11}^* + \Delta_{22} F_{21}^*) + z_3 F_{11}^* = 0 \\ -z_2 \Delta_{21}^* (1 + \Delta_{11} F_{11}^* + \Delta_{12} F_{21}^*) - z_1 \Delta_{22}^* (\Delta_{21} F_{11}^* + \Delta_{22} F_{21}^*) + z_4 F_{21}^* = 0 \end{cases}$$

and we obtain

$$\begin{cases} -z_2 \Delta_{11}^* - z_2 |\Delta_{11}|^2 F_{11}^* - z_2 \Delta_{11}^* \Delta_{12} F_{21}^* - z_1 \Delta_{12}^* \Delta_{21} F_{11}^* - z_1 \Delta_{12}^* \Delta_{22} F_{21}^* + z_1 z_2 z_3 F_{11}^* = 0 \\ -z_2 \Delta_{21}^* - z_2 \Delta_{11} \Delta_{21}^* F_{11}^* - z_2 \Delta_{12} \Delta_{21}^* F_{21}^* - z_1 \Delta_{21} \Delta_{22}^* F_{11}^* - z_1 |\Delta_{22}|^2 F_{21}^* + z_1 z_2 z_4 F_{21}^* = 0 \end{cases}$$

$$\begin{cases} -(z_2 |\Delta_{11}|^2 + z_1 \Delta_{12}^* \Delta_{21} - z_1 z_2 z_3) F_{11}^* = (z_2 \Delta_{11}^* \Delta_{12} + z_1 \Delta_{12}^* \Delta_{22}) F_{21}^* + z_2 \Delta_{11}^* \\ (z_2 \Delta_{12} \Delta_{21}^* + z_1 |\Delta_{22}|^2 - z_1 z_2 z_4) F_{21}^* = -(z_2 \Delta_{11} \Delta_{21}^* + z_1 \Delta_{21} \Delta_{22}^*) F_{11}^* - z_2 \Delta_{21}^* \end{cases}$$

now we can derive:

$$\begin{cases} F_{11}^* = \frac{z_2 \Delta_{21}^* (z_2 \Delta_{11}^* \Delta_{12} - z_1 \Delta_{12}^* \Delta_{22}) + (z_2 \Delta_{12} \Delta_{21}^* + z_1 |\Delta_{22}|^2 - z_1 z_2 z_4) z_2 \Delta_{11}^*}{(z_2 |\Delta_{11}|^2 + z_1 \Delta_{12}^* \Delta_{21} - z_1 z_2 z_3) (z_2 \Delta_{12} \Delta_{21}^* + z_1 |\Delta_{22}|^2 - z_1 z_2 z_4) - (z_2 \Delta_{11}^* \Delta_{12} + z_1 \Delta_{12}^* \Delta_{22}) (z_2 \Delta_{11} \Delta_{21}^* + z_1 \Delta_{21} \Delta_{22}^*)} \\ F_{21}^* = \frac{z_2 \Delta_{11}^* (z_2 \Delta_{12} \Delta_{21}^* + z_1 |\Delta_{22}|^2 - z_1 z_2 z_4) - z_2 |\Delta_{11}|^2 + z_1 \Delta_{12}^* \Delta_{21} - z_1 z_2 z_3) z_2 \Delta_{21}^*}{(z_2 |\Delta_{11}|^2 + z_1 \Delta_{12}^* \Delta_{21} - z_1 z_2 z_3) (z_2 \Delta_{11} \Delta_{21}^* + z_1 \Delta_{21} \Delta_{22}^*) - (z_2 \Delta_{11}^* \Delta_{12} + z_1 \Delta_{12}^* \Delta_{22}) (z_2 \Delta_{12} \Delta_{21}^* + z_1 |\Delta_{22}|^2 - z_1 z_2 z_4)} \end{cases} \quad (\text{A.5})$$

We substitute F_{11}^* and F_{21}^* in the Eqs. (A.4) and after algebraic transformations we get:

$$\begin{cases} F_{11}^* = \frac{z_2 z_4 \Delta_{11}^* - \Delta_{11}^* |\Delta_{22}|^2 + \Delta_{12}^* \Delta_{21}^* \Delta_{22}}{z_1 z_2 z_3 z_4 - z_2 z_4 |\Delta_{11}|^2 - z_1 z_3 |\Delta_{22}|^2 - z_4 z_1 \Delta_{12}^* \Delta_{21} - z_2 z_3 \Delta_{12} \Delta_{21}^* + (\Delta_{11} \Delta_{22} - \Delta_{12} \Delta_{21}) (\Delta_{11}^* \Delta_{22}^* - \Delta_{12}^* \Delta_{21}^*)} \\ F_{21}^* = \frac{z_2 z_3 \Delta_{21}^* - \Delta_{12}^* |\Delta_{21}|^2 + \Delta_{11}^* \Delta_{21} \Delta_{22}^*}{z_1 z_2 z_3 z_4 - z_2 z_4 |\Delta_{11}|^2 - z_1 z_3 |\Delta_{22}|^2 - z_4 z_1 \Delta_{12}^* \Delta_{21} - z_2 z_3 \Delta_{12} \Delta_{21}^* + (\Delta_{11} \Delta_{22} - \Delta_{12} \Delta_{21}) (\Delta_{11}^* \Delta_{22}^* - \Delta_{12}^* \Delta_{21}^*)} \\ G_{11} = \frac{z_2 z_3 z_4 - z_3 |\Delta_{22}|^2 - z_4 \Delta_{12}^* \Delta_{21}}{z_1 z_2 z_3 z_4 - z_2 z_4 |\Delta_{11}|^2 - z_1 z_3 |\Delta_{22}|^2 - z_4 z_1 \Delta_{12}^* \Delta_{21} - z_2 z_3 \Delta_{12} \Delta_{21}^* + (\Delta_{11} \Delta_{22} - \Delta_{12} \Delta_{21}) (\Delta_{11}^* \Delta_{22}^* - \Delta_{12}^* \Delta_{21}^*)} \\ G_{21} = \frac{z_4 \Delta_{11}^* \Delta_{21} + z_3 \Delta_{21}^* \Delta_{22}}{z_1 z_2 z_3 z_4 - z_2 z_4 |\Delta_{11}|^2 - z_1 z_3 |\Delta_{22}|^2 - z_4 z_1 \Delta_{12}^* \Delta_{21} - z_2 z_3 \Delta_{12} \Delta_{21}^* + (\Delta_{11} \Delta_{22} - \Delta_{12} \Delta_{21}) (\Delta_{11}^* \Delta_{22}^* - \Delta_{12}^* \Delta_{21}^*)} \end{cases} \quad (\text{A.6})$$

We apply the same procedure to recover all the Green function in the matrix.

We write explicitly the system from the second column of the Green function matrix (Eq. (A.1)):

$$\begin{cases} z_1 G_{12} - \Delta_{11} F_{12}^* - \Delta_{12} F_{22}^* = 0 \\ z_2 G_{22} - \Delta_{21} F_{12}^* - \Delta_{22} F_{22}^* = 1 \\ -\Delta_{11}^* G_{12} - \Delta_{12}^* G_{22} + z_3 F_{12}^* = 0 \\ -\Delta_{21}^* G_{12} - \Delta_{22}^* G_{22} + z_4 F_{22}^* = 0 \end{cases} \quad (\text{A.7})$$

that becomes

$$\begin{cases} z_1 G_{12} = \Delta_{11} F_{12}^* + \Delta_{12} F_{22}^* \\ z_2 G_{22} = 1 + \Delta_{21} F_{12}^* + \Delta_{22} F_{22}^* \\ z_1 z_2 [-\Delta_{11}^* G_{12} - \Delta_{12}^* G_{22} + z_3 F_{12}^*] = 0 \\ z_1 z_2 [-\Delta_{21}^* G_{12} - \Delta_{22}^* G_{22} + z_4 F_{22}^*] = 0 \end{cases} \quad (\text{A.8})$$

and we find:

$$\begin{cases} F_{12}^* = \frac{z_1 z_4 \Delta_{12}^* - |\Delta_{12}|^2 \Delta_{21}^* + \Delta_{11}^* \Delta_{12} \Delta_{22}^*}{z_1 z_2 z_3 z_4 - z_2 z_4 |\Delta_{11}|^2 - z_1 z_3 |\Delta_{22}|^2 - z_1 z_4 \Delta_{12}^* \Delta_{21} - z_2 z_3 \Delta_{12} \Delta_{21}^* + (\Delta_{11} \Delta_{22} - \Delta_{12} \Delta_{21}) (\Delta_{11}^* \Delta_{22}^* - \Delta_{12}^* \Delta_{21}^*)} \\ F_{22}^* = \frac{z_1 z_3 \Delta_{22}^* - |\Delta_{11}|^2 \Delta_{22}^* + \Delta_{11}^* \Delta_{12} \Delta_{21}^*}{z_1 z_2 z_3 z_4 - z_2 z_4 |\Delta_{11}|^2 - z_1 z_3 |\Delta_{22}|^2 - z_1 z_4 \Delta_{12}^* \Delta_{21} - z_2 z_3 \Delta_{12} \Delta_{21}^* + (\Delta_{11} \Delta_{22} - \Delta_{12} \Delta_{21}) (\Delta_{11}^* \Delta_{22}^* - \Delta_{12}^* \Delta_{21}^*)} \\ G_{12} = \frac{z_4 \Delta_{11} \Delta_{12}^* + z_3 \Delta_{22}^* \Delta_{12}}{z_1 z_2 z_3 z_4 - z_2 z_4 |\Delta_{11}|^2 - z_1 z_3 |\Delta_{22}|^2 - z_1 z_4 \Delta_{12}^* \Delta_{21} - z_2 z_3 \Delta_{12} \Delta_{21}^* + (\Delta_{11} \Delta_{22} - \Delta_{12} \Delta_{21}) (\Delta_{11}^* \Delta_{22}^* - \Delta_{12}^* \Delta_{21}^*)} \\ G_{22} = \frac{z_1 z_3 z_4 - z_4 |\Delta_{11}|^2 - z_3 \Delta_{12} \Delta_{21}^*}{z_1 z_2 z_3 z_4 - z_2 z_4 |\Delta_{11}|^2 - z_1 z_3 |\Delta_{22}|^2 - z_1 z_4 \Delta_{12}^* \Delta_{21} - z_2 z_3 \Delta_{12} \Delta_{21}^* + (\Delta_{11} \Delta_{22} - \Delta_{12} \Delta_{21}) (\Delta_{11}^* \Delta_{22}^* - \Delta_{12}^* \Delta_{21}^*)} \end{cases} \quad (\text{A.9})$$

We write explicitly the system from the third column of the Green function matrix (Eq. (A.1)):

$$\begin{cases} z_1 F_{11} - \Delta_{11} G_{11}^* - \Delta_{12} G_{21}^* = 0 \\ z_2 F_{21} - \Delta_{21} G_{11}^* - \Delta_{22} G_{21}^* = 0 \\ -\Delta_{11}^* F_{11} - \Delta_{12}^* F_{21} + z_3 G_{11}^* = 1 \\ -\Delta_{21}^* F_{11} - \Delta_{22}^* F_{21} + z_4 G_{21}^* = 0 \end{cases} \quad (\text{A.10})$$

that becomes

$$\begin{cases} z_3 z_4 [z_1 F_{11} - \Delta_{11} G_{11}^* - \Delta_{12} G_{21}^*] = 0 \\ z_3 z_4 [z_2 F_{21} - \Delta_{21} G_{11}^* - \Delta_{22} G_{21}^*] = 0 \\ 1 + \Delta_{11}^* F_{11} + \Delta_{12}^* F_{21} = z_3 G_{11}^* \\ \Delta_{21}^* F_{11} + \Delta_{22}^* F_{21} = z_4 G_{21}^* \end{cases} \quad (\text{A.11})$$

and we find:

$$\begin{cases} F_{11} = \frac{(z_2 z_4 \Delta_{11} - \Delta_{11} |\Delta_{22}|^2 + \Delta_{12} \Delta_{21} \Delta_{22}^*)}{z_1 z_2 z_3 z_4 - z_2 z_4 |\Delta_{11}|^2 - z_2 z_3 \Delta_{12} \Delta_{21}^* - z_1 z_4 \Delta_{12}^* \Delta_{21} - z_1 z_3 |\Delta_{22}|^2 + (\Delta_{11} \Delta_{22} - \Delta_{12} \Delta_{21}) (\Delta_{11}^* \Delta_{22}^* - \Delta_{12}^* \Delta_{21}^*)} \\ F_{21} = \frac{(z_1 z_4 \Delta_{21} - \Delta_{12} |\Delta_{21}|^2 + \Delta_{11} \Delta_{21}^* \Delta_{22})}{z_1 z_2 z_3 z_4 - z_2 z_4 |\Delta_{11}|^2 - z_2 z_3 \Delta_{12} \Delta_{21}^* - z_1 z_4 \Delta_{12}^* \Delta_{21} - z_1 z_3 |\Delta_{22}|^2 + (\Delta_{11} \Delta_{22} - \Delta_{12} \Delta_{21}) (\Delta_{11}^* \Delta_{22}^* - \Delta_{12}^* \Delta_{21}^*)} \\ G_{11}^* = \frac{z_1 z_2 z_4 - z_1 |\Delta_{22}|^2 - z_2 \Delta_{12} \Delta_{21}^*}{z_1 z_2 z_3 z_4 - z_2 z_4 |\Delta_{11}|^2 - z_1 z_3 |\Delta_{22}|^2 - z_2 z_3 \Delta_{12} \Delta_{21}^* - z_1 z_4 \Delta_{12}^* \Delta_{21} + (\Delta_{11} \Delta_{22} - \Delta_{12} \Delta_{21}) (\Delta_{11}^* \Delta_{22}^* - \Delta_{12}^* \Delta_{21}^*)} \\ G_{21}^* = \frac{z_4 \Delta_{11} \Delta_{21}^* + z_3 \Delta_{21} \Delta_{22}^*}{z_1 z_2 z_3 z_4 - z_2 z_4 |\Delta_{11}|^2 - z_1 z_3 |\Delta_{22}|^2 - z_4 z_1 \Delta_{12} \Delta_{21}^* - z_2 z_3 \Delta_{12}^* \Delta_{21} + (\Delta_{11} \Delta_{22} - \Delta_{12} \Delta_{21}) (\Delta_{11}^* \Delta_{22}^* - \Delta_{12}^* \Delta_{21}^*)} \end{cases} \quad (\text{A.12})$$

We write explicitly the system from the fourth column of the Green function matrix (Eq. (A.1)):

$$\begin{cases} z_1 F_{12} - \Delta_{11} G_{12}^* - \Delta_{12} G_{22}^* = 0 \\ z_2 F_{22} - \Delta_{21} G_{12}^* - \Delta_{22} G_{22}^* = 0 \\ -\Delta_{11}^* F_{12} - \Delta_{12}^* F_{22} + z_3 G_{12}^* = 0 \\ -\Delta_{21}^* F_{12} - \Delta_{22}^* F_{22} + z_4 G_{22}^* = 1 \end{cases} \quad (\text{A.13})$$

that becomes

$$\begin{cases} z_3 z_4 [z_1 F_{12} - \Delta_{11} G_{12}^* - \Delta_{12} G_{22}^*] = 0 \\ z_3 z_4 [z_2 F_{22} - \Delta_{21} G_{12}^* - \Delta_{22} G_{22}^*] = 0 \\ \Delta_{11}^* F_{12} + \Delta_{12}^* F_{22} = z_3 G_{12}^* \\ 1 + \Delta_{21}^* F_{12} + \Delta_{22}^* F_{22} = z_4 G_{22}^* \end{cases} \quad (\text{A.14})$$

and we find:

$$\begin{cases} F_{12} = \frac{z_2 z_3 \Delta_{12} - |\Delta_{12}|^2 \Delta_{21} + \Delta_{11} \Delta_{12}^* \Delta_{22}}{z_1 z_2 z_3 z_4 - z_2 z_4 |\Delta_{11}|^2 - z_1 z_3 |\Delta_{22}|^2 - z_2 z_3 \Delta_{12} \Delta_{21}^* - z_1 z_4 \Delta_{12}^* \Delta_{21} + (\Delta_{11} \Delta_{22} - \Delta_{12} \Delta_{21}) (\Delta_{11}^* \Delta_{22}^* - \Delta_{12}^* \Delta_{21}^*)} \\ F_{22} = \frac{z_1 z_3 \Delta_{22} - |\Delta_{11}|^2 \Delta_{22} + \Delta_{11}^* \Delta_{12} \Delta_{21}}{z_1 z_2 z_3 z_4 - z_2 z_4 |\Delta_{11}|^2 - z_1 z_3 |\Delta_{22}|^2 - z_2 z_3 \Delta_{12} \Delta_{21}^* - z_1 z_4 \Delta_{12}^* \Delta_{21} + (\Delta_{11} \Delta_{22} - \Delta_{12} \Delta_{21}) (\Delta_{11}^* \Delta_{22}^* - \Delta_{12}^* \Delta_{21}^*)} \\ G_{12}^* = \frac{z_4 \Delta_{11}^* \Delta_{12} + z_3 \Delta_{22} \Delta_{12}^*}{z_1 z_2 z_3 z_4 - z_2 z_4 |\Delta_{11}|^2 - z_1 z_3 |\Delta_{22}|^2 - z_1 z_4 \Delta_{12} \Delta_{21}^* - z_2 z_3 \Delta_{12}^* \Delta_{21} + (\Delta_{11} \Delta_{22} - \Delta_{12} \Delta_{21}) (\Delta_{11}^* \Delta_{22}^* - \Delta_{12}^* \Delta_{21}^*)} \\ G_{22}^* = \frac{z_1 z_3 z_4 - z_4 |\Delta_{11}|^2 - z_3 \Delta_{12}^* \Delta_{21}}{z_1 z_2 z_3 z_4 - z_2 z_4 |\Delta_{11}|^2 - z_1 z_3 |\Delta_{22}|^2 - z_1 z_4 \Delta_{12} \Delta_{21}^* - z_2 z_3 \Delta_{12}^* \Delta_{21} + (\Delta_{11} \Delta_{22} - \Delta_{12} \Delta_{21}) (\Delta_{11}^* \Delta_{22}^* - \Delta_{12}^* \Delta_{21}^*)} \end{cases} \quad (\text{A.15})$$

We chose the order parameter Δ_{nj} , to be real. This is always possible in the absence of an external field, since the equations of the Green function defined in Chapter 3 are invariant under the transformation

$$\Delta(k) \rightarrow \Delta(k) e^{2i\phi}, \quad \Delta(k)^* \rightarrow \Delta^*(k) e^{-2i\phi}, \quad (\text{A.16})$$

for a constant phase ϕ . With this choice we can rewrite the Green functions as

$$\left\{ \begin{array}{l} F_{11} = \frac{z_2 z_4 \Delta_{11} - \Delta_{11} \Delta_{22}^2 + \Delta_{12} \Delta_{21} \Delta_{22}}{z_1 z_2 z_3 z_4 - z_2 z_4 \Delta_{11}^2 - z_1 z_3 \Delta_{22}^2 - (z_2 z_3 + z_1 z_4) \Delta_{12} \Delta_{21} + (\Delta_{11} \Delta_{22} - \Delta_{12} \Delta_{21})^2} \\ F_{21} = \frac{z_1 z_4 \Delta_{21} - \Delta_{12} \Delta_{21}^2 + \Delta_{11} \Delta_{21} \Delta_{22}}{z_1 z_2 z_3 z_4 - z_2 z_4 \Delta_{11}^2 - z_1 z_3 \Delta_{22}^2 - (z_2 z_3 + z_1 z_4) \Delta_{12} \Delta_{21} + (\Delta_{11} \Delta_{22} - \Delta_{12} \Delta_{21})^2} \\ F_{12} = \frac{z_2 z_3 \Delta_{12} - \Delta_{12}^2 \Delta_{21} + \Delta_{11} \Delta_{12} \Delta_{22}}{z_1 z_2 z_3 z_4 - z_2 z_4 \Delta_{11}^2 - z_1 z_3 \Delta_{22}^2 - (z_2 z_3 + z_1 z_4) \Delta_{12} \Delta_{21} + (\Delta_{11} \Delta_{22} - \Delta_{12} \Delta_{21})^2} \\ F_{22} = \frac{z_1 z_3 \Delta_{22} - \Delta_{11}^2 \Delta_{22} + \Delta_{11} \Delta_{12} \Delta_{21}}{z_1 z_2 z_3 z_4 - z_2 z_4 \Delta_{11}^2 - z_1 z_3 \Delta_{22}^2 - (z_2 z_3 + z_1 z_4) \Delta_{12} \Delta_{21} + (\Delta_{11} \Delta_{22} - \Delta_{12} \Delta_{21})^2} \end{array} \right. \quad (\text{A.17})$$

$$\left\{ \begin{array}{l} G_{11} = \frac{z_2 z_3 z_4 - z_3 \Delta_{22}^2 - z_4 \Delta_{12} \Delta_{21}}{z_1 z_2 z_3 z_4 - z_2 z_4 \Delta_{11}^2 - z_1 z_3 \Delta_{22}^2 - (z_2 z_3 + z_1 z_4) \Delta_{12} \Delta_{21} + (\Delta_{11} \Delta_{22} - \Delta_{12} \Delta_{21})^2} \\ G_{21} = \frac{z_4 \Delta_{11} \Delta_{21} + z_3 \Delta_{21} \Delta_{22}}{z_1 z_2 z_3 z_4 - z_2 z_4 \Delta_{11}^2 - z_1 z_3 \Delta_{22}^2 - (z_2 z_3 + z_1 z_4) \Delta_{12} \Delta_{21} + (\Delta_{11} \Delta_{22} - \Delta_{12} \Delta_{21})^2} \\ G_{12} = \frac{z_4 \Delta_{11} \Delta_{12} + z_3 \Delta_{22} \Delta_{12}}{z_1 z_2 z_3 z_4 - z_2 z_4 \Delta_{11}^2 - z_1 z_3 \Delta_{22}^2 - (z_2 z_3 + z_1 z_4) \Delta_{12} \Delta_{21} + (\Delta_{11} \Delta_{22} - \Delta_{12} \Delta_{21})^2} \\ G_{22} = \frac{z_1 z_3 z_4 - z_4 \Delta_{11}^2 - z_3 \Delta_{12} \Delta_{21}}{z_1 z_2 z_3 z_4 - z_2 z_4 \Delta_{11}^2 - z_1 z_3 \Delta_{22}^2 - (z_2 z_3 + z_1 z_4) \Delta_{12} \Delta_{21} + (\Delta_{11} \Delta_{22} - \Delta_{12} \Delta_{21})^2} \end{array} \right. \quad (\text{A.18})$$

To write the expression in a more compact way we rewrite the denominator:

$$\begin{aligned} & (i\hbar\omega - \xi_1^{(e)})(i\hbar\omega - \xi_2^{(e)})(i\hbar\omega + \xi_1^{(h)})(i\hbar\omega + \xi_2^{(h)}) - (i\hbar\omega - \xi_2^{(e)})(i\hbar\omega + \xi_2^{(h)})\Delta_{11}^2 \\ & - (i\hbar\omega - \xi_1^{(e)})(i\hbar\omega + \xi_1^{(h)})\Delta_{22}^2 - ((i\hbar\omega - \xi_2^{(e)})(i\hbar\omega + \xi_1^{(h)}) + (i\hbar\omega - \xi_1^{(e)})(i\hbar\omega + \xi_2^{(h)}))\Delta_{12}\Delta_{21} \\ & + (\Delta_{11}\Delta_{22} - \Delta_{12}\Delta_{21})^2 = (i\hbar\omega - \chi_1)(i\hbar\omega - \chi_2)(i\hbar\omega + \chi_3)(i\hbar\omega + \chi_4) \end{aligned} \quad (\text{A.19})$$

where,

$$\chi_1 = \delta\tilde{\xi}_1 + \sqrt{\frac{a+b}{2}}, \quad \chi_2 = \delta\tilde{\xi}_2 + \sqrt{\frac{a-b}{2}}, \quad \chi_3 = -\delta\tilde{\xi}_1 + \sqrt{\frac{a+b}{2}}, \quad \chi_4 = -\delta\tilde{\xi}_2 + \sqrt{\frac{a-b}{2}}, \quad (\text{A.20})$$

with

$$\begin{aligned} \delta\tilde{\xi}_\gamma &= (\xi_\gamma^{(e)} - \xi_\gamma^{(h)})/2, \quad \tilde{\xi}_\gamma = (\xi_\gamma^{(e)} + \xi_\gamma^{(h)})/2, \quad E_\gamma^2 = \Delta_{\gamma\gamma}^2 + \tilde{\xi}_\gamma^2, \quad T_\gamma^2 = \Delta_{\gamma\gamma}^2 + \xi_\gamma^{(e)}\xi_\gamma^{(h)}, \\ a &= E_1^2 + E_2^2 + 2\Delta_{12}\Delta_{21}, \\ b &= \delta\tilde{\xi}_1^2 - \delta\tilde{\xi}_2^2 + \sqrt{(T_1^2 - T_2^2)^2 + 4\Delta_{12}\Delta_{21}((\xi_1^{(e)} - \xi_2^{(e)})(\xi_1^{(h)} - \xi_2^{(h)}) + (\Delta_{11} + \Delta_{22})^2)}. \end{aligned} \quad (\text{A.21})$$

We can rewrite the Green functions in Eqs. (A.17)-(A.18) as function of ω and k :

$$\begin{aligned}
 F_{11}[i\omega, \mathbf{k}] &= \frac{(i\hbar\omega - \tilde{\zeta}_2^{(e)})(i\hbar\omega + \tilde{\zeta}_2^{(h)})\Delta_{11} - (\Delta_{11}\Delta_{22} - \Delta_{12}\Delta_{21})\Delta_{22}}{(i\hbar\omega - \chi_1)(i\hbar\omega - \chi_2)(i\hbar\omega + \chi_3)(i\hbar\omega + \chi_4)}, \\
 F_{21}[i\omega, \mathbf{k}] &= \frac{(i\hbar\omega - \tilde{\zeta}_1^{(e)})(i\hbar\omega + \tilde{\zeta}_2^{(h)})\Delta_{21} + (\Delta_{11}\Delta_{22} - \Delta_{12}\Delta_{21})\Delta_{21}}{(i\hbar\omega - \chi_1)(i\hbar\omega - \chi_2)(i\hbar\omega + \chi_3)(i\hbar\omega + \chi_4)}, \\
 F_{12}[i\omega, \mathbf{k}] &= \frac{(i\hbar\omega - \tilde{\zeta}_2^{(e)})(i\hbar\omega + \tilde{\zeta}_1^{(h)})\Delta_{12} + (\Delta_{11}\Delta_{22} - \Delta_{12}\Delta_{21})\Delta_{12}}{(i\hbar\omega - \chi_1)(i\hbar\omega - \chi_2)(i\hbar\omega + \chi_3)(i\hbar\omega + \chi_4)}, \\
 F_{22}[i\omega, \mathbf{k}] &= \frac{(i\hbar\omega - \tilde{\zeta}_1^{(e)})(i\hbar\omega + \tilde{\zeta}_1^{(h)})\Delta_{22} - (\Delta_{11}\Delta_{22} - \Delta_{12}\Delta_{21})\Delta_{11}}{(i\hbar\omega - \chi_1)(i\hbar\omega - \chi_2)(i\hbar\omega + \chi_3)(i\hbar\omega + \chi_4)}, \\
 G_{11}[i\omega, \mathbf{k}] &= \frac{(i\hbar\omega + \tilde{\zeta}_1^{(h)})[(i\hbar\omega - \tilde{\zeta}_2^{(e)})(i\hbar\omega + \tilde{\zeta}_2^{(h)}) - \Delta_{22}^2] - (i\hbar\omega + \tilde{\zeta}_2^{(h)})\Delta_{12}\Delta_{21}}{(i\hbar\omega - \chi_1)(i\hbar\omega - \chi_2)(i\hbar\omega + \chi_3)(i\hbar\omega + \chi_4)}, \\
 G_{21}[i\omega, \mathbf{k}] &= \frac{(i\hbar\omega + \tilde{\zeta}_2^{(h)})\Delta_{11}\Delta_{21} + (i\hbar\omega + \tilde{\zeta}_1^{(h)})\Delta_{21}\Delta_{22}}{(i\hbar\omega - \chi_1)(i\hbar\omega - \chi_2)(i\hbar\omega + \chi_3)(i\hbar\omega + \chi_4)}, \\
 G_{12}[i\omega, \mathbf{k}] &= \frac{(i\hbar\omega + \tilde{\zeta}_2^{(h)})\Delta_{11}\Delta_{12} + (i\hbar\omega + \tilde{\zeta}_1^{(h)})\Delta_{22}\Delta_{12}}{(i\hbar\omega - \chi_1)(i\hbar\omega - \chi_2)(i\hbar\omega + \chi_3)(i\hbar\omega + \chi_4)}, \\
 G_{22}[i\omega, \mathbf{k}] &= \frac{(i\hbar\omega + \tilde{\zeta}_2^{(h)})[(i\hbar\omega - \tilde{\zeta}_1^{(e)})(i\hbar\omega + \tilde{\zeta}_1^{(h)}) - \Delta_{11}^2] - (i\hbar\omega + \tilde{\zeta}_1^{(h)})\Delta_{12}\Delta_{21}}{(i\hbar\omega - \chi_1)(i\hbar\omega - \chi_2)(i\hbar\omega + \chi_3)(i\hbar\omega + \chi_4)}.
 \end{aligned} \tag{A.22}$$

To obtain the mean field superfluid gaps (Eq. (3.40)) and density (Eq. (3.42)) defined in Chapter 3, we need to sum over the Matsubara frequencies ω . We obtain the temperature dependent Green functions as a function of \mathbf{k} :

$$\begin{aligned}
 F_{11} &= \frac{n_F[\chi_1, T] \left((\chi_1 + \tilde{\zeta}_2^{(h)})(\chi_1 - \tilde{\zeta}_2^{(e)})\Delta_{11} - \mathfrak{D}\Delta_{22} \right)}{(\chi_1 - \chi_2)(\chi_1 + \chi_3)(\chi_1 + \chi_4)} - \frac{n_F[-\chi_3, T] \left((\chi_3 - \tilde{\zeta}_2^{(h)})(\chi_3 + \tilde{\zeta}_2^{(e)})\Delta_{11} - \mathfrak{D}\Delta_{22} \right)}{(\chi_1 + \chi_3)(\chi_2 + \chi_3)(\chi_3 - \chi_4)} \\
 &\quad - \frac{n_F[\chi_2, T] \left((\chi_2 + \tilde{\zeta}_2^{(h)})(\chi_2 - \tilde{\zeta}_2^{(e)})\Delta_{11} - \mathfrak{D}\Delta_{22} \right)}{(\chi_1 - \chi_2)(\chi_2 + \chi_3)(\chi_2 + \chi_4)} + \frac{n_F[-\chi_4, T] \left((\chi_4 - \tilde{\zeta}_2^{(h)})(\chi_4 + \tilde{\zeta}_2^{(e)})\Delta_{11} - \mathfrak{D}\Delta_{22} \right)}{(\chi_1 + \chi_4)(\chi_2 + \chi_4)(\chi_3 - \chi_4)},
 \end{aligned} \tag{A.23}$$

$$\begin{aligned}
 F_{12} &= \Delta_{12} \left[\frac{n_F[\chi_1, T] \left((\chi_1 + \tilde{\zeta}_1^{(h)})(\chi_1 - \tilde{\zeta}_2^{(e)}) + \mathfrak{D} \right)}{(\chi_1 - \chi_2)(\chi_1 + \chi_3)(\chi_1 + \chi_4)} - \frac{n_F[-\chi_3, T] \left((\chi_3 - \tilde{\zeta}_1^{(h)})(\chi_3 + \tilde{\zeta}_2^{(e)}) + \mathfrak{D} \right)}{(\chi_1 + \chi_3)(\chi_2 + \chi_3)(\chi_3 - \chi_4)} \right. \\
 &\quad \left. - \frac{n_F[\chi_2, T] \left((\chi_2 + \tilde{\zeta}_1^{(h)})(\chi_2 - \tilde{\zeta}_2^{(e)}) + \mathfrak{D} \right)}{(\chi_1 - \chi_2)(\chi_2 + \chi_3)(\chi_2 + \chi_4)} + \frac{n_F[-\chi_4, T] \left((\chi_4 - \tilde{\zeta}_1^{(h)})(\chi_4 + \tilde{\zeta}_2^{(e)}) + \mathfrak{D} \right)}{(\chi_1 + \chi_4)(\chi_2 + \chi_4)(\chi_3 - \chi_4)} \right],
 \end{aligned} \tag{A.24}$$

$$\begin{aligned}
 F_{21} &= \Delta_{21} \left[\frac{n_F[\chi_1, T] \left((\chi_1 - \tilde{\zeta}_1^{(e)})(\chi_1 + \tilde{\zeta}_2^{(h)}) + \mathfrak{D} \right)}{(\chi_1 - \chi_2)(\chi_1 + \chi_3)(\chi_1 + \chi_4)} - \frac{n_F[-\chi_3, T] \left((\chi_3 + \tilde{\zeta}_1^{(e)})(\chi_3 - \tilde{\zeta}_2^{(h)}) + \mathfrak{D} \right)}{(\chi_1 + \chi_3)(\chi_2 + \chi_3)(\chi_3 - \chi_4)} \right. \\
 &\quad \left. - \frac{n_F[\chi_2, T] \left((\chi_2 + \tilde{\zeta}_2^{(h)})(\chi_2 - \tilde{\zeta}_1^{(e)}) + \mathfrak{D} \right)}{(\chi_1 - \chi_2)(\chi_2 + \chi_3)(\chi_2 + \chi_4)} + \frac{n_F[-\chi_4, T] \left((\chi_4 - \tilde{\zeta}_2^{(h)})(\chi_4 + \tilde{\zeta}_1^{(e)}) + \mathfrak{D} \right)}{(\chi_1 + \chi_4)(\chi_2 + \chi_4)(\chi_3 - \chi_4)} \right],
 \end{aligned} \tag{A.25}$$

$$\begin{aligned}
 F_{22} = & \frac{n_F[\chi_1, T] \left((\chi_1 - \xi_1^{(e)})(\chi_1 + \xi_1^{(h)})\Delta_{22} - \mathfrak{D}\Delta_{11} \right)}{(\chi_1 - \chi_2)(\chi_1 + \chi_3)(\chi_1 + \chi_4)} - \frac{n_F[-\chi_3, T] \left((\chi_3 + \xi_1^{(e)})(\chi_3 - \xi_1^{(h)})\Delta_{22} - \mathfrak{D}\Delta_{11} \right)}{(\chi_1 + \chi_3)(\chi_2 + \chi_3)(\chi_3 - \chi_4)} \\
 & - \frac{n_F[\chi_2, T] \left((\chi_2 + \xi_1^{(h)})(\chi_2 - \xi_1^{(e)})\Delta_{22} - \mathfrak{D}\Delta_{11} \right)}{(\chi_1 - \chi_2)(\chi_2 + \chi_3)(\chi_2 + \chi_4)} + \frac{n_F[-\chi_4, T] \left((\chi_4 - \xi_1^{(h)})(\chi_4 + \xi_1^{(e)})\Delta_{22} - \mathfrak{D}\Delta_{11} \right)}{(\chi_1 + \chi_4)(\chi_2 + \chi_4)(\chi_3 - \chi_4)}, \tag{A.26}
 \end{aligned}$$

where $\mathfrak{D} = \Delta_{11}\Delta_{22} - \Delta_{12}\Delta_{21}$.

$$\begin{aligned}
 G_{11} = & \frac{n_F[\chi_1, T] \left((\chi_1 - \xi_2^{(e)})(\chi_1 + \xi_1^{(h)})(\chi_1 + \xi_2^{(h)}) - \Delta_{22}^2(\chi_1 + \xi_1^{(h)}) - \Delta_{12}\Delta_{21}(\chi_1 + \xi_2^{(h)}) \right)}{(\chi_1 - \chi_2)(\chi_1 + \chi_3)(\chi_1 + \chi_4)} \\
 & - \frac{n_F[\chi_2, T] \left((\chi_2 - \xi_2^{(e)})(\chi_2 + \xi_1^{(h)})(\chi_2 + \xi_2^{(h)}) - \Delta_{22}^2(\chi_2 + \xi_1^{(h)}) - \Delta_{12}\Delta_{21}(\chi_2 + \xi_2^{(h)}) \right)}{(\chi_1 - \chi_2)(\chi_2 + \chi_3)(\chi_2 + \chi_4)} \\
 & + \frac{n_F[-\chi_3, T] \left((\chi_3 + \xi_2^{(e)})(\chi_3 - \xi_1^{(h)})(\chi_3 - \xi_2^{(h)}) - \Delta_{22}^2(\chi_3 - \xi_1^{(h)}) - \Delta_{12}\Delta_{21}(\chi_3 - \xi_2^{(h)}) \right)}{(\chi_1 + \chi_3)(\chi_2 + \chi_3)(\chi_3 - \chi_4)} \\
 & - \frac{n_F[-\chi_4, T] \left((\chi_4 + \xi_2^{(e)})(\chi_4 - \xi_1^{(h)})(\chi_4 - \xi_2^{(h)}) - \Delta_{22}^2(\chi_4 - \xi_1^{(h)}) - \Delta_{12}\Delta_{21}(\chi_4 - \xi_2^{(h)}) \right)}{(\chi_1 + \chi_4)(\chi_2 + \chi_4)(\chi_3 - \chi_4)}, \tag{A.27}
 \end{aligned}$$

$$\begin{aligned}
 G_{12} = \Delta_{12} \left[\frac{n_F[\chi_1, T] \left((\chi_1 + \xi_2^{(h)})\Delta_{11} + (\chi_1 + \xi_1^{(h)})\Delta_{22} \right)}{(\chi_1 - \chi_2)(\chi_1 + \chi_3)(\chi_1 + \chi_4)} + \frac{n_F[-\chi_3, T] \left((\chi_3 - \xi_2^{(h)})\Delta_{11} + (\chi_3 - \xi_1^{(h)})\Delta_{22} \right)}{(\chi_1 + \chi_3)(\chi_2 + \chi_3)(\chi_3 - \chi_4)} \right. \\
 \left. - \frac{n_F[\chi_2, T] \left((\chi_2 + \xi_2^{(h)})\Delta_{11} + (\chi_2 + \xi_1^{(h)})\Delta_{22} \right)}{(\chi_1 - \chi_2)(\chi_2 + \chi_3)(\chi_2 + \chi_4)} + \frac{n_F[-\chi_4, T] \left((\chi_4 - \xi_2^{(h)})\Delta_{11} + (\chi_4 - \xi_1^{(h)})\Delta_{22} \right)}{(\chi_1 + \chi_4)(\chi_2 + \chi_4)(-\chi_3 + \chi_4)} \right], \tag{A.28}
 \end{aligned}$$

$$\begin{aligned}
 G_{12} = \Delta_{21} \left[\frac{n_F[\chi_1, T] \left((\chi_1 + \xi_2^{(h)})\Delta_{11} + (\chi_1 + \xi_1^{(h)})\Delta_{22} \right)}{(\chi_1 - \chi_2)(\chi_1 + \chi_3)(\chi_1 + \chi_4)} + \frac{n_F[-\chi_3, T] \left((\chi_3 - \xi_2^{(h)})\Delta_{11} + (\chi_3 - \xi_1^{(h)})\Delta_{22} \right)}{(\chi_1 + \chi_3)(\chi_2 + \chi_3)(\chi_3 - \chi_4)} \right. \\
 \left. - \frac{n_F[\chi_2, T] \left((\chi_2 + \xi_2^{(h)})\Delta_{11} + (\chi_2 + \xi_1^{(h)})\Delta_{22} \right)}{(\chi_1 - \chi_2)(\chi_2 + \chi_3)(\chi_2 + \chi_4)} + \frac{n_F[-\chi_4, T] \left((\chi_4 - \xi_2^{(h)})\Delta_{11} + (\chi_4 - \xi_1^{(h)})\Delta_{22} \right)}{(\chi_1 + \chi_4)(\chi_2 + \chi_4)(-\chi_3 + \chi_4)} \right], \tag{A.29}
 \end{aligned}$$

$$\begin{aligned}
 G_{22} = & \frac{n_F[\chi_1, T] \left((\chi_1 - \xi_1^{(e)})(\chi_1 + \xi_1^{(h)})(\chi_1 + \xi_2^{(h)}) - \Delta_{11}^2(\chi_1 + \xi_2^{(h)}) - \Delta_{12}\Delta_{21}(\chi_1 + \xi_1^{(h)}) \right)}{(\chi_1 - \chi_2)(\chi_1 + \chi_3)(\chi_1 + \chi_4)} \\
 & - \frac{n_F[\chi_2, T] \left((\chi_2 + \xi_1^{(h)})(\chi_2 - \xi_1^{(e)})(\chi_2 + \xi_2^{(h)}) - \Delta_{11}^2(\chi_2 + \xi_2^{(h)}) - \Delta_{12}\Delta_{21}(\chi_2 + \xi_1^{(h)}) \right)}{(\chi_1 - \chi_2)(\chi_2 + \chi_3)(\chi_2 + \chi_4)} \\
 & + \frac{n_F[-\chi_3, T] \left((\chi_3 + \xi_1^{(e)})(\chi_3 - \xi_1^{(h)})(\chi_3 - \xi_2^{(h)}) - \Delta_{11}^2(\chi_3 - \xi_2^{(h)}) - \Delta_{12}\Delta_{21}(\chi_3 - \xi_1^{(h)}) \right)}{(\chi_1 + \chi_3)(\chi_2 + \chi_3)(\chi_3 - \chi_4)} \\
 & - \frac{n_F[-\chi_4, T] \left((\chi_4 + \xi_1^{(e)})(\chi_4 - \xi_1^{(h)})(\chi_4 - \xi_2^{(h)}) - \Delta_{11}^2(\chi_4 - \xi_2^{(h)}) - \Delta_{12}\Delta_{21}(\chi_4 - \xi_1^{(e)}) \right)}{(\chi_1 + \chi_4)(\chi_2 + \chi_4)(\chi_3 - \chi_4)}. \tag{A.30}
 \end{aligned}$$

The functions contain four Fermi distributions at temperature T , $n_F[\chi_n, T] = (e^{\chi_n/k_B T} + 1)^{-1}$ and $n_F[-\chi_n, T] = 1 - n_F[\chi_n, T]$. From this equations we can recover the particular cases described in Chapter 4 and Chapter 6 in the limit of zero temperature with:

$$n_F[\chi_n, 0] = \begin{cases} 1 & \chi_n < 0 \\ 0 & \chi_n > 0 \end{cases} = 1 - \theta[\chi_n], \tag{A.31}$$

where $\theta[\chi_n]$ is a Heaviside step function.

A.1 Double Bilayer Graphene Green Functions

For Double Bilayer Graphene we reduce the equations Eqs. (A.23)-(A.30) without interband pairing with $\Delta_{12} = \Delta_{21} = 0$, $\mathcal{D} = \Delta_{11}\Delta_{22}$.

With bilayer graphene parabolic identical bands we get $\chi_1 = \chi_3 = E_+$ and $\chi_2 = \chi_4 = E_-$, so we have $n_F[-\chi_3, T] = 1 - n_F[\chi_1, T] = 1 - n_F[E_+, T]$ and $n_F[-\chi_4, T] = 1 - n_F[\chi_2, T] = 1 - n_F[E_-, T]$.

$$F_{++} = -\frac{\Delta_{++}}{2E_+}(1 - 2n_F[E_+, T]), \quad (\text{A.32})$$

$$F_{--} = -\frac{\Delta_{--}}{2E_-}(1 - 2n_F[E_-, T]), \quad (\text{A.33})$$

$$G_{++} = \frac{E_+ - \xi_+}{2E_+}(1 - n_F[E_+, T]) + \frac{E_+ + \xi_+}{2E_+}n_F[E_+, T], \quad (\text{A.34})$$

$$G_{--} = \frac{E_- - \xi_-}{2E_-}(1 - n_F[E_-, T]) + \frac{E_- + \xi_-}{2E_-}n_F[E_-, T]. \quad (\text{A.35})$$

A.2 Double TMD monolayer Green Functions

For double TMD monolayer system we reduce the equations Eqs. (A.23)-(A.30) without interband pairing with $\Delta_{12} = \Delta_{21} = 0$, $\mathcal{D} = \Delta_{11}\Delta_{22}$. With TMD monolayer parabolic bands we get $\chi_1 = \chi_3 = E_b$, $\chi_2 = -\delta\lambda/2 + E_t$ and $\chi_4 = \delta\lambda/2 + E_t$

$$F_{bb} = -\frac{\Delta_{bb}}{2E_b}(1 - 2n_F[E_b, T]), \quad (\text{A.36})$$

$$F_{tt} = \frac{\Delta_{tt}}{2E_t}n_F[\chi_2, T] - \frac{\Delta_{tt}}{2E_t}(1 - n_F[\chi_4, T]), \quad (\text{A.37})$$

$$G_{bb} = \frac{E_b - \xi_b}{2E_b}(1 - n_F[E_b, T]) + \frac{E_b + \xi_b}{2E_b}n_F[E_b, T], \quad (\text{A.38})$$

$$\begin{aligned} G_{tt} &= \frac{n_F[\chi_2, T](\chi_2 + \xi_t^{(h)})}{2E_t} + \frac{(1 - n_F[\chi_4, T])(\chi_4 - \xi_t^{(h)})}{2E_t} \\ &= \frac{E_t + \xi_t}{2E_t}n_F[\chi_2, T] + \frac{E_t - \xi_t}{2E_t}(1 - n_F[\chi_4, T]). \end{aligned} \quad (\text{A.39})$$

Appendix B

Density Response Function in the Superfluid State

The density response functions that appear in the screened interaction are introduced in Chapter 3. The normal and anomalous polarizabilities in presence of superfluidity are calculated as loops consisting of two normal or anomalous Green functions, respectively [76]:

$$\Pi_N^{nm,ij}(\mathbf{q}, \Omega) = \frac{T}{L^2} \sum_{\mathbf{k}, \omega} \mathcal{F}_{nm,ij}(\mathbf{k}, \mathbf{k} + \mathbf{q}) G_{nm}[i\omega + i\Omega, \mathbf{k} + \mathbf{q}] G_{ij}[i\omega, \mathbf{k}], \quad (\text{B.1})$$

$$\Pi_A^{nm,ij}(\mathbf{q}, \Omega) = \frac{T}{L^2} \sum_{\mathbf{k}, \omega} \mathcal{F}_{nm,ij}(\mathbf{k}, \mathbf{k} + \mathbf{q}) F_{nm}[i\omega + i\Omega, \mathbf{k} + \mathbf{q}] F_{ij}[i\omega, \mathbf{k}], \quad (\text{B.2})$$

where the $\{i, j, n, m\}$ indexes label the band of the system, T is the temperature, $\omega = k_B T(2n + 1)\pi$ are the fermionic Matsubara frequencies and $\Omega = k_B T 2n\pi$ are the bosonic Matsubara frequencies.

The total normal and anomalous polarizabilities are:

$$\Pi_N(\mathbf{q}, \Omega) = g_s g_v \sum_{n,m,i,j} \Pi_N^{nm,ij}(\mathbf{q}, \Omega), \quad (\text{B.3})$$

$$\Pi_A(\mathbf{q}, \Omega) = g_s g_v \sum_{n,m,i,j} \Pi_A^{nm,ij}(\mathbf{q}, \Omega). \quad (\text{B.4})$$

B.1 Double Bilayer Graphene Polarizabilities

In the specific case of Double Bilayer Graphene with intraband pairing and Josephson-like transfer, $n = m = \gamma$ ($i = j = \gamma'$) and the polarizabilities are:

$$\Pi_N^{\gamma\gamma'}(\mathbf{q}, \Omega) = \frac{T}{L^2} \sum_{\mathbf{k}, \omega} \mathcal{F}_{\gamma,\gamma'}(\mathbf{k}, \mathbf{k} + \mathbf{q}) G_{\gamma\gamma}[i\omega + i\Omega, \mathbf{k} + \mathbf{q}] G_{\gamma'\gamma'}[i\omega, \mathbf{k}], \quad (\text{B.5})$$

$$\Pi_A^{\gamma\gamma'}(\mathbf{q}, \Omega) = \frac{T}{L^2} \sum_{\mathbf{k}, \omega} \mathcal{F}_{\gamma,\gamma'}(\mathbf{k}, \mathbf{k} + \mathbf{q}) F_{\gamma\gamma}[i\omega + i\Omega, \mathbf{k} + \mathbf{q}] F_{\gamma'\gamma'}[i\omega, \mathbf{k}] \quad (\text{B.6})$$

The Green functions in terms of Bogoliubov amplitudes (Eq. (4.14)) are,

$$G_{\gamma\gamma}[i\omega, k] = \frac{u_\gamma^2(k)}{(i\hbar\omega - E_\gamma(k))} + \frac{v_\gamma^2(k)}{(i\hbar\omega + E_\gamma(k))}, \quad (\text{B.7})$$

$$F_{\gamma\gamma}[i\omega, k] = \frac{u_\gamma(k)v_\gamma(k)}{(i\hbar\omega - E_\gamma(k))} - \frac{u_\gamma(k)v_\gamma(k)}{(i\hbar\omega + E_\gamma(k))}.$$

In this system, Eqs. (B.5)-(B.6) become:

$$\begin{aligned} \Pi_N^{\gamma\gamma'}(\mathbf{q}, \Omega) = & \frac{T}{L^2} \sum_{\mathbf{k}, i\omega_n} \mathcal{F}_{\gamma, \gamma'}(\mathbf{k}, \mathbf{k}') \\ & \left[\frac{u_\gamma^2(k)}{(i\hbar\omega - E_\gamma(k))} \frac{u_{\gamma'}^2(k')}{(i\hbar\omega + i\Omega - E_{\gamma'}(k'))} + \frac{v_\gamma^2(k)}{(i\hbar\omega + E_\gamma(k))} \frac{u_{\gamma'}^2(k')}{(i\hbar\omega + i\Omega - E_{\gamma'}(k'))} \right. \\ & \left. + \frac{u_\gamma^2(k)}{(i\hbar\omega - E_\gamma(k))} \frac{v_{\gamma'}^2(k')}{(i\hbar\omega + i\Omega + E_{\gamma'}(k'))} + \frac{v_\gamma^2(k)}{(i\hbar\omega + E_\gamma(k))} \frac{v_{\gamma'}^2(k')}{(i\hbar\omega + i\Omega + E_{\gamma'}(k'))} \right], \end{aligned} \quad (\text{B.8})$$

$$\begin{aligned} \Pi_A^{\gamma\gamma'}(\mathbf{q}, \Omega) = & \frac{T}{L^2} \sum_{\mathbf{k}, i\omega_n} \mathcal{F}_{\gamma, \gamma'}(\mathbf{k}, \mathbf{k}') \\ & \left[\frac{u_\gamma(k)v_\gamma(k)}{(i\hbar\omega - E_\gamma(k))} \frac{u_{\gamma'}(k')v_{\gamma'}(k')}{(i\hbar\omega + i\Omega - E_{\gamma'}(k'))} - \frac{u_\gamma(k)v_\gamma(k)}{(i\hbar\omega + E_\gamma(k))} \frac{u_{\gamma'}(k')v_{\gamma'}(k')}{(i\hbar\omega + i\Omega - E_{\gamma'}(k'))} \right. \\ & \left. - \frac{u_\gamma(k)v_\gamma(k)}{(i\hbar\omega - E_\gamma(k))} \frac{u_{\gamma'}(k')v_{\gamma'}(k')}{(i\hbar\omega + i\Omega + E_{\gamma'}(k'))} + \frac{u_\gamma(k)v_\gamma(k)}{(i\hbar\omega + E_\gamma(k))} \frac{u_{\gamma'}(k')v_{\gamma'}(k')}{(i\hbar\omega + i\Omega + E_{\gamma'}(k'))} \right], \end{aligned} \quad (\text{B.9})$$

with $\mathbf{k}' = \mathbf{k} + \mathbf{q}$.

We work in the static limit, so $\Omega \rightarrow 0$. We divide the sum in four terms and we perform the sum over the Matsubara frequencies ω :

$$\begin{aligned} \Pi_N^{\gamma\gamma'}(\mathbf{q}) = & \frac{1}{L^2} \sum_{\mathbf{k}} \mathcal{F}_{\gamma, \gamma'}(\mathbf{k}, \mathbf{k}') \\ & \left[u_\gamma^2(k)u_{\gamma'}^2(k') \frac{n_F[E_\gamma(k), T] - n_F[E_{\gamma'}(k'), T]}{E_\gamma(k) - E_{\gamma'}(k')} + v_\gamma^2(k)u_{\gamma'}^2(k') \frac{1 - n_F[E_\gamma(k), T] - n_F[E_{\gamma'}(k'), T]}{-E_\gamma(k) - E_{\gamma'}(k')} \right. \\ & \left. + u_\gamma^2(k)v_{\gamma'}^2(k') \frac{1 - n_F[E_\gamma(k), T] - n_F[E_{\gamma'}(k'), T]}{-E_\gamma(k) - E_{\gamma'}(k')} + v_\gamma^2(k)v_{\gamma'}^2(k') \frac{n_F[E_\gamma(k), T] - n_F[E_{\gamma'}(k'), T]}{E_\gamma(k) - E_{\gamma'}(k')} \right], \end{aligned} \quad (\text{B.10})$$

$$\begin{aligned} \Pi_A^{\gamma\gamma'}(\mathbf{q}) = & \frac{1}{L^2} \sum_{\mathbf{k}} \mathcal{F}_{\gamma, \gamma'}(\mathbf{k}, \mathbf{k}') u_\gamma(k)v_\gamma(k)u_{\gamma'}(k')v_{\gamma'}(k') \\ & \left[\frac{n_F[E_\gamma(k), T] - n_F[E_{\gamma'}(k'), T]}{E_\gamma(k) - E_{\gamma'}(k')} - \frac{1 - n_F[E_\gamma(k), T] - n_F[E_{\gamma'}(k'), T]}{-E_\gamma(k) - E_{\gamma'}(k')} \right. \\ & \left. - \frac{1 - n_F[E_\gamma(k), T] - n_F[E_{\gamma'}(k'), T]}{-E_\gamma(k) - E_{\gamma'}(k')} + \frac{n_F[E_\gamma(k), T] - n_F[E_{\gamma'}(k'), T]}{E_\gamma(k) - E_{\gamma'}(k')} \right]. \end{aligned} \quad (\text{B.11})$$

After simplification we get:

$$\begin{aligned} \Pi_N^{\gamma\gamma'}(\mathbf{q}) = & \frac{1}{L^2} \sum_{\mathbf{k}} \mathcal{F}_{\gamma, \gamma'}(\mathbf{k}, \mathbf{k}') \left[\left(u_\gamma^2(k)u_{\gamma'}^2(k') + v_\gamma^2(k)v_{\gamma'}^2(k') \right) \frac{n_F[E_\gamma(k), T] - n_F[E_{\gamma'}(k'), T]}{E_\gamma(k) - E_{\gamma'}(k')} \right. \\ & \left. - \left(v_\gamma^2(k)u_{\gamma'}^2(k') + u_\gamma^2(k)v_{\gamma'}^2(k') \right) \frac{1 - n_F[E_\gamma(k), T] - n_F[E_{\gamma'}(k'), T]}{E_\gamma(k) + E_{\gamma'}(k')} \right], \end{aligned} \quad (\text{B.12})$$

$$\Pi_A^{\gamma\gamma'}(\mathbf{q}) = \frac{1}{L^2} \sum_{\mathbf{k}} \mathcal{F}_{\gamma,\gamma'}(\mathbf{k}, \mathbf{k}') 2 u_\gamma(k) v_\gamma(k) u_{\gamma'}(k') v_{\gamma'}(k') \left[\frac{n_F[E_\gamma(k), T] - n_F[E_{\gamma'}(k'), T]}{E_\gamma(k) - E_{\gamma'}(k')} + \frac{1 - n_F[E_\gamma(k), T] - n_F[E_{\gamma'}(k'), T]}{E_\gamma(k) + E_{\gamma'}(k')} \right]. \quad (\text{B.13})$$

Note that the first term of the $\Pi_N^{\gamma\gamma'}$ at $q = 0$ is proportional to the Density Of State, as in the normal state.

At zero temperature, the Fermi distribution is $n_F[E_\gamma(k), T] = 0$, so we obtain:

$$\Pi_N^{\gamma\gamma'}(\mathbf{q}) = -\frac{1}{L^2} \sum_{\mathbf{k}} \mathcal{F}_{\gamma,\gamma'}(\mathbf{k}, \mathbf{k}') \frac{v_\gamma^2(k) u_{\gamma'}^2(k') + u_\gamma^2(k) v_{\gamma'}^2(k')}{E_\gamma(k) + E_{\gamma'}(k')}, \quad (\text{B.14})$$

$$\Pi_A^{\gamma\gamma'}(\mathbf{q}) = \frac{1}{L^2} \sum_{\mathbf{k}} \mathcal{F}_{\gamma,\gamma'}(\mathbf{k}, \mathbf{k}') \frac{2 u_\gamma(k) v_\gamma(k) u_{\gamma'}(k') v_{\gamma'}(k')}{E_\gamma(k) + E_{\gamma'}(k')}. \quad (\text{B.15})$$

B.2 Double TMD monolayer Polarizabilities

In the specific case of double TMD monolayer with only intraband scattering allowed due to spin-orbit coupling, $n = m = i = j = \beta$, and the polarizability is:

$$\Pi_N^{\beta\beta}(\mathbf{q}, \Omega) = \frac{T}{L^2} \sum_{\mathbf{k}, \omega} \mathcal{F}_{\beta,\beta}(\mathbf{k}, \mathbf{k} + \mathbf{q}) G_{\beta\beta}[i\omega + i\Omega, \mathbf{k} + \mathbf{q}] G_{\beta\beta}[i\omega, \mathbf{k}], \quad (\text{B.16})$$

$$\Pi_A^{\beta\beta}(\mathbf{q}, \Omega) = \frac{T}{L^2} \sum_{\mathbf{k}, \omega} \mathcal{F}_{\beta,\beta}(\mathbf{k}, \mathbf{k} + \mathbf{q}) F_{\beta\beta}[i\omega + i\Omega, \mathbf{k} + \mathbf{q}] F_{\beta\beta}[i\omega, \mathbf{k}], \quad (\text{B.17})$$

with Green functions in terms of Bogoliubov amplitudes (Eq. (6.11)),

$$\begin{aligned} G_{bb}[i\omega, k] &= \frac{u_b^2(k)}{(i\hbar\omega - E_b(k))} + \frac{v_b^2(k)}{(i\hbar\omega + E_b(k))}, \\ G_{tt}[i\omega, k] &= \frac{u_t^2(k)}{(i\hbar\omega - \chi_2(k))} + \frac{v_t^2(k)}{(i\hbar\omega + \chi_4(k))}, \\ F_{bb}[i\omega, k] &= \frac{u_b(k)v_b(k)}{(i\hbar\omega - E_b(k))} - \frac{u_b(k)v_b(k)}{(i\hbar\omega + E_b(k))}, \\ F_{tt}[i\omega, k] &= \frac{u_t(k)v_t(k)}{(i\hbar\omega - \chi_2(k))} - \frac{u_t(k)v_t(k)}{(i\hbar\omega + \chi_4(k))}, \end{aligned} \quad (\text{B.18})$$

where $\chi_2 = -\delta\lambda/2 + E_t$ and $\chi_4 = \delta\lambda/2 + E_t$.

For this system, Eqs. (B.5)-(B.6) become:

$$\Pi_N^{bb}(\mathbf{q}, \Omega) = \frac{T}{L^2} \sum_{\mathbf{k}, \omega} \mathcal{F}_{b,b}(\mathbf{k}, \mathbf{k}') \left[\frac{u_b^2(k)}{(i\hbar\omega - E_b(k))} \frac{u_b^2(k')}{(i\hbar\omega + i\Omega - E_b(k'))} + \frac{v_b^2(k)}{(i\hbar\omega + E_b(k))} \frac{u_b^2(k')}{(i\hbar\omega + i\Omega - E_b(k'))} + \frac{u_b^2(k)}{(i\hbar\omega - E_b(k))} \frac{v_b^2(k')}{(i\hbar\omega + i\Omega + E_b(k'))} + \frac{v_b^2(k)}{(i\hbar\omega + E_b(k))} \frac{v_b^2(k')}{(i\hbar\omega + i\Omega + E_b(k'))} \right], \quad (\text{B.19})$$

$$\begin{aligned}
 \Pi_N^{tt}(\mathbf{q}, \Omega) &= \frac{T}{L^2} \sum_{\mathbf{k}, \omega} \mathcal{F}_{t,t}(\mathbf{k}, \mathbf{k}') \\
 &= \left[\frac{u_t^2(k)}{(i\hbar\omega - \chi_2(k))} \frac{u_t^2(k')}{(i\hbar\omega + i\Omega - \chi_2(k'))} + \frac{v_t^2(k)}{(i\hbar\omega + \chi_4(k))} \frac{u_t^2(k')}{(i\hbar\omega + i\Omega - \chi_2(k'))} \right. \\
 &\quad \left. + \frac{u_t^2(k)}{(i\hbar\omega - \chi_2(k))} \frac{v_t^2(k')}{(i\hbar\omega + i\Omega + \chi_4(k'))} + \frac{v_t^2(k)}{(i\hbar\omega + \chi_4(k))} \frac{v_t^2(k')}{(i\hbar\omega + i\Omega + \chi_4(k'))} \right], \tag{B.20}
 \end{aligned}$$

$$\begin{aligned}
 \Pi_A^{bb}(\mathbf{q}, \Omega) &= \frac{T}{L^2} \sum_{\mathbf{k}, \omega} \mathcal{F}_{b,b}(\mathbf{k}, \mathbf{k}') \\
 &= \left[\frac{u_b(k)v_b(k)}{(i\hbar\omega - E_b(k))} \frac{u_b(k')v_b(k')}{(i\hbar\omega + i\Omega - E_b(k'))} - \frac{u_b(k)v_b(k)}{(i\hbar\omega + E_b(k))} \frac{u_b(k')v_b(k')}{(i\hbar\omega + i\Omega - E_b(k'))} \right. \\
 &\quad \left. - \frac{u_b(k)v_b(k)}{(i\hbar\omega - E_b(k))} \frac{u_b(k')v_b(k')}{(i\hbar\omega + i\Omega + E_b(k'))} + \frac{u_b(k)v_b(k)}{(i\hbar\omega + E_b(k))} \frac{u_b(k')v_b(k')}{(i\hbar\omega + i\Omega + E_b(k'))} \right], \tag{B.21}
 \end{aligned}$$

$$\begin{aligned}
 \Pi_A^{tt}(\mathbf{q}, \Omega) &= \frac{T}{L^2} \sum_{\mathbf{k}, \omega} \mathcal{F}_{t,t}(\mathbf{k}, \mathbf{k}') \\
 &= \left[\frac{u_t(k)v_t(k)}{(i\hbar\omega - \chi_2(k))} \frac{u_t(k')v_t(k')}{(i\hbar\omega + i\Omega - \chi_2(k'))} - \frac{u_t(k)v_t(k)}{(i\hbar\omega + \chi_4(k))} \frac{u_t(k')v_t(k')}{(i\hbar\omega + i\Omega - \chi_2(k'))} \right. \\
 &\quad \left. - \frac{u_t(k)v_t(k)}{(i\hbar\omega - \chi_2(k))} \frac{u_t(k')v_t(k')}{(i\hbar\omega + i\Omega + \chi_4(k'))} + \frac{u_t(k)v_t(k)}{(i\hbar\omega + \chi_4(k))} \frac{u_t(k')v_t(k')}{(i\hbar\omega + i\Omega + \chi_4(k'))} \right], \tag{B.22}
 \end{aligned}$$

with $\mathbf{k}' = \mathbf{k} + \mathbf{q}$.

We work in the static limit, so $\Omega \rightarrow 0$. We divide the sum in four terms, we perform the sum over the Matsubara frequencies ω :

$$\begin{aligned}
 \Pi_N^{bb}(\mathbf{q}) &= \frac{1}{L^2} \sum_{\mathbf{k}} \mathcal{F}_{b,b}(\mathbf{k}, \mathbf{k}') \\
 &= \left[u_b^2(k)u_b^2(k') \frac{n_F[E_b(k), T] - n_F[E_b(k'), T]}{E_b(k) - E_b(k')} + v_b^2(k)u_b^2(k') \frac{1 - n_F[E_b(k), T] - n_F[E_b(k'), T]}{-E_b(k) - E_b(k')} \right. \\
 &\quad \left. + u_b^2(k)v_b^2(k') \frac{1 - n_F[E_b(k), T] - n_F[E_b(k'), T]}{-E_b(k) - E_b(k')} + v_b^2(k)v_b^2(k') \frac{n_F[E_b(k), T] - n_F[E_b(k'), T]}{E_b(k) - E_b(k')} \right], \tag{B.23}
 \end{aligned}$$

$$\begin{aligned}
 \Pi_N^{tt}(\mathbf{q}) &= \frac{1}{L^2} \sum_{\mathbf{k}} \mathcal{F}_{t,t}(\mathbf{k}, \mathbf{k}') \\
 &= \left[u_t^2(k)u_t^2(k') \frac{n_F[\chi_2(k), T] - n_F[\chi_2(k'), T]}{\chi_2(k) - \chi_2(k')} + v_t^2(k)u_t^2(k') \frac{1 - n_F[\chi_4(k), T] - n_F[\chi_2(k'), T]}{-\chi_4(k) - \chi_2(k')} \right. \\
 &\quad \left. + u_t^2(k)v_t^2(k') \frac{1 - n_F[\chi_2(k), T] - n_F[\chi_4(k'), T]}{-\chi_2(k) - \chi_4(k')} + v_t^2(k)v_t^2(k') \frac{n_F[\chi_4(k), T] - n_F[\chi_4(k'), T]}{\chi_4(k) - \chi_4(k')} \right], \tag{B.24}
 \end{aligned}$$

$$\begin{aligned} \Pi_A^{bb}(\mathbf{q}) &= \frac{1}{L^2} \sum_{\mathbf{k}} \mathcal{F}_{b,b}(\mathbf{k}, \mathbf{k}') u_b(k) v_b(k) u_b(k') v_b(k') \\ &\left[\frac{n_F[E_b(k), T] - n_F[E_b(k'), T]}{E_b(k) - E_b(k')} - \frac{1 - n_F[E_b(k), T] - n_F[E_b(k'), T]}{-E_b(k) - E_b(k')} \right. \\ &\left. - \frac{1 - n_F[E_b(k), T] - n_F[E_b(k'), T]}{-E_b(k) - E_b(k')} + \frac{n_F[E_b(k), T] - n_F[E_b(k'), T]}{E_b(k) - E_b(k')} \right], \end{aligned} \quad (\text{B.25})$$

$$\begin{aligned} \Pi_A^{tt}(\mathbf{q}) &= \frac{1}{L^2} \sum_{\mathbf{k}} \mathcal{F}_{t,t}(\mathbf{k}, \mathbf{k}') u_t(k) v_t(k) u_t(k') v_t(k') \\ &\left[\frac{n_F[\chi_2(k), T] - n_F[\chi_2(k'), T]}{\chi_2(k) - \chi_2(k')} - \frac{1 - n_F[\chi_4(k), T] - n_F[\chi_2(k'), T]}{-\chi_4(k) - \chi_2(k')} \right. \\ &\left. - \frac{1 - n_F[\chi_2, T] - n_F[\chi_4(k'), T]}{-\chi_2(k) - \chi_4(k')} + \frac{n_F[\chi_4, T] - n_F[\chi_4(k'), T]}{\chi_4(k) - \chi_4(k')} \right]. \end{aligned} \quad (\text{B.26})$$

After simplification we get:

$$\begin{aligned} \Pi_N^{bb}(\mathbf{q}) &= \frac{1}{L^2} \sum_{\mathbf{k}} \mathcal{F}_{b,b}(\mathbf{k}, \mathbf{k}') \left[(u_b^2(k) u_b^2(k') + v_b^2(k) v_b^2(k')) \frac{n_F[E_b(k), T] - n_F[E_b(k'), T]}{E_b(k) - E_b(k')} \right. \\ &\left. - (v_b^2(k) u_b^2(k') + u_b^2(k) v_b^2(k')) \frac{1 - n_F[E_b(k), T] - n_F[E_b(k'), T]}{E_b(k) + E_b(k')} \right], \end{aligned} \quad (\text{B.27})$$

$$\begin{aligned} \Pi_N^{tt}(\mathbf{q}) &= \frac{1}{L^2} \sum_{\mathbf{k}} \mathcal{F}_{t,t}(\mathbf{k}, \mathbf{k}') \\ &\left[u_t^2(k) u_t^2(k') \frac{n_F[\chi_2(k), T] - n_F[\chi_2(k'), T]}{E_t(k) - E_t(k')} - v_t^2(k) u_t^2(k') \frac{1 - n_F[\chi_4(k), T] - n_F[\chi_2(k'), T]}{E_t(k) + E_t(k')} \right. \\ &\left. - u_t^2(k) v_t^2(k') \frac{1 - n_F[\chi_2(k), T] - n_F[\chi_4(k'), T]}{E_t(k) + E_t(k')} + v_t^2(k) v_t^2(k') \frac{n_F[\chi_4(k), T] - n_F[\chi_4(k'), T]}{E_t(k) - E_t(k')} \right], \end{aligned} \quad (\text{B.28})$$

$$\begin{aligned} \Pi_A^{bb}(\mathbf{q}) &= \frac{1}{L^2} \sum_{\mathbf{k}} \mathcal{F}_{b,b}(\mathbf{k}, \mathbf{k}') 2 u_b(k) v_b(k) u_b(k') v_b(k') \\ &\left[\frac{n_F[E_b(k), T] - n_F[E_b(k'), T]}{E_b(k) - E_b(k')} + \frac{1 - n_F[E_b(k), T] - n_F[E_b(k'), T]}{E_b(k) + E_b(k')} \right], \end{aligned} \quad (\text{B.29})$$

$$\begin{aligned} \Pi_A^{tt}(\mathbf{q}) &= \frac{1}{L^2} \sum_{\mathbf{k}} \mathcal{F}_{t,t}(\mathbf{k}, \mathbf{k}') u_t(k) v_t(k) u_t(k') v_t(k') \\ &\left[\frac{1}{E_t(k) - E_t(k')} (n_F[\chi_2(k), T] - n_F[\chi_2(k'), T] + n_F[\chi_4(k), T] - n_F[\chi_4(k'), T]) \right. \\ &\left. \frac{1}{E_t(k) + E_t(k')} (2 - n_F[\chi_4(k), T] - n_F[\chi_2(k'), T] - n_F[\chi_2(k'), T] - n_F[\chi_4(k'), T]) \right]. \end{aligned} \quad (\text{B.30})$$

At zero temperature, the Fermi distributions, $n_F[E_b, 0] = 0$, $n_F[\chi_4, 0] = 0$, and $n_F[\chi_2, 0] = 1 - \theta[E_t(k) - \frac{\delta\lambda}{2}]$.

For the bottom band polarizability we recover the one-band expression [10]:

$$\Pi_N^{bb}(\mathbf{q}) = -\frac{1}{L^2} \sum_{\mathbf{k}} \mathcal{F}_{b,b}(\mathbf{k}, \mathbf{k}') \frac{v_b^2(k)u_b^2(k') + u_b^2(k)v_b^2(k')}{E_b(k) + E_b(k')}, \quad (\text{B.31})$$

$$\Pi_A^{bb}(q, \Omega) = \frac{1}{L^2} \sum_{\mathbf{k}} \mathcal{F}_{b,b}(\mathbf{k}, \mathbf{k}') \frac{2u_b(k)v_b(k)u_b(k')v_b(k')}{E_b(k) + E_b(k')}, \quad (\text{B.32})$$

while for the top bands we obtain:

$$\begin{aligned} \Pi_N^{tt}(\mathbf{q}) = & -\frac{1}{L^2} \sum_{\mathbf{k}} \mathcal{F}_{t,t}(\mathbf{k}, \mathbf{k}') \left[u_t^2(k)u_t^2(k') \frac{\theta[E_t(k) - \frac{\delta\lambda}{2}] - \theta[E_t(k') - \frac{\delta\lambda}{2}]}{E_t(k) - E_t(k')} \right. \\ & \left. + v_t^2(k)u_t^2(k') \frac{\theta[E_t(k') - \frac{\delta\lambda}{2}]}{E_t(k) + E_t(k')} + u_t^2(k)v_t^2(k') \frac{\theta[E_t(k) - \frac{\delta\lambda}{2}]}{E_t(k) + E_t(k')} \right], \end{aligned} \quad (\text{B.33})$$

$$\begin{aligned} \Pi_A^{tt}(\mathbf{q}) = & \frac{1}{L^2} \sum_{\mathbf{k}} \mathcal{F}_{t,t}(\mathbf{k}, \mathbf{k}') u_t(k)v_t(k)u_t(k')v_t(k') \\ & \frac{\theta[E_t(\mathbf{k}) - \frac{\delta\lambda}{2}] + \theta[E_t(\mathbf{k}') - \frac{\delta\lambda}{2}]}{E_t(k) + E_t(k')} - \frac{\theta[E_t(\mathbf{k}) - \frac{\delta\lambda}{2}] - \theta[E_t(\mathbf{k}') - \frac{\delta\lambda}{2}]}{E_t(k) - E_t(k')}. \end{aligned} \quad (\text{B.34})$$

In the limit of small misalignment $\delta\lambda \rightarrow 0$, the theta function $\theta[E_t(k)] = 1$, so the polarizability in the top bands go to the familiar expression.

Appendix C

Two-Body Binding Energy

This Appendix contains the explicit calculation of the two-body binding energy E_B . The solutions of this calculations give the value of the chemical potential μ in the limit of zero density for the different systems investigated in Chapter 4 (Fig. 4.6), Chapters 5 (Fig. 5.9, Table 5.1) and Chapter 6 (Fig. 6.5 and Table 6.3).

In order to obtain the two-body binding energy E_B we solve the two-body Schroedinger Equation for a one-band model. The Hamiltonian of the system is

$$H = H_e + H_h + H_{eh}, \quad (\text{C.1})$$

and the binding energy is the eigenvalue $E_B = E_e + E_h - E_{eh}$. As explained in Chapter 3 we neglect the intralayer interactions so $E_e = 0$, $E_h = 0$ and $E_B = -E_{eh}$.

$$H_{eh} = -\frac{\hbar^2}{2m_r} \left(\frac{\partial^2}{\partial \rho^2} + \frac{1}{\rho} \frac{\partial}{\partial \rho} + \frac{1}{\rho^2} \frac{\partial^2}{\partial \phi^2} \right) - \frac{e^2}{4\pi\epsilon\epsilon_0\sqrt{\rho^2 + d^2}}, \quad (\text{C.2})$$

with m_r reduced mass, d distance between the carriers and ϵ the dielectric constant of the barrier.

We evaluate E_{eh} using a variational approach with parameter α :

$$E_{eh} = \int d^2\rho \phi_\alpha(\rho) H_{eh} \phi_\alpha(\rho), \quad (\text{C.3})$$

with variational wave function

$$\phi_\alpha(\rho) = N e^{-\frac{\sqrt{\rho^2 + d^2}}{\alpha}} \rightarrow N = \sqrt{\frac{2}{\pi}} e^{d/\alpha} \frac{1}{\alpha \sqrt{1 + \frac{2d}{\alpha}}}. \quad (\text{C.4})$$

We obtain in this way $E_{eh}(\alpha)$. The numerical value E_B corresponds to the minimum of $-E_{eh}(\alpha)$.

C.1 Double Bilayer Graphene Binding Energy

To obtain E_B for DBG as we show in Chapter 4 we simply include the band gap E_g in Eq. (C.2):

$$H_{eh} = -\frac{\hbar^2}{2m_r} \left(\frac{\partial^2}{\partial \rho^2} + \frac{1}{\rho} \frac{\partial}{\partial \rho} + \frac{1}{\rho^2} \frac{\partial^2}{\partial \phi^2} \right) - \frac{e^2}{4\pi\epsilon\sqrt{\rho^2 + d^2}} + E_g, \quad (\text{C.5})$$

Equation (C.3) is evaluated for different values of E_g with $m^{(e)} = m^{(h)} = 0.04m_e$, $d = 1$ nm and $\epsilon = 2$. The numerical values $E_B/2$ are listed in Table 5.1.

The binding energy in Chapter 5 is calculated including the effect of the screening.

$$H_{eh} = -\frac{\hbar^2}{2m_r} \left(\frac{\partial^2}{\partial \rho^2} + \frac{1}{\rho} \frac{\partial}{\partial \rho} + \frac{1}{\rho^2} \frac{\partial^2}{\partial \phi^2} \right) - V_{eh}(\rho) + E_g, \quad (\text{C.6})$$

where $V_{eh}(\rho)$ is the Fourier transform of $V_{eh}(q)$ (Eq. (5.2)) in the zero density limit for the corresponding E_g . Equation (C.3) is evaluated with $m^{(e)} = m^{(h)} = 0.04$, $d = 1$ nm and $\epsilon = 2$. The numerical values $E_B/2$ are listed in Table 5.1.

C.2 Double TMD monolayer Binding Energy

To obtain E_B for Double TMD Monolayers as we show in Chapter 6 we use Eq. (C.2). The different values in Table 6.3 are the result of the evaluation of Eq. (C.3) using the values of the masses from Table 6.1, $d = 1$ nm and $\epsilon = 2$.

Bibliography

- ¹H. K. Onnes, “The resistance of pure mercury at helium temperatures”, *Commun. Phys. Lab. Univ. Leiden* **12**, 120 (1911).
- ²J. F. Allen and A. D. Misener, “Flow phenomena in liquid helium II”, *Nature* **142**, 643 (1938).
- ³P. Kapitza, “Viscosity of liquid helium below the λ -point”, *Nature* **141**, 74 (1938).
- ⁴J. M. Blatt, K. W. Böer, and W. Brandt, “Bose-Einstein condensation of excitons”, *Phys. Rev.* **126**, 1691 (1962).
- ⁵Y. E. Lozovik and V. I. Yudson, “Feasibility of superfluidity of paired spatially separated electrons and holes”, *JETP Lett. (USSR)* **22**, (Pis’ma Zh. Eksp. Teor. Fiz. **22**, 556 (1975)), 274 (1975).
- ⁶J. P. Eisenstein and A. H. MacDonald, “Bose-Einstein condensation of excitons in bilayer electron systems”, *Nature* **432**, 691 (2004).
- ⁷A. A. High, J. R. Leonard, A. T. Hammack, M. M. Fogler, L. V. Butov, A. V. Kavokin, K. L. Campman, and A. C. Gossard, “Spontaneous coherence in a cold exciton gas”, *Nature* **483**, 584 (2012).
- ⁸K. S. Novoselov, A. K. Geim, S. V. Morozov, D. Jiang, Y. Zhang, S. V. Dubonos, I. V. Grigorieva, and A. A. Firsov, “Electric field effect in atomically thin carbon films”, *Science* **306**, 666 (2004).
- ⁹Y. E. Lozovik and A. A. Sokolik, “Electron-hole pair condensation in a graphene bilayer”, *JETP Lett* **87**, 55 (2008).
- ¹⁰A. Perali, D. Neilson, and A. R. Hamilton, “High-temperature superfluidity in double-bilayer graphene”, *Phys. Rev. Lett.* **110**, 146803 (2013).
- ¹¹M. M. Fogler, L. V. Butov, and K. S. Novoselov, “High-temperature superfluidity with indirect excitons in van der Waals heterostructures”, *Nat. Commun.* **5**, 4555 (2014).
- ¹²M. V. Milošević and A. Perali, “Emergent phenomena in multicomponent superconductivity: an introduction to the focus issue”, *Supercond. Sci. Techn.* **28**, 060201 (2015).
- ¹³G. W. Burg, N. Prasad, K. Kim, T. Taniguchi, K. Watanabe, A. H. MacDonald, L. F. Register, and E. Tutuc, “Strongly enhanced tunneling at total charge neutrality in double-bilayer graphene-WSe₂ heterostructures”, *Phys. Rev. Lett.* **120**, 177702 (2018).
- ¹⁴Z. Wang, D. A. Rhodes, K. Watanabe, T. Taniguchi, J. C. Hone, J. Shan, and K. F. Mak, “Evidence of high-temperature exciton condensation in two-dimensional atomic double layers”, *Nature* **574**, 76 (2019).
- ¹⁵S. Conti, A. Perali, F. M. Peeters, and D. Neilson, “Multicomponent electron-hole superfluidity and the BCS-BEC crossover in double bilayer graphene”, *Phys. Rev. Lett.* **119**, 257002 (2017).
- ¹⁶S. Conti, A. Perali, D. Neilson, and F. M. Peeters, “Tuning the BEC-BCS crossover in electron-hole double bilayer graphene superfluidity using multiband effects.”, *Belgian Physical Society Magazine* **03**, 6 (2017).

- ¹⁷S. Conti, A. Perali, F. M. Peeters, and D. Neilson, "Multicomponent screening and superfluidity in gapped electron-hole double bilayer graphene with realistic bands", *Phys. Rev. B* **99**, 144517 (2019).
- ¹⁸S. Conti, M. V. der Donck, A. Perali, F. M. Peeters, and D. Neilson, *A doping-dependent switch from one- to two-component superfluidity at temperature above 100K in coupled electron-hole Van der Waals heterostructures*, 2019.
- ¹⁹S. Conti, D. Neilson, F. M. Peeters, and A. Perali, "Transition metal dichalcogenides as strategy for high temperature electron-hole superfluidity", *Condens. Matter* **5**, 22 (2020).
- ²⁰M. Zarenia, S. Conti, F. M. Peeters, and D. Neilson, "Coulomb drag in strongly coupled quantum wells: temperature dependence of the many-body correlations", *App. Phys. Lett.* **115**, 202105 (2019).
- ²¹M. V. der Donck, S. Conti, A. Perali, A. R. Hamilton, B. Partoens, F. M. Peeters, and D. Neilson, *Three-dimensional electron-hole superfluidity in a superlattice close to room temperature*, 2019.
- ²²S. Saberi-Pouya, S. Conti, A. Perali, A. F. Croxall, A. R. Hamilton, F. M. Peeters, and D. Neilson, "Experimental conditions for the observation of electron-hole superfluidity in gas heterostructures", *Phys. Rev. B* **101**, 140501 (2020).
- ²³Fonds Wetenschappelijk Onderzoek - Vlaanderen, <https://www.fwo.be/nl/>.
- ²⁴P. Nozières and S. Schmitt-Rink, "Bose condensation in an attractive fermion gas: from weak to strong coupling superconductivity", *Journal of Low Temperature Physics* **59**, 195 (1985).
- ²⁵J. Bardeen, L. N. Cooper, and J. R. Schrieffer, "Theory of superconductivity", *Phys. Rev.* **108**, 1175 (1957).
- ²⁶L. N. Cooper, "Microscopic quantum interference effects in the theory of superconductivity", in *Nobel lectures*, edited by S. Lundqvist, Physics 1971-1980 (World Scientific Publishing Co., 1992), p. 73.
- ²⁷I. Giaever, "Energy gap in superconductors measured by electron tunneling", *Phys. Rev. Lett.* **5**, 147 (1960).
- ²⁸W. Zwerger, *The BCS-BEC crossover and the unitary Fermi gas*, Vol. 836 (Springer Science & Business Media, 2011).
- ²⁹M. H. Anderson, J. R. Ensher, M. R. Matthews, C. E. Wieman, and E. A. Cornell, "Observation of Bose-Einstein condensation in a dilute atomic vapor", *Science* **269**, 198 (1995).
- ³⁰C. A. Regal, M. Greiner, and D. S. Jin, "Observation of resonance condensation of fermionic atom pairs", *Phys. Rev. Lett.* **92**, 040403 (2004).
- ³¹M. W. Zwierlein, C. A. Stan, C. H. Schunck, S. M. F. Raupach, A. J. Kerman, and W. Ketterle, "Condensation of pairs of fermionic atoms near a Feshbach resonance", *Phys. Rev. Lett.* **92**, 120403 (2004).
- ³²J. R. Engelbrecht, M. Randeria, and C. A. R. Sáde Melo, "BCS to Bose crossover: broken-symmetry state", *Phys. Rev. B* **55**, 15153 (1997).
- ³³L. V. Keldysh and A. N. Kozlov, "Collective properties of excitons in semiconductors", *Sov. Phys. JETP* **27**, 521 (1968).
- ³⁴C. Comte and P. Nozières, "Exciton Bose condensation : The ground state of an electron-hole gas - I. Mean field description of a simplified model", *J. Phys. France* **43**, 1069 (1982).

- ³⁵P. Nozières and C. Comte, "Exciton Bose condensation : the ground state of an electron-hole gas - II. Spin states, screening and band structure effects", *J. Phys. France* **43**, 1083 (1982).
- ³⁶S. G. Tikhodeev, G. A. Kopelevich, and N. A. Gippius, "Exciton transport in Cu_2O : Phonon wind versus superfluidity", *Phys. Status Solidi B* **206**, 45 (1998).
- ³⁷J. I. Jang and J. P. Wolfe, "Auger recombination and biexcitons in Cu_2O : A case for dark excitonic matter", *Phys. Rev. B* **74**, 045211 (2006).
- ³⁸X. Zhu, P. B. Littlewood, M. S. Hybertsen, and T. M. Rice, "Exciton condensate in semiconductor quantum well structures", *Phys. Rev. Lett.* **74**, 1633 (1995).
- ³⁹Y. E. Lozovik and V. I. Yudson, "A new mechanism for superconductivity: pairing between spatially separated electrons and holes", *Sov. Phys. JETP* **44**, (Zh. Eksp. Teor. Fiz. **71**, 738 (1976)), 389 (1976).
- ⁴⁰K. S. Novoselov, D. Jiang, F. Schedin, T. J. Booth, V. V. Khotkevich, S. V. Morozov, and A. K. Geim, "Two-dimensional atomic crystals", *Proc. Natl. Acad. Sci. U.S.A* **102**, 10451 (2005).
- ⁴¹S. De Palo, F. Rapisarda, and G. Senatore, "Excitonic condensation in a symmetric electron-hole bilayer", *Phys. Rev. Lett.* **88**, 206401 (2002).
- ⁴²D. Neilson, A. Perali, and A. R. Hamilton, "Excitonic superfluidity and screening in electron-hole bilayer systems", *Phys. Rev. B* **89**, 060502 (2014).
- ⁴³J. P. Eisenstein, L. N Pfeiffer, and K. W. West, "Independently contacted two-dimensional electron systems in double quantum wells", *Appl. Phys. Lett.* **57**, 2324 (1990).
- ⁴⁴B. N. Narozhny and A. Levchenko, "Coulomb drag", *Rev. Mod. Phys.* **88**, 025003 (2016).
- ⁴⁵T. J. Gramila, J. P. Eisenstein, A. H. MacDonald, L. N. Pfeiffer, and K. W. West, "Mutual friction between parallel two-dimensional electron systems", *Phys. Rev. Lett.* **66**, 1216 (1991).
- ⁴⁶D. Nandi, A. D. K. Finck, J. P. Eisenstein, L. N. Pfeiffer, and K. W. West, "Exciton condensation and perfect Coulomb drag", *Nature* **488**, 481 (2012).
- ⁴⁷G. Vignale and A. H. MacDonald, "Drag in paired electron-hole layers", *Phys. Rev. Lett.* **76**, 2786 (1996).
- ⁴⁸L. Świerkowski, J. Szymański, and Z. W. Gortel, "Coupled electron-hole transport: beyond the mean field approximation", *Phys. Rev. Lett.* **74**, 3245 (1995).
- ⁴⁹I. B. Spielman, J. P. Eisenstein, L. N. Pfeiffer, and K. W. West, "Resonantly enhanced tunneling in a double layer quantum Hall ferromagnet", *Phys. Rev. Lett.* **84**, 5808 (2000).
- ⁵⁰T. Huber, A. Zrenner, W. Wegscheider, and M. Bichler, "Electrostatic exciton traps", *Phys. Status Solidi. A* **166**, R5 (1998).
- ⁵¹D. P. Trauernicht, A. Mysyrowicz, and J. P. Wolfe, "Strain confinement and thermodynamics of free excitons in a direct-gap semiconductor", *Phys. Rev. B* **28**, 3590 (1983).
- ⁵²K. Brunner, U. Bockelmann, G. Abstreiter, M. Walther, G. Böhm, G. Tränkle, and G. Weimann, "Photoluminescence from a single GaAs/AlGaAs quantum dot", *Phys. Rev. Lett.* **69**, 3216 (1992).
- ⁵³P. C. M. Christianen, F. Piazza, J. G. S. Lok, J. C. Maan, and W. Van der Vleuten, "Magnetic trap for excitons", *Phys. B: Cond. Matter* **249**, 624 (1998).
- ⁵⁴A. T. Hammack, M. Griswold, L. V. Butov, L. E. Smallwood, A. L. Ivanov, and A. C. Gossard, "Trapping of cold excitons in quantum well structures with laser light", *Phys. Rev. Lett.* **96**, 227402 (2006).

- ⁵⁵L. V. Butov, A. C. Gossard, and D. S. Chemla, "Macroscopically ordered state in an exciton system", *Nature* **418**, 751 (2002).
- ⁵⁶V. B. Timofeev and A. V. Gorbunov, "Collective state of the Bose gas of interacting dipolar excitons", *J. Appl. Phys.* **101**, 081708 (2007).
- ⁵⁷M. Combescot, O. Betbeder-Matibet, and R. Combescot, "Bose-Einstein condensation in semiconductors: the key role of dark excitons", *Phys. Rev. Lett.* **99**, 176403 (2007).
- ⁵⁸R. Anankine, M. Beian, S. Dang, M. Alloing, E. Cambril, K. Merghem, C. G. Carbonell, A. Lemaître, and F. Dubin, "Quantized vortices and four-component superfluidity of semiconductor excitons", *Phys. Rev. Lett.* **118**, 127402 (2017).
- ⁵⁹Y. J. Chen, E. S. Koteles, B. S. Elman, and C. A. Armiento, "Effect of electric fields on excitons in a coupled double-quantum-well structure", *Phys. Rev. B* **36**, 4562 (1987).
- ⁶⁰A. F. Croxall, K. Das Gupta, C. A. Nicoll, M. Thangaraj, H. E. Beere, I. Farrer, D. A. Ritchie, and M. Pepper, "Anomalous Coulomb drag in electron-hole bilayers", *Phys. Rev. Lett.* **101**, 246801 (2008).
- ⁶¹J. A. Seamons, C. P. Morath, J. L. Reno, and M. P. Lilly, "Coulomb drag in the exciton regime in electron-hole bilayers", *Phys. Rev. Lett.* **102**, 026804 (2009).
- ⁶²A. A. High, J. R. Leonard, M. Remeika, L. V. Butov, M. Hanson, and A. C. Gossard, "Condensation of excitons in a trap", *Nano Lett.* **12**, 2605 (2012).
- ⁶³P. Pieri, D. Neilson, and G. C. Strinati, "Effects of density imbalance on the BCS-BEC crossover in semiconductor electron-hole bilayers", *Phys. Rev. B* **75**, 113301 (2007).
- ⁶⁴P. Fulde and R. A. Ferrell, "Superconductivity in a strong spin-exchange field", *Phys. Rev.* **135**, A550 (1964).
- ⁶⁵G. Sarma, "On the influence of a uniform exchange field acting on the spins of the conduction electrons in a superconductor", *J. Phys. Chem. Solids* **24**, 1029 (1963).
- ⁶⁶J. J. Kinnunen, J. E. Baarsma, J.-P. Martikainen, and P. Törmä, "The Fulde-Ferrell-Larkin-Ovchinnikov state for ultracold fermions in lattice and harmonic potentials: a review", *Rep. Prog. Phys.* **81**, 046401 (2018).
- ⁶⁷C. Ravensbergen, V. Corre, E. Soave, M. Kreyer, E. Kirilov, and R. Grimm, "Production of a degenerate Fermi-Fermi mixture of dysprosium and potassium atoms", *Phys. Rev. A* **98**, 063624 (2018).
- ⁶⁸B. Frank, J. Lang, and W. Zwerger, "Universal phase diagram and scaling functions of imbalanced Fermi gases", *J. Exp. Theor. Phys.* **127**, 812 (2018).
- ⁶⁹C. R. Dean, A. F. Young, I. Meric, C. Lee, L. Wang, S. Sorgenfrei, K. Watanabe, T. Taniguchi, P. Kim, K. L. Shepard, and J. Hone, "Boron nitride substrates for high-quality graphene electronics", *Nat. Nanotechnol.* **5**, 722 (2010).
- ⁷⁰L. Britnell, R. V. Gorbachev, R. Jalil, B. D. Belle, F. Schedin, M. I. Katsnelson, L. Eaves, S. V. Morozov, A. S. Mayorov, N. M. R. Peres, A. H. Castro Neto, J. Leist, A. K. Geim, L. A. Ponomarenko, and K. S. Novoselov, "Electron tunneling through ultrathin Boron Nitride crystalline barriers", *Nano Lett.* **12**, 1707 (2012).
- ⁷¹H. Min, R. Bistritzer, J.-J. Su, and A. H. MacDonald, "Room-temperature superfluidity in graphene bilayers", *Phys. Rev. B* **78**, 121401 (2008).
- ⁷²A. K. Geim and I. V. Grigorieva, "Van der Waals heterostructures", *Nature (London)* **499**, 419 (2013).
- ⁷³K. S. Novoselov, A. Mishchenko, A. Carvalho, and A. H. Castro Neto, "2D materials and van der Waals heterostructures", *Science* **353**, aac9439 (2016).

- ⁷⁴A. H. Castro Neto, F. Guinea, N. M. R. Peres, K. S. Novoselov, and A. K. Geim, "The electronic properties of graphene", *Rev. Mod. Phys.* **81**, 109 (2009).
- ⁷⁵K. S. Novoselov and A. K. Geim, "The rise of graphene", *Nat. Mater* **6**, 183 (2007).
- ⁷⁶Y. E. Lozovik, S. L. Ogarkov, and A. A. Sokolik, "Condensation of electron-hole pairs in a two-layer graphene system: Correlation effects", *Phys. Rev. B* **86**, 045429 (2012).
- ⁷⁷R. V. Gorbachev, A. K. Geim, M. I. Katsnelson, K. S. Novoselov, T. Tudorovskiy, I. V. Grigorieva, A. H. MacDonald, S. V. Morozov, K. Watanabe, T. Taniguchi, and L. A. Ponomarenko, "Strong Coulomb drag and broken symmetry in double-layer graphene", *Nat. Phys.* **8**, 896 (2012).
- ⁷⁸M Zarenia, A Perali, D Neilson, and F. Peeters, "Enhancement of electron-hole superfluidity in double few-layer graphene", *Sci. Rep.* **4**, 7319 (2014).
- ⁷⁹Y. Zhang, T. T. Tang, C. Girit, Z. Hao, M. C. Martin, A. Zettl, M. F. Crommie, Y. R. Shen, and F. Wang, "Direct observation of a widely tunable bandgap in bilayer graphene", *Nature (London)* **459**, 820 (2009).
- ⁸⁰J. I. A. Li, T. Taniguchi, K. Watanabe, J. Hone, A. Levchenko, and C. R. Dean, "Negative Coulomb drag in double bilayer graphene", *Phys. Rev. Lett.* **117**, 046802 (2016).
- ⁸¹K. Lee, J. Xue, D. C. Dillen, K. Watanabe, T. Taniguchi, and E. Tutuc, "Giant frictional drag in double bilayer graphene heterostructures", *Phys. Rev. Lett.* **117**, 046803 (2016).
- ⁸²K. Lee, B. Fallahazad, J. Xue, D. C. Dillen, K. Kim, T. Taniguchi, K. Watanabe, and E. Tutuc, "Chemical potential and quantum Hall ferromagnetism in bilayer graphene", *Science* **345**, 58 (2014).
- ⁸³M. Zarenia, A. R. Hamilton, F. M. Peeters, and D. Neilson, "Multiband mechanism for the sign reversal of Coulomb drag observed in double bilayer graphene heterostructures", *Phys. Rev. Lett.* **121**, 036601 (2018).
- ⁸⁴F. Xia, H. Wang, and Y. Jia, "Rediscovering black phosphorus as an anisotropic layered material for optoelectronics and electronics", *Nat. Commun.* **5**, 1 (2014).
- ⁸⁵V. Tran, R. Soklaski, Y. Liang, and L. Yang, "Layer-controlled band gap and anisotropic excitons in few-layer black phosphorus", *Phys. Rev. B* **89**, 235319 (2014).
- ⁸⁶A. Carvalho, M. Wang, X. Zhu, A. S. Rodin, H. Su, and A. H. Castro Neto, "Phosphorene: from theory to applications", *Nat. Rev. Mater.* **1**, 1 (2016).
- ⁸⁷T. Low, A. S. Rodin, A. Carvalho, Y. Jiang, H. Wang, F. Xia, and A. H. Castro Neto, "Tunable optical properties of multilayer black phosphorus thin films", *Phys. Rev. B* **90**, 075434 (2014).
- ⁸⁸X. Wang, A. M. Jones, K. L. Seyler, V. Tran, Y. Jia, H. Zhao, H. Wang, L. Yang, X. Xu, and F. Xia, "Highly anisotropic and robust excitons in monolayer black phosphorus", *Nature nanotechnology* **10**, 517 (2015).
- ⁸⁹S. Saberi-Pouya, T. Vazifeshenas, T. Salavati-fard, M. Farmanbar, and F. M. Peeters, "Strong anisotropic optical conductivity in two-dimensional puckered structures: The role of the Rashba effect", *Phys. Rev. B* **96**, 075411 (2017).
- ⁹⁰R. Zhang, J. Waters, A. K. Geim, and I. V. Grigorieva, "Intercalant-independent transition temperature in superconducting black phosphorus", *Nat. Commun.* **8**, 1 (2017).
- ⁹¹A. S. Rodin and A. H. Castro Neto, "Collective modes in anisotropic double-layer systems", *Phys. Rev. B* **91**, 075422 (2015).
- ⁹²S. Saberi-Pouya, T. Vazifeshenas, M. Farmanbar, and T. Salavati-Fard, "Coulomb drag in anisotropic systems: a theoretical study on a double-layer phosphorene", *J. Phys.: Cond. Matter* **28**, 285301 (2016).

- ⁹³O. L. Berman, G. Gumbs, and R. Y. Kezerashvili, "Bose-Einstein condensation and superfluidity of dipolar excitons in a phosphorene double layer", *Phys. Rev. B* **96**, 014505 (2017).
- ⁹⁴S. Saberi-Pouya, M. Zarenia, A. Perali, T. Vazifeshenas, and F. M. Peeters, "High-temperature electron-hole superfluidity with strong anisotropic gaps in double phosphorene monolayers", *Phys. Rev. B* **97**, 174503 (2018).
- ⁹⁵Y. Chen and S. Y. Quek, "Tunable bright interlayer excitons in few-layer black phosphorus based van der Waals heterostructures", *2D Materials* **5**, 045031 (2018).
- ⁹⁶T. C. Berkelbach, M. S. Hybertsen, and D. R. Reichman, "Theory of neutral and charged excitons in monolayer transition metal dichalcogenides", *Phys. Rev. B* **88**, 045318 (2013).
- ⁹⁷F. Wu, F. Qu, and A. H. MacDonald, "Exciton band structure of monolayer MoS₂", *Phys. Rev. B* **91**, 075310 (2015).
- ⁹⁸K. F. Mak and J. Shan, "Photonics and optoelectronics of 2D semiconductor transition metal dichalcogenides", *Nature Photonics* **10**, 216 (2016).
- ⁹⁹E. V. Calman, C. J. Dorow, M. M. Fogler, L. V. Butov, S. Hu, A. Mishchenko, and A. K. Geim, "Control of excitons in multi-layer van der Waals heterostructures", *Appl. Phys. Lett.* **108**, 101901 (2016).
- ¹⁰⁰I. C. Gerber and X. Marie, "Dependence of band structure and exciton properties of encapsulated WSe₂ monolayers on the hBN-layer thickness", *Phys. Rev. B* **98**, 245126 (2018).
- ¹⁰¹Y. Gong, J. Lin, X. Wang, G. Shi, S. Lei, Z. Lin, X. Zou, G. Ye, R. Vajtai, B. I. Yakobson, H. Terrones, M. Terrones, B. K. Tay, J. Lou, S. T. Pantelides, Z. Liu, W. Zhou, and P. M. Ajayan, "Vertical and in-plane heterostructures from WS₂/MoS₂ monolayers", *Nat. Mater.* **13**, 1135 (2014).
- ¹⁰²A. Chaves, J. G. Azadani, V. O. Öz çelik, R. Grassi, and T. Low, "Electrical control of excitons in van der waals heterostructures with type-II band alignment", *Phys. Rev. B* **98**, 121302 (2018).
- ¹⁰³M. Förg, L. Colombier, R. K. Patel, J. Lindlau, A. D Mohite, H. Yamaguchi, M. M. Glazov, D. Hunger, and A. Högele, "Cavity-control of interlayer excitons in van der Waals heterostructures", *Nat. Commun.* **10**, 3697 (2019).
- ¹⁰⁴P. Rivera, J. R. Schaibley, A. M. Jones, J. S. Ross, S. Wu, G. Aivazian, P. Klement, K. Seyler, G. Clark, N. J. Ghimire, J. Yan, D. G. Mandrus, W. Yao, and X. Xu, "Observation of long-lived interlayer excitons in monolayer MoSe₂-WSe₂ heterostructures", *Nat. Commun.* **6**, 6242 (2015).
- ¹⁰⁵O. L. Berman and R. Y. Kezerashvili, "Superfluidity of dipolar excitons in a transition metal dichalcogenide double layer", *Phys. Rev. B* **96**, 094502 (2017).
- ¹⁰⁶K. Kośmider, J. W. González, and J. Fernández-Rossier, "Large spin splitting in the conduction band of transition metal dichalcogenide monolayers", *Phys. Rev. B* **88**, 245436 (2013).
- ¹⁰⁷H. Suhl, B. T. Matthias, and L. R. Walker, "Bardeen-Cooper-Schrieffer theory of superconductivity in the case of overlapping bands", *Phys. Rev. Lett.* **3**, 552 (1959).
- ¹⁰⁸J. Nagamatsu, N. Nakagawa, T. Muranaka, Y. Zenitani, and J. Akimitsu, "Superconductivity at 39 K in magnesium diboride", *Nature* **410**, 63 (2001).
- ¹⁰⁹H. Takahashi, K. Igawa, K. Arii, Y. Kamihara, M. Hirano, and H. Hosono, "Superconductivity at 43 K in an iron-based layered compound LaO_{1-x}F_xFeAs", *Nature* **453**, 376 (2008).

- ¹¹⁰A. Bianconi, “Quantum materials: Shape resonances in superstripes”, *Nat. Phys.* **9**, 536 (2013).
- ¹¹¹A. A. Abrikosov, L. P. Gorkov, and I. E. Dzyaloshinski, *Methods of quantum field theory in statistical physics* (Courier Corporation, 2012).
- ¹¹²F. G. Kochorbe and M. E. Palistrant, “Superconductivity in a two-band system with low carrier density”, *J. Exp. Theor. Phys.* **77**, (Zh. Eksp. Teor. Fiz. **104**, 3084 (1993)), 442 (1993).
- ¹¹³A. A. Vargas-Paredes, A. A. Shanenko, A. Vagov, M. V. Milošević, and A. Perali, “Crossband versus intraband pairing in superconductors: signatures and consequences of the interplay”, *Phys. Rev. B* **101**, 094516 (2020).
- ¹¹⁴Y. E. Lozovik and A. A. Sokolik, “Multi-band pairing of ultrarelativistic electrons and holes in graphene bilayer”, *Phys. Rev. A* **374**, 326 (2009).
- ¹¹⁵G. Strinati, “A survey on the crossover from BCS superconductivity to Bose-Einstein condensation”, *Phys. Essays* **13**, 427 (2000).
- ¹¹⁶S. Giorgini, L. P. Pitaevskii, and S. Stringari, “Condensate fraction and critical temperature of a trapped interacting Bose gas”, *Phys. Rev. A* **54**, 4633 (1996).
- ¹¹⁷L. Salasnich, N. Manini, and A. Parola, “Condensate fraction of a Fermi gas in the BCS-BEC crossover”, *Phys. Rev. A* **72**, 023621 (2005).
- ¹¹⁸P. López Ríos, A. Perali, R. J. Needs, and D. Neilson, “Evidence from quantum Monte Carlo simulations of large-gap superfluidity and BCS-BEC crossover in double electron-hole layers”, *Phys. Rev. Lett.* **120**, 177701 (2018).
- ¹¹⁹A. Guidini and A. Perali, “Band-edge BCS-BEC crossover in a two-band superconductor: physical properties and detection parameters”, *Supercond. Sci. Tech.* **27**, 124002 (2014).
- ¹²⁰J. I. A. Li, T. Taniguchi, K. Watanabe, J. Hone, and C. Dean, “Excitonic superfluid phase in double bilayer graphene”, *Nat. Phys.* **13**, 751 (2017).
- ¹²¹G. Giuliani and G. Vignale, *Quantum theory of the electron liquid*, Masters Series in Physics and Astronomy (Cambridge University Press, 2005).
- ¹²²O. V. Gamayun, “Dynamical screening in bilayer graphene”, *Phys. Rev. B* **84**, 085112 (2011).
- ¹²³M. Y. Kharitonov and K. B. Efetov, “Excitonic condensation in a double-layer graphene system”, *Semicond. Sci. Technol.* **25**, 034004 (2010).
- ¹²⁴I. Sodemann, D. A. Pesin, and A. H. MacDonald, “Interaction-enhanced coherence between two-dimensional Dirac layers”, *Phys. Rev. B* **85**, 195136 (2012).
- ¹²⁵R. Maezono, P. López Ríos, T. Ogawa, and R. J. Needs, “Excitons and biexcitons in symmetric electron-hole bilayers”, *Phys. Rev. Lett.* **110**, 216407 (2013).
- ¹²⁶E. V. Castro, K. S. Novoselov, S. V. Morozov, N. M. R. Peres, J. M. B. L. dos Santos, J. Nilsson, F. Guinea, A. K. Geim, and A. H. Castro Neto, “Biased bilayer graphene: semiconductor with a gap tunable by the electric field effect”, *Phys. Rev. Lett.* **99**, 216802 (2007).
- ¹²⁷S. Rinott, K. B. Chashka, A. Ribak, E. D. L. Rienks, A. Taleb-Ibrahimi, P. Le Fevre, F. Bertran, M. Randeria, and A. Kanigel, “Tuning across the BCS-BEC crossover in the multiband superconductor $\text{Fe}_{1+y}\text{Se}_x\text{Te}_{1-x}$: An angle-resolved photoemission study”, *Sci. Adv.* **3**, e1602372 (2017).

- ¹²⁸L. Komendová, Y. Chen, A. A. Shanenko, M. V. Milošević, and F. M. Peeters, “Two-band superconductors: hidden criticality deep in the superconducting state”, *Phys. Rev. Lett.* **108**, 207002 (2012).
- ¹²⁹J. Kortus, I. I. Mazin, K. D. Belashchenko, V. P. Antropov, and L. L. Boyer, “Superconductivity of metallic boron in MgB_2 ”, *Phys. Rev. Lett.* **86**, 4656 (2001).
- ¹³⁰K. K. Kim, A. Hsu, X. Jia, S. M. Kim, Y. Shi, M. Dresselhaus, T. Palacios, and J. Kong, “Synthesis and characterization of hexagonal boron nitride film as a dielectric layer for graphene devices”, *ACS Nano* **6**, 8583 (2012).
- ¹³¹N. W. Ashcroft and M. N. D., *Solid state physics*, edited by T. Press (Singapore, 2003).
- ¹³²A. B. Kuzmenko, I. Crassee, D. van der Marel, P. Blake, and K. S. Novoselov, “Determination of the gate-tunable band gap and tight-binding parameters in bilayer graphene using infrared spectroscopy”, *Phys. Rev. B* **80**, 165406 (2009).
- ¹³³E. V. Castro, K. S. Novoselov, S. V. Morozov, N. M. R. Peres, J. M. B. L. Dos Santos, J. Nilsson, F. Guinea, A. K. Geim, and A. H. Castro Neto, “Electronic properties of a biased graphene bilayer”, *J. Phys. Condens. Mat.* **22**, 175503 (2010).
- ¹³⁴E. McCann and M. Koshino, “The electronic properties of bilayer graphene”, *Rep. Prog. Phys.* **76**, 056503 (2013).
- ¹³⁵X.-F. Wang and T. Chakraborty, “Coulomb screening and collective excitations in biased bilayer graphene”, *Phys. Rev. B* **81**, 081402 (2010).
- ¹³⁶K. Zou, X. Hong, and J. Zhu, “Effective mass of electrons and holes in bilayer graphene: electron-hole asymmetry and electron-electron interaction”, *Phys. Rev. B* **84**, 085408 (2011).
- ¹³⁷A. A. Shanenko, J. A. Aguiar, A. Vagov, M. D. Croitoru, and M. V. Milošević, “Atomically flat superconducting nanofilms: multiband properties and mean-field theory”, *Supercond. Sci. Tech.* **28**, 054001 (2015).
- ¹³⁸P. Kumar, Y. S. Chauhan, A. Agarwal, and S. Bhowmick, “Thickness and stacking dependent polarizability and dielectric constant of graphene–hexagonal boron nitride composite stacks”, *J. Phys. Chem. C* **120**, 17620 (2016).
- ¹³⁹Y. Barlas, T. Pereg-Barnea, M. Polini, R. Asgari, and A. H. MacDonald, “Chirality and correlations in graphene”, *Phys. Rev. Lett.* **98**, 236601 (2007).
- ¹⁴⁰E. H. Hwang, R. Sensarma, and S. Das Sarma, “Coulomb drag in monolayer and bilayer graphene”, *Phys. Rev. B* **84**, 245441 (2011).
- ¹⁴¹L. Brey and H. A. Fertig, “Elementary electronic excitations in graphene nanoribbons”, *Phys. Rev. B* **75**, 125434 (2007).
- ¹⁴²T. Stauber, N. M. R. Peres, F. Guinea, and A. H. Castro Neto, “Fermi liquid theory of a Fermi ring”, *Phys. Rev. B* **75**, 115425 (2007).
- ¹⁴³T. Ohta, A. Bostwick, T. Seyller, K. Horn, and E. Rotenberg, “Controlling the electronic structure of bilayer graphene”, *Science* **313**, 951 (2006).
- ¹⁴⁴E. H. Hwang and S. Das Sarma, “Screening, Kohn anomaly, Friedel oscillation, and RKKY interaction in bilayer graphene”, *Phys. Rev. Lett.* **101**, 156802 (2008).
- ¹⁴⁵G. Borghi, M. Polini, R. Asgari, and A. H. MacDonald, “Dynamical response functions and collective modes of bilayer graphene”, *Phys. Rev. B* **80**, 241402 (2009).
- ¹⁴⁶H. Min, E. H. Hwang, and S. Das Sarma, “Polarizability and screening in chiral multilayer graphene”, *Phys. Rev. B* **86**, 081402 (2012).

- ¹⁴⁷C. Triola and E. Rossi, "Screening and collective modes in gapped bilayer graphene", *Phys. Rev. B* **86**, 161408 (2012).
- ¹⁴⁸C.-H. Park and S. G. Louie, "Tunable excitons in biased bilayer graphene", *Nano Lett.* **10**, 426 (2010).
- ¹⁴⁹E. V. Calman, M. M. Fogler, L. V. Butov, S. Hu, A. Mishchenko, and A. K. Geim, "Indirect excitons in van der Waals heterostructures at room temperature", *Nat. Commun.* **9**, 1 (2018).
- ¹⁵⁰K. F. Mak, C. Lee, J. Hone, J. Shan, and T. F. Heinz, "Atomically thin MoS₂: a new direct-gap semiconductor", *Phys. Rev. Lett.* **105**, 136805 (2010).
- ¹⁵¹H. Jiang, "Electronic band structures of molybdenum and tungsten dichalcogenides by the GW approach", *J. Phys. Chem. C* **116**, 7664 (2012).
- ¹⁵²D. Xiao, G. B. Liu, W. Feng, X. Xu, and W. Yao, "Coupled spin and valley physics in monolayers of MoS₂ and other group-VI dichalcogenides", *Phys. Rev. Lett.* **108**, 196802 (2012).
- ¹⁵³A. A. Shanenko, M. D. Croitoru, A. V. Vagov, V. M. Axt, A. Perali, and F. M. Peeters, "Atypical BCS-BEC crossover induced by quantum-size effects", *Phys. Rev. A* **86**, 033612 (2012).
- ¹⁵⁴Y. Mizohata, M. Ichioka, and K. Machida, "Multiple-gap structure in electric-field-induced surface superconductivity", *Phys. Rev. B* **87**, 014505 (2013).
- ¹⁵⁵G. Singh, A. Jouan, G. Herranz, M. Scigaj, F. Sánchez, L. Benfatto, S. Caprara, M. Grilli, G. Saiz, F. Couëdo, C. Feuillet-Palma, J. Lesueur, and N. Bergeal, "Gap suppression at a Lifshitz transition in a multi-condensate superconductor", *Nat. Mater.* **18**, 948 (2019).
- ¹⁵⁶M. Van der Donck and F. M. Peeters, "Interlayer excitons in transition metal dichalcogenide heterostructures", *Phys. Rev. B* **98**, 115104 (2018).
- ¹⁵⁷Z. Y. Zhu, Y. C. Cheng, and U. Schwingenschlögl, "Giant spin-orbit-induced spin splitting in two-dimensional transition-metal dichalcogenide semiconductors", *Phys. Rev. B* **84**, 153402 (2011).
- ¹⁵⁸H. Fang, C. Battaglia, C. Carraro, S. Nemsak, B. Ozdol, J. S. Kang, H. A. Bechtel, S. B. Desai, F. Kronast, A. A. Unal, et al., "Strong interlayer coupling in van der waals heterostructures built from single-layer chalcogenides", *Proc. Natl. Acad. Sci.* **111**, 6198 (2014).
- ¹⁵⁹F.-F. Yu, S.-S. Ke, S.-S. Guan, H.-X. Deng, Y. Guo, and H.-F. Lü, "Effects of Se substitution and transition metal doping on the electronic and magnetic properties of a MoS_xSe_{2-x}/h-BN heterostructure", *Phys. Chem. Chem. Phys.* **21**, 20073 (2019).
- ¹⁶⁰A. Kormányos, V. Zólyomi, N. D. Drummond, P. Rakyta, G. Burkard, and V. I. Fal'ko, "Monolayer MoS₂: Trigonal warping, the Γ valley, and spin-orbit coupling effects", *Phys. Rev. B* **88**, 045416 (2013).
- ¹⁶¹M. Randeria, J.-M. Duan, and L.-Y. Shieh, "Superconductivity in a two-dimensional Fermi gas: Evolution from Cooper pairing to Bose condensation", *Phys. Rev. B* **41**, 327 (1990).
- ¹⁶²F. Pistolesi and G. C. Strinati, "Evolution from BCS superconductivity to Bose condensation: role of the parameter $k_F\zeta$ ", *Phys. Rev. B* **49**, 6356 (1994).
- ¹⁶³J. M. Kosterlitz and D. J. Thouless, "Ordering, metastability and phase transitions in two-dimensional systems", *J. Phys. C: Solid State* **6**, 1181 (1973).

- ¹⁶⁴L. Benfatto, M. Capone, S. Caprara, C. Castellani, and C. Di Castro, "Multiple gaps and superfluid density from interband pairing in a four-band model of the iron oxypnictides", *Phys. Rev. B* **78**, 140502 (2008).
- ¹⁶⁵S. S. Botelho and C. A. R. Sá de Melo, "Vortex-antivortex lattice in ultracold fermionic gases", *Phys. Rev. Lett.* **96**, 040404 (2006).
- ¹⁶⁶S. Rist, A. A. Varlamov, A. H. MacDonald, R. Fazio, and M. Polini, "Photoemission spectra of massless Dirac fermions on the verge of exciton condensation", *Phys. Rev. B* **87**, 075418 (2013).
- ¹⁶⁷H. Miao, P. Richard, Y. Tanaka, K. Nakayama, T. Qian, K. Umezawa, T. Sato, Y.-M. Xu, Y. B. Shi, N. Xu, X.-P. Wang, P. Zhang, H.-B. Yang, Z.-J. Xu, J. S. Wen, G.-D. Gu, X. Dai, J.-P. Hu, T. Takahashi, and H. Ding, "Isotropic superconducting gaps with enhanced pairing on electron Fermi surfaces in $\text{FeTe}_{0.55}\text{Se}_{0.45}$ ", *Phys. Rev. B* **85**, 094506 (2012).
- ¹⁶⁸D. Daghero, P. Pecchio, G. A. Ummarino, F. Nabeshima, Y. Imai, A. Maeda, I. Tsukada, S. Komiya, and R. S. Gonnelli, "Point-contact Andreev-reflection spectroscopy in Fe (Te, Se) films: multiband superconductivity and electron-boson coupling", *Supercond. Sci. Tech.* **27**, 124014 (2014).
- ¹⁶⁹T. E. Kuzmicheva, S. A. Kuzmichev, A. V. Sadakov, A. V. Muratov, A. S. Usoltsev, V. P. Martovitsky, A. R. Shipilov, D. A. Chareev, E. S. Mitrofanova, and V. M. Pudalov, "Direct evidence of two superconducting gaps in $\text{FeSe}_{0.5}\text{Te}_{0.5}$: n-Andreev spectroscopy and the lower critical field", *JETP Lett.* **104**, 852 (2016).
- ¹⁷⁰J. X. Yin, Z. Wu, J. H. Wang, Z. Y. Ye, J. Gong, X. Y. Hou, L. Shan, A. Li, X. J. Liang, X. X. Wu, et al., "Observation of a robust zero-energy bound state in iron-based superconductor Fe (Te, Se)", *Nat. Phys.* **11**, 543 (2015).
- ¹⁷¹A. Perali, P. Pieri, G. C. Strinati, and C. Castellani, "Pseudogap and spectral function from superconducting fluctuations to the bosonic limit", *Phys. Rev. B* **66**, 024510 (2002).
- ¹⁷²L. Salasnich, A. A. Shanenko, A. Vagov, J. A. Aguiar, and A. Perali, "Screening of pair fluctuations in superconductors with coupled shallow and deep bands: A route to higher-temperature superconductivity", *Phys. Rev. B* **100**, 064510 (2019).
- ¹⁷³A. Chaves and D. Neilson, "Two-dimensional semiconductors host high-temperature exotic state", *Nature* **574**, 39 (2019).
- ¹⁷⁴M. Franz, "Importance of fluctuations", *Nat. Phys.* **3**, 686 (2007).
- ¹⁷⁵N. D. Mermin and H. Wagner, "Absence of ferromagnetism or antiferromagnetism in one- or two-dimensional isotropic Heisenberg models", *Phys. Rev. Lett.* **17**, 1133 (1966).
- ¹⁷⁶P. C. Hohenberg, "Existence of long-range order in one and two dimensions", *Phys. Rev.* **158**, 383 (1967).
- ¹⁷⁷V. L. Berezinsky, "Destruction of long-range order in one-dimensional and two-dimensional systems possessing a continuous symmetry group. II. quantum systems.", *Sov. Phys. JETP* **34**, (Zh. Eksp. Teor. Fiz. **61**, 1144 (1972)), 610 (1972).
- ¹⁷⁸M. D. Croitoru and A. I. Buzdin, "Extended Lawrence-Doniach model: The temperature evolution of the in-plane magnetic field anisotropy", *Phys. Rev. B* **86**, 224508 (2012).
- ¹⁷⁹L. B. Ioffe and A. J. Millis, "Superconductivity and the c axis spectral weight of high- T_c superconductors", *Science* **285**, 1241 (1999).
- ¹⁸⁰D. G. Clarke and S. P. Strong, "'Confined coherence' in strongly correlated anisotropic metals", *Adv. Phys.* **46**, 545 (1997).

- ¹⁸¹A. Laturia, M. L. Van de Put, and W. G. Vandenberghe, "Dielectric properties of hexagonal boron nitride and transition metal dichalcogenides: from monolayer to bulk", *npj 2D Materials and Applications* **2**, 6 (2018).
- ¹⁸²R. Haussmann, "Properties of a Fermi liquid at the superfluid transition in the crossover region between BCS superconductivity and Bose-Einstein condensation", *Phys. Rev. B* **49**, 12975 (1994).
- ¹⁸³M. Pini, P. Pieri, and G. C. Strinati, "Fermi gas throughout the BCS-BEC crossover: Comparative study of t -matrix approaches with various degrees of self-consistency", *Phys. Rev. B* **99**, 094502 (2019).
- ¹⁸⁴C. J. Pethick and H. Smith, *Bose-Einstein Condensation in dilute gases*, 2nd (Cambridge University Press, 2008).
- ¹⁸⁵E. Burovski, E. Kozik, N. Prokof'ev, B. Svistunov, and M. Troyer, "Critical temperature curve in BEC-BCS crossover", *Phys. Rev. Lett.* **101**, 090402 (2008).
- ¹⁸⁶C. C. Bradley, C. A. Sackett, J. J. Tollett, and R. G. Hulet, "Evidence of Bose-Einstein condensation in an atomic gas with attractive interactions", *Phys. Rev. Lett.* **75**, 1687 (1995).
- ¹⁸⁷K. B. Davis, M. O. Mewes, M. R. Andrews, N. J. van Druten, D. S. Durfee, D. M. Kurn, and W. Ketterle, "Bose-Einstein condensation in a gas of Sodium atoms", *Phys. Rev. Lett.* **75**, 3969 (1995).
- ¹⁸⁸M. J. Yang, C. H. Yang, B. R. Bennett, and B. V. Shanabrook, "Evidence of a hybridization gap in "semimetallic" InAs/GaSb systems", *Phys. Rev. Lett.* **78**, 4613 (1997).
- ¹⁸⁹Y. E. Lozovik and A. A. Sokolik, "Coherent phases and collective electron phenomena in graphene", *J. Phys. Conf. Ser.* **129**, 012003 (2008).
- ¹⁹⁰Y. Cao, V. Fatemi, S. Fang, K. Watanabe, T. Taniguchi, E. Kaxiras, and P. Jarillo-Herrero, "Unconventional superconductivity in magic-angle graphene superlattices", *Nature* **556**, 43 (2018).
- ¹⁹¹R. Bistritzer and A. H. MacDonald, "Moiré bands in twisted double-layer graphene", *Proc. Natl. Acad. Sci.* **108**, 12233 (2011).
- ¹⁹²M. Zarenia, D. Neilson, B. Partoens, and F. M. Peeters, "Wigner crystallization in transition metal dichalcogenides: a new approach to correlation energy", *Phys. Rev. B* **95**, 115438 (2017).
- ¹⁹³L. Du, X. Li, W. Lou, G. Sullivan, K. Chang, J. Kono, and R.-R. Du, "Evidence for a topological excitonic insulator in InAs/GaSb bilayers", *Nat. Commun.* **8**, 1971 (2017).
- ¹⁹⁴Y.-C. Zhang, F. Maucher, and T. Pohl, "Supersolidity around a critical point in dipolar Bose-Einstein condensates", *Phys. Rev. Lett.* **123**, 015301 (2019).
- ¹⁹⁵M. Zarenia, D. Neilson, and F. M. Peeters, "Inhomogeneous phases in coupled electron-hole bilayer graphene sheets: charge density waves and coupled Wigner crystals.", *Sci. Rep.* **7**, 11510 (2017).
- ¹⁹⁶Y. Pan, S. Fölsch, Y. Nie, D. Waters, Y.-C. Lin, B. Jariwala, K. Zhang, K. Cho, J. A. Robinson, and R. M. Feenstra, "Quantum-confined electronic states arising from the moiré pattern of MoS₂-WSe₂ heterobilayers", *Nano Lett.* **18**, 1849 (2018).
- ¹⁹⁷K. L. Seyler, P. Rivera, H. Yu, N. P. Wilson, E. L. Ray, D. G. Mandrus, J. Yan, W. Yao, and X. Xu, "Signatures of moiré-trapped valley excitons in MoSe₂/WSe₂ heterobilayers", *Nature* **567**, 66 (2019).

- ¹⁹⁸K. Tran, G. Moody, F. Wu, X. Lu, J. Choi, K. Kim, A. Rai, D. A. Sanchez, J. Quan, A. Singh, J. Embley, A. Zepeda, M. Campbell, T. Autry, T. Taniguchi, K. Watanabe, N. Lu, S. K. Banerjee, K. L. Silverman, S. Kim, E. Tutuc, L. Yang, M. A. H., and X. Li, "Evidence for moiré excitons in van der Waals heterostructures", *Nature* **567**, 71 (2019).

Curriculum Vitae

Name: Sara Conti

Address: Raafstraat 4/1, 2018, Antwerpen, Belgium

Phone number: +39 3389805803

E-mail: saraconti19@gmail.com

Web Page: <https://www.linkedin.com/in/saraconti19/>

Skype:saraconti19



Date of birth: 19 November 1989

Nationality: Italian

Gender: Female

Education and training

- **Joint PhD in Theoretical and Experimental Physics** 2016 - present
University of Camerino, Camerino(MC), Italy.
University of Antwerpen, CMT group, Antwerp, Belgium.
- **Qualifying Course for Didactics** 2017–2018
University of Camerino, Camerino(MC), Italy.
 - Didactic and educational methods
 - Didactic technologies
 - Anthropology
 - Learning processes Psychology
- **2nd level degree in Theretical Physics** 2013–2016
University of Camerino, Camerino(MC), Italy.
Thesis: Electron-hole superfluidity in non conventional semiconductor systems.
- **1st level degree in Physics** 2008–2012
University of Camerino, Camerino(MC), Italy.
Thesis: Didactic of Physics for high school students on Statistical Mechanics.

Publications

- S. Conti, A. Perali, D. Neilson and F. Peeters, *Tuning the BEC-BCS crossover in electron-hole double bilayer graphene superfluidity using multiband effects.*, Feature article in Belgian Physical Society Magazine - 03/2017.
- S. Conti, A. Perali, F. M. Peeters, and D. Neilson, *Multicomponent Electron-Hole Superfluidity and the BCS-BEC Crossover in Double Bilayer Graphene.*, Phys. Rev. Lett. 119, 257002 (2017).

-
- S. Conti, A. Perali, F. M. Peeters, and D. Neilson, *Multicomponent screening and superfluidity in gapped electron-hole double bilayer graphene with realistic bands*. Phys. Rev. B, 99, 144517 (2019).
 - M. Zarenia, S. Conti, F. M. Peeters, and D. Neilson, *Coulomb drag in strongly coupled quantum wells: temperature dependence of the many-body correlations*. Appl. Phys. Lett. 115, 202105 (2019).
 - S. Conti, M. Van der Donck, A. Perali, F. M. Peeters, and D. Neilson, *A doping-dependent switch from one- to two-component superfluidity at temperature above 100K in coupled electron-hole Van der Waals heterostructures*. ArXiv:1909.03411 (2019).
 - M. Van der Donck, S. Conti, A. Perali, A. R. Hamilton, B. Partoens, F. M. Peeters, *Three-dimensional electron-hole superfluidity in a superlattice close to room temperature*. ArXiv:1911.01123 (2019).
 - S. Saberi-Pouya, S. Conti, A. Perali, A. F. Croxall, A. R. Hamilton, F. M. Peeters, D. Neilson, *Experimental conditions for observation of electron-hole superfluidity in GaAs heterostructures*. Phys. Rev. B, 101, 140501(R) (2020).
 - S. Conti, D. Neilson, F. M. Peeters, and A. Perali, *Transition Metal Dichalcogenides as Strategy for High Temperature Electron-Hole Superfluidity*. Condens. Matter 5, 22 (2020).

Awards

- Best poster from Belgian Physical Society (05/2017).
- Best poster from Strongly Coupled Coulomb Systems (08/2017).
- Travel award from Graphene Flagship for Graphene week 2018 (09/2018)
- Travel award from FWO for Recent Progress in Many Body Physics 2019 (09/2019)
- Zonta International price Women In Technologies from Zonta club Antwerp.
- Ovshinsky Travel award from APS for APS March meeting 2020 (03/2020)

Conferences and Workshops

- Ugo Fano Symposium 2016, Rome, Italy (Poster presentation)
- Belgian Physics Society general scientific meeting 2017, Mons, Belgium (Poster presentation)
- Strongly Coupled Coulomb Systems 2017, Kiel, Germany (Poster presentation)
- Solvay workshop 2017 "From physics of graphene to graphene for physics", Brussels, Belgium
- MultiCondensate Superconductivity and Superfluidity in Solids and Ultracold Gases 2018, Trieste, Italy (Poster presentation)
- Low Energy Electrodynamics in Solids 2018, Portonovo (AN), Italy (Invited Talk)
- Graphene Week 2018, San Sebastian, Spain (Poster presentation)

-
- APS March meeting 2019, Boston, USA (Talk)
 - Superfluctuation 2019, Padova, Italy (Invited Talk)
 - Recent Progress in Many Body Physics 2019, Toulouse, France (Poster presentation)

Teaching Activities

- 03/2017 - Seminar on Superconductivity for high school students.
- 2018/2019 - Didactic Tutor of Classical Mechanics for bachelor degrees in Physics (University of Camerino).
- 11/2019 - "Elements of Physics" for degrees in Pharmacy (University of Camerino).

Personal Skills

- **LANGUAGES**

NATIVE Italian

FOREIGN English (B2), French (B1)

- **COMPUTER SKILLS**

OPERATING SYSTEMS

Linux, Windows

TEXT AND TYPESETTING EDITORS

Excel, Powerpoint, Word, LaTeX

PROGRAMMING LANGUAGES

Fortran, Python

MATHEMATICAL SOFTWARE

Mathematica, Gnuplot